uOttawa

L'Université canadienne
Canada's university

FACULTÉ DES ÉTUDES SUPÉRIEURES ET POSTOCTORALES

uOttawa

L'Université canadienne
Canada's university

FACULTY OF GRADUATE AND POSDOCTORAL STUDIES

Tamer El-Bokl

AUTEUR DE LA THÈSE / AUTHOR OF THESIS

Ph.D. (Chemistry)

GRADE / DEGREE

Department of Chemistry

FACULTÉ, ÉCOLE, DÉPARTEMENT / FACULTY, SCHOOL, DEPARTMENT

Nanohybrid and Nanocomposite Materials from Kaolinite

TITRE DE LA THÈSE / TITLE OF THESIS

Christian Detellier

DIRECTEUR (DIRECTRICE) DE LA THÈSE / THESIS SUPERVISOR

CO-DIRECTEUR (CO-DIRECTRICE) DE LA THÈSE / THESIS CO-SUPERVISOR

EXAMINATEURS (EXAMINATRICES) DE LA THÈSE / THESIS EXAMINERS

Kathleen Carrado-Argonne

Darrin Richeson

Muralee Murugesu

John Ripmeester

Gary W. Slater

Le Doyen de la Faculté des études supérieures et postdoctorales / Dean of the Faculty of Graduate and Postdoctoral Studies

# Nanohybrid and Nanocomposite Materials from Kaolinite

by

**Tamer A. El Bokl**

A thesis submitted to the
Faculty of Graduate and Postdoctoral Studies
University of Ottawa

in partial fulfillment of the requirements for the

**Ph.D. degree in Chemistry**

in the
Ottawa–Carleton Chemistry Institute
Ottawa, Ontario
August 2007

Ph.D. Candidate
Tamer Abd Elhady El Bokl

Research Supervisor
Professor Christian Detellier

Library and
Archives Canada

Published Heritage
Branch

395 Wellington Street
Ottawa ON K1A 0N4
Canada

Bibliothèque et
Archives Canada

Direction du
Patrimoine de l'édition

395, rue Wellington
Ottawa ON K1A 0N4
Canada

*Your file Votre référence*
*ISBN: 978-0-494-49341-0*
*Our file Notre référence*
*ISBN: 978-0-494-49341-0*

*This thesis is dedicated with love to my mother; my father; my wife, Mariem; my son, Fareed; my daughter, Jana; my brother; and my sister.*

*It is also dedicated to my late grandparents.*

# Acknowledgements

In the first place, I would like to emphasize that this thesis could not have been completed without the guidance and close supervision of my research supervisor, Professor Christian Detellier. He not only supervised the work but also continuously encouraged and challenged my capabilities, never accepting less than my best efforts, at every stage of the thesis. His unlimited, extraordinary knowledge enriched my learning experience in many ways. I am truly indebted to him more than I can think.

This thesis is the result of the years of research that has been done since I joined Detellier's group in the University of Ottawa. During that time, I have worked with a great number of people whose contribution in many ways, including merely friendship, to the research and the making of the thesis deserved special mention. It is my pleasure to record my gratitude to them all in my humble acknowledgment, namely, Guillaume Defontaine, Sadok Letaief, Najat Zougagh, Ziyad Taha, Wenxing Kuang, Mathieu Frenette, Jan Rhynhardt, Catherine Grgicak, Amir Jabri, and many others.

I am grateful to the administration members in the department of chemistry and the graduate-studies office. The XRD help from Ron Hartree is gratefully acknowledged. Dr. Glenn A. Facey and Cheryl McDowall are acknowledged for their help with NMR analysis. I also thank Judy Busnarda, Carol McKinley, and Evelyn Kidd at NRC Research Press for their continuous support. Finally, I would like to thank all members of my family in Canada and in Egypt for their love, help, and support during my studies, especially my wife, Mariem, and my mother for their patience. ***It is to them I dedicate this thesis.***

# Abstract

A variety of organic moieties, including biodegradable polyesters, were intercalated into the interlayer spaces of kaolinite, a naturally occurring clay mineral, in an attempt to explore and extend its interlamellar chemistry. Several novel intercalated nanohybrids of kaolinite and cyclic imides were synthesized by simply performing the reactions at ambient temperatures. Intercalation is generally achieved by displacing the pre-intercalated guest organic molecules from the intermediate intercalate. The complete displacement of the guest molecules by the cyclic imides was confirmed by the results of XRD and $^{13}C$ NMR analyses. The interaction between the intercalated molecules and the interlamellar surfaces of kaolinite was studied by FTIR analysis. Furthermore, the intercalation of alditols, adonitol and D-sorbitol, into the interlamellar spaces of kaolinite was achieved, and the grafting of the hydroxyl groups of these alditols onto the aluminol internal surfaces of kaolinite followed the intercalation via thermal treatment. Also, the modification of the interlamellar surfaces of kaolinite by the direct grafting of two different alditols, namely, D-mannitol and dulcitol, from the melt is reported. Several starting materials were used among which the kaolinite–DMSO intercalate was the most effective. This was done directly from the alditol melt at temperatures just above the melting point of these polyols. The intercalated polyols are arranged in a flattened monolayer arrangement, as indicated by the interlayer expansions. $^{13}C$ CP/ and DD/MAS NMR indicated the complete replacement of the DMSO by the alditol, and that the alditols were rigidly constrained in the interlamellar spaces of kaolinite. Thermal analysis shows that the loss of the grafted alditols coincides with the dehydroxylation of the kaolinite layers. The intercalation process was followed with time in the

case of adonitol. The reaction proceeds via a partial collapse of the Kao–DMSO intercalate before the steps corresponding to the intercalation of adonitol.

In addition, a new family of kaolinite–polymer nanocomposites was prepared by the intercalation of a series of biodegradable polyesters in the interlayer spaces of kaolinite. The intercalation was achieved directly from the polymer melt. The results of the TGA/DTA analyses showed enhanced thermal stabilities of the produced nanohybrids and nanocomposites compared to the starting materials.

Finally, promising attempts that involved alternative synthesis strategies for the preparation of kaolinite–polymer nanocomposites are presented.

# Table of contents

# List of figures

# List of tables

# Chapter 1

# Introduction

## 1.1 Kaolinite as a mineral precursor

Kaolinite is the most abundant mineral of the kaolin group, which also includes dickite, nacrite, and halloysite, their hydrated analogue. These are 1:1 phyllosilicates, characterized by a 1:1 dioctahedral structure, with the chemical composition $Al_2Si_2O_5(OH)_4$. Since it is made up of two types of interlayer surfaces, $(SiO)_6$ macrorings on one side and aluminol groups on the other side, kaolinite is remarkable by its non-centrosymmetric structure. This asymmetry creates large superposed dipoles in the lamellar structure, resulting in a large cohesive energy (1). Consequently, the intercalation chemistry of kaolinite is less developed than that of the swelling smectites (2), but the intercalation of salts and of dipolar organic molecules is well-documented (3–28), and the factors controlling the intercalation include particle size and degree of ordering (29). More recently, the functionalization of the aluminol surface of kaolinite was achieved through the covalent grafting of organic molecules such as methanol, ethylene glycol, diols, and recently polyols (7–8, 15–17, 19, 21, 23). The grafting of other compounds such as phenylphosphonic acid was also reported (10).

Recently, organic–inorganic nanohybrid materials, known as polymer nanocomposites, have become an effective alternative to conventional polymer composites in many applications. Polymer–layered silicate (PLS) nanocomposites have one characteristic dimension in the order of the nanometer for the inorganic phase. They exhibit enhanced mechanical and thermal

properties in addition to decreased gas permeability, improved flame retardation properties, and increased solvent resistance. In general, two types of polymer–layered clay nanocomposites can be obtained, intercalates and exfoliates (30–34). Intercalates are obtained when a single polymer chain is located between clay layers in a manner that increases layer spacing, while attractive forces between the layers keep these in regularly spaced stacks. Exfoliates are obtained when the layer spacing is increased enough to overcome the interactions between layers, which become randomly dispersed in a continuous polymer matrix (31). Several methods can be employed for the synthesis of PLS nanocomposites. While smectites are widely used for the preparation of PLS (31), a few examples of kaolinite–polymer intercalated nanocomposites have been reported (9, 12, 13, 18, 20, 22, 24, 35).

## 1.2 Generalities

### 1.2.1 Description of the Clay Minerals

Clay minerals are naturally occurring minerals that formed as a result of the weathering of rocks, usually feldspars. Thus, the type of clay depends on the environmental conditions in which the weathering process occurred. Then, the clays either remain where they are to give rise to "residual clays" or they can be transported by water, wind, and (or) ice to be deposited as beds of clay in the sea, in lakes, or as land deposits. Clay minerals belong to the family of minerals called "phyllosilicates" (Greek: phyllon = leaf) or layered silicates (LS) (1).

#### 1.2.1.1 Structure

Layered silicates may be thought of as being composed from two types of extended two-dimensional units. The first is a sheet of corner-linked tetrahedra, and the second is a sheet of edge-linked octahedra. The manner in which these two units are joined and arranged determines the type of clay mineral. One clay layer is made up of two or three of these sheets which are joined together. Then, the layers are stacked upon each other.

The structural unit of a tetrahedral sheet is composed primarily of $Si^{4+}$ cations in tetrahedral coordination with oxygen. $Al^{3+}$ or $Fe^{3+}$ usually substitute for $Si^{4+}$, thus imparting a net negative charge to the sheet. Each tetrahedron can be thought to rest on a triangular face with the oxygens on all three corners being shared with neighbouring tetrahedra. The fourth apical oxygen points upward, perpendicular to the base. Under zero-strain conditions, this sheet would be hexagonal, with the Si–O bond distance equal to 1.62 Å, and the O–O distance equal to 2.64 Å. Figure 1.1a shows the idealized hexagonal pattern (1, 36, 37).

The octahedral sheet consists of two planes of closest-packed oxygen or hydroxyl ions with cations occupying the resulting octahedral sites between the two planes (Fig. 1.1b). The cations are usually $Al^{3+}$ or $Mg^{2+}$, although many transition-metal cations or $Li^{+}$ may also be found in the octahedral holes. The minerals gibbsite ($Al(OH)_3$) and brucite ($Mg(OH)_2$) are the two prototypes commonly used to describe dioctahedral and trioctahedral clay minerals, respectively. In gibbsite, two out of three octahedral holes are occupied by $Al^{3+}$ cations, whereas in brucite, all three octahedral holes are occupied by $Mg^{2+}$. In the free octahedral sheets, the lateral b dimension of the unit cells is 8.64 Å for the dioctahedral gibbsite and 9.36 Å for the trioctahedral brucite (37).

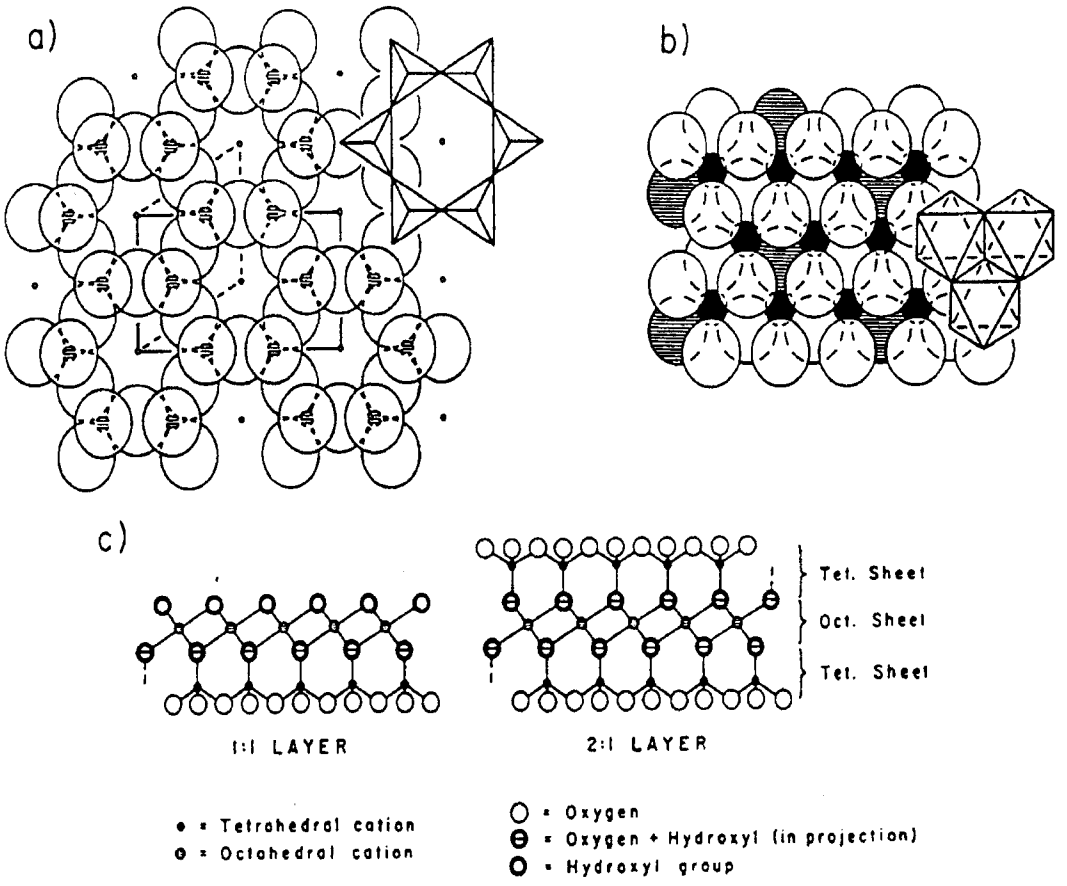


**Fig.1.1.** (a) Idealized tetrahedral sheet with hexagonal (dashed line) and orthogonal (full line) cells; (b) idealized octahedral sheet with OH groups of lower anion plane (dashed circles) shown shaded; for a 1:1 layer, upper anion plane (full circles) will be entirely OH groups; for a 2:1 layer, upper anion plane will be of same composition as lower anion plane; (c) combination of sheets to form 1:1 and 2:1 layers. (reproduced from ref. 1 with permission).

Consequently, the tetrahedral and octahedral sheets are joined together by the replacement of two out of three hydroxyls in one of the octahedral planes by the apical oxygens of the tetrahedral sheet. The third hydroxyl fits into the middle of the hexagonal ring of the tetrahedral sheet. When one tetrahedral and one octahedral sheet are joined together, this is called a 1:1 layered silicate structure (Fig. 1.1c). If an additional tetrahedral layer is joined in the same manner to the free hydroxyl surface of the 1:1 layered silicate structure, a 2:1 layered silicate structure is formed (Fig. 1.1c).

The lateral dimensions of the tetrahedral sheet rarely fit that of the octahedral sheet. A tetrahedral sheet containing only silicon has an ideal lateral b dimension intermediate between those of the ideal octahedral sheets containing only Mg (brucite) or only Al (gibbsite). The misfit is approximately 3%–5% for these cases (37). Consequently, distortions or adjustments to the tetrahedral and (or) octahedral sheets are necessary to join the sheets together. The rotation or tilting of the tetrahedra or the thickening or thinning of octahedral or tetrahedral sheets are common ways of adjustments. Notably, the isomorphic substitution of the larger $Al^{3+}$ for $Si^{4+}$ in the tetrahedral sheet increases its *b* dimension.

When tetrahedral and octahedral sheets are assembled into layers, they may be electrically neutral or negatively charged because of the isomorphic substitution of a lower valent cation in the sheets. However, net negative charge must be balanced by an interlayer cation, which is usually $Na^{+}$ or $Ca^{2+}$, but other cations may be found in the interlayers. The counter cations are often in a hydrated form and may be readily exchanged with other cations.

#### 1.2.1.2 Polytypism

The different stacking arrangements of identical layers results in what is called "polytypes". In clay minerals, the stacking of layers in polytypes may be regular or random. In ordered stacking, the relationship of one layer to another can be explained on the basis of a rotation of some integral value of 60°, which is repeated from one layer to another. In random stacking, rotation from one layer to another must also be an integral value of 60°, but the integer multipliers are random.

Other types could also be identified, e.g., turbostratic, which is a highly disordered stacking arrangement that can be thought of as resembling a pile of cards lying flat on each other but with little or no alignment of the edges (36).

#### 1.2.1.3 Classification of the layered silicates

Layered silicates may be classified on the basis of the layer type (1:1 or 2:1), layer charge, and type of interlayers. According to the Clay Minerals Society Nomenclature Committee, layered silicates are classified on the basis of their superstructures. These include the planar hydrous phyllosilicates (Table 1.1) and the non-planar hydrous phyllosilicates (Table 1.2) (37, 38).

##### 1.2.1.3.1 Planar hydrous phyllosilicates

These are arranged into eight main groups with subgroups being determined on the basis of the octahedral character (dioctahedral or trioctahedral with 2.5 cations as the boundary). Species in a given subgroup are distinguished by different compositions, stacking arrangements, or

**Table 1.1.** Classification of planar hydrous phyllosilicates. Modified from ref. 1 with permission.

| Layer Type | Interlayer Material[1] | Group | Octahedral Character | Species[2] |
|---|---|---|---|---|
| 1:1 | None or $H_2O$ only ($x \approx 0$) | Serpentine-Kaolin | Trioctahedral<br>Dioctahedral<br><br>Di-trioctahedral | Lizardite, Berthierite, Amesite<br>Kaolinite, Dickite, Nacrite, Halloysite (planar)<br>Odinite |
| 2:1 | None ($x \approx 0$) | Talc-Pyrophyllite | Trioctahedral<br>Dioctahedral | Talc, Willemsite, Kerolite, Pimelite<br>Pyrophyllite, Ferripyrophyllite |
| | Hydrated exchangeable cations ($x \approx 0.2$-$0.6$) | Smectite | Trioctahedral<br>Dioctahedral | Saponite, Hectorite, Sauconite<br>Montmorillonite, Beidellite, Nontronite |
| | Hydrated exchangeable cations ($x \approx 0.6$-$0.9$) | Vermiculite | Trioctahedral<br>Dioctahedral | Trioctahedral Vermiculite<br>Dioctahedral Vermiculite |
| | Non-hydrated monovalent cations ($x \approx 0.6$-$1.0$) | True (flexible) Mica | Trioctahedral<br>Dioctahedral | Biotite, Phlogopite, Lepidolite<br>Muscovite, Illite, Glauconite |
| | Non-hydrated divalent cations ($x \approx 1.8$-$2.0$) | Brittle mica | Trioctahedral<br>Dioctahedral | Clintonite, Anandite, Bityite<br>Margarite |
| | Hydroxide sheet ($x \approx$ variable) | Chlorite | Trioctahedral<br>Dioctahedral<br>Di-trioctahedral | Clinochlore, Chamosite, Nimite<br>Donbassite<br>Cookeite, Sudoite |
| 2:1 | Regularly Interstratified ($x \approx$ variable) | Variable | Trioctahedral<br>Dioctahedral | Corrensite, Hydrobiotite<br>Rectorite |

[1]x is the net layer charge per $O_{10}(OH)_2$ formula unit.
[2]Only examples are given.

**Table 1.2.** Classification of non-planar hydrous phyllosilicates. Modified from ref. 1 with permission.

| Layer Type | Modulated Component | Linkage Configuration | Unit Layer, c sin ß value | Traditional Affiliation | Species[1] |
|---|---|---|---|---|---|
| A. Modulated Structures | | | | | |
| 1:1 | Tet. Sheet | Strips | 7 Å | Serpentine | Antigorite, Bemenite |
| | | Islands | 7 Å | Serpentine | Greenalite, Caryopilite, Pyrosmalite |
| 2:1 | Tet. Sheet | Strips | 9.5 Å | Talk | Minnesotaite |
| | | | 12.5 Å | Mica | Ganophyllite, Eggletonite |
| | | Islands | 9.6-12.5 Å | Mica/complex | Zussmanite, Parssettenite |
| | | Other | 12.3 Å | None | Bannisterite |
| | | | 14 Å | Chlorite | Gonyerite |
| | Oct. Sheet | Strips | 12.7-13.4 Å | Pyribole | Sepiolite, Palygorskite, Loughlinite |
| B. Rolled and Spheroidal Structures | | | | | |
| 1:1 | None | Trioctahedral | - | Serpentine | Chrysotile, Pecoraite |
| | | Dioctahedral | - | Kaolin | Halloysite (non-planar) |

[1]Only examples are given.

octahedral-vacancy sequences. The structures of some of the major non-modulated hydrous phyllosilicates groups are given in Fig. 1.2. These include the neutral kaolin, pyrophyllite, and talc groups, as well as the mica, smectite, and chlorite groups, which all possess negative layer charges. Mica has a high charge density ($x \approx 1.0$), and the layers are held rigidly shut with the interlayer cation (usually potassium) held in 12-fold coordination with the oxygens of the two tetrahedral-sheet surfaces. On the other hand, smectites have a lower charge density ($x \approx$ 0.25–0.6), compared with micas, and have exchangeable interlayer cations. Chlorites, like micas and smectites are also made up of negatively charged 2:1 layers; however, in this case, the negative charges of the 2:1 layers are counterbalanced by positively charged interlayer octahedral hydroxide sheets.

#### 1.2.1.3.2 Non-planar hydrous phyllosilicates

In those layered silicates, there is a periodic perturbation of the basic silicate structure. The classification scheme is given in Table 1.2. Differing compositions and further structural variations within the subdivisions determine the species. Structural models of the tetrahedrally modulated layer silicates palygorskite and sepiolite are given in Fig. 1.3. Notably, both of these structures have a continuous two-dimensional tetrahedral sheet, but unlike the planar 2:1 hydrous phyllosilicates, they lack a continuous octahedral sheet (39–41).

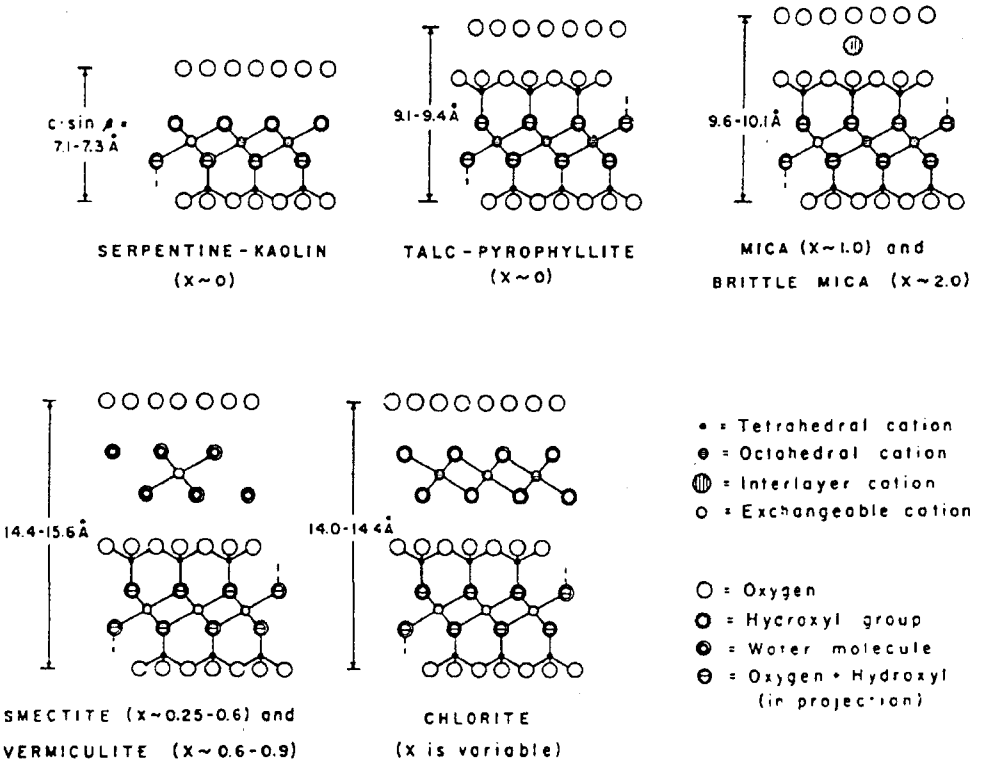


**Fig. 1.2.** [001] View of structures of major non-modulated hydrous phyllosilicate groups. Reproduced from ref. 1 with permission.

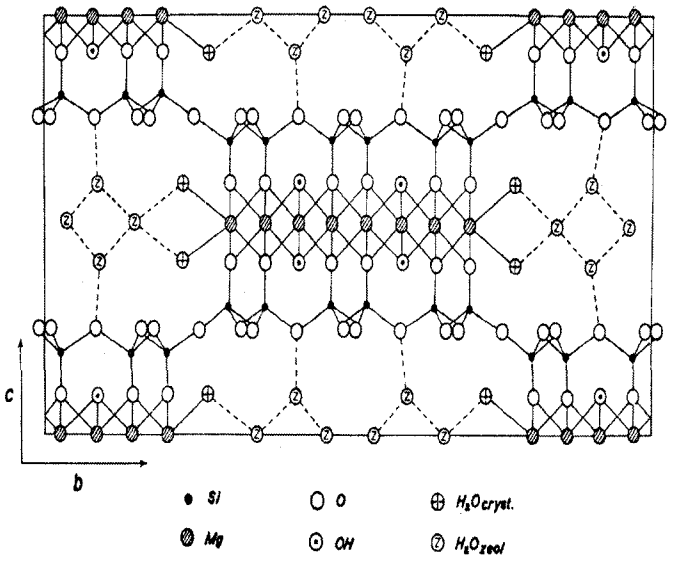


(a)

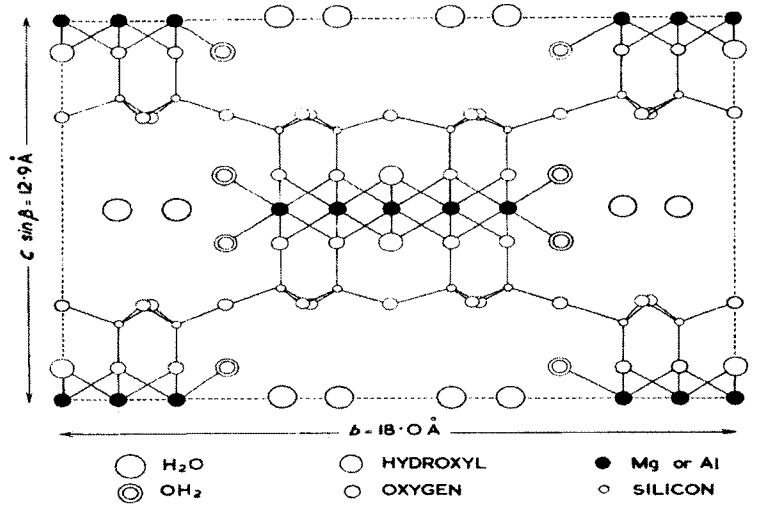


(b)

**Fig. 1.3.** [100] Projection of sepiolite (a) and palygorskite (b) structures. Reproduced from ref. 37 with permission from the Mineralogical Society of Great Britain and Ireland.

### 1.2.2 Description of the kaolin minerals

The origin of the word kaolin is believed to be derived from one of two sources, both involving derivations of the Chinese word: "Kau-Ling". In one interpretation, kaolin takes its name from the Chinese word for "high ridge" from where it was mined for many centuries near Jau-chau Fu (42, 43). An alternate interpretation is that kaolin takes its name from the locality of Kau-Ling in Kiangsi Province where it was also mined from the 11$^{th}$ century until 1964 (44, 45). Kaolin is also known to many as China clay. The origin of this expression is also unclear, although some trace its origin to Marco Polo, who brought back large ceramic urns from China and referred to them as "Chinaware". When kaolin was discovered in Cornwall, England, and was found to be similar to the type of clay used in China to make Chinaware, it was therefore called "China Clay" (42). Other commercial terms associated with various types of kaolinitic clays are ballclays, fireclays, flintclays, and underclays. Each of these terms describe kaolin with certain physical properties and uses primarily in the ceramics and refractory industries (36, 42).

Kaolin is one of the most important natural industrial substances. In 1980s, it was estimated that the worldwide production of kaolin was 20 million tons (42), i.e., the worldwide average was ~4 kg per person. Approximately 60% of this was used in the paper industry, where kaolin is used as a filler in the interstices of the cellulose fibres that form the paper sheet and as a coating on the surface of the sheet to improve the fidelity of printing using colored inks. Other major uses of kaolin are in the ceramics, paints, rubbers, plastics, and catalysis industries.

Kaolin-group minerals are dioctahedral 1:1 hydrous phyllosilicates (Tables 1.1 and 1.2) and

are made up of the minerals kaolinite, halloysite, dickite, and nacrite. They all have the approximate composition $Al_2Si_2O_5(OH)_4$, and they are neutral. Small quantities of iron, titanium, potassium, or magnesium are normally found in natural kaolins. Traces of other minerals such as vermiculite, mica, or smectites may also be detected by XRD, and these impurities are the source of the small negative charge found on some kaolinites (46).

Kaolinite is the most abundant kaolin mineral. It is white, greyish-white, or slightly colored. It is made up of tiny, thin, pseudohexagonal, flexible sheets of triclinic crystal with a diameter of 0.2–12 μm. The density of kaolinite is in the range of 2.1–2.6 g/cm$^3$. It is found primarily in soils and permeable bedrock in warm and moist regions. It is formed mainly as a weathering product or by hydrothermal alteration (44). The most common parent minerals from which the kaolin minerals form, are feldspars and muscovite. For example, the transformation of potassium feldspar into kaolinite occurs by intense weathering of the feldspar and leaching of potassium and $SiO_2$ according to the reaction (42):

$$2KAlSi_3O_8 \text{ (Potash feldspar)} + 3H_2O \rightarrow Al_2Si_2O_5(OH)_4 + 4SiO_2 \text{ (silica)} + 2K(OH) \text{ (potash)}$$

In this process, all of the potassium is lost in solution, and the much less-soluble kaolinite and silica are left behind.

The conditions for the formation of the rarer minerals, dickite and nacrite, is believed to be restricted almost exclusively to hydrothermal occurrences (36, 42). Halloysite is a disordered form of kaolinite, enough to allow water into the interlayers (47). It is also composed of a

tetrahedral sheet with a greater amount of aluminum for silicon substitution than is found for the other kaolin minerals. This causes bending of the layers into a tubular morphology (42, 48).

#### 1.2.2.1 Polytypism in kaolin minerals

As mentioned before, kaolin minerals are made up of nearly identical 7.2 Å thick, 1:1 layers of the composition $Al_2Si_2O_5(OH)_4$. Many different polytypes for the kaolin minerals are possible (37). Newnham for example claimed that six one-layer and 108 two-layer structures were theoretically possible (49). Later, Zvyagin (50) showed that only 52 theoretical dioctahedral structures with periodicities between one and six layers were possible, since some of Newnham's theoretical structures were equivalent. Only three of the polytype structures have been conclusively shown to exist, because of stability considerations (1, 44), kaolinite, dickite, and nacrite. Understanding the stacking arrangement and exact structure of halloysite in both its collapsed 7 Å form and its expanded 10 Å hydrated form is still developing (44, 47.).

### 1.2.3 The structural model of kaolinite

All the experimental work in this thesis involved the use of kaolinite as the mineral precursor material; thus, it is useful to give a general description of the structure of kaolinite. Since Pauling first deduced the basic structure of kaolinite by analogy with other phyllosilicates (54), many researchers have tried to verify this proposed basic structure, determine its space group, and locate all the atoms that make up the unit cell of kaolinite (51–54). The relevant work that

has been done pertaining to this subject until 1988 has been nicely summarized by Giese (44). While it is accepted that kaolinite is triclinic, there has been considerable controversy regarding the space group assignment of kaolinite. Suitch and Young (55) and Young and Hewat (56) proposed a primitive lattice space group $P1$, based on X-ray and neutron diffraction refinement studies. On the other hand, Bish and von Dreele (57) have insisted on the more commonly accepted $C1$ as the space group. This is important, since the choice of a $P1$ lattice requires twice the number of independent atoms in a more asymmetric unit cell by allowing crystallographically identical atoms in $C1$ to occupy non-equivalent sites in $P1$. While it is accepted that the non hydrogen atoms of the structure largely obey $C$-centring, Young and co-workers concluded that the hydroxyl groups that were equivalent in $C1$ were inequivalent in $P1$ (55, 56).

A major criticism of the crystal structure proposed by Young and Hewat has been the presence of several unrealistic Si–O and Al–O internuclear distances, and the IR data was inconsistent with the $P1$ structure (44, 57).

More recently, Bish has used neutron-diffraction data to refine the kaolinite structure to a $C1$ lattice (58). Since the $C1$ space-group model fits both diffraction and spectroscopic data, it is therefore this model that we will be assuming.

The unit cell parameters for the non hydrogen atoms refinement of a highly ordered kaolinite, using a $C1$ space group, are $a$ = 5.1554 Å, $b$ = 8.9448 Å, $c$ = 7.4048 Å; $\alpha$ = 91.700°, $\beta$ = 104.862°, and $\gamma$ = 89.822° (57, 58).

This refinement indicates that Si–O distances are 1.60–1.63 Å, Al–O distances are 1.87–1.97

Å, and the tetrahedral rotation angle is 6.9°. The distance between tetrahedral-sheet basal oxygens is 2.58–2.63 Å, whereas the distance between surface hydroxyls from the octahedral sheet is 2.78–2.81 Å. The tetrahedral basal oxygen plane is corrugated with one oxygen approximately 0. 16 Å higher in the cell (away from the interlayer) than the other two. The inner OH group is in the plane of the layers, and the three inner-surface (outer) OH groups make angles of 60°–73° with the (001) plane. The long hydrogen bonds between layers were found to be between 2.95–3.09 Å. The differences in the distance of the three interlayer hydrogen bonds is believed to be responsible for the presence of the three interlamellar ν(OH) bands. This is in contrast to the conventional view that these bands are due to the coupling of the surface hydroxyl stretching vibrations (59, 60).

A structural model proposed by Deng at al. for kaolinite using the parameters proposed by Bish is shown in Fig. 1.4 (61). Finally, in reality, kaolinite is an imperfect material covering a broad range of structural disorders. Disorder is important, since not only it greatly influences the diffraction patterns generated by the material, it also affects many of the physico-chemical properties, such as particle size and intercalation chemistry (62, 63). Depending on the origin of the kaolinite itself, structural disorder is present in widely varying degrees (44, 47, 64, 65).

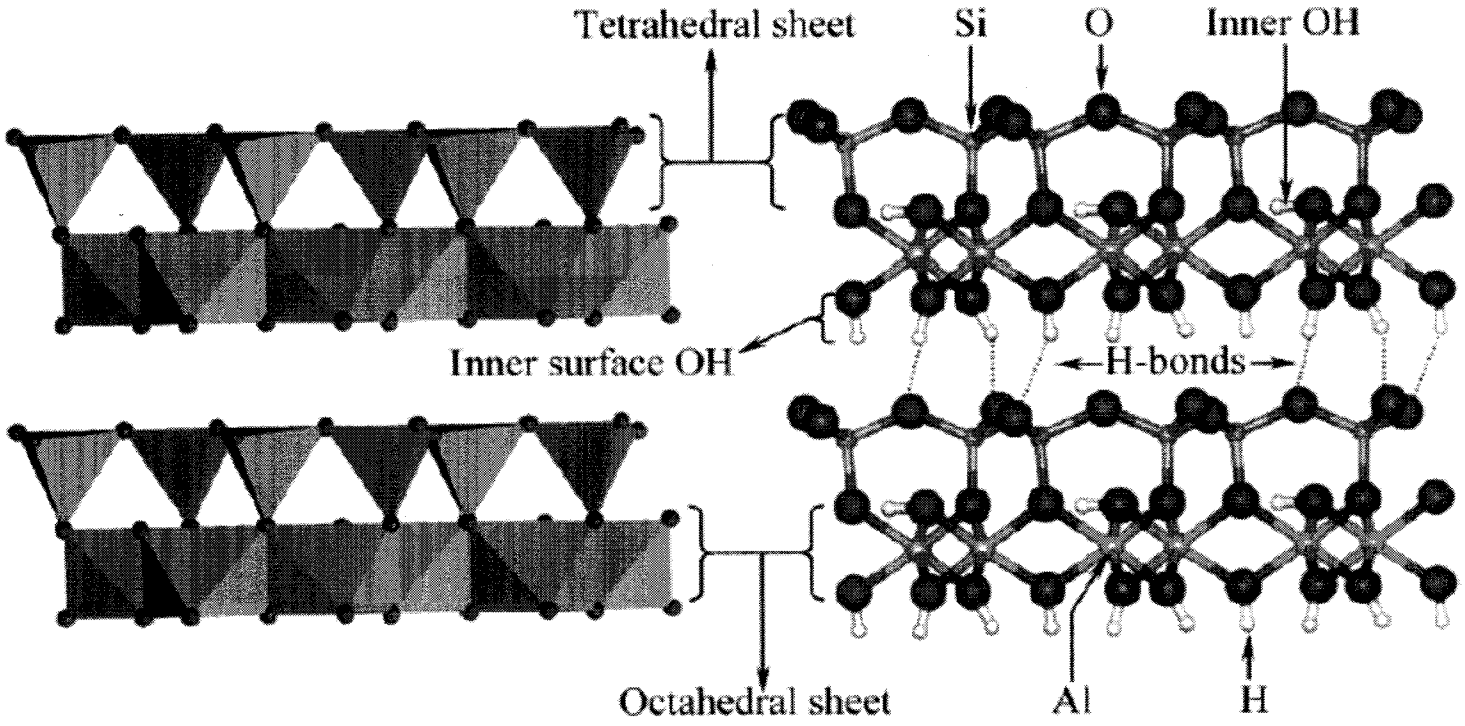


**Fig. 1.4.**A structural model of kaolinite. Reproduced from ref. 61 with permission.

### 1.2.4 Intercalation of organic guest molecules into kaolinite

Halloysite is the only kaolin mineral that exists in nature as a hydrate, with water molecules occupying the interlayers of the mineral. Thus, the *c*-spacing is expanded to 10 Å. Halloysite is also known to intercalate a wide range of organic compounds. In contrast, the other kaolin minerals, kaolinite, dickite, and nacrite were thought to be completely non-expandable with respect to both water intercalation and intercalation with organic compounds (66, 67).

The discovery by Wada that kaolinite can be intercalated with potassium acetate and other salts of organic acids of low molecular mass (4) initiated the research on the intercalation chemistry of kaolinite. The work in this thesis will be focused on the intercalation chemistry of kaolinite. Organic molecules can be intercalated into kaolinite directly or indirectly (Fig. 1.5). The direct route involves the preparation of the organokaolinite intercalation compound through the direct reaction of the mineral with the organic substance. This may be done from the liquid, from the melt, by grinding the two solids together, or from a concentrated solution (62, 68). Some of the more common organokaolinite intercalates, which are formed in this manner involve the direct reaction of DMSO (25, 27, 69–75), NMF (27, 71, 76–78), urea (26, 79), hydrazine (26, 74, 79–81), formamide (26, 82), pyridine *N*-oxide (26, 71), potassium acetate (83), and ammonium acetate (83) with kaolinite. Compounds that intercalate directly into kaolinite have certain properties including high dipole moments and a tendency to form strong hydrogen bonds. Also, included in this group are various ionic species such as potassium, rubidium, and cesium carboxylic acid salts (84) as well as inorganic salts such as NaCl, CsBr, and CsCl (85–88).

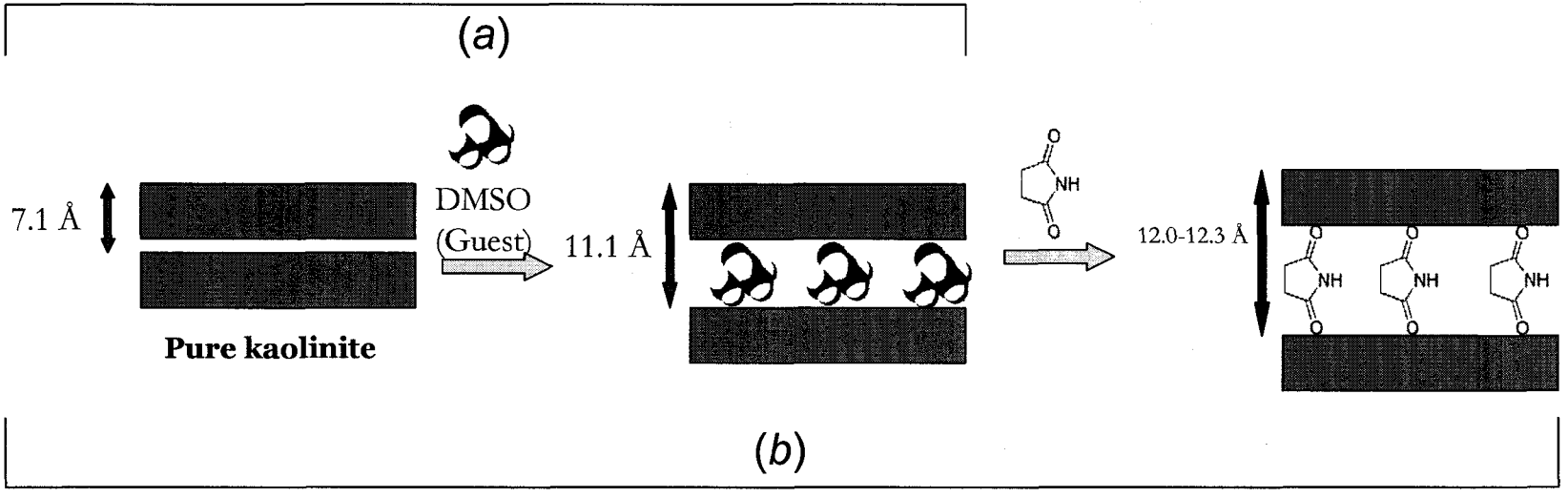


**Fig. 1.5.** Schematic representation of (*a*) direct intercalation of DMSO vs. (*b*) indirect (guest-displacement) intercalation of organic molecules in kaolinite (the molecule shown here is a cyclic imide (see Chapter 2).

Many more organokaolinite intercalation compounds may be formed indirectly by the replacement of a previously intercalated molecule (guest) with another molecule (Fig. 1.5). Weiss and co-workers have intercalated a wide range of alkali and alkaline halides, amino acids, amines, and other organic molecules in this manner by using either hydrazine or ammonium acetate as an "entraining" agent to first open up the layers, followed by its displacement with the desired compound (68, 83, 84).

Polar molecules such as acetone, ethylene glycol, glycerol, acetonitrile, and nitrobenzene have been intercalated by the displacement of previously intercalated DMSO (69, 71). Also, lactams (2-pyrrolidine and 2-piperidone) were intercalated via the displacement of previously intercalated NMF (89). Additionally, different hydrates of kaolinite (8.4–10 Å) were also reported by displacing other intercalated (guest) molecules (90–96). Moreover, the prepared hydrates were used as starting materials for the preparation of other intercalated compounds (97–99). A refined guest-displacement method was also reported to prepare a kaolinite–poly(vinyl pyrrolidone) intercalated nanocomposite (24). A few cases of interlamellar grafting of organic molecules to the aluminol surface of kaolinite were also reported (7, 8, 16, 17, 19).

### 1.2.4.1 Estimating the extent of intercalation

The ratio of intercalation is generally used to estimate the extent of intercalation in kaolinite by XRD. Simply, the relative intensities of the $d_{001}$ reflections ($I_{001}$) corresponding to both the expanded modified phase ($I_{001(complex)}$: $d_{001} > 7.2$ Å) and the unmodified kaolinite phase

($I_{001(kaolinite)}$: $d_{001} \approx 7.2$ Å). Applying equation [1.1] gives the ratio of intercalation (RI) (5).

[1.1] $RI = I_{001(complex)}/[I_{001(complex)} + I_{001(kaolinite)}]$

Notably, the RI is extensively used when studying organokaolinites, as it provides a readily measurable qualitative estimate of the extent of modification. The RI cannot be considered quantitative, since one should correct for the variation of the scattering, Lorentz and polarization factors at low angles (1, 37). The layer expansion is generally estimated from the $d_{001}$ XRD reflections of the modified phase.

### 1.2.4.2 The mechanism of intercalation

It is difficult to expand a fully collapsed kaolinite, but expansion is easier once the layers have been opened up slightly. Understanding the interlayer cohesion energy in kaolinite is important to fully understand the mechanism of intercalation. The estimated energy to separate the individual layers to a 10 Å distance was ~300 kJ per kaolinite unit (100). Cruz et al. (101) also estimated the interlayer cohesion energy of kaolinite using a different approach. They separated the interlayer bonding energy of kaolinite into three components: (*i*) van der Waals' attractive forces between layers, (*ii*) hydrogen bonding between octahedral hydroxyl groups on one layer and tetrahedral oxygen atoms on the adjacent layer, and (*iii*) electrostatic interactions arising from the dipolar nature of kaolinite. Calculations provided a value of 200 kJ per $Al_2Si_2O_5(OH)_4$

unit, with the main contribution from the electrostatic energy term.

The electrostatic term is attributed to the electrostatic component of long interlayer hydrogen bonds. Therefore, the driving force of the intercalation process may be envisaged as the solvation of dipolar kaolinite layers. Consequently, molecules that can form strong hydrogen bonds with the interlamellar kaolinite surface and that have high dielectric constants and dipole moments should be favored for the intercalation process.

The intercalation behavior of kaolinite is not entirely interpreted. Generally, intercalation processes must involve the expansion of the individual layers to accommodate the guest molecule. Thus, the energy that is required to separate the kaolinite layers must be balanced in some manner, usually through strong host–guest interactions.

Many factors have been attributed to influencing the reaction rate. These include particle size and degree of crystallinity of the kaolinite, reaction temperature, concentration of the intercalating material, and the degree of association of the reactant in the solvent mixture (63, 71, 77).

In kaolinite, particle size has a reversed reactivity trend in during the intercalation reaction: the finer kaolinite particles are usually intercalated slower than coarse particles, and some fine kaolinite particles cannot be intercalated at all. Wiewiora and Brindley attributed the lower reactivity of the finer kaolinite particles to their higher crystallinity (102). However, better crystallinity" is not likely the reason, as there is no consistent trend in crystallinity associated with particle size, and highly crystalline kaolin minerals are generally more readily intercalated. The reversed particle-size effect was explained using a "ring mechanism", it is widely believed

that the intercalation reaction begins at the edges of the kaolinite crystal, with the intercalating molecules then penetrating towards the interior of the crystal with the same rate between each pair of layers (62, 63). However, during the intercalation process, an XRD pattern indicative of an interlayering phenomena, where one has a random stacking of expanded and non-expanded layers, is not observed. The constant-rate assumption in which the molecules act as wedges on the kaolinite crystal and cause the layers to be elastically deformed at the interphase is used to explain that observation.

Another model for the intercalation mechanism is based on the idea that, macroscopically, kaolinite is made up of one or more screw-dislocation axes (103, 104). In this mechanism, the organic molecules would first enter via edge dislocations and then diffuse through the crystal layer by layer, since these are connected in a manner similar to a spiral staircase. Expansion of the layers would therefore take place in an orderly manner as the reaction proceeds. This mechanism is consistent with the formation of an ordered complex at all stages of the intercalation process. Recently, after studying the crystallinity and impurity effects on the interclation rate, Deng et al. (61) proposed that structural stress is a driving force in the intercalation. The lateral size of the tetrahedral sheet is larger than the octahedral sheet in kaolinite; thus, structural stress is induced from the misfit of the tetrahedral sheet and the octahedral sheet in the 1:1 kaolinite. They showed in their study that part of the structural stress can be relieved when kaolinite is intercalated. Coarser particles intercalate faster because of their larger structural stress.

### 1.2.5 Polymer–layered silicates (PLS) nanocomposites

In general, a composite material is a hybrid of different phases with overall improved properties compared with the properties of the individual phases. A composite material is formed when a reinforcing element (filler) is dispersed in a host matrix. Fillers are classified into fibers or particles, and the matrix material could be organic (e.g. polymer), mineral, or metallic. Composites based on an organic matrix (a polymer) have the most extended range of applications. The use of fibrous or particulate fillers mainly depends on the desired properties and potential applications of the produced composites. The concept of polymer filling has always been effective in enhancing several properties of the polymers including the mechanical (e.g., stiffness, elastic moduli, and tensile strength) and thermal properties compared with the pure polymer. Over the years, conventional (micro) polymer composites have played an important role in the reinforcement of polymers, but they require high filler content (10–30 wt%), which leads to an increase in the density and deterioration of the properties of the pristine polymer as a result of incompatibility between the filler and organic material.

Recently, "nano" has been an extremely popular prefix, and a new era of research has emerged with the use of nano-size materials as fillers or additives for polymers. Nanoscale filling also proved to be effective at very low filler contents (3–5 wt %) with much better performance compared with the conventional micro-scale fillers.

Clearly, the unique properties of polymer nanocomposites have given them the potential to be the alternative to conventional composites in a wide variety of applications. Nanocomposites are particle-filled polymers that have at least one characteristic dimension of the dispersed

particles in the order of nanometer, which is the case of polymer–layered silicate (clay) nanocomposites. Two other types exist, and those are the isodimensional nanoparticles, e.g., spherical silica nanoparticles, that have three dimensions in the nanometer range, and finally, whiskers- or carbon nanotubes-filled nanocomposites where two dimensions are in the nanometer scale and the third is in the order of few centimeters, forming an elongated structure. The potential applications of these nanocomposites are very important both environmentally and economically (2, 30, 31). Examples of the layered materials that could be intercalated by a polymer to form nanocomposites are given in Table 1.3.

**Table 1.3.** Example of layered host crystals susceptible to intercalation by a polymer (data are reproduced from ref. 31 with permission).

| Chemical nature | Examples |
|---|---|
| Element | Graphite |
| Metal chalcogenides | $(PbS)_{1.18}(TiS_2)_2$, $MoS_2$ |
| Carbon oxides | Graphite oxide |
| Metal phosphates | $Zr(HPO_4)$ |
| Clays and layered silicates | Montmorillonite, hectorite, saponite, fluoromica, fluorohectorite, vermiculite, kaolinite, magadiite, . . . |
| Layered double hydroxides | $M_6Al_2(OH)_{16}CO_3 \cdot nH_2O$; M: Mg , Zn |

The study of the polymer–layered silicate (PLS) nanocomposites will constitute one of the main objects of this thesis. PLS nanocomposites form a novel class of material that has attracted considerable scientific interest, and those are materials in which nanoscopic inorganic particles are dispersed in an organic polymer matrix in order to dramatically improve the performance properties of the polymer, mainly due to the potential technological applications that include impact resistance, flame retardancy, elastic modulus, and barrier properties for various polymer matrices. PLS nanocomposites have received considerable attention in the last two decades, because of the availability of the cheap starting clay materials (naturally occurring) and the extensive study of the intercalation chemistry of the layered silicates. Smectites, such as montmorillonite, hectorite, and saponite, are the most commonly used layered silicates. The first PLS nanocomposite was reported when researchers from Toyota exploited the improved mechanical and physical properties of their PA-6–MMT nanocomposite in under-the-hood applications (105).

### 1.2.5.1 Types and structure of the nanocomposites

PLS nanocomposites are exclusively obtained by the intercalation of the polymer (or a monomer, followed by subsequent polymerization) inside the galleries of layered host crystals. Generally, three main types of composites may be obtained when a layered clay is associated with a polymer (Fig. 1.6). When the polymer is unable to intercalate between the silicate sheets, a phase-separated (traditional or micro) composite (Fig. 1.6a) is obtained. In addition to this classical microcomposite, two types of nanocomposites are identified. Intercalated structure

(Fig. 1.6b) in which usually a single extended polymer chain is intercalated between the silicate layers, resulting in alternating polymeric and inorganic layers. When the silicate layers are uniformly dispersed in a continuous polymer matrix, an exfoliated or delaminated structure is obtained (Fig. 1.6c).

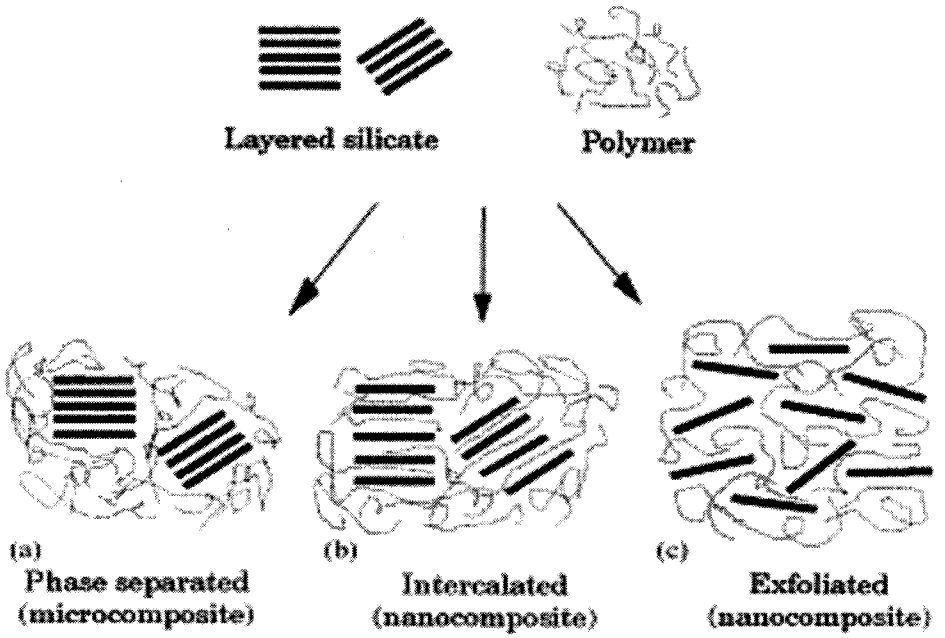


**Fig. 1.6.** Different types of composites resulting from the mixing of layered silicates with polymers: (a) phase-separated microcomposite, (b) intercalated nanocomposite, and (c) exfoliated nanocomposite. Reprinted from ref. 31 with permission.

### 1.2.5.2 Preparation of nanocomposites

Several strategies can be employed to prepare polymer–layered silicate nanocomposites. The main processes include (*i*) the preparation from the solution of the polymer; (*ii*) in situ intercalative polymerization in which the layered silicate is swollen within the liquid monomer (or a monomer solution), and the polymer is formed between the intercalated sheets; generally, polymerization can be initiated either by heat or radiation or by the diffusion of a suitable initiator; and finally (*iii*) melt intercalation in which the layered silicate is mixed with the polymer matrix in the molten state, and no solvent is needed (30, 31).

### 1.2.5.3 Charaterization of the prepared nanocomposites

Characterization of the produced nanocomposites is one of the most important aspects of nanocomposite synthesis. In fact, characterization is crucial in understanding the new produced materials and to obtain the complete structural information which is an important step to predict the potential applications. Mainly, two techniques are used to characterize PLS nanocomposites. XRD is used to identify intercalated structures. The intercalated polymer chains increase the interlayer spacing, in comparison with the spacing of the pristine clay used.

For the exfoliated type, no diffraction peaks are visible in the XRD diffractograms either because of a much too large spacing between the layers (i.e., exceeding 8 nm in the case of ordered exfoliated structure) or because the nanocomposite does not possess an ordered structure. In this case, transmission electronic spectroscopy (TEM) is used to characterize the nanocomposite morphology.

Other techniques, especially those exploited in this thesis, include infrared (FTIR) and NMR spectroscopy as well as thermogravimetric analysis (TGA).

## 1.3 Purpose of the research

As mentioned before in this chapter, most of the research on the intercalation chemistry of clay minerals was directed towards the use of smectites as precursors for the preparation of novel nanohybrid and nanocomposite materials. Smectites are readily expandable by solvents and exhibit high cation exchange capacity as well as large internal surface area.

On the other hand, kaolin minerals are essentially neutral and have very small cation exchange capacities; thus, they are much more difficult to expand. In fact, it is generally not possible to completely expand all the interlayers of kaolinite. It is not surprising therefore, that smectites are the clay minerals of choice as precursors for the development of many new microporous and catalytic materials.

However, kaolinite could also be an ideal candidate as a precursor for the preparation of some types of nanocomposite materials. Like the smectites, kaolinite is readily available at a very cheap price. It is a big industrial product, with extensive use in the pulp and paper and ceramics industries. Kaolinite has a greater theoretical internal surface area per unit mass than do the smectites (1000 $m^2/g$ vs. ~700 $m^2/g$), and it exhibits a much greater crystallinity than do the smectites. From a practical point of view, the high degree of ordering characteristic of kaolinite make the analysis of host–guest interactions easier. Unlike the 2:1 smectites, which have only one type of interlamellar surface, kaolin minerals possess two types of surfaces (Fig. 1.5): $(SiO)_6$

macrorings on one side and aluminol groups on the other side. Consequently, kaolinite is remarkable by its non-centrosymmetric structure. This asymmetry creates large superposed dipoles in the lamellar structure, resulting in a large cohesive energy. Herein, lies the most powerful advantage of kaolinite as a nanocomposite precursor material. Not only does the hydroxylated aluminate surface provide an abundance of reactive hydroxyl groups for guest species to attach (graft) themselves to, but the dipolar interlamellar environment induced by this second surface may cause the spontaneous alignment of polar guest species. Moreover, the functionalization of the aluminol surface of kaolinite could be achieved through the covalent grafting of organic molecules in an ordered and reproducible manner.

It is clear that kaolinite could provide an attractive precursor for nanocomposite materials if some of the problems surrounding the difficulty in expanding the interlayers of kaolinite could be solved. A few examples of polymer–kaolinite intercalated nanocomposites have been reported (30). Polyethylene glycol was the first reported direct intercalation from the melt (18). Other examples of melt intercalation include polyethylene oxide and polyhydroxybutyrate (9). The exploitation of other preparation techniques is still limited in case of polymer–kaolinite nanocomposites, although it is well explored incase of smectite precursors. Also, the number of polymers involved in nanocomposite interactions with kaolinite is still limited and not covering a wide variety of polymers.

Additionally, the research pertaining to the interlamellar chemistry of kaolinite has shown a transition from the use of "soft" methods of intercalation that involves the intercalation of non-destructive reagents at temperatures less than 100 °C and at atmospheric pressures to the

use of harsher reaction regimes, involving the grafting of molecules at high temperatures or the prepration of nanocomposites from the melt of the polymers. To utilize some of the unique advantages that kaolinite has as a precursor material for the preparation of nanocomposite dipolar assemblies, one must first expand the interlamellar chemistry of kaolinite. New methods should be explored for the incorporation of guest molecules into the interlayers of kaolinite and novel interlamellar surface modification schemes could be explored by the grafting of organic groups to the interlamellar surface of kaolinite.

Considering the previous argument, the broad purpose of this research was to explore and extend the interlamellar chemistry through the preparation and characterization of new kaolinite-based nanohybrid materials using a variety of innovative synthesis methodologies. Moreover, the goal was to prepare organ-kaolinite materials where polymeric organic units would be covalently grafted to the interlayers of kaolinite and to prepare novel polymer–kaolinite nanocomposites using new types of polymers with commercial, technological, and environment-friendly applications. The produced nanohybrid materials are expected to possess enhanced thermal stabilities, compared with the crude organic molecules and polymers, and to be resistant to decomposition.

# Chapter 2

# Nanohybrids from the intercalation of cyclic imides in kaolinite

## 2.1 Introduction

As mentioned before, the interlamellar space of kaolinite is made up of two types of surfaces, $(SiO)_6$ macrorings on one side and aluminol groups on the other side, and consequently kaolinite is remarkable by its non-centrosymmetric structure. This asymmetry creates large superposed dipoles in the lamellar structure, resulting in a large cohesive energy. As a result, the intercalation chemistry of kaolinite is less developed than that of the swelling smectites. With its aluminol surface and its non-centrosymmetric structure, kaolinite is an interesting mineral for the design of nanohybrid materials; thus, it is important to develop its interlamellar chemistry (4, 5, 26, 70, 71). Its non-centrosymmetric structure is particularly interesting for potential non linear optical applications. An example of the selective intercalation of nitroanilines in kaolinite was reported by Takenawa et al. (14). The intercalated organic guest molecules adopted a unique orientation caused by the asymmetric nature of the interlayer space of kaolinite.

In this chapter, intercalation compounds, i.e., nanohybrids, of kaolinite with two different cyclic imides, namely, 2,5-pyrrolidinedione (succinimide, SIM) and 2,6-piperidinedione (glutarimide, GIM) (see Chart 2.1), are reported for the first time by displacing other intercalated guest molecules (intermediates). Interestingly, the new cyclic-imide intercalates

of kaolinite were prepared by what will be called a "soft guest-displacement method", as the displacements were achieved at ambient temperatures, similar to the temperatures at which the guest molecules were intercalated, yet at a relatively short time (hours) compared with the intercalation of the intermediate (guest) molecules to prepare the starting materials (months). It is noteworthy that attempts to directly intercalate the cyclic imides in the unexpanded kaolininte (KGa-1b) were unsuccessful (see Section 2.2).


**Chart 2.1.**Structures of (*a*) succinimide and (*b*) glutarimide.

Succinimide is a diketopyrrolidine that is prepared by heating succinic anhydride with aqueous ammonia, followed by rapid distillation of ammonium succinate (106–107). Succinimide and glutarimide derivatives are of important biological and pharmacological interest. Succinimide and other cyclic carboximides are used as starting materials in organic synthesis. Their nitranions are also important intermediates in many chemical reactions (106–109). In addition, succinimide itself is a hypo-oxaluric agent. On the other hand, glutarimide derivatives possess anticancer activity, and they are also components of some modern antibiotics with antiviral and fungicidal activities. The biological activity of glutarimide drugs is determined by the hydrogen bonding of the CO–NH–CO imide groups and the other molecules in the biological system. It is believed that the ability of glutarimide drugs to intercalate between nucleic base pairs in the DNA helix is significantly due to the flattening of the glutarimide ring (110). Similarly, the investigation of the first reported kaolinite – cyclic imides intercalated nanohybrids is expected to contribute to the continued series of studies on the interlamellar chemistry of kaolinite. The results of the XRD, FTIR, and TGA analyses confirmed the intercalation of the cyclic imides molecules in the interlamellar spaces of kaolinite. $^{13}C$ CP and DD/MAS spectra indicated the complete displacement of the guest molecules of the starting materials by the imides latter in the interlamellar space. $^{29}Si$ and $^{27}Al$ NMR spectra of the starting materials and the products are also discussed.

## 2.2 Preparation, X-ray diffraction, and a structural model

For the first time, two different intercalation compounds of kaolinite with cyclic imides, namely, 2,5-pyrrolidinedione (succinimide, SIM) and 2,6-piperidinedione (glutarimide, GIM), were prepared using a guest-displacement technique, i.e., by displacing other intercalates. First, the dimethyl sulfoxide (DMSO) or *N*-methyl formamide (NMF) intercalates of kaolinite were prepared, and then these intercalates were reacted directly with the solution of the appropriate cyclic imide. Typically, 1–2 g of Kao–DMSO intercalate were mixed with ~50–100 mL of 10% solution (*w*/*v*) of either succinimide (SIM) (99%, Alfa Aesar) or glutarimide (GIM) (98%, Aldrich) (see Chart 2.1). The mixture was stirred at room temperature for a given period of time, followed by the reaction workup (mainly, washing with excess 2-propanol, vacuum filtration, and drying in vacuum). The reaction details for the individual reactions are given in the Experimental Section, and a summary of the main reactions is given in Table 1. The product codes and reaction conditions are given, along with the interlayer *d*-spacing, and the ratio of intercalation (RI) for the final product. The interlayer or *d*-spacings were calculated from the first $d_{001}$ reflections of the principal phase. Since the intercalations were achieved at ambient temperatures throughout the synthesis, the technique could be described as a "soft guest-displacement technique". Both the directly intercalated "guest" molecules and the second organic species, i.e., imides, were intercalated at room temperature. As mentioned before, the intercalation was achieved much faster in case of the cyclic imide, compared with the guest molecules (1–2 month). Also, water was the solvent used to prepare the imide solution.

The majority of the reported guest-displacement intercalations were usually achieved at

elevated reaction temperature, above the melting points, or using organic solvents (5). However, recent methanol intercalation at room temperature required extended reaction time and work up (111). Also, the intercalation of poly(vinylpyrrolidone) at ambient temperature required an additional guest-displacement step, and the reported intercalation of benzamide at ambient environmental conditions, using ethanol as a solvent, resulted in a co-intercalated product, i.e., both benzamide and the guest molecules (NMF) were co-intercalated in the interlamellar spaces of the final product (112) in addition to a relatively low ratio of intercalation, whereas in this chapter, cyclic imides displaced the guest molecules (DMSO) completely, as shown by XRD patterns (see Fig. 2.1) and the absence of DMSO resonances in the $^{13}C$ NMR spectra of the products (see later).

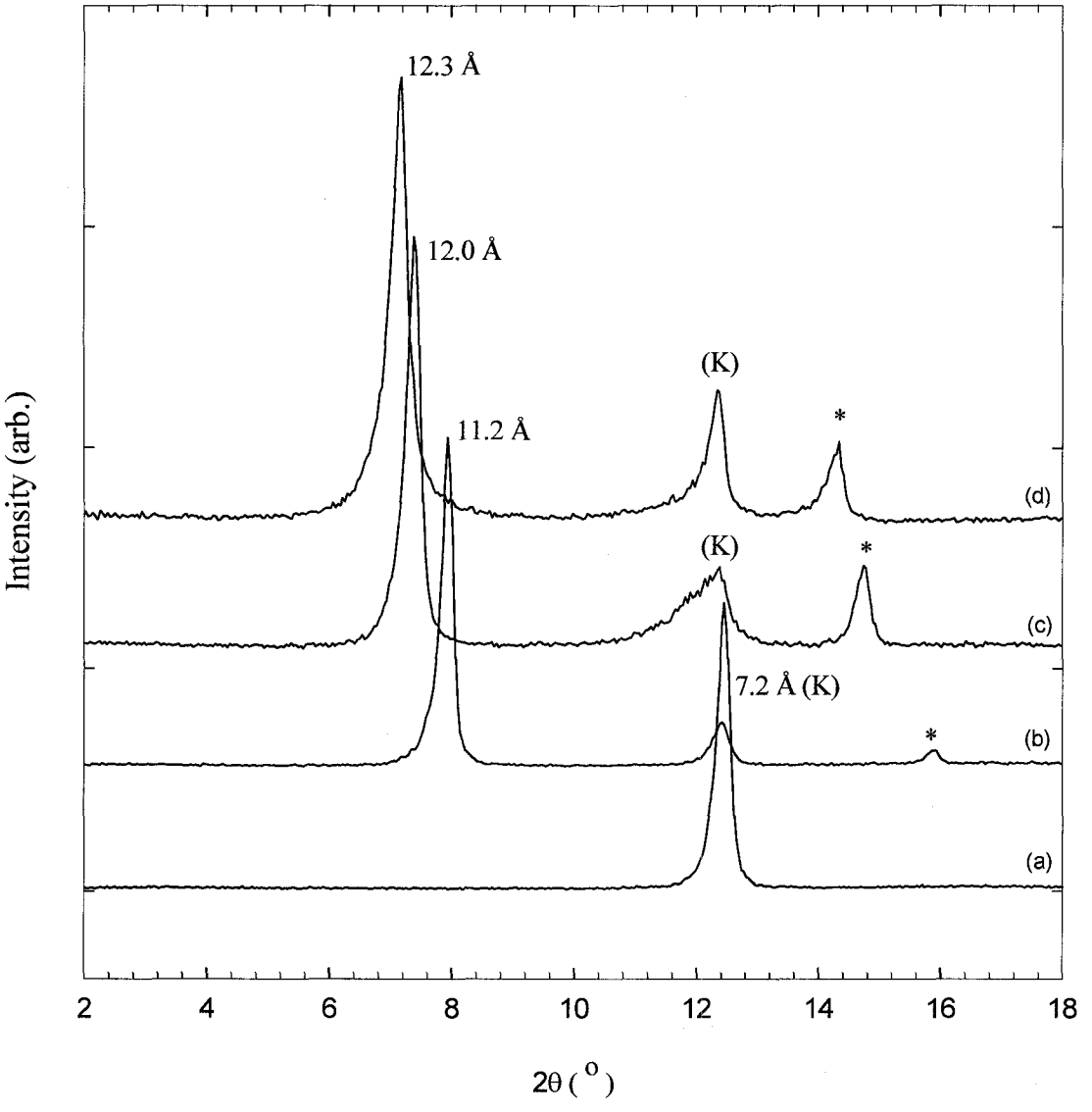


**Fig. 2.1.** XRD powder diffraction patterns ($2\theta$ = 2–18°) of (a) kaolinite, (b) Kao–DMSO, (c) Kao–SIM, and (d) Kao–GIM. (K): Residual kaolinite $d_{001}$ peaks. $d_{002}$ of the intercalate is marked by an asterisk.

**Table 2.1.** Summary of product codes, reaction conditions, and product X-ray characterization for the prepared nanohybrids.

| | Reaction conditions [a] | | | Product X-ray results | | |
|---|---|---|---|---|---|---|
| Code[a] | Starting material (SM)[b] | Reaction medium (RM) | $t_r$ [c] (h) | $d_{001}$ [d] (Å) | $d_{001K}$ [e] (Å) | RI [f] (%) |
| Kao–SIM1 | Kao–DMSO | (10% succinimide solution, *w/v*) | 114 | 12.00 | 7.13 | 91.5 |
| Kao–SIM2 | Kao–DMSO | (10% succinimide solution, *w/v*) | 23 | 12.00 | 7.15 | 84.0 |
| Kao–SIM3 | Kao–NMF | (10% succinimide solution, *w/v*) | 43 | 12.20 | 7.3 | 3.1 |
| Kao–SIM4 | Kao–DMSO | (10% succinimide solution, *w/v*) | 43 | 11.91 | 7.17 | 92.2 |
| Kao–SIM5 | Kaolinite (KGa-1b) | (10% succinimide solution, *w/v*) | 75 | — | 7.17 | — |
| Kao–GIM1 | Kao–DMSO | (10% glutarimide solution, *w/v*) | 69 | 12.33 | 7.23 | 70.7 |
| Kao–GIM2 | Kao–DMSO | (10% glutarimide solution, *w/v*) | 24 | 12.33 | 7.16 | 77.4 |

**Note:** Reaction details are given in the Experimental Section.

[a] All reactions took place at ambient tempaerature.

[b] SIM, succinimide; GIM, glutarimide; DMSO, dimethyl sulfoxide; NMF, *N*-methyl formamide; and Kao, kaolinite.

[c] Approximate reaction time.

[d] The specified interlayer distance (*d*) is that of the principal product phase calculated using (00l) reflections (see text).

[e] *d*001 reflections of the residual unexpanded kaolinite.

[f] Ratio of intercalation is the ratio of the intensities of the $d_{001}$ reflection of the modified phase over the sum total of all the $d_{001}$ reflections of the modified phase(s) and residual unexpanded kaolinite.

The interlayer expansions for the products were comparable. Succinimide expanded the kaolinite lattice to ~12.0 Å, while the observed $d_{001}$ for Kao–GIM intercalation compound was ~12.3 Å. After subtracting an average basal spacing of 7.15 Å for the pristine kaolinite (KGa-1b), this corresponds to an expansion of approximately 4.85–5.15 Å, which is the roughly expected interlayer expansion, corresponding to a flattened monolayer arrangement of the organic molecules in the interlamellar space. Comparable values for the interlayer expansion because of the monolayer intercalation of the organic molecules into kaolinite were reported elsewhere, e.g., an expansion of ~3.7–4.8 Å for Kao–polyols (adonitol, D-sorbitol, and D-mannitol) ((7); see next chapter), as well as 4.0 Å for Kao–PEG (18), and an expansion to 12.4 Å when poly(vinylpyrrolidone) was intercalated in kaolinite (24). For other layered materials, interlayer expansions, attributed to monolayer intercalation, of 3.7 Å for ethylene glycol intercalated into vermiculite (113), 4.0 Å for 15-crown-5 intercalated into $Na^+$-montmorillonite (114, 115), 3.9 Å for 18-crown-6 intercalated into $Ba^{2+}$-montmorillonite (114, 115), 2.8 Å for PEG intercalated into layered α-zirconium phosphate (116), and 4.5 Å for poly(ethylene oxide) intercalated into $V_2O_5$ (117) were also reported.

Based on a CPK model of glutarimide, the thickness of the molecule is approximately 4 Å. This value agrees with the observed expansion from XRD patterns. Moreover, cyclic imide molecules (see Chart 2.1) are not expected to adopt a conformation similar to that proposed for pyridine by Sugahara and co-workers (97) where the imide nitrogen fits in the $SiO_6$ macrorings of the silicate sheet, as this would be hindered by the proximity of the two carbonyl groups in the cyclic imide molecule. In addition, the main driving force for the

intercalation reaction is expected to result from the orientation of the oxygens of the molecule in a manner that permits the formation of hydrogen bonds with the hydroxyls of the aluminate interlamellar surface. The maximum hydrogen-bonding interaction could only be obtained should the organic molecules adopt a conformation in which its oxygens match up with the hydroxyl groups of the aluminol surface. The interatomic distance between the oxygens in the glutarimide molecule is approximately 5.6 Å, based on a CPK model. This is exactly two times the interhydroxyl distance, which is determined to be 2.8 Å by a Rietveld refinement of the kaolinite structure (57).

Finally, in a blank experiment when kaolinite itself (KGa-1b) was used as a starting material, it was recuperated unreacted. Typical X-ray powder patterns of the starting materials (kaolinite and Kao–DMSO) and of the resulting nanohybrids are shown in Fig. 2.1 for the range of 2–18° $2\theta$. Full XRD patterns of the intercalation compound resulting from the reaction of Kao–DMSO with the GIM are shown in Fig. 2.2, in comparison with the XRD patterns of the pure kaolinite (KGa-1b). It is worth noting that the $d_{060}$ reflection, characteristic of a dioctahedral clay mineral, remains at 1.49 Å in all cases. XRD patterns of the other Kao – cyclic imides reported in Table 2.1 are similar to this, and in all cases at least four (00l) reflections could be indexed. Thus, the layered structure of kaolinite remains largely unaffected, the only major variation being the value of the *d*-spacing.

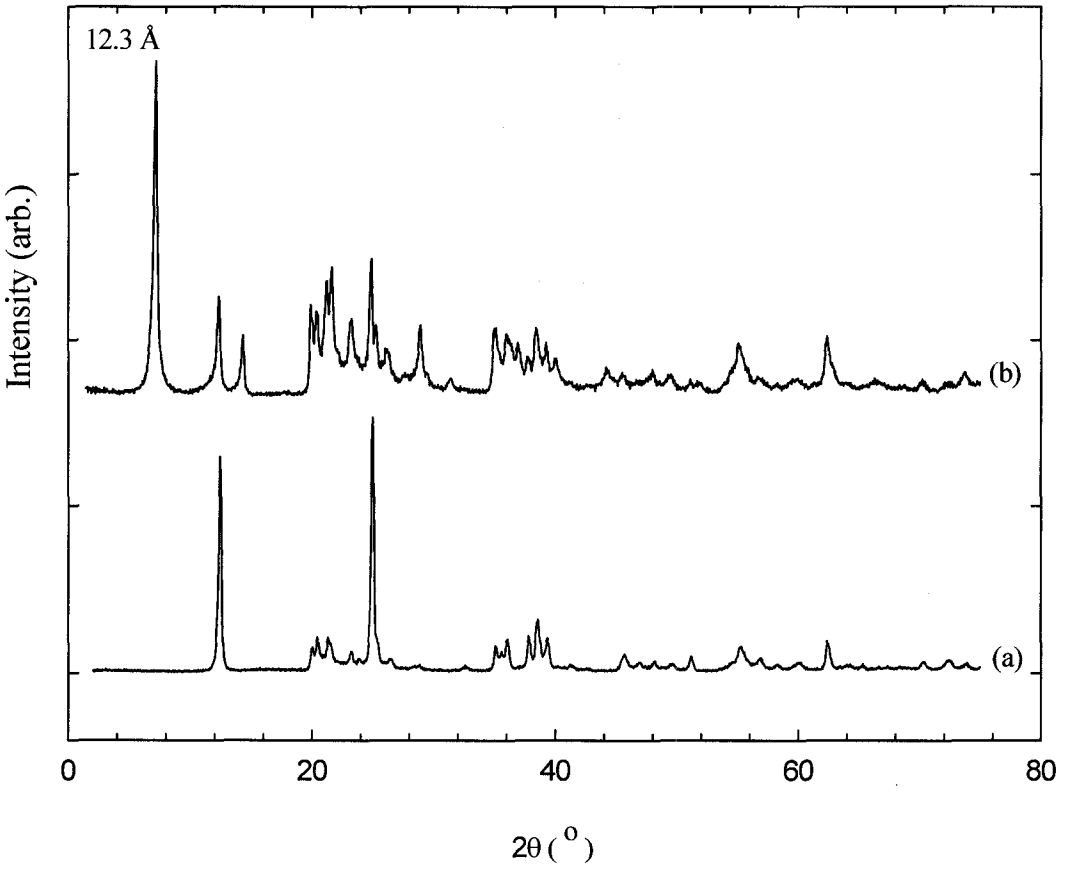


**Fig. 2.2.** XRD powder diffraction patterns ($2\theta$ = 2–75°) of (a) kaolinite and (b) Kao–GIM.

It is noteworthy that the products of the preliminary attempts, using Kao–NMF as a starting material, exhibited very low intercalation ratios (RI > 10%) even after similar reaction times to those of the reactions that involved the use of Kao–DMSO as a starting material. Clearly, from Table 2.1 and XRD diffraction patterns, Kao–DMSO was the most effective starting material, resulting in products with high ratios of intercalation (avg. RI = 90%). As mentioned before, the typical reaction conditions used (see Chapter 6) resulted in the complete displacement of the guest molecules, i.e., DMSO by the imides (see NMR Section); therefore, the reported interlayer expansion can only be attributed to the intercalated cyclic imides.

The lower intercalation ratio observed in case of Kao–GIM is plausibly due to the need to wash the product with DIW to dissolve the excess GIM, which might partially result in the de-intercalation of glutarimide molecules from the product.

### 2.2.1. Attempt for de-intercalation

Figure 2.3 shows XRD patterns of the Kao-SIM nanohybrid washed with only 2-propanol and of the same nanohybrid after washing with DIW for only 10 min. The interlayer expansion remained the same for the latter; however, the ratio of intercalation decreased dramatically, as most of the SIM molecules were de-intercalated. These results indicate the possibility of the use of the kaolinite intercalates as media for the controlled release of imide-based drugs in aqueous conditions.

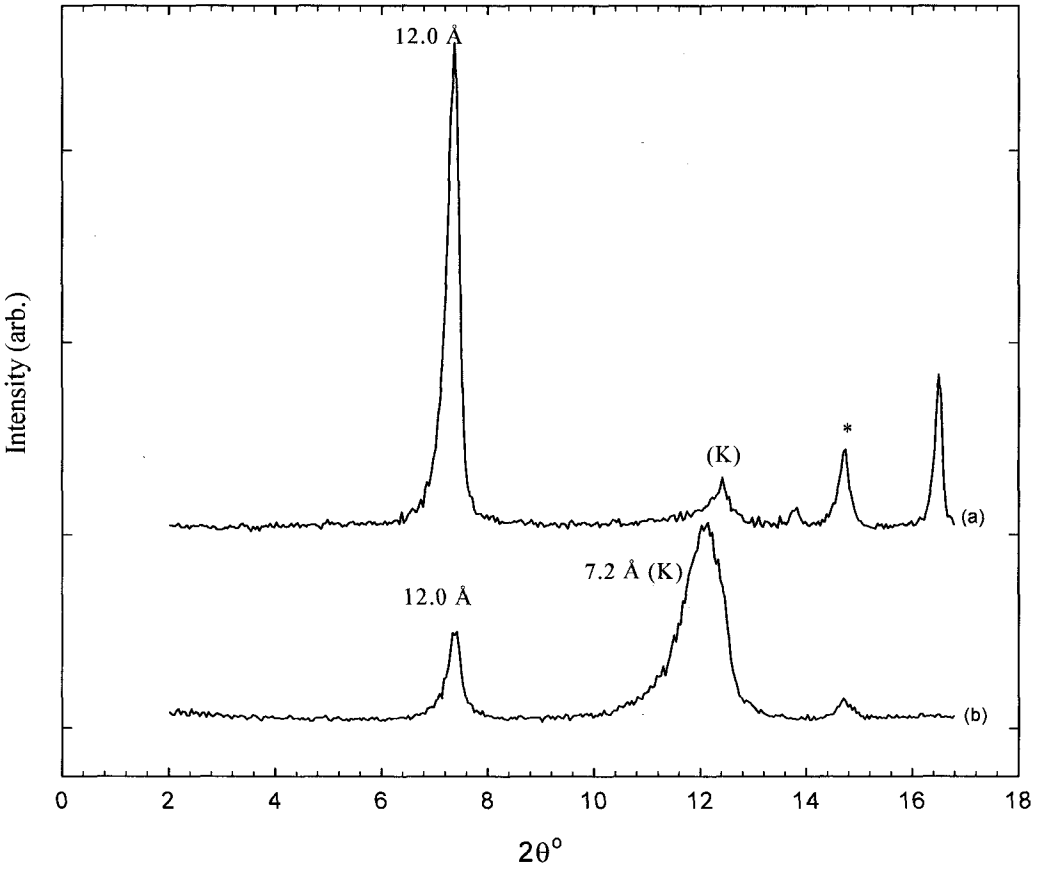


**Fig. 2.3.** XRD powder diffraction patterns ($2\theta$= 2–17°) of (a) Kao–SIM and (b) Kao–SIM.after washing with DIW for 10 min.

## 2.3 Elemental analysis

The results of the elemental analyses of typical Kao – cyclic imide samples are given in Table 2.2. The analyses was performed at very high temperatures (>1000 °C) to ensure the complete combustion of the analyzed nanohybrids. Kao–SIM2 sample gave C: 7.01%, H: 1.92%, and N: 2.44%. Thus, the stoichiometry of this sample is $Al_2Si_2O_5(OH)_4 \cdot (C_4H_5NO_2)_{0.63}$, using the average of the C, H, and N results. This sample was proven to be free of residual co-intercalated DMSO, since the sulphur content detected in the sample is <0.2% (see Table 2.2), and the elemental analysis of a typical starting material (Kao–DMSO) sample gave S ≈8% (see Table 2.2, and also see NMR Section). Similarly, Kao–SIM4 sample gave C: 8.31%, H: 1.91%, and N: 2.33%. Similarly, the stoichiometry of this sample is $Al_2Si_2O_5(OH)_4 \cdot (C_4H_5NO_2)_{0.65}$.

Kao–GIM2 sample gave C: 6.97%, H: 1.86%, and N: 1.62%. Similar to Kao–SIM4, the calculated stoichiometry of Kao–GIM2 is $Al_2Si_2O_5(OH)_4 \cdot (C_5H_7NO_2)_{0.49}$. The higher average occupancy value of ~0.64 unit of SIM per unit cell of kaolinite, compared with that of GIM (0.49), is expected because of the smaller succinimide molecule. Moreover, the lower occupancy value in case of Kao–SIM2 and Kao–GIM2, compared with Kao–SIM4, is consistent with the lower intercalation ratios for the first two intercalates (see Table 2.1).

**Table 2.2.** Summary of the elemental analysis results of the starting material (Kao–DMSO) and some of the produced nanohybrids.

| Sample | C (%) | H (%) | N (%) | S (%) |
|---|---|---|---|---|
| Kao–DMSO | 5.96 | 2.49 | 0.25 | 7.78 |
| Kao–SIM2 | 7.01 | 1.92 | 2.44 | <0.2 |
| Kao–SIM4 | 8.31 | 1.91 | 2.33 | — |
| Kao–GIM2 | 6.97 | 1.86 | 1.62 | — |

## 2.4 FTIR analysis

As mentioned before, FTIR analysis of the intercalates of succinimide and glutarimide is important to help understand the mechanism of hydrogen bonding to which the biological activity of the molecules is attributed (106, 110).

### 2.4.1 O–H stretching region (3800–3200 $cm^{-1}$)

Detailed assignments of the observed bands in the FTIR spectra of the produced nanohybrids are given in Tables 2.3 and 2.4. Kaolinite itself has a characteristic, signature O–H stretching pattern that consists of four bands at approximately 3697, 3667, 3652, and 3620 $cm^{-1}$ (Fig. 2.4a). The band at ~3620 $cm^{-1}$ is attributed to the stretching frequency of the internal (inner) hydroxyl group of kaolinite (See Fig.1.4, Chapter 1 for the structure of kaolinite). This hydroxyl group is believed to be aligned almost parallel to the direction of the (00l) layers, thus pointing in the direction of the unoccupied octahedral hole. This inner-hydroxyl stretching band is not usually influenced by the interlamellar modification of kaolinite. The remaining bands (3697, 3667, and 3652) are associated with the inner-surface (outer) hydroxyl groups that are believed to make an angle of 60–73° with the (001) plane, and these groups are accessible for hydrogen bonding with the appropriate intercalated molecules. Therefore, these inner-surface hydroxyl stretching bands are influenced by interlamellar modifications (59, 60), as it can be observed for Kao–DMSO (Fig. 2.4b).

Observing the O–H stretching patterns for Kao–SIM and Kao–GIM (Fig. 2.3c and d, respectively) one can notice significant differences from both kaolinite and Kao–DMSO (Fig. 2.4a and 2.4b, respectively). For Kao–DMSO (the starting material), the bands at 3694 and 3665 $cm^{-1}$ were attributed to the non H-bonded, coupled inner-surface hydroxyls; the coupling of these inner-surface hydroxyls is lost in case of the new intercalated nanohybrids. The band at 3697 $cm^{-1}$ is reduced in intensity compared with the corresponding band in the kaolinite spectrum but not with Kao–DMSO band. The Kao–DMSO band at 3665 $cm^{-1}$ disappeared completely, and a new band appears, in both cases, at ~3650 $cm^{-1}$, suggesting that one of these hydroxyls could be H-bonded to the intercalated cyclic imide. Similarly, in case of the Kao–DMSO, the bands at 3540 and 3505 $cm^{-1}$ were attributed to the stretching frequency of the coupled inner-surface hydroxyls that are H-bonded to the intercalated DMSO molecules. In the spectra of the new nanohybrids, these bands were replaced by three weak bands at ~3598, 3575, and 3538 $cm^{-1}$, and two broad ill-defined band can be observed at ~3438 and ~3300 $cm^{-1}$. The intensity and the band position of the band at 3620 $cm^{-1}$ remain unaffected. The significant modifications of the O–H stretching patterns, compared with those of the kaolinite and of the Kao–DMSO intercalate, indicate the complete replacement of the DMSO by the new organic molecules in the interlamellar space of kaolinite (see Table 2.3).

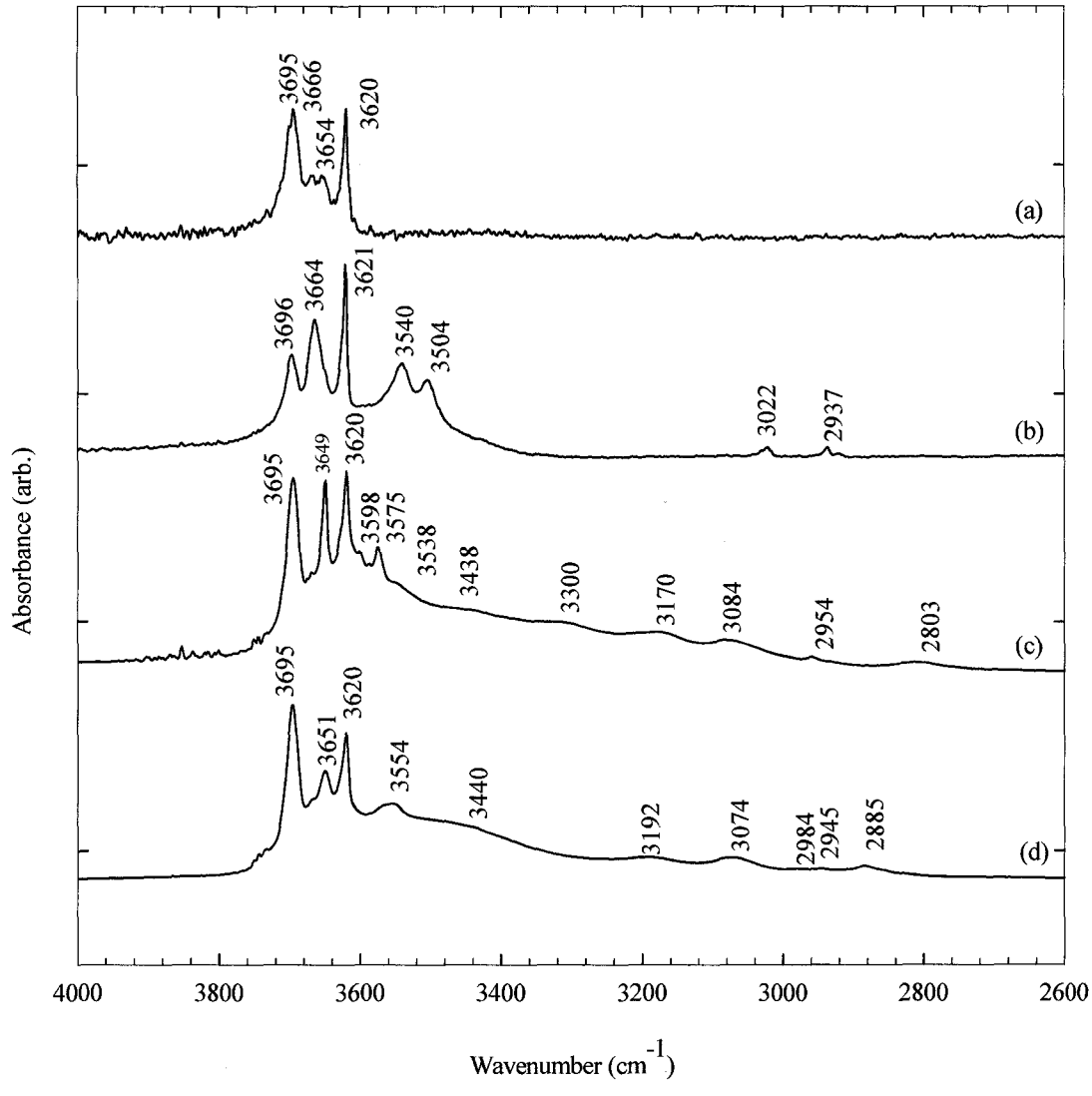


**Fig. 2.4.** FTIR spectra (4000–2600 $cm^{-1}$) of (a) kaolinite, (b) Kao–DMSO, (c) Kao–SIM, and (d) Kao–GIM.

**Table 2.3.** Observed FTIR absorbances, in the 4000–2000 $cm^{-1}$ range, and their assignments for the produced nanohybrids.

| Wavenumber ($cm^{-1}$) | | Assignments |
|---|---|---|
| Kao–SIM | Kao–GIM | |
| 3696 (vs) | 3695 (vs) | ν(O–H) (outer) |
| 3650 (vs) | 3651 (s) | ν(O–H) (H-bonded) |
| 3620 (vs) | 3620 (m) | ν(O–H) (inner) |
| 3598 (vw, sh)<br>3575 (m)<br>3538 (w)<br>3438 (w, br) | 3554 (m)<br>3440 (m, br) | ν(O–H) (H-bonded) |
| 3300 (w, br)<br>3170 (w) | 3192 (w) | ν(N–H) and ν(N–H···O) |
| 3084 (w) | 3074 (w) | ν(C=O) + δ(N–H) |
| 2954 (vw)<br>2803 (vw) | 2984 (vw)<br>2945 (vw)<br>2885 (vw) | ν($CH_2$) (asymmetric and symmetric stretching) |

**Note:** The absorptions are w, weak; m, medium; s, strong; vw, very weak; vs, very strong; sh, shoulder; and br, broad.

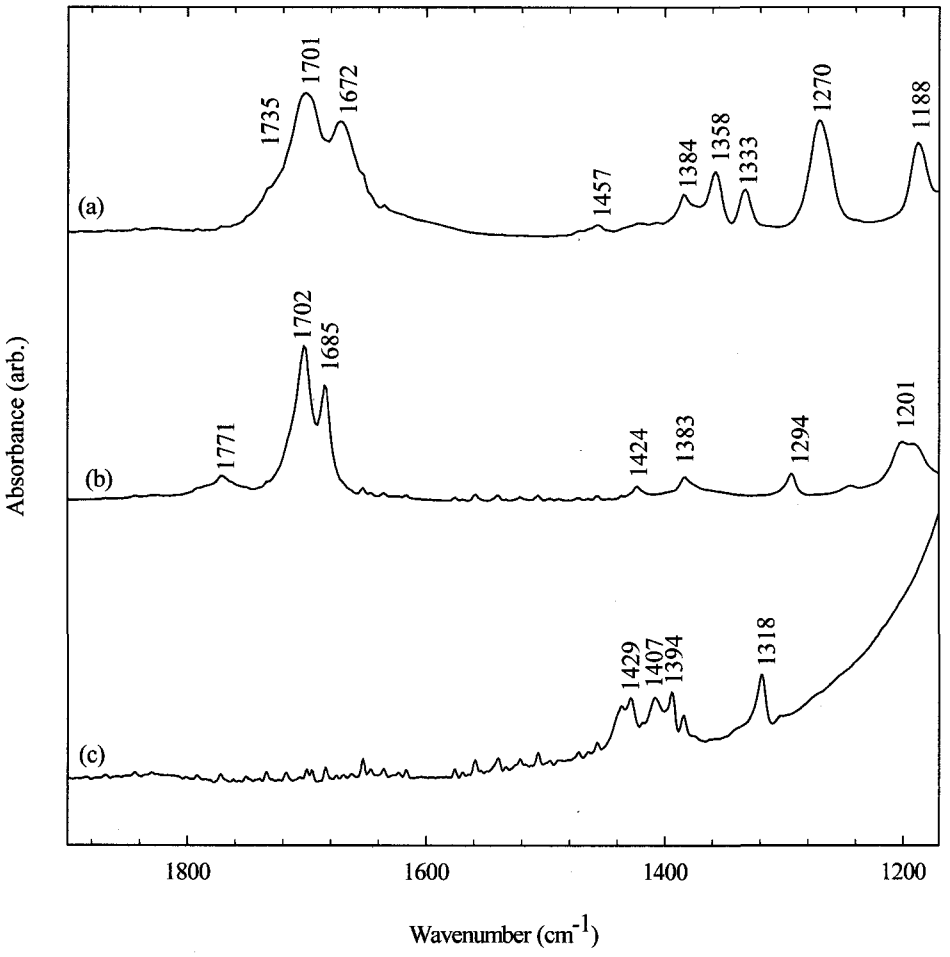


**Fig. 2.5.** FTIR spectra (1800–1200 $cm^{-1}$) of (a) Kao–GIM, (b) Kao–SIM, and (c) Kao–DMSO.

## 2.4.2 Characteristic frequencies of the imide OC–NH–CO group

The bands at 3170 and 3192 $cm^{-1}$ in the infrared spectra of Kao–SIM and Kao–GIM, respectively (see Fig. 2.4), can be assigned to the stretching vibrations of the H-bonded NH groups. For monomeric glutarimide, the N–H stretching mode was reported at 3400 $cm^{-1}$ (110), which is ~210 $cm^{-1}$ higher than the value observed for the solid polycrystalline glutarimide (3189 $cm^{-1}$; see Fig. 2.4) (118, 119) where the molecules are linked by NH···O hydrogen bonds. In case of the Kao–GIM intercalate, observing the band roughly at the same wavenumber (3192 $cm^{-1}$) indicated that NH groups are involved in hydrogen bonding in the interlamellar space.

The N–H in-plane bending vibration is observed at 1424 $cm^{-1}$ for Kao–SIM and at 1407 $cm^{-1}$ for Kao–GIM. The characteristic absorption bands at ~3080 $cm^{-1}$ in both nanohybrids can be attributed to a combination tone: $\nu$(C=O) + $\delta$(N–H).

Infrared spectra of cyclic imides have complex patterns in the region 1800–1600 $cm^{-1}$. The splitting of the bands in this region is characteristic of the all cyclic imides containing two C=O groups in the cis position. It was concluded that the two intense carbonyl stretches in the spectra of cyclic imides correspond to the symmetric (weak, high-frequency band) and antisymmetric (for the strong, low-frequency one) stretching of the two carbonyl groups (106, 110, 120, 121). Early assumptions that the lower wavenumber bands, in case of SIM (122) and GIM (119), correspond to the stretching of the C=O groups of the H-bonded molecules were ruled out. Moreover, the observed similar patterns for the produced nanohybrids (Fig. 2.5 and Table 2.4) confirmed the recent conclusion, as the both carbonyl

groups would have been expected to become involved in H-bonding interactions upon intercalation of the imide molecules in the interlamellar spaces. Finally, other signals in the 1800–1600 $cm^{-1}$ region (1771 $cm^{-1}$ for SIM, and 1672 $cm^{-1}$ for GIM) correspond to some combination tones (110, 123).

### 2.4.3 C–H stretching region (3100–2800 $cm^{-1}$)

The bands in this region are diagnostic of the incorporation of organic moieties (18). Bands, associated with the methylene groups of the appropriate imides, are observed upon intercalation into the interlayers of kaolinite. In case of Kao–SIM, distinct asymmetric and symmetric C–H stretching bands at ~2954 and 2803 $cm^{-1}$ (Fig. 2.4). Kao–GIM, which has an additional $CH_2$, exhibited bands at ~2984, 2945, and 2885 $cm^{-1}$ (Fig. 2.4).

Clearly, close examination of this region reveals the absence of residual interlayer DMSO, as the bands at approximately 3022 and 2937 $cm^{-1}$, attributed to the symmetric and asymmetric stretching of the methylene groups of the DMSO molecules, respectively, completely disappeared in all cases (see Fig. 2.4).

Full assignments of the observed OH and CH stretching bands of three different novel nanohybrids are reported in Table 3.

### 2.4.4 HOH bending region (1680–1600 $cm^{-1}$)

The presence of an ill-defined δ(HOH) band at ~1653 $cm^{-1}$ for both Kao–SIM and Kao–GIM suggests that co-intercalated water molecules are present to some extent (Fig. 2.5) (18). However, in case of the Kao–GIM intercalate, the observed band at 1636 $cm^{-1}$

**Table 2.4.** Observed FTIR absorbances, in the 1800–400 $cm^{-1}$ range, and their assignments for the produced intercalates.

| Wavenumber ($cm^{-1}$) | | Assignments |
|---|---|---|
| Kao–SIM | Kao–GIM | |
| 1771 (m) | — | $\delta(CH_2)$ deformation × 2 (combination tone) |
| 1702 (vs)<br>1685 (vs) | 1735 (m, sh)<br>1701 (vs) | $\nu$(C=O) (symmetric and antisymmetric stretching) |
| — | 1672 (s) | Combination tone |
| 1653 (vw) | 1653 (vw) | $\delta$(HOH) co-intercalated |
| — | 1636 (vw) | $\delta$(HOH) adsorbed |
| 1424 (w)<br>1201 (s) | 1407 (vw) | $\delta$(N–H) + $\nu_{as}$(C–N–C) |
| 1383 (w) | 1384 (w)<br>1358 (m) | $\nu_s$(C–N–C) + $\nu$(C–C) |
| 1294 (w)<br>1244 (vw)<br>1113 (vs) | 1457 (vw)<br>1436 (vw)<br>1420 (vw)<br>1333 (m)<br>1271 (s)<br>1188 (s)<br>1083 (vs) | $\delta(CH_2)$ deformation bands |
| 1059 (vs) | 1056 (vs) | $\nu_{as}$(C–C) |
| 1033 (vs)<br>1008 (vs) | 1033 (vs)<br>1011 (vs) | Si–O stretching |
| 917 (vs) | 915 (vs) | O–H bending (inner) |
| 791 (w)<br>755 (m)<br>695 (s)<br>641 (m)<br>427 (s) | 802 (w)<br>757 (w)<br>697 (m)<br>430 (s) | Si–O |
| 539 (vs) | 541 (vs) | Al–O–Si deformation |
| 473 (vs) | 473 (vs) | Si–O–Si deformation |

**Note:** The bands are w, weak; m, medium; s, strong; vw, very weak; vs, very strong; sh, shoulder; and br, broad.

indicates that water molecules were also adsorbed on the surface in addition to being co-intercalated.

### 2.4.5 C–H deformation bands (1500-1200 $cm^{-1}$)

Bands, indicative of various CH deformations, can be observed in the FTIR spectra of these nanohybrids. Kao–DMSO shows deformation bands at 1428, 1410, 1394, and 1319 $cm^{-1}$ (see Fig. 2.5) (70). New patterns were observed for Kao–SIM and Kao–GIM (Fig. 2.5), the C–H deformation bands are in the range of ~1460–1100 $cm^{-1}$. The broad ill-defined band(s) centered around 1056 $cm^{-1}$ can be attributed to $\nu_{as}$(C–C). Other bands at this region cannot be attributed to residual DMSO, since these sample were shown to have no residual interlayer DMSO (see NMR section). Also, other IR bands, indicating the presence of DMSO (Fig. 2.3), have completely disappeared.

Finally, the bands around 1384 and 1358 $cm^{-1}$ could be attributed to some combination tones, e.g., $\nu_s$(C–N–C) + $\nu$(C–C).

### 2.4.6 The kaolinite-lattice vibrations and Al–O–H bending region (1200-800 $cm^{-1}$)

The bands at this region provide information regarding any perturbations to the kaolinite lattice vibrations (1150–1000 $cm^{-1}$) and any changes in the Al–O–H bending modes of kaolinite (900–980 $cm^{-1}$). Figure 2.6 shows the FTIR patterns (1200–400 $cm^{-1}$) for kaolinite, Kao–DMSO, and Kao–SIM, respectively. The patterns of Kao–SIM (Fig. 2.6c) show some perturbation of the kaolinite lattice vibrations. The two most-intense vibrations of kaolinite at 1033 and 1010 $cm^{-1}$ remain relatively unaffected expect for a small shift for the latter in both nanohybrids (see Table 3). These bands have been previously assigned to the in-plane Si–O–Si stretching vibrations of kaolinite (59) and are often shifted slightly upon the intercalation of a guest species such as DMSO, as can be seen for the Kao–DMSO starting material, where these bands are blue-shifted slightly to 1039 and 1016 $cm^{-1}$ (Fig. 2.6b).

The perpendicular Si–O vibrations, found in kaolinite at 1102 and 1116 $cm^{-1}$ (59) (Fig. 2.6a), are also slightly perturbed for the Kao–SIM and for the Kao–GIM compared with the pristine kaolinite and the starting material (Kao–DMSO). In addition, a new band at ~1059 $cm^{-1}$ can be assigned to the asymmetric stretching of the C–C bonds of the organic molecules.

The kaolinite band at 939 $cm^{-1}$ has been assigned to the in-plane bending vibrations of the inner-surface (outer, accessible) hydroxyl groups, whereas the band at 914 $cm^{-1}$ has been assigned to the bending vibrations of the inner (internal, inaccessible) hydroxyls (59, 60).

Upon intercalation of DMSO, the intensity of the band at 939 $cm^{-1}$ is greatly reduced, and another band of higher frequency appears at 958 $cm^{-1}$ (Fig. 2.6b). The band at 914 $cm^{-1}$ shows a characteristic slight shift to a lower frequency at 905 $cm^{-1}$, presumably because of the repulsive interaction between one methyl group of the DMSO molecule, which is supposed to be keyed into the $(SiO)_6$ macro-ring of the silicate surface, and the internal hydroxyls of kaolinite (72, 73, 75). For Kao–SIM and Kao–GIM, the inner hydroxyl band of kaolinite is almost unaffected, and this is plausibly due to the inability of the organic molecules to key in the $(SiO)_6$ macro-rings of the silicate surface. Similar results were observed for most other kaolinite intercalates (7, 8, 18).

Upon intercalation of the imide, the kaolinite band at 939 $cm^{-1}$ almost disappeared, as well as the new Kao–DMSO starting material band at 958 $cm^{-1}$. This result, along with all the previously mentioned observations, is in agreement with the complete displacement of the DMSO molecules in the interlamellar space by the appropriate imide molecules, and the formation of H-bonds between the imide molecules and the inner-surface hydroxyls. A complete list of all the observed vibrations is given in Tables 2.3 and 2.4.

In general, FTIR observations also confirm the proposed structural model for the intercalated cyclic imides in which the organic molecules are arranged in a flattened monolayer arrangement in the interlamellar space with most of the interaction taking place between the carbonyl groups of the imides and the hydroxyl groups of the aluminol surface of kaolinite (in the form of hydrogen bonding).

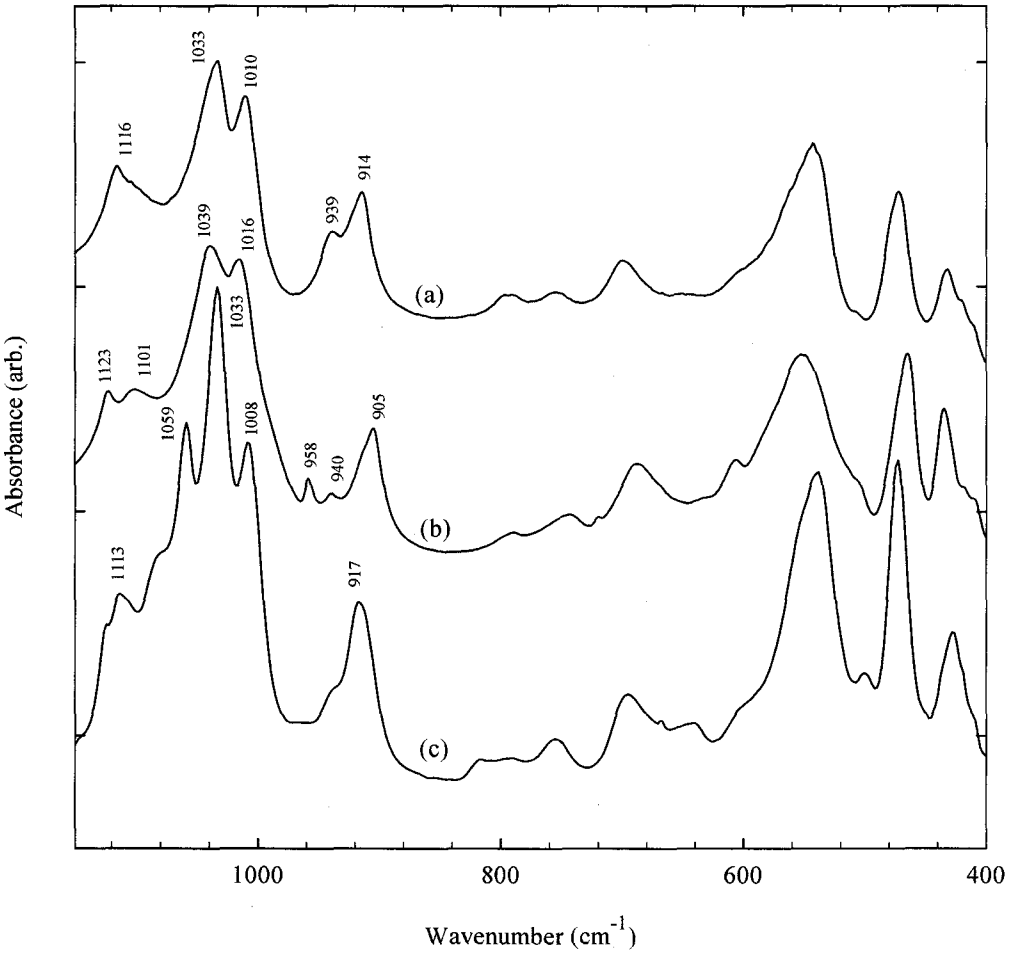


**Fig. 2.6.** FTIR spectra (1200–400 $cm^{-1}$) of (a) kaolinite, (b) Kao–DMSO, and (c) Kao–SIM.

## 2.5 Solid-state NMR analysis

### 2.5.1 $^{13}C$ NMR analysis

#### 2.5.1.1 Identification of the intercalated species

A series of $^{13}C$ NMR CP/MAS and DD/MAS experiments were performed on the produced nanohybrids to identify and study the nature of the intercalated molecules and to obtain preliminary information regarding the dynamics of these intercalated molecules. The results are summarized in Tables 2.5 and 2.6. Information on the dynamics of the intercalated organic molecules could also be obtained using dipolar dephasing experiments. A list of the observed $^{13}C$ chemical-shift and linewidth values of the starting materials (crude organic molecules; SIM in this case) and of the produced intercalated nanohybrids is depicted in Table 2.5. Assignments of the peaks are also shown in Table 2.5. The spectrum of the crude SIM was in excellent agreement with the reported in the literature (125) (see Fig. 2.7).

The $^{13}C$ NMR spectra of the produced Kao–SIM nanohybrid and Kao–DMSO starting material are also shown in Fig. 2.7. Assignments of the observed signals are listed in Table 2.5.

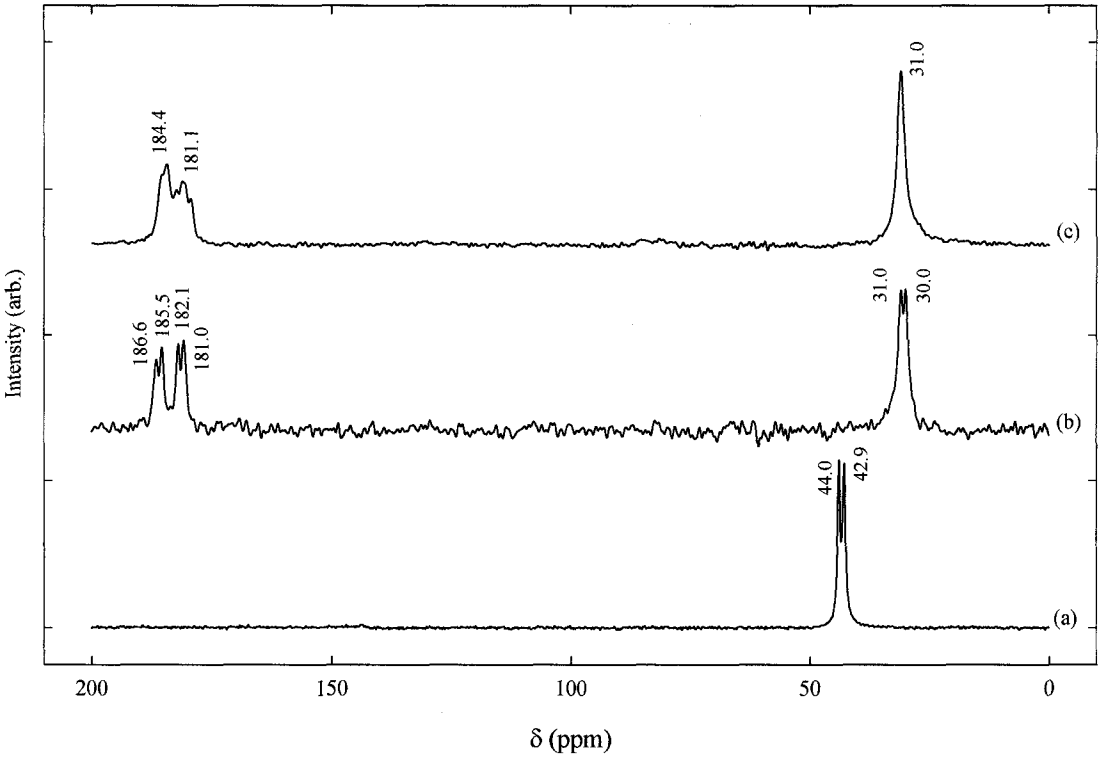


**Fig. 2.7.** Solid-state $^{13}C$ CP/MAS NMR spectra (50.31 MHz) of (a) Kao–DMSO, (b) crude SIM, and (c) Kao–SIM.

**Table 2.5.** Observed $^{13}C$ NMR chemical shifts (δ), peakwidth at half height (FWHM)($\nu_{1/2}$), and their assignments for the crude organic material and produced nanohybrids, using Kao–DMSO as a starting material.

| Crude succinimide | | Kao–SIM | | Kao–GIM | | |
|---|---|---|---|---|---|---|
| δ (ppm) | $\nu_{1/2}$ (Hz) | δ (ppm) | $\nu_{1/2}$ (Hz) | δ (ppm) | $\nu_{1/2}$ (Hz) | Assignment |
| — | — | — | — | 18.9 | 137 | $CH_2$ |
| 30.0<br>31.0 | 58.6<br>68.1 | 31 | 90.2 | 33.2 | 186 | $CH_2$ (adjacent to C=O) |
| 181<br>182<br>185.5<br>186.6 | 69.4<br>56.1<br>62.8<br>63.3 | 179.4<br>181.2<br>182.4<br>184.4<br>185.5 | Broad envelop with five maxima | 176.8 | 201 | $C$=O |

**Note:** The spectra were obtained on a Bruker AVANCE-500 instrument, operating at 125.77 MHz.

[a]Non-applicable or not detected.

For crude SIM, the signals at ~30.0 and 31.0 ppm are unambiguously attributed to the methylene carbons of the succinimide molecule (see Chart 2.1), while the signals at ~180–186 ppm are attributed to the carbons of the carbonyl groups, and the presence of more than one signal can be attributed to the hydrogen bonding interaction between succinimide molecules in the crystalline state (123). Upon intercalation, one signal at ~31.0 ppm was observed for the methylene carbons, and a broad envelope with five maxima was recorded for the carbonyls (Fig. 2.7c). The results confirm that the cyclic imide molecule keeps its structure in the interlamellar space of kaolinite. In case of the intercalated compound, the observed broadness of the measured linewidths at half-height of the peaks $\nu_{1/2}$ (see Table 2.5), compared with the crude crystalline SIM, indicate that the organic molecules are now present in a different local environment. This increase in linewidths can plausibly be attributed to the fact that, upon intercalation, the molecular motion is greatly reduced, and it can also be due to the loss of crystallinity upon intercalation.

Complete displacement of the guest DMSO molecules of the starting material was obtained. No DMSO signals were observed in the spectrum of Kao–SIM, thus indicating that only succinimide molecules were present in the interlamellar space. This result ruled out any possible co-intercalation.

In this study, Kao–GIM nanohybrid gave resonances at ~18.9, 33.2, and 176.8 ppm (Fig. 2.8 and Table 2.5). These chemical shifts are attributed to the carbons of the $CH_2$, $2 \times CH_2$

groups adjacent to the carbonyls, and carbonyl groups, respectively. Similar to the case of Kao –SIM, DMSO signals were not observed in Kao–GIM spectrum, indicating the complete displacement of the guest DMSO molecules by the glutarimide molecules.

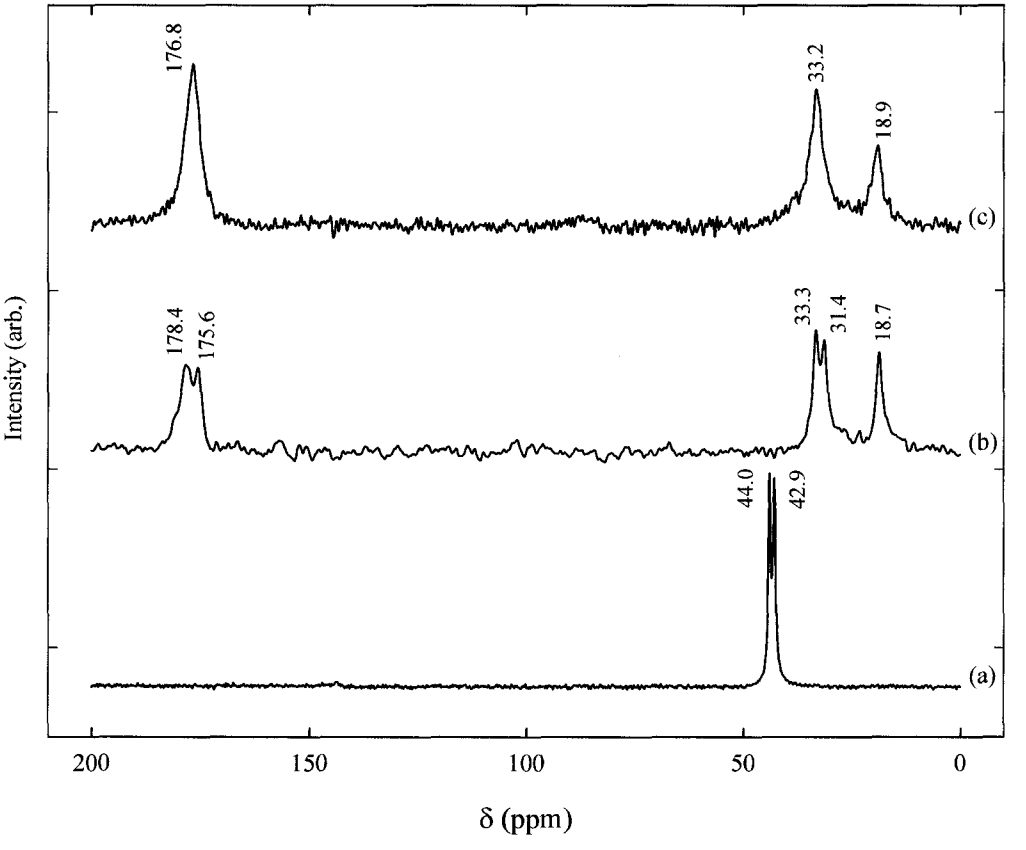


**Fig. 2.8.** Solid-state $^{13}C$ CP/MAS NMR spectra (50.31 MHz) of (a) Kao–DMSO, (b) Kao–GIM1 with excess unintercalated GIM, and (c) Kao–GIM2.

Figure 2.8b shows the spectrum of the first prepared Kao–GIM sample that contained traces of excess non-intercalated crystalline glutarimide. In addition to the relatively broad intercalated-GIM lines, two other sharp signals are present in the spectrum at 33.3 and 175.6 ppm. These signals are attributed to the crude GIM. Washing and centrifuging the product with excess water dissolved the excess glutarimide, and the $^{13}C$ NMR spectrum for the washed sample was recorded (Fig. 2.8c). Crude material peaks disappeared from the spectrum of the washed sample, confirming that the remaining signals can only be attributed to the intercalated molecules.

### 2.5.1.2 Dipolar dephasing experiments and dynamic studies

A series of dipolar dephasing (DD)/MAS experiments was performed on the Kao–GIM sample (Fig. 2.9).

Dipolar dephasing is a technique that can be used to differentiate between different types of carbons in the $^{13}C$ NMR spectrum (126). The overall signal decay for carbons strongly coupled to protons, such as methylene carbons has been shown to be best described by equation [2.1]

[2.1] $$I_{DD} = I_o e^{-\tau^2/(2T_2^2)}$$

where $\tau$ is the dipolar dephasing delay time and $T_2$ is the transverse relaxation time constant. $I_{DD}/I_o$ is the ratio of the intensities of the $^{13}C$ resonances obtained with ($I_{DD}$) and

without ($I_o$) dipolar dephasing (127), and this ratio is used to discriminate between carbons that are strongly bound to protons, e.g., methine and methyl carbons, for which the overall signal decay has been described by equation [2.1], and other types of carbons, i.e., weakly bound to protons, carbonyls, and methyl groups. This ratio can also be used as a semi-quantitative measure of the dynamic states of the molecular group studied by the dipolar dephasing technique. If the molecular group is rigidly bound, this ratio will decrease, whereas the molecular motion will cause an increase of the ratio up to a maximum of one.

#### 2.5.1.2.1 Kao–GIM intercalate

The DD/MAS results for Kao–GIM are illustrated in Fig. 2.9. Additional data are also reported in Table 2.6. Thus, in a series of experiments, the dipolar dephasing time ($\tau$) was varied from 0 to 50 μs for the sample, and the variation in intensity was monitored (Fig. 2.9). This qualitatively showed that the organic molecules are constrained in the interlamellar spaces of kaolinite. After 40 μs dephasing time, almost no signal for the methylene carbons of glutarimide could be detected. The intensity of the carbonyl signal remained almost unaffected in all cases, even after 40–50 μs dephasing time (see Table 2.6).

**Table 2.6.** Summary of the $^{13}C$ CP/MAS and DD/MAS results for some of Kao–GIM nanohybrid.

| Chemical shift (δ ppm)[a] | $I_{DD}/I_o$[b] | $\nu_{1/2}$ (CP/MAS) (Hz) | $\nu_{1/2}$ (DD/MAS)[d] (Hz) |
|---|---|---|---|
| 18.9 | —[c] | 147 | — |
| 33.2 | — | 234 | — |
| 176.8 | 0.8 | 201.4 | 222.7 |

**Note:** The spectra were obtained on a Bruker ASX-200 instrument, operating at 50.31 MHz.
[a]For carbon types (assignments), see Table 5.
[b]$I_{DD}$ is the peak intensity obtained with $\tau = 40$ μs, and $I_o$ is the peak intensity obtained with the CP/MAS experiment, using the same number of scans.
[c]—: Residual or no signal for the peak in the DD/MAS spectrum.
[d]For $\tau = 40$ μs.

The results for Kao–GIM sample are plotted in Fig. 2.10, as the ratio for each type of methylene carbons vs. the dipolar dephasing time. To test the validity of equation [2.1], the same data were plotted in Fig. 2.11 as $\ln(I_{DD}/I_o)$ vs. $\tau^2$. The result should be a straight line with a slope = $-1/(2T_2^2)$. For the methylene carbon signal at ~19 ppm, the graph was linear; the points were fitted to a first-order equation by a non-linear least-squares approach, using the "Solver" option of Microsoft® Excel (statistical linear regression factor $R^2$ of 0.997) with a $T_2$ value of ~15.4 μs for $\tau$ values up to 30 μs. For higher values of $\tau$ (40 and 50 μs), there were no residual dipolar dephased peaks detected. Similarly, for the signal at ~33 ppm, the graph was linear, and the points were fitted to a first-order equation by a non-linear least-squares approach, resulting in a statistical linear regression factor $R^2$ of 0.98 with a $T_2$ value of ~14.7 μs for $\tau$ values up to 30 μs (see Table 2.6). This breakdown in the linearity at higher values of $\tau$ is again due to the difficulty in obtaining accurate intensity ratio measurement for the residual peaks.

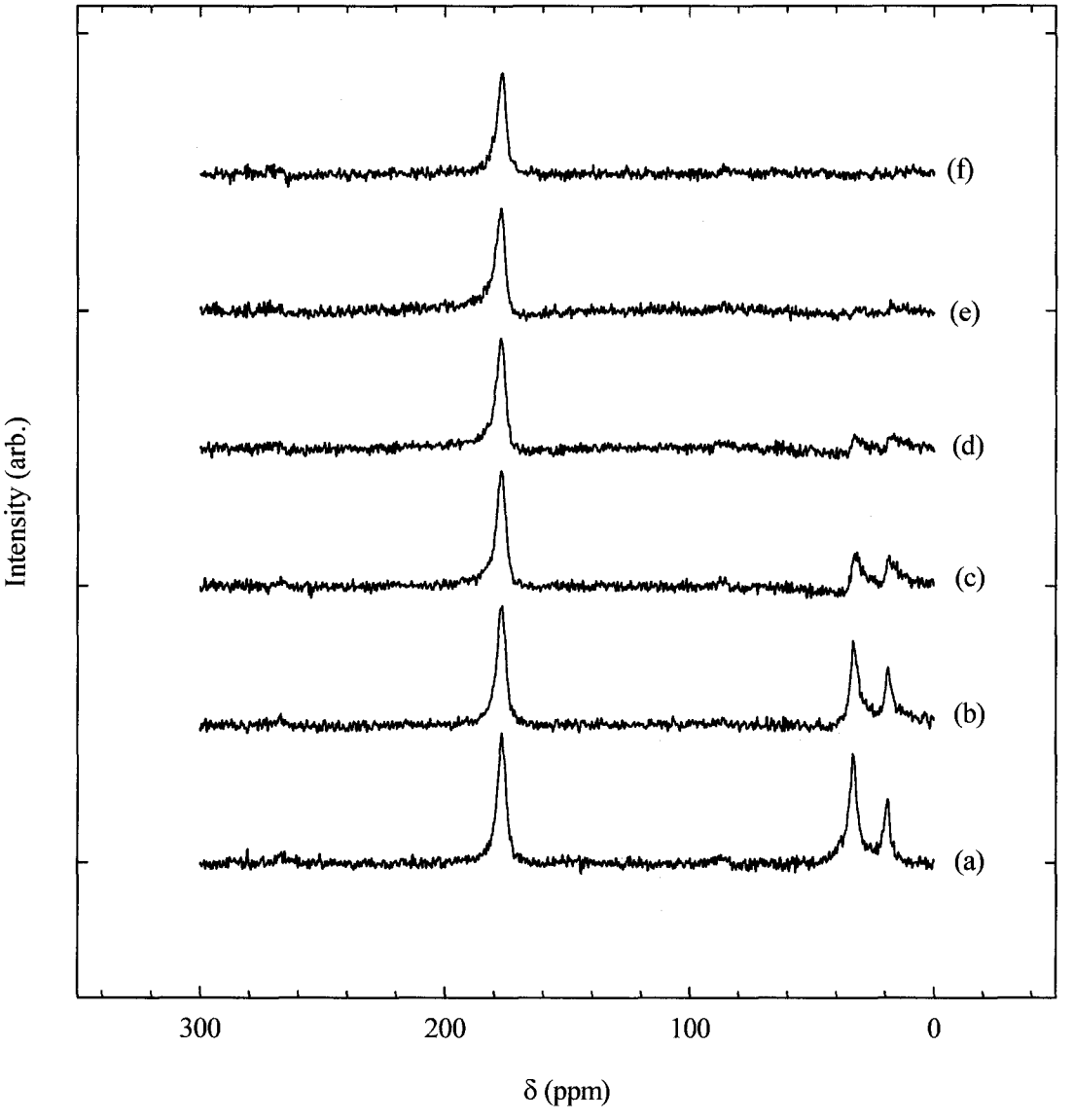


**Fig. 2.9.** Solid-state $^{13}C$ NMR spectra (50.31 MHz) of Kao–GIM2: (a) CP/MAS; (b–f) dipolar dephasing, $\tau$ = 10, 20, 30, 40, and 50 μs, respectively.

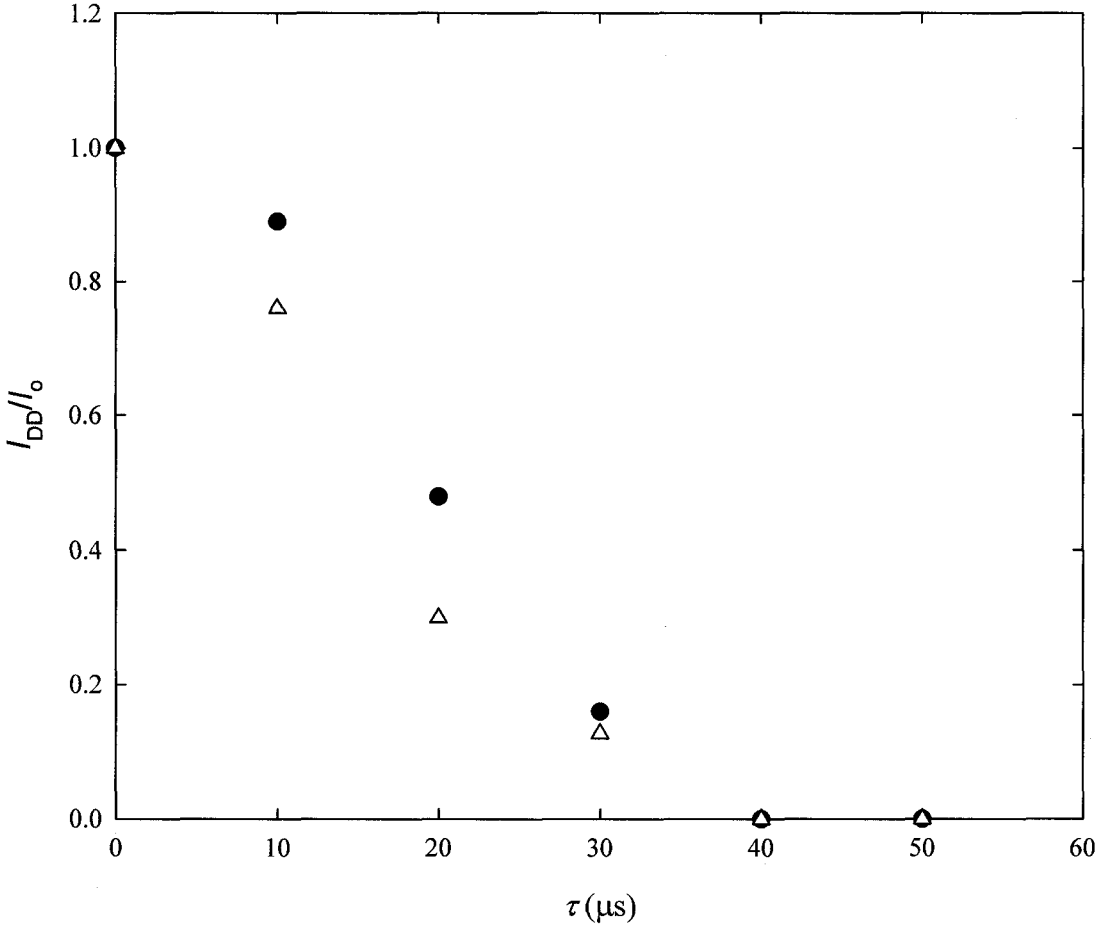


**Fig. 2.10.** Plots of $I_{DD}/I_o$ vs. dipolar dephasing time ($\tau$) for the $^{13}C$ NMR DD/MAS spectra acquired for Kao–GIM2; data for the 19 ppm signal: (•) and the 33 ppm signal: (Δ).

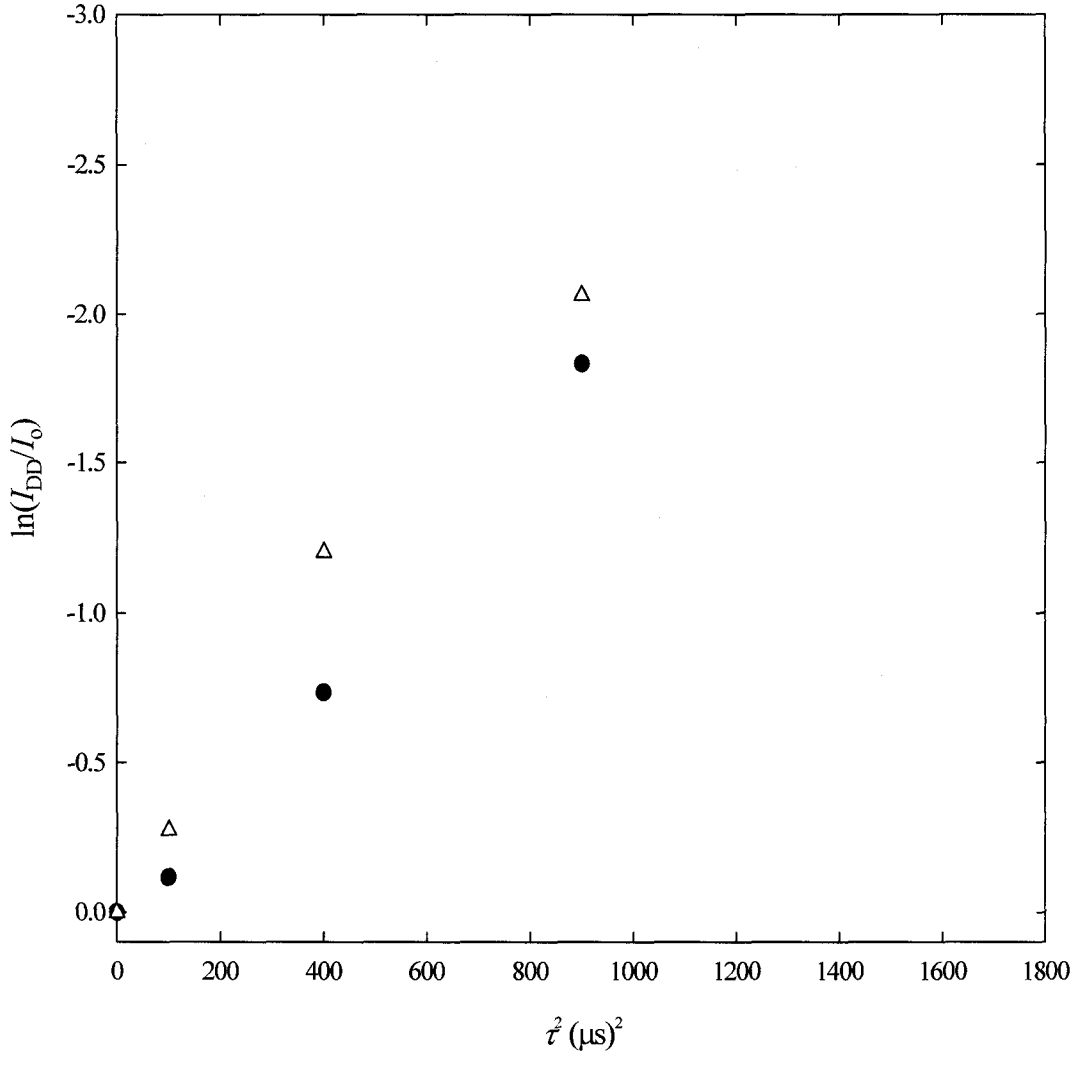


**Fig. 2.11.** Plots of $\ln(I_{DD}/I_0)$ vs. the square of the dipolar dephasing time ($\tau^2$) for the $^{13}C$ NMR DD/MAS spectra acquired for Kao–GIM2; data for the 19 ppm signal: (•) and the 33 ppm signal: (Δ).

### 2.5.2 $^{29}$Si NMR measurements

Kaolinite silicons can be described as $Q_3$(0Al)-type silicons. Early measurements reported only one $^{29}$Si resonance in kaolinite, and it was attributed to the existence of only one silicon environment in kaolinite (129). Using a high-frequency instruments, the $^{29}$Si peak in the kaolinite spectrum can be resolved into two components (130). The difference in chemical shift, causing the splitting of the kaolinite signal, is due to two inequivalent silicon sites. Thus, the splitting was attributed to the existence of two different but equally populated silicon sites or environments. However, the small shift difference between the signals (<0.5 ppm) indicated only a slight difference between the two sites. Primarily, it was suggested that the two different sites are due to distortion within the layer, the need to accommodate interlayer hydrogen bonding (130), or to the differences in Si–Al distances (74, 131). Based on the study of different kaolinites with different degrees of crystallinity, it was concluded that interlayer hydrogen bonding, causing two different silicon environments, is the main reason for signal splitting in kaolinite (132).

In this chapter, several $^{29}$Si MAS measurements were obtained for the starting materials and the produced Kao–SIM intercalated nanohybrid on a Bruker AVANCE-500 instrument, operating at 99.35 MHz. The recorded chemical shifts, referenced to tetramethyl silane (TMS) at 0.0 ppm, are listed in Table 2.7, and the spectra are stacked in Fig. 2.12.

The recorded $^{29}$Si NMR results for the pristine kaolinite and for Kao–DMSO intercalate were in agreement with literature values. Generally, the shift to lower frequency, observed in most intercalates, was attributed to weaker interaction between the guest molecules and

the silicate sheet. This was confirmed for the SIM intercalation compound, as the spectrum showed a strong signal centered at about –92.3 ppm with two medium signals at ~ –91.5 and –90.5 ppm. These downfield shoulders can be attributed to the residual (non-intercalated) kaolinite.

**Table 2.7.** Summary of the $^{29}Si$ MAS signals for the starting materials and the produced nanohybrids.

| Sample | Chemical shift (δ ppm) |
|---|---|
| KGa-1b | One strong signal with two resolved maxima at –90.9 and –91.5. |
| Kao–DMSO | –90.9 (w)<br>–91.5 (w)<br>–92.7 (vs) |
| Kao–SIM | –90.5 (m)<br>–91.5 (m)<br>–92.3 (s) |

**Note:** The spectra were obtained on a Bruker AVANCE-500 instrument, operating at 99.35 MHz with a spinning speed of 6 kHz. Signal intensities: s, strong; m, medium; w, weak; vs, very strong; vw, very weak.

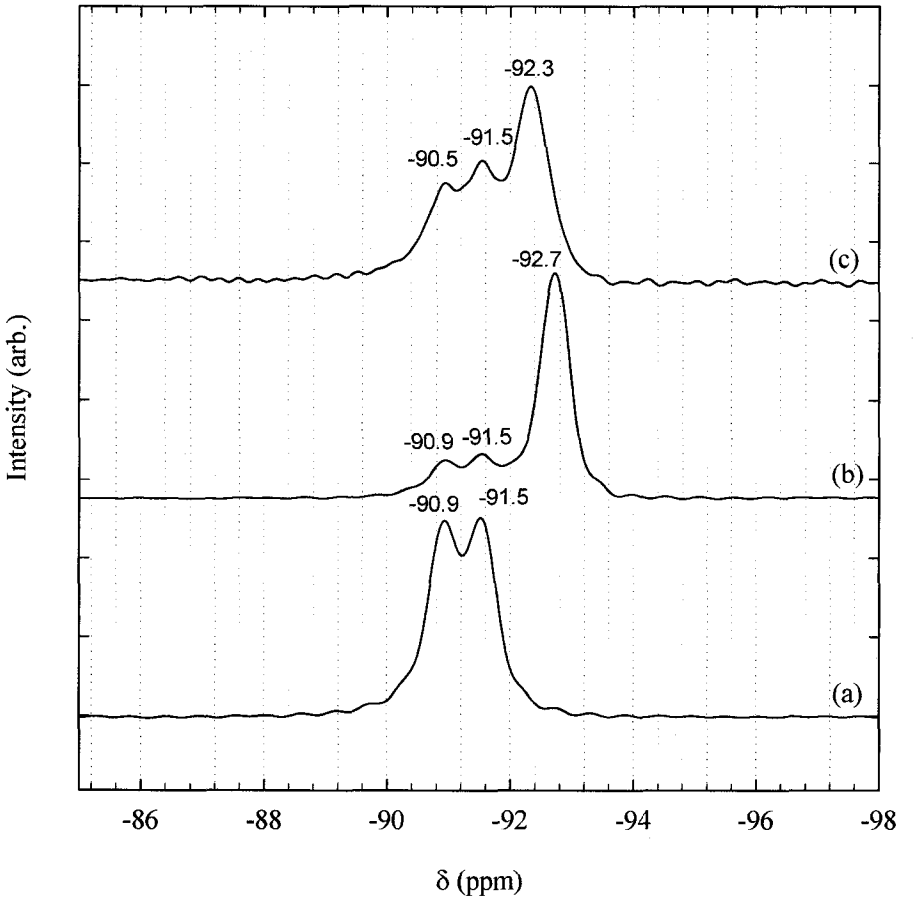


**Fig. 2.12.** $^{29}$Si MAS NMR spectra (99.35 MHz) of (a) kaolinite, (b) Kao–DMSO, and (c) Kao–SIM.

## 2.5.3 $^{27}$Al NMR measurements

$^{27}$Al NMR spectra of kaolinite and intercalates usually show signals that are attributed to both octahedral and a small amount of tetrahedral aluminum sites (133). The $^{27}$Al MAS NMR spectra of kaolinite and Kao–SIM intercalate were obtained at 130.32 MHz at a spinning rate of 14.0 kHz, and they are depicted in Fig. 2.13. Generally, a broad signal is observed, with a maximum in the range 3.3 to 3.6 ppm for the octahedral site in agreement with previous studies (72, 75, 134, 135). This is an indication that the octahedral environment (coordination) of Al is only slightly affected by intercalation.

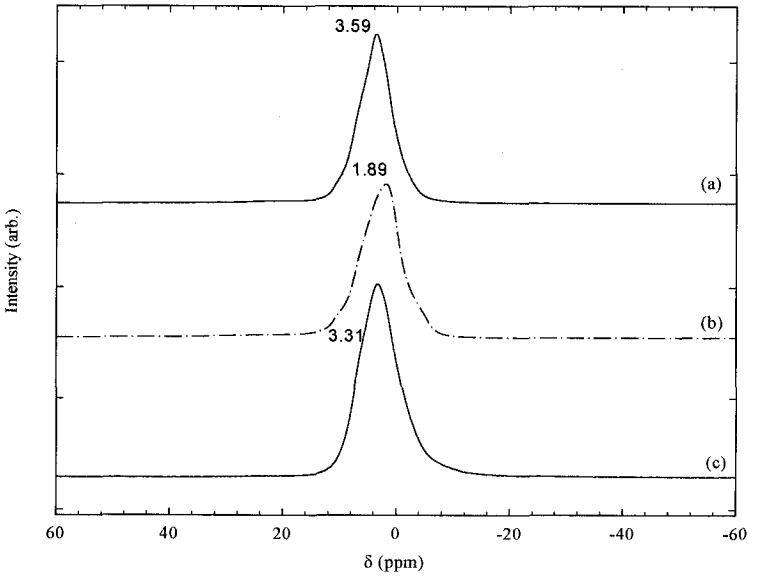


**Fig. 2.13.** $^{27}$Al MAS NMR spectra (130.32 MHz) of (a) kaolinite, (b) Kao–DMSO, and (c) Kao–SIM.

## 2.6 Thermogravimetric analysis

The thermal behavior and stability of the produced intercalated compounds were investigated with simultaneous thermogravimetric and differential thermal analysis (TGA/DTA). The results were compared with the thermal behavior of the starting materials and revealed that the new nanohybrids possessed enhanced thermal stability compared with its individual components.

One of the main features of the DTA thermogram of kaolinite is the major endotherm near 550 °C that is attributed to the loss of water because of the dehydroxylation of the crystal lattice, i.e., formation of meta-kaolinite. This endotherm roughly corresponds to ~13.8 % weight loss in the TGA, which is also related to a maximum in the DTG. Another feature of the DTA of the pristine kaolinite is a characteristic exotherm around 1000 °C, attributed to structural reorganization and formation of the spinel phase. Another minor exotherm could be observed at 1150 °C and up and is attributed to mullite formation. The TGA of the well-ordered kaolinite might also show another <0.2 % weight loss that is usually attributed to a very small amount of adsorbed water, accompanied by a very weak endotherm in the corresponding DTA thermogram (136–138).

In this chapter, these values for the $T_{max}$ in the DTA were observed using a heating rate of 10 °C/min. However, the peak positions are usually shifted to higher temperatures using faster heating rates.

**Table 2.8.** Summary of the TGA/DTA results for the starting materials and some of the produced nanohybrids.

| Sample | Atmosphere | Temperature range (°C) | TGA weight loss (%) | DTA event (°C) Endothermic | DTA event (°C) Exothermic | Total TGA weight loss (%) |
|---|---|---|---|---|---|---|
| **KGa-1b** | air | RT–300 | | 61 | | 13.5 |
| | | 300–600 | 13.5 | 516 | | |
| | | 600–1100 | | | 1000 | |
| **Kao–DMSO** | air | RT–245 | 17.3 | 98, 195 | | 28.7 |
| | | 245–1000 | 11.4 | 513 | 1000 | |
| **Kao–SIM2** | air | RT–256 | 15 | 56, 102, 210 | | 29.5 |
| | | 256–695 | 13.1 | 515 | | |
| | | 695–1100 | 1.4 | | 999 | |
| **Kao–SIM4** | air | RT–280 | 18 | 51, 101, 211 | | 32.8 |
| | | 280–700 | 13.4 | 521 | | |
| | | 700–1100 | 1.4 | | 1000 | |
| **Kao–GIM2** | air | RT–78 | 1 | 55 | | 30 |
| | | 78–306 | 13.5 | 177 | | |
| | | 306–715 | 18.4 | 514 | | |
| | | 715–1100 | 5.6 | | 1001 | |

**Note:** All experiments were carried out at a flow rate of 100 mL $min^{-1}$ and at a heating rate of 10 °C $min^{-1}$; sh: shoulder, br: broad.

The Kao–DMSO intercalate (starting materials) exhibits two weight losses in the TGA, accompanied with two endotherms centered at ~190 °C and 510 °C. The former is attributed to the loss of the organic moiety, and the latter is attributed to the usual dehydroxylation step of kaolinite. From the literature, thermogravimetric analyses of various kaolinite intercalates revealed similar results to that of Kao–DMSO. However, for the majority of kaolinite intercalates, the decomposition of kaolinite represented in the dehydroxylation temperature is usually slightly altered from that of the unmodified kaolinite.

The thermal decomposition of the produced Kao – cyclic imide samples in air atmosphere can be observed in Figs. 2.14 and 2.15. The data obtained are also detailed in Table 2.8. Generally, the decomposition followed a multistep process with a total weight loss for the TGA run up to ~30%. An initial small weight loss, associated with an endotherm in the DTA around 55 °C, can be attributed to the loss of surface-adsorbed water and other volatiles. These endotherms cannot be attributed to the melting of the cyclic imides, as the characteristic melting points are much higher (~125 °C for SIM). The characteristic endothermic DTA peaks, associated with the melting of the organic material, were missing in the DTA of samples (see Figs. 2.14 and 2.15). This confirms the absence of crystalline material in the intercalates and that the organic material is only present in the interlamellar space.

From 100 to ~300 °C, the observed weight loss, attributed to the combustion of organic material (Figs. 2.14 and 2.15) is centered around 210 °C for Kao–SIM and 177 °C for

Kao–GIM, i.e., Kao–SIM is relatively more thermally stable than Kao–GIM. These values are totally different from the Kao–DMSO starting material, and the absence of the characteristic Kao–DMSO endotherms confirmed that DMSO molecules were completely displaced by the cyclic imides, as can be seen from $^{13}C$ NMR results.

The observed single weight loss for the de-intercalation of the imide, for different nanohybrids, indicated that the cyclic imide molecules adopt one single type of arrangement in the interlamellar space.

The dehydroxylation weight loss of kaolinite itself occurred around 515 °C. The dehydroxylation weight loss recorded was ~14%–18%, compared with a weight loss of 13.5% found for the kaolinite starting material (see Table 2.8; theoretical weight loss 14.0%).

Finally, the characteristic exothermic event for the reorganization of the kaolinite structure is observed around 1000 °C (Figs. 2.14 and 2.15) for all samples under air. Surprisingly, these events, which normally should have no associated weight loss, were associated with ~1.5%–5% weight losses. The overlapping of the structural collapse and the dehydroxylation of the kaolinite itself causes the residual interlayer carbonaceous material to be trapped within a metakaolinite matrix, forming a carbon–aluminosilicate nanocomposite material. Some of this carbonaceous material is then released upon the structural reorganization above 1000 °C, resulting in the observed weight losses.

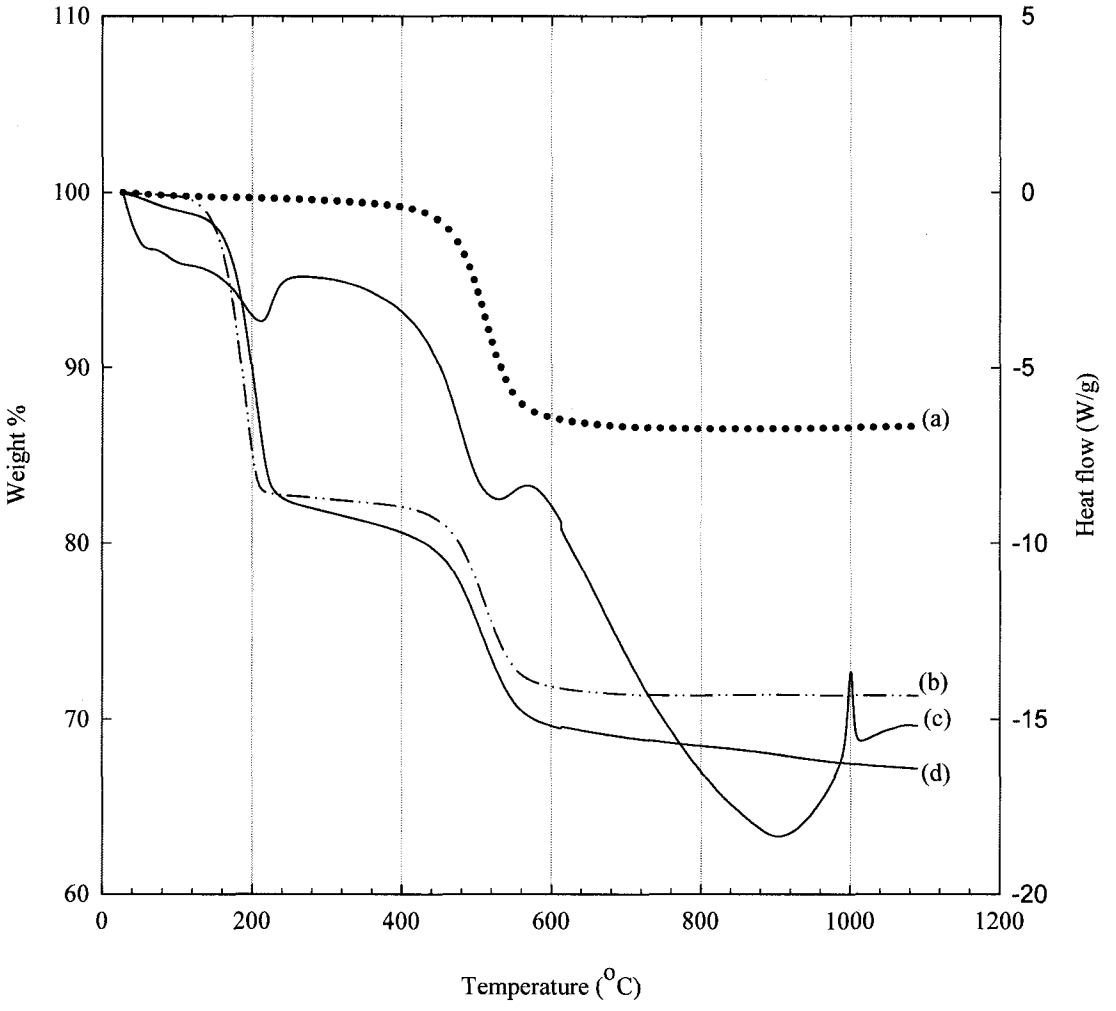


**Fig. 2.14.** TGA curves (RT–1100 °C) of (a) kaolinite, (b) Kao–DMSO, and (d) Kao–SIM4. TGA runs were performed under air. (c) DTA curve (RT–1100 °C) of (d).

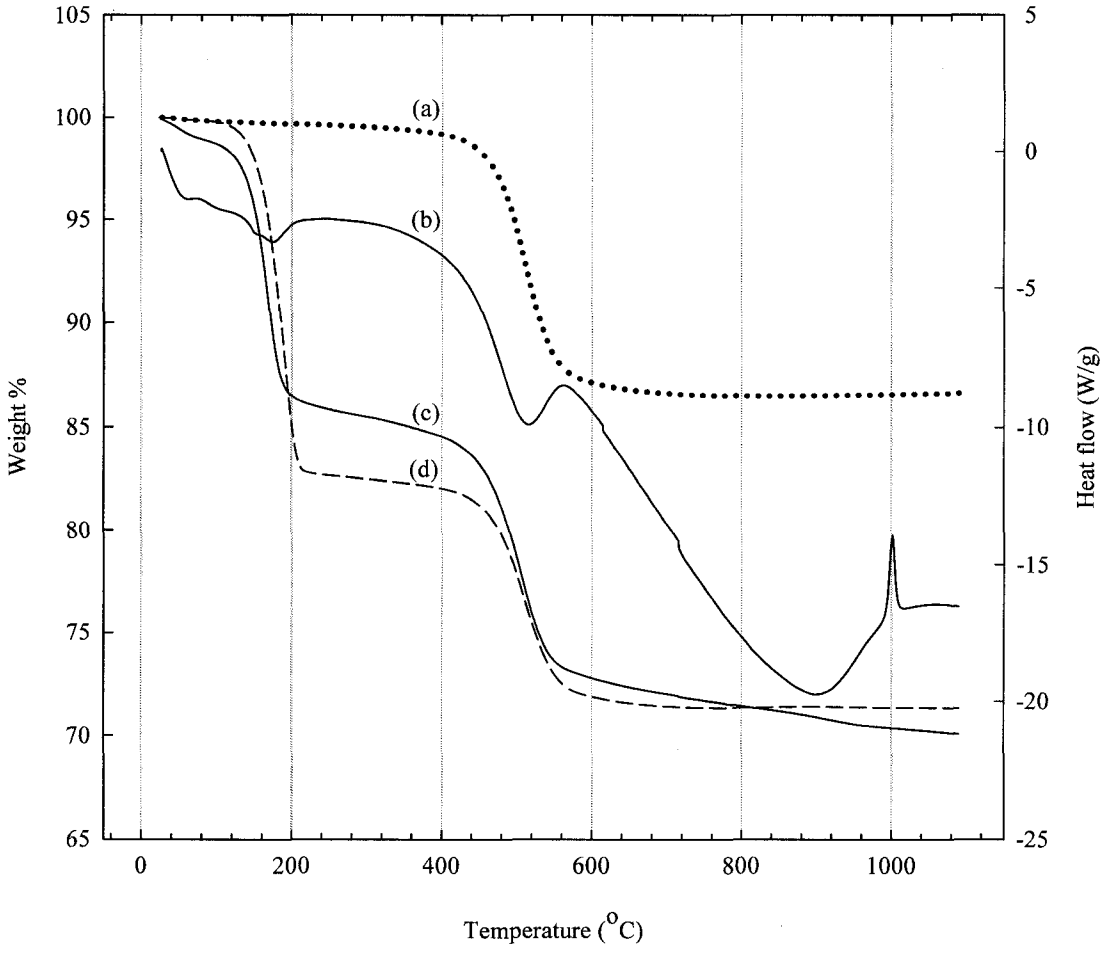


**Fig. 2.15.** TGA curves (RT–1100 °C) of (a) kaolinite, (c) Kao–GIM2, and (d) Kao–DMSO. TGA runs were performed under air. (b) DTA curve (RT–1100 °C) of (c).

# Chapter 3

# Interlamellar grafting of polyols in kaolinite

# Part I: Intercalation and interlamellar grafting of polyols in layered aluminosilicates. D-Sorbitol and adonitol derivatives of kaolinite

## 3.1 Introduction

The intimate mixing of organic and inorganic structural entities at the nanoscale level has received much attention in the last two decades (2, 4, 5, 31), since such nanostructured materials open the way to the controlled design of advanced functional materials. Of particular interest are the nanohybrid materials that are derived from the covalent grafting of organic units on the internal surfaces of extended, layered inorganic structures via the formation of ~(surface–O–C)~ bonds (139–144).

Among the various inorganic layered materials, which have been organically grafted so far, kaolinite is characterized by its quite unique interlayer structural asymmetry. This asymmetry imparts a dipolar character to the interlayer spaces, resulting in a large cohesive energy (44), and consequently, resulting in intercalations more difficult to achieve than in the case of the swelling smectites. In fact, the kaolin group of minerals had been classified as a nonexpandable layered aluminosilicate until 1946, when it was demonstrated that halloysite – organic complexes could be obtained from the hydrated form of halloysite by replacing the interlayer water with alcohols (3). As mentioned before, organic derivatives of kaolinite were

obtained from the expansion of kaolinite layers by polar compounds, e.g., Kuroda and his co-workers have shown that a kaolinite–NMF–methanol intercalation compound is an efficient intermediate for the subsequent intercalation of alkylamines (145). Polymers can be intercalated in kaolinite either from the in situ polymerization of the previously intercalated monomers (20, 22, 146) or directly, by replacement of previously intercalated guests (18, 24). The first grafting of organic moieties on the interlamellar surfaces of kaolinite was reported in 1993 (15). Various alcohols were covalently attached to the aluminate surface, in particular, ethylene glycol (16), methanol (17), and recently ethanolamines (19, 147). The methoxy derivative of kaolinite, Kao–OMe, was described as a non-centrosymmetric array of methyl groups rigidly fixed through Al–O–C bonds and keyed into the $(SiO)_6$ macrorings of the adjacent silicate surface (17). This grafted nanohybrid could also be prepared from the kaolinite–methanol intercalation compound obtained at room temperature (111), under less severe conditions than those previously reported. Recently, propanediols and butanediols were grafted on the internal aluminol surfaces, by reaction with the methoxy-modified kaolinite (21, 23). Phenylphosphonate groups were also successfully grafted on the internal surfaces of kaolinite (11).

The previous work on the grafting processes on the interlamellar aluminol surfaces of kaolinite instigated the preparation and characterization of intercalated kaolinite–polyol nanohybrids as the first step towards the preparation of covalently linked aluminosilicate nanohybrids. The first section of this chapter reports the intercalation and the subsequent interlamellar grafting of two different alditols, namely adonitol, a meso compound, and D-sorbitol (Chart 3.1). The

intercalation was performed by displacing DMSO from the Kao–DMSO intercalate, directly from the melt of the alditol at temperatures just above the melting points of the respective polyol.

The second part of this chapter will deal with the direct one-step interlamellar grafting of different polyols, with higher $T_m$ values, without a preliminary intercalation step.

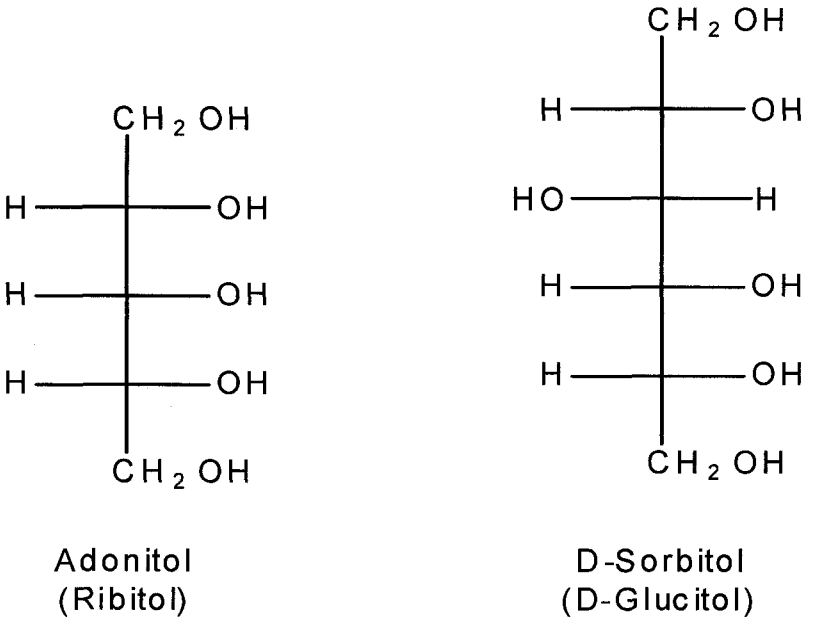


**Chart 3.1.** Structures of adonitol and D-sorbitol.

## 3.2 Preparation and XRD

The preparation of the organo-clays was carried out by first preparing the DMSO intercalate of kaolinite (Kao–DMSO) and then reacting this directly with adonitol or D-sorbitol ($T_m$: 110–120 °C for 5–6 days). The alditols were heated just above their melting points (adonitol: 102–104 °C; D-sorbitol: 98–100 °C) in the presence of dispersed Kao–DMSO intercalate. Typically 0.3-0.5 g of the Kao–DMSO intercalate were mixed with an excess (five- or seven-fold) of the alditol (Aldrich). Table 3.1 summarizes the product names and codes, the reaction conditions, and the results of the preferred-orientation X-ray powder diffraction analysis. The X-ray powder patterns of te products of some of these intercalation processes are presented in Fig. 3.1 for the range of 2–18° 2$\theta$. They indicate that the intercalation complexes are in an ordered interlamellar conformation. However, the $d_{020}$ reflection of the Kao–alditol intercalates was modified (more intense and broad) compared with the powder pattern observed for the parent kaolinite mineral, suggesting that the presence of the organic species introduced intralayer disorder (Fig. 3.2). The $d_{060}$ reflection remains at 1.49 Å, characteristic of a dioctahedral clay mineral (Fig. 3.2). The $d_{001}$ reflection is 10.4 Å for Kao–adonitol and 11.9 Å for Kao–D-sorbitol, compared with a recoreded value in this case of 11.5 Å for the starting material (Kao–DMSO) and 7.3 Å for the pristine kaolinite (Figs. 3.1 and 3.2).

This corresponds to an interlamellar distance of 3.1 and 4.6 Å, respectively (subtracting a clay layer thickness of 7.3 Å from the observed $d_{001}$ values for kaolinite, Fig. 3.1a), which is indicative of a flattened horizontal arrangement of the alditol chains between the kaolinite layers. Similar layer expansion values for halloysite complexes with ethylene glycol and

glycerol have been reported (68). The intercalation of ethylene glycol (15, 16), polyethylene glycol (18), and several alkanediols (21, 23), for example, show comparable values for a flattened monolayer arrangement between the kaolinite layers.

**Table 3.1.** Summary of product names, codes, reaction conditions, and results of the XRD analysis for the intercalation of alditols into kaolinite (KGa-1b).

| Name | Code | RM[a] | SM[b] | RM/SM (g/g) | $T_{rxn}$ (°C) | Reaction time (h) | $d_{001}$ (Å) | RI[c] |
|---|---|---|---|---|---|---|---|---|
| Kao–D-sorbitol | **Ia** | D-Sorbitol | Kao–DMSO | 5 | 125 | 216 | 11.88 | 0.82 |
| Kao–D-Sorbitol [d] | **Ib** | D-Sorbitol | Kao–DMSO | 7 | 125 | 264 | 10.67 (11.88 sh.) | 0.80 |
| Kao–D-Sorbitol [d] | **Ic** | D-Sorbitol | Kao–DMSO | 7 | 125 | 264 | 10.43 (11.87 sh.) | 0.64 |
| Kao–D-Sorbitol [d] | **Id** | D-Sorbitol | Kao–DMSO | 5 | 110 | 144 | 10.55 (8.52)[e] | 0.46[e] |
| Kao–adonitol | **IIa** | Adonitol | Kao–DMSO | 5 | 120 | 156 | 10.36 | 0.85 |
| Kao–adonitol | **IIb** | Adonitol | Kao–DMSO | 5 | 110 | 144 | 10.28 | 0.82 |

[a]RM = reaction media.
[b]SM = starting material
[c]RI = ratio of intercalation (ratio of the intensities of the $d_{001}$ reflection of the product divided by the sum of intensities of the $d_{001}$ reflections of the product and residual kaolinite).
[d]The RI is based on the peak intensity of the most intense $d_{001}$ reflection.
[e]Incomplete intercalation id due to insufficient reaction time.

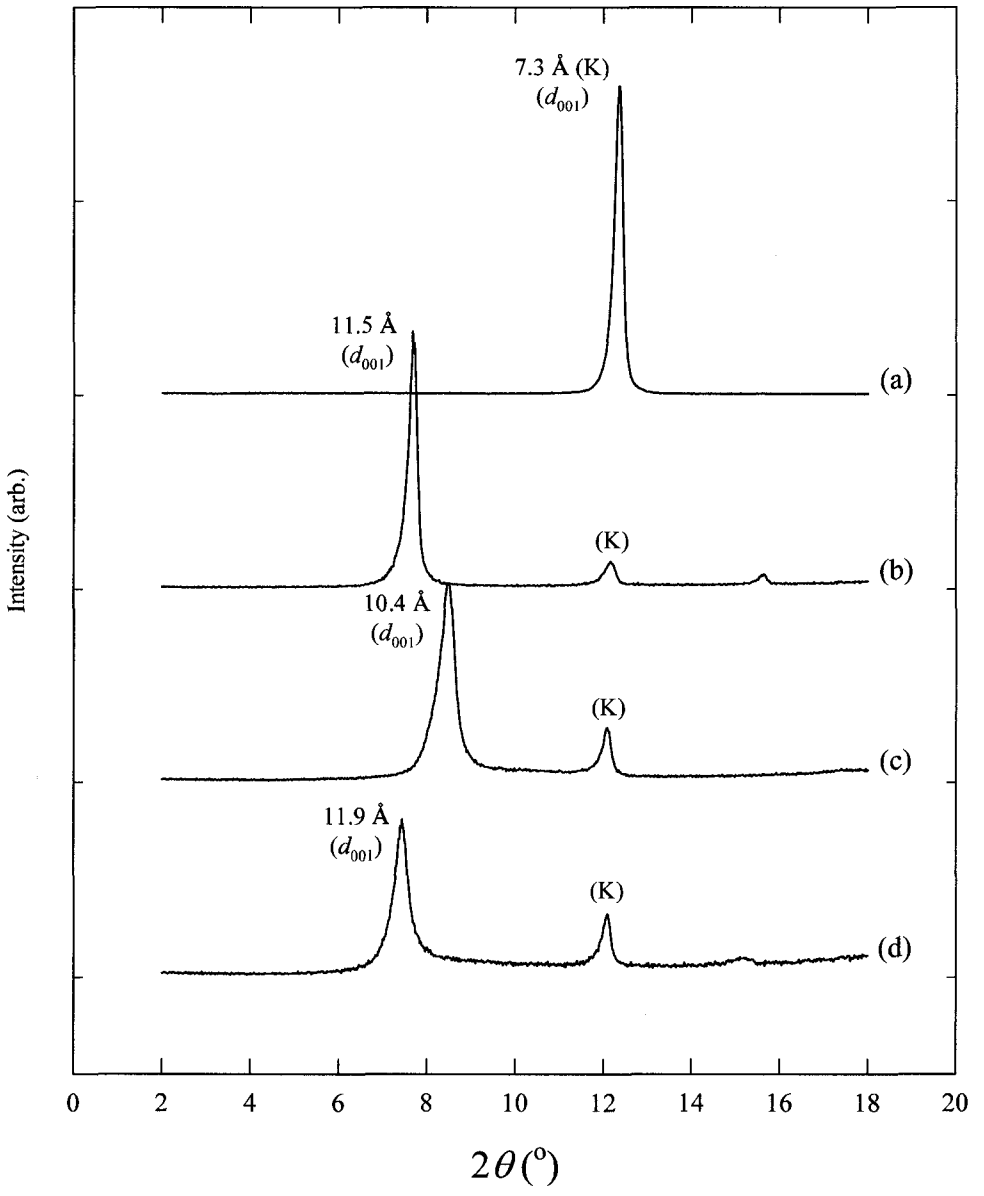


**Fig. 3.1.** Powder XRD partterns ($2\theta$= 2–18°) of (a) KGa-1b (< 2 μm), (b) Kao–DMSO, (c) Kao–adonitol, and (d) Kao–D-Sorbitol.

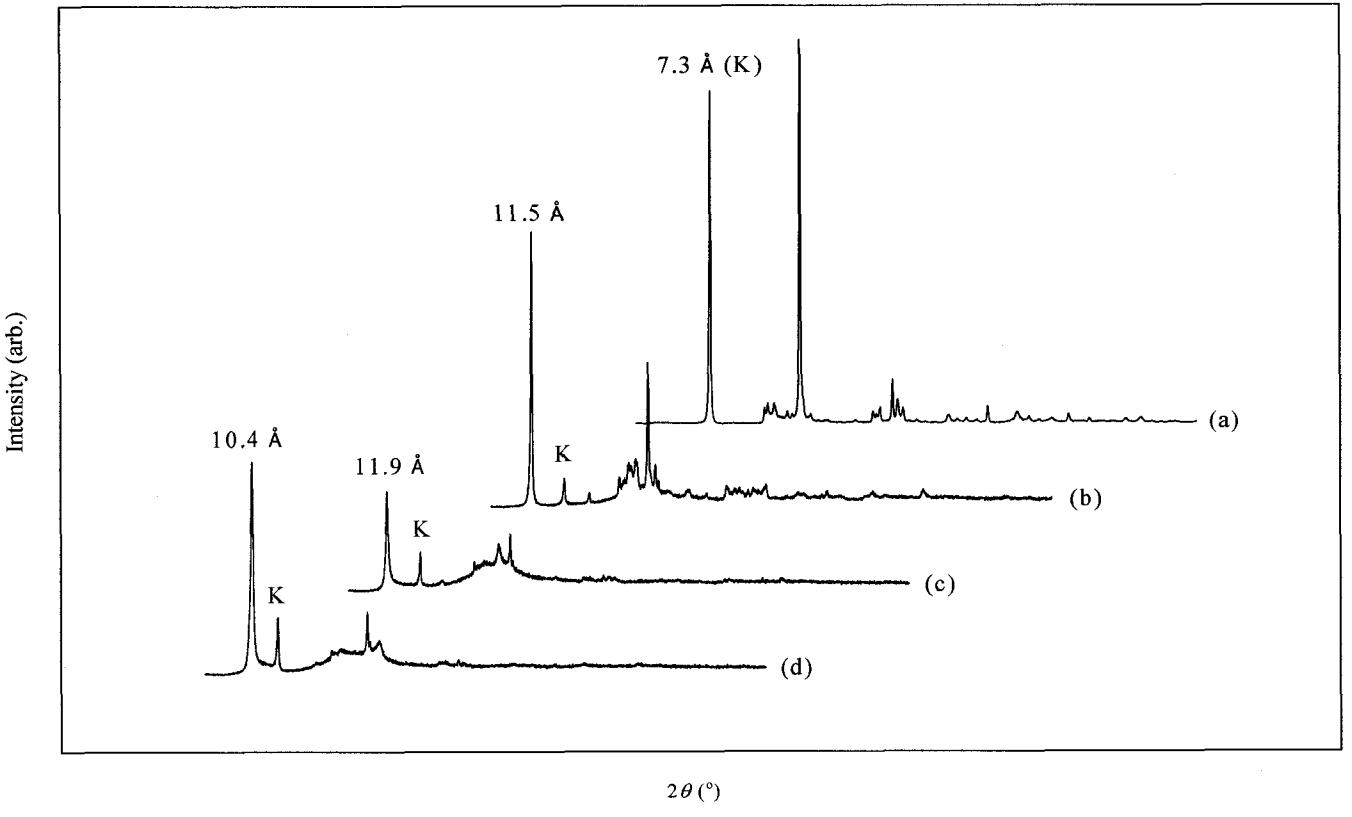


**Fig. 3.2.** Powder XRD partterns (full range) of (a) KGa-1b (< 2 μm), (b) Kao–DMSO, (c) Kao–adonitol, and (d) Kao–D-Sorbitol.

## 3.3 Study of the mechanism of intercalation with time: Kao–adonitol

Approximately 0.3 g of the Kao–DMSO intercalation product and 1.5 g of adonitol were heated in an oil bath at 125 °C with continuous stirring. At selected times, small aliquots of the reaction mixture were removed from the flask and worked up by repeated washings with deionized distilled water to remove excess unreacted (unintercalated) adonitol. The resulting products were air-dried and their XRD patterns were obtained to monitor the progress of the intercalation process.

Figure 3.3 shows the intercalation process for adonitol into the interlamellar space of kaolinite. Clearly, the reaction proceeds via a partial collapse of the Kao–DMSO intercalate before the steps corresponding to the intercalation of adonitol. Initially (0–4 h), the intercalated DMSO molecules are lost, as indicated by a shoulder at 10.2 Å (coming down from 11.5 Å) on the broad 8.4 Å phase. The 6–7 h samples only show one broad phase at 8.4 Å, and after 21 h, two phases at 8.4 Å and 10.4 Å can be observed with the latter being indicative of the beginning of the intercalation of adonitol into kaolinite. After 72 h, the intercalation process is complete, as indicated by the presence of only one phase at 10.4 Å.

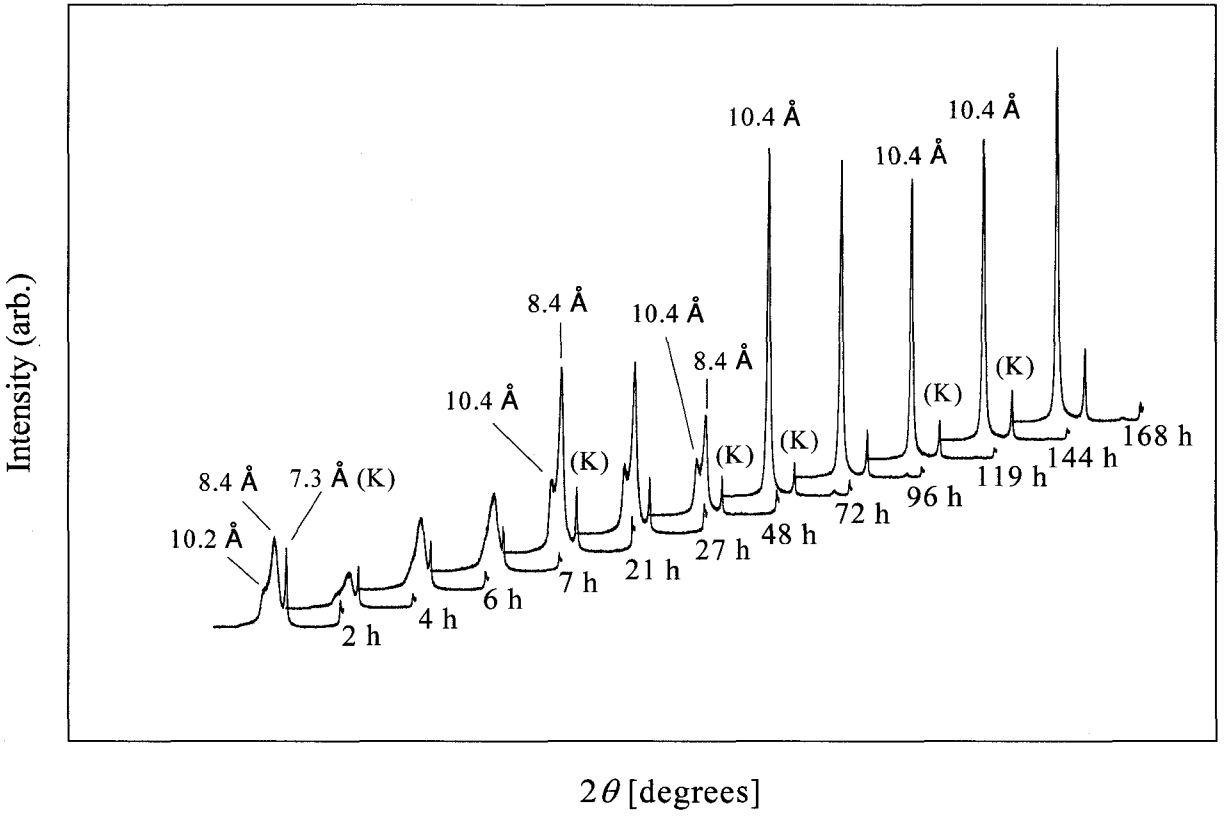


**Fig. 3.3.** XRD powder patterns of the process of intercalation of adonitol into kaolinite, recorded after gradually increasing the intercalation time.

## 3.4 Thermal treatment

Powder XRD patterns of preferentially oriented thin films of Kao–adonitol on quartz discs were obtained after first heating the samples for 4 h at 100 °C, then for another 4 h at 150 °C, and subsequently at each 50 °C interval up to 350 °C (heating rate: 40 °C/min). The samples were allowed to cool to room temperature, and their XRD powder patterns were recorded after each heating interval.

Thermal treatment (Fig. 3.4) causes the grafting of the alditol molecules to the interlayer aluminol surface. This can be observed by a reduction of the interlayer spacing from 10.4 Å to 8.4 Å. This reduction is similar to a reduction from 10.8 Å to 9.4 Å in the case of Kao–EG (16), and to 8.2 Å in the case of the grafting of methoxy groups (17, 111). Above 250 °C, the nanohybrid collapsed to the pure kaolinite (~7.3 Å); this result is in good agreement with the TGA results (see later sections).

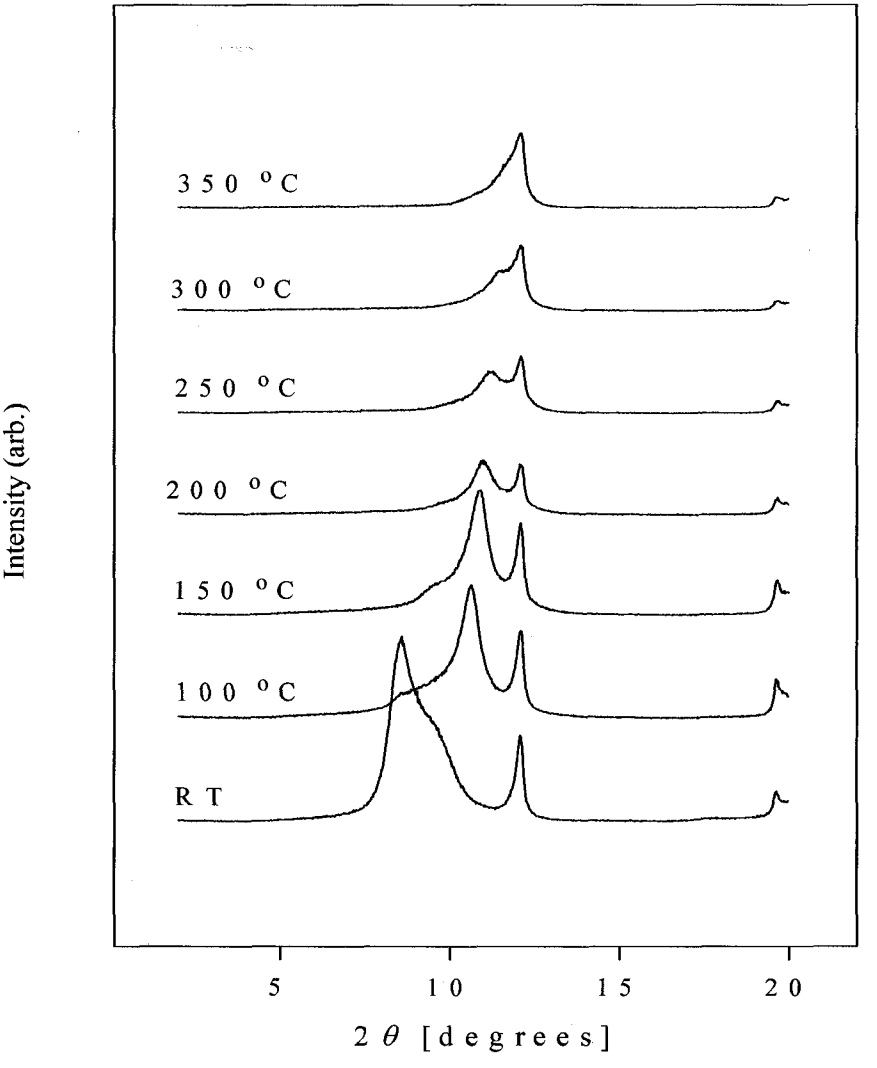


**Fig. 3.4.** XRD patterns of Kao–adonitol after thermal treatment.

## 3.5 Solid-state $^{13}C$ NMR analysis

### 3.5.1 Identification of the intercalated species

Figures 3.5 and 3.6 present the results of the $^{13}C$ cross-polarization/magic-angle spinning (CP/MAS) and the $^{13}C$ dipolar dephased (DD/MAS) NMR experiments, which were obtained to characterize the adonitol and D-sorbitol intercalation complexes of kaolinite, i.e., to identify the nature and structure of the intercalated species and to obtain information on the dynamic state of the intercalated molecules. The detailed spectroscopic data are summarized in Chapter 6 (the Experimental Chapter).

The $^{13}C$ CP/MAS NMR spectrum of pure (crude) adonitol (Aldrich) is presented in Fig. 3.5a. Four resonances were observed at 60.6 ppm, 62.3 ppm, 72.1 ppm, and 72.7 ppm, corresponding to the five carbons that are present in the unit cell of adonitol. Grinding 10 wt% of pure adonitol in kaolinite results in a physical mix of the two compounds, which displays a $^{13}C$ CP/MAS NMR spectrum that is identical to the spectrum of pure adonitol (Fig. 3.5b). Analogously, the $^{13}C$ CP/MAS NMR spectrum of pure D-sorbitol (Fig. 3.5c) was obtained. It displayed 12 resonances in the range of 62.7–75.4 ppm, attributed to the presence of two D-sorbitol molecules, each with six carbons, in the unit cell of the pure alditol. Similarly, grinding pure D-sorbitol (10 wt%) with kaolinite also results in a physical mix, which displays a $^{13}C$ CP/MAS NMR spectrum that is identical to the pure D-sorbitol spectrum. Solid-state $^{13}C$ CP/MAS NMR spectra (125.77 MHz, 12.5 kHz spinning rate) of intercalated Kao–adonitol and Kao–D-sorbitol are presented in Fig. 3.6.

A broad envelope of peaks in the same range of the crude adonitol (see Fig. 3.5) with maxima at ~63.5 ppm and ~72 ppm can be observed for Kao–adonitol (Fig. 3.6a). Kao–D-sorbitol also displays a broad envelope of peaks with maxima at 64.8, 66.7, 72.3, and 76.1 ppm (Fig. 3.6b). These chemical shifts are in good agreement with the chemical shifts of the corresponding alditols, indicating that the structures of the intercalated alditols were not affected upon intercalation.

These two spectra do not show the resonances corresponding to the Kao–DMSO intercalate, expected to appear at 43.1 ppm (methyl group located parallel to the sheet) and 44.2 ppm (methyl group keyed in the ditrigonal hole of the silicate sheet) (see Chapter 2 for the spectrum of Kao–DMSO) (72, 134). Dimethylsulfoxide was completely replaced by the alditols in the intercalation process. This is in contrast with the case of the Kao–PEG complexes, in which DMSO was found to be co-intercalated with the oxyethylene species with only one methyl resonance observed at 41–42 ppm (18).

The solid-state $^{13}C$ CP/MAS NMR spectra of Kao–adonitol and Kao–D-sorbitol (50.31 MHz, 4 kHz spinning speed) are also shown in Fig. 3.7.

### 3.5.2 Dipolar dephasing experiments

As mentioned in the previous chapter, the dipolar dephasing technique can be used to evaluate the dynamic state of the molecular group (126–128). The ratio of the intensities of the dipolar dephased $^{13}C$ resonance and of the $^{13}C$ resonance without dipolar dephasing

($I_{DD}/I_o$) decreases if a molecular group is rigidly bound. The disappearance of all signals for the kaolinite complexes with adonitol and D-sorbitol under DD conditions, with a dephasing time of 40 μs, indicates that the alditol chains are rigidly fixed in the interlamellar space of kaolinite (Fig. 3.7 a.2 and b.2).

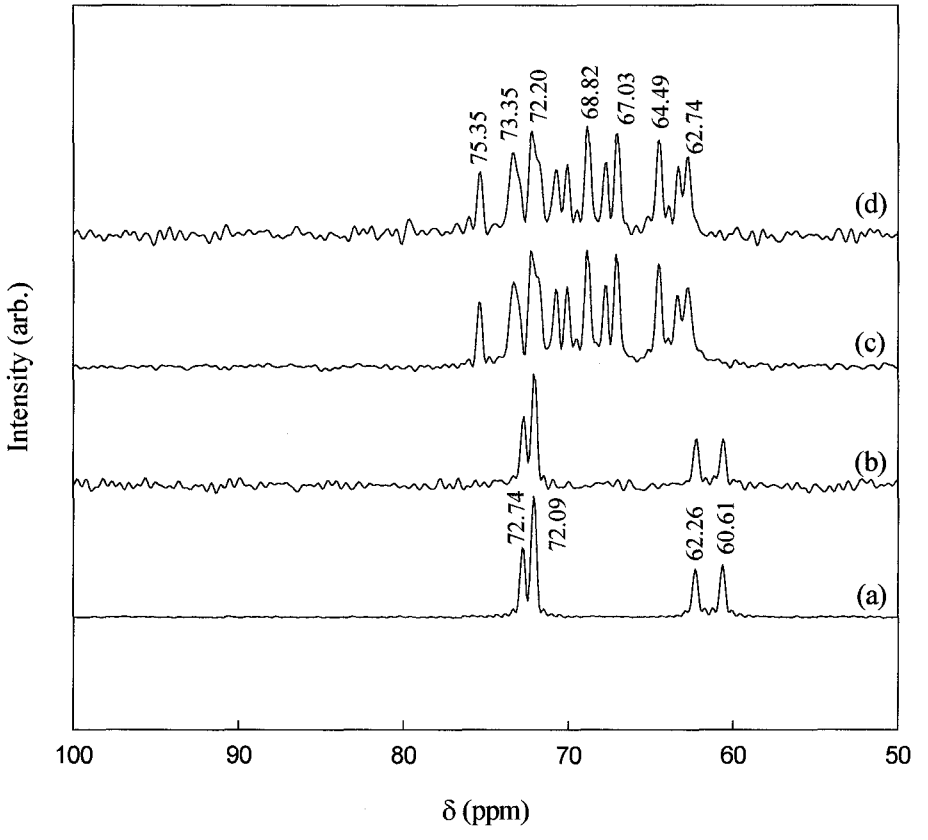


**Fig. 3.5.** Solid-state $^{13}C$ CP/MAS NMR spectra (50.31 MHz, 4 kHz spinning rate) of (a) pure adonitol, (b) 10 wt% adonitol physically mixed with kaolinite, (c) pure D-sorbitol, and (d) 10 wt% D-sorbitol physically mixed with kaolinite.

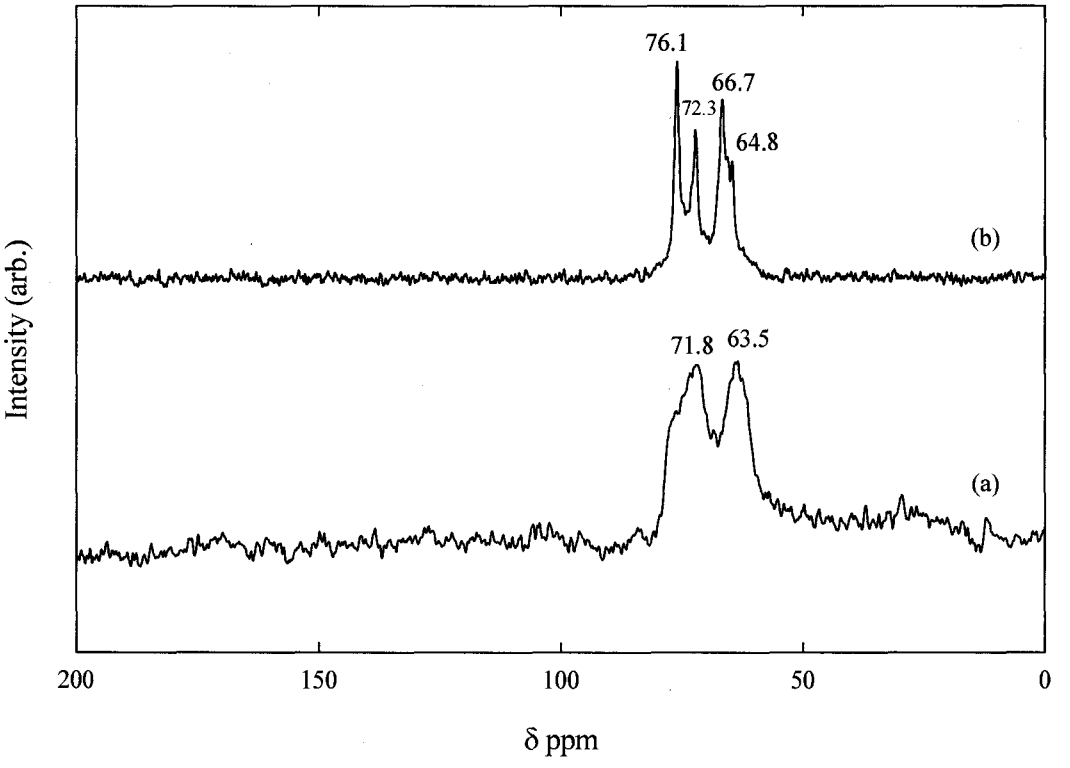


**Fig. 3.6.** Solid-state $^{13}C$ CP/MAS NMR spectra (125.77 MHz, 12.5 kHz spinning rate) of (a) Intercalated Kao–adonitol and (b) Intercalated Kao–D-sorbitol.

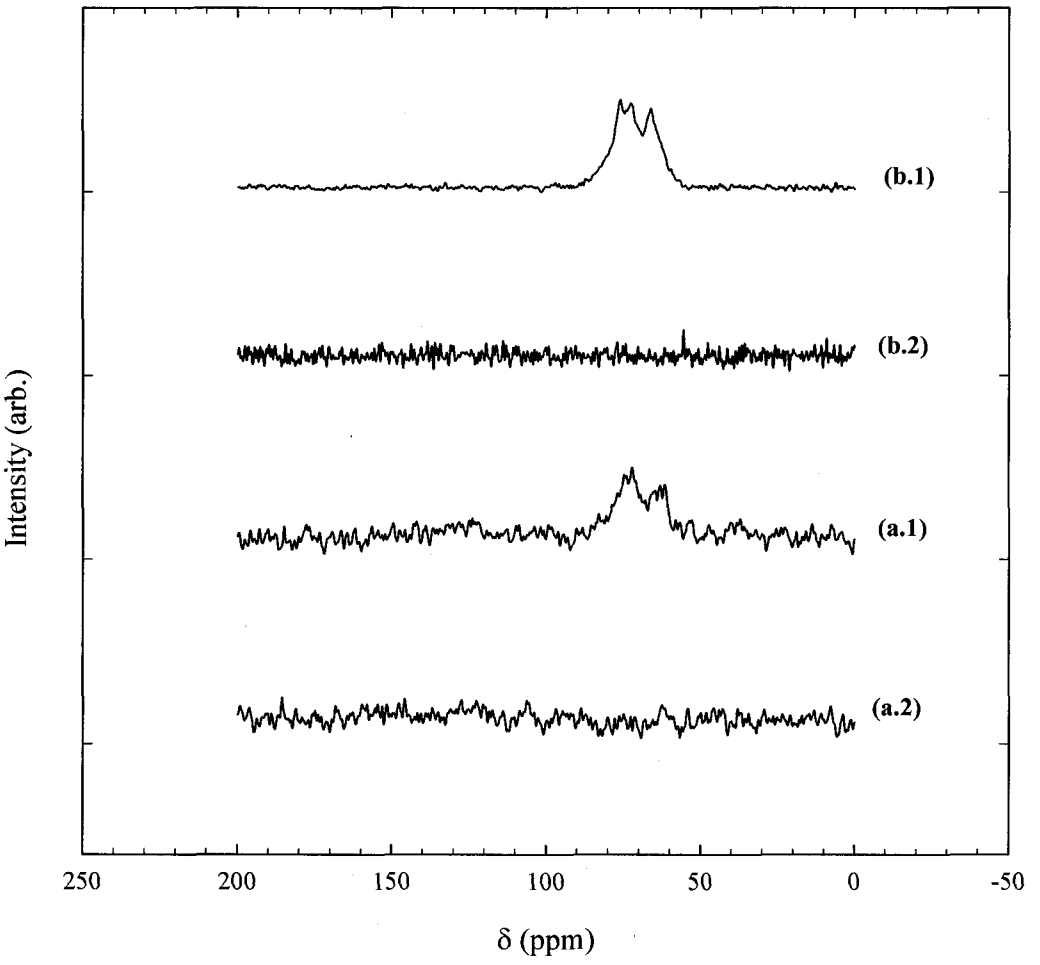


**Fig. 3.7.** Solid-state $^{13}C$ NMR spectra (50.31 MHz) of (a.1) Kao–adonitol, CP/MAS; (a.2) Kao–adonitol, DD/MAS, $\tau$ = 40 μs; (b.1) Kao–D-sorbitol, CP/MAS; (b.2) Kao–D-sorbitol, DD/MAS, $\tau$ = 40 μs.

## 3.6 $^{29}$Si NMR measurements

$^{29}$Si MAS measurements were obtained for the starting materials and the produced intercalated and grafted (thermally treated) nanohybrids on a Bruker AVANCE-500 instrument, operating at 99.35 MHz. The spectra are presented in Fig. 3.8.

The recorded $^{29}$Si NMR results for the pristine kaolinite and for Kao–DMSO intercalate were in agreement with literature values. The degeneracy of the two $^{29}$Si signals of the pristine kaolinite, observed in most intercalates, was also observed for both intercalated compounds (Fig. 3.8), and it is indicative of the loss of H-bonding dissymmetry observed in pristine kaolinite. The spectra for both intercalated Kao–adonitol and Kao–sorbitol showed a strong signal centered at about –91.4 ppm. Upon thermal treatment, the grafted compounds showed two signals at ~ –91.0 and –91.5 ppm. These two signals can be attributed to the presence of two different silicon environments; however, unlike pure kaolinite, the two environments are not equally populated. The change in the spectra of the thermally treated compounds could be a result of the grafting of the alditols to the aluminol surface.

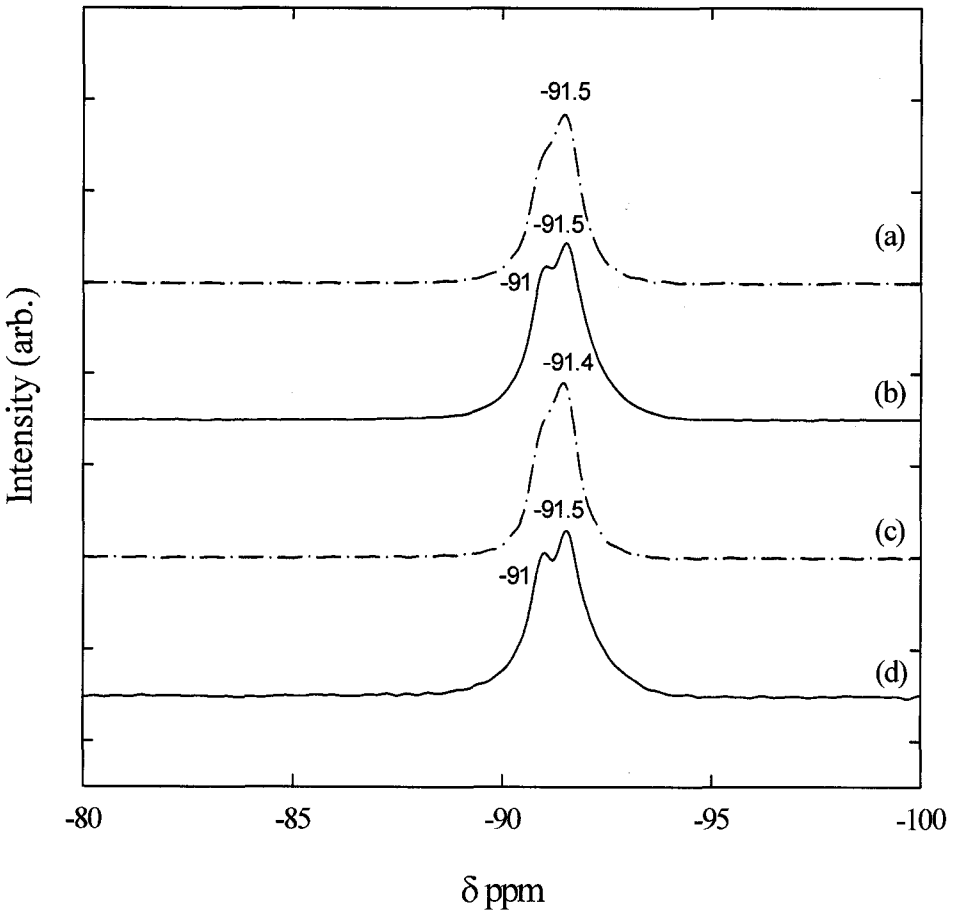


**Fig. 3.8.** $^{29}$Si CP/MAS NMR spectra of (a) intercalated Kao–adonitol, (b) grafted Kao–adonitol, (c) intercalated Kao–D-sorbitol, and (d) grafted Kao–D-sorbitol.

## 3.7 $^{27}$Al NMR spectra

The $^{27}$Al MAS NMR spectra of kaolinite and of several alditol intercalates were obtained at 130.32 MHz at a spinning rate of 14.0 kHz. Generally, a broad signal is observed with a maximum in the range of 4.0 to 4.5 ppm, corresponding to the octahedral Al site (Fig. 3.9). A small shift of the signal maximum is also observed for the grafted nanohybrids, compared with the intercalated analogues.

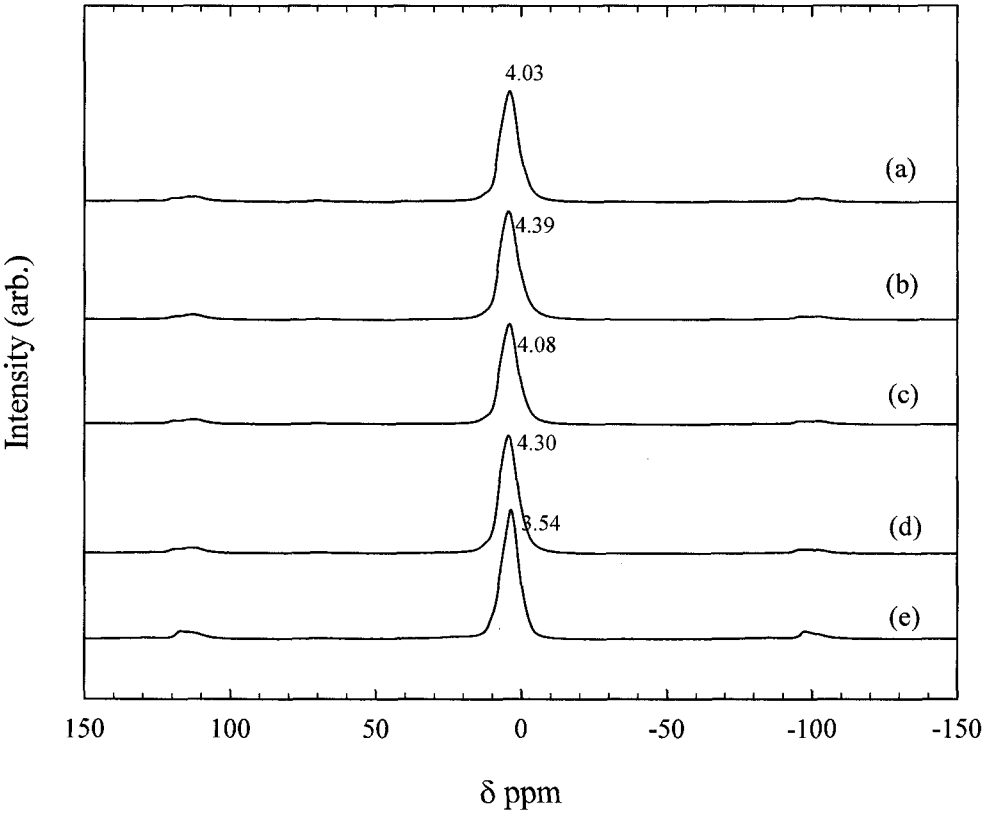


**Fig. 3.9.** $^{27}$Al MAS NMR spectra of (a) kaolinite, (b) grafted Kao–adonitol, (c) intercalated Kao–adonitol, (d) intercalated Kao-D-sorbitol, and (e) grafted Kao-D-sorbitol.

## 3.8 FTIR analysis

### 3.8.1 O–H stretching region (3800–3200 $cm^{-1}$)

Detailed assignments of the observed bands in the FTIR spectra of the produced intercalated and grafted nanohybrids are given in the Experimental Chapter. Figure 3.10 presents the O–H stretching patterns for kaolinite, Kao–DMSO, Kao–adonitol, and Kao–D-sorbitol. The O–H stretching region is very sensitive to interlayer modification (15–17, 26, 70). Consequently, the O–H stretching regions for the kaolinite complexes with adonitol and D-sorbitol shows significant modifications, compared with that of kaolinite and of the Kao–DMSO intercalate. As expected, the band at 3619 $cm^{-1}$, attributed to the stretching frequency of the inner hydroxy groups of kaolinite that are aligned parallel to the direction of the (001) layers and towards the unoccupied octahedral hole (58), was not significantly affected, but the intensity of the 3697 $cm^{-1}$ was considerably reduced and the bands at 3652 and 3667 $cm^{-1}$ disappeared completely. Two new peaks appear at ~3555 and ~3600 $cm^{-1}$.

The pattern observed is similar to the one that was obtained after the intercalation of ethylene glycol (EG) into kaolinite to form the 10.8 Å intercalate, previously described in the literature (16). In all cases, a sharp band appears close to 3600 $cm^{-1}$ with a broader band around 3550 $cm^{-1}$. These bands are superposed on a broad hydrogen bonded OH stretching at lower frequency, attributed to the hydroxyl groups of the alditol.

In the case of the DMSO intercalate (Fig. 3.10b), Johnston et al. (25) attributed the 3540

and 3505 $cm^{-1}$ bands to the stretching frequency of coupled inner-surface (outer) hydroxyl groups that are perpendicular to the (001) plane, hydrogen-bonded to DMSO molecules in the interlamellar space. The bands at 3696 and 3665 $cm^{-1}$ were attributed to the equivalent, non H-bonded, coupled inner-surface hydroxyl groups. In the case of EG (16) as well as of D-sorbitol and adonitol (Fig. 3.10), the coupling of the two inner-surface hydroxyls is lost. As for the DMSO case, the bands at 3696 and 3555 $cm^{-1}$ are present, suggesting that one of the two types of hydroxyls can be either non H-bonded or H-bonded to the intercalated molecules. However, the band at 3662 $cm^{-1}$ is replaced by a sharp band at ~3600 $cm^{-1}$, suggesting that these hydroxyls are H-bonded to the polyols, in a structured way.

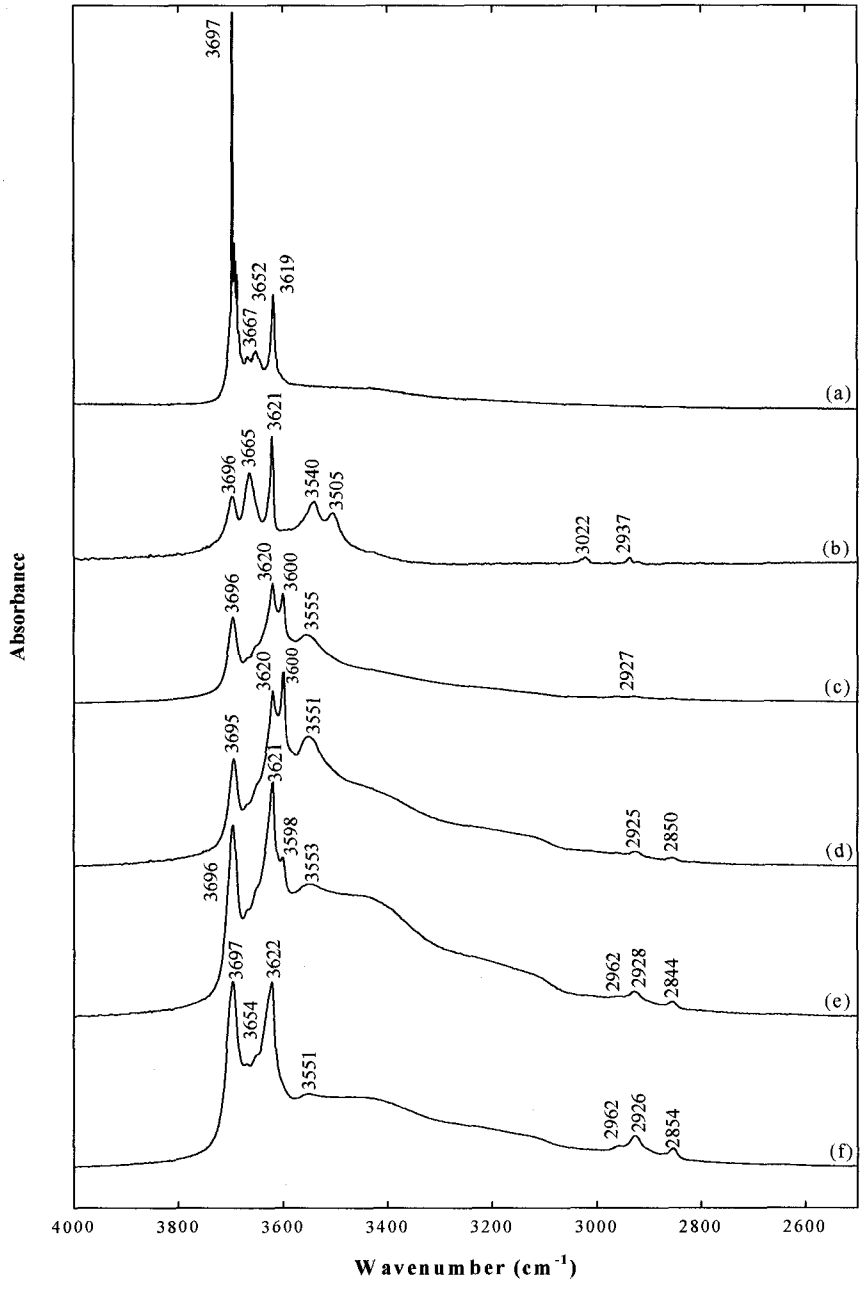


**Fig. 3.10.** FTIR spectra (4000–2500 $cm^{-1}$) of (a) kaolinite, (b) Kao–DMSO, (c) Kao–D-sorbitol, (d) Kao–adonitol, (e) Kao–D-sorbitol after heating for 1 h at 200 °C, and (f) Kao–adonitol after heating for 1 h at 200 °C.

### 3.8.2 Effect of thermal treatment on the O–H stretching bands: evidence for grafting

Similar to what was observed in the case of EG, where heating the 10.8 Å intercalate at 200 °C for 1 h resulted in the formation of a 9.4 Å phase, attributed to the grafting of EG on the aluminol inner surface, in the cases of D-sorbitol and of adonitol, heating the intercalated material at 200 °C for 1 h resulted in a material characterized by a smaller $d_{001}$ (see previous sections) and by an IR spectrum shown in Fig. 3.10e and 3.10f. The major modification in the IR spectra resulting from the heating is the strong reduction in intensity of the band at ~3600 $cm^{-1}$, a result similar to what was observed in the case of Kao–EG (16). Also, the 3555 $cm^{-1}$ band is reduced in intensity, and a very small band reappears in the 3640–3670 $cm^{-1}$ region. All these results (together with the previous XRD results of the thermally treated sample) are in excellent agreement with the grafting of the alditols on the inner aluminol surface of kaolinite. Apparently, the aluminol hydroxy groups involved in the grafting reaction are those, which were strongly involved in the H-bonding with the alditols.

### 3.8.3 C–H stretching region (2800–3100 $cm^{-1}$)

The bands in this region are diagnostic of the incorporation of organic moieties (18). Bands, associated with the methylene groups of the alditols, are observed upon intercalation into the interlayers of kaolinite. In case of Kao–D-sorbitol, asymmetric and symmetric C–H stretching bands are observed at ~2927 and 2850 $cm^{-1}$ (Fig. 3.10c). Similarly, Kao–adonitol exhibited bands at ~2925 and 2850 $cm^{-1}$ (Fig. 3.10d).

The absence of residual interlayer DMSO in these intercalates is confirmed, as the bands at approximately 3022 and 2937 $cm^{-1}$, attributed to the symmetric and asymmetric stretching of the methylene groups of the DMSO molecules, respectively, completely disappeared in all cases (see Fig. 3.10).

Full assignments of the observed OH and CH stretching bands of three different novel nanohybrids are reported in Experimental Chapter (Chapter 6).

### 3.8.4 HOH bending region (1680–1600 $cm^{-1}$)

The characteristic deformation band of water is observed at 1630 $cm^{-1}$, indicating that water is exclusively present as an adsorbate on the external surfaces of the materials. The deformation band of intercalated water molecules would be expected around 1650 $cm^{-1}$ (16, 18, 124).

### 3.8.5 C–H deformation bands (1500-1200 $cm^{-1}$)

Bands, attributed to CH deformations, can be observed in the FTIR spectra of these nanohybrids. Normally, Kao–DMSO shows deformation bands at 1428, 1410, 1394, and 1319 $cm^{-1}$ (see previous chapter). New patterns were observed for Kao–adonitol and Kao–D-sorbitol (see Experimental Section, Chapter 6). Interestingly, contrary to the observations made in the case of the 9.4 Å intercalate of EG in kaolinite, there is no band at 1325 $cm^{-1}$; the main band in that region is a sharp band at 1383 $cm^{-1}$. This is an indication of a gauche conformation for the alditol chain, as expected on the basis of the $d_{001}$ value. In

the case of Kao–EG (9.4 Å) intercalate, a trans conformation was observed, suggesting that one end of EG was grafted to the aluminol sheet, while the other hydroxyl group was keyed into the siloxane macro-ring of the silicate side by H-bonding (15, 16).

### 3.8.6 O–H Bending region and the kaolinite-lattice vibrations

Major changes are also observed in the hydroxyl bending regions of the IR spectra. The kaolinite band at 938 $cm^{-1}$ has been assigned to the in-plane bending vibrations of surface hydroxyl groups (124). Upon intercalation of D-sorbitol and adonitol, this band is greatly reduced in intensity, while a new band appears at 969 $cm^{-1}$ (a similar change is observed in the case of Kao–DMSO, with a band appearing at 958 $cm^{-1}$) (Fig. 3.11). This band disappears almost completely after heating at 200 °C for 1 h, which is in agreement with the grafting assumption of the alditols.

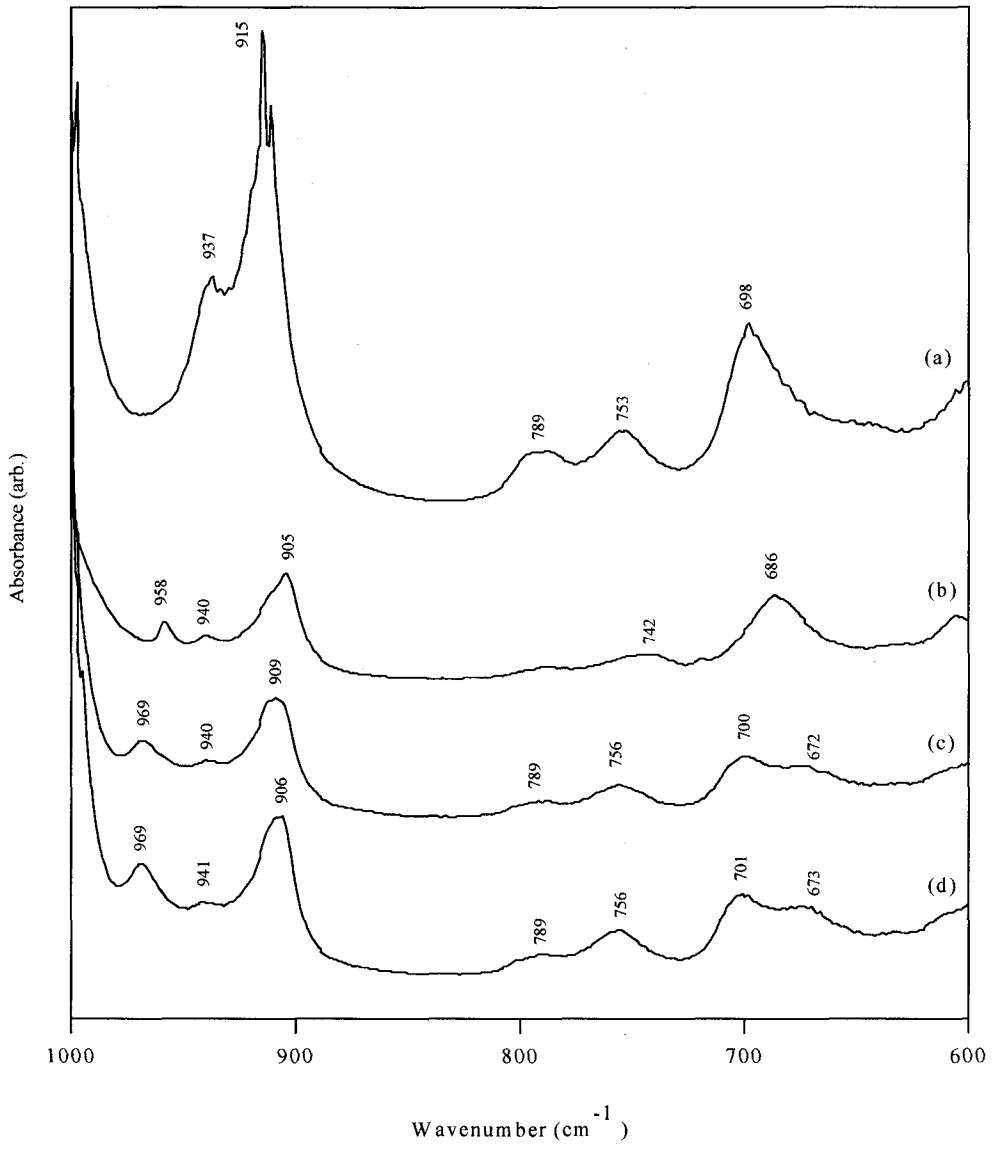


**Fig. 3.11.** FTIR spectra (1000–600 $cm^{-1}$) of (a) kaolinite, (b) Kao–DMSO, (c) Kao–D-sorbitol, and (d) Kao–adonitol.

## 3.9 Thermogravimetric analysis

The thermal behavior and stability of the produced intercalated compounds were investigated with simultaneous thermogravimetric and differential thermal analysis (TGA/DTA). The results were compared with the thermal behavior of the starting materials and revealed that the new compounds possessed enhanced thermal stability compared with the starting material.

Figure 3.12 presents the results obtained from the thermal analysis for the kaolinite starting material, the Kao-DMSO complex, Kao–adonitol, and Kao–D-sorbitol, recorded under $N_2$ atmosphere. The DTA thermogram of kaolinite shows an endotherm at 528 °C, attributed to the dehydroxylation of the crystal lattice, and an exotherm at ~1000 °C, attributed to a structural organization, i.e., the spinel-phase crystallization. The total weight loss during the thermogravimetric analysis corresponds to ~13.8% and coincides with the expected weight loss for the dehydroxylation of the kaolinite layers. As can be seen in Fig. 3.12a, there is virtually no weight loss for the desorption of water (ambient to 110 °C); this is in agreement with previously reported results for well-ordered kaolinite specimen (136–138).

The Kao–DMSO intercalate exhibits two weight-loss steps, totaling ~27.7% (Fig. 3.12d). The first step corresponds to the loss of DMSO at ~217 °C (16.5%), and the second step is a result of the dehydroxylation of the kaolinite lattice observed at 539 °C (11.2%). The spinel-phase crystallization occurred at 1009 °C, as indicated by an exothermic peak in the DTA thermogram (see Chapter 2).

Both Kao–adonitol and Kao–D-sorbitol undergo two main weight-loss (decomposition)

stages between ~100 °C and 600 °C (total observed weight loss is ~20%), showing thermal behavior comparable to the previously reported grafted derivatives of kaolinite, e.g., EG, propanediols, and butanediols (16, 21, 23). The first weight-loss stage of ~5%–6% occurs in the range of 100–450 °C ($T_{ons}$ is broadly defined in both cases around 200 °C).

The second decomposition step, with a weight loss of ~12.0% in both nanohybrids, occurs from 400–650 °C. The DTA run shows well-defined endothermic minimum for this range at ~502 °C and ~488 °C for Kao–adonitol and Kao–D-sorbitol, respectively. This stage is attributed to the dehydroxylation of the kaolinite layers.

Generally, for all kaolinite intercalates, the decomposition of kaolinite represented in the dehydroxylation temperature is altered from that of the unmodified kaolinite. Moreover, for the grafted nanohybrids, the dehydroxylation temperatures were greatly reduced even compared with other intercalates (16, 17, 21, 23). The dehydroxylation temperatures for thermally treated Kao–alditol nanohybrids are in agreement with partial grafting of the alditols on the aluminol surfaces.

Finally, a gradual 2.7% (Kao–adonitol) and 1.8% (Kao–D-sorbitol) weight loss is observed from ~650–1100 °C. This is generally attributed to the carbonaceous residue of the decomposed alditols, trapped in the interlamellar spaces of kaolinite. The exothermic peak (DTA) accompanying the spinel-phase crystallization is observed around 1005 °C in both cases.

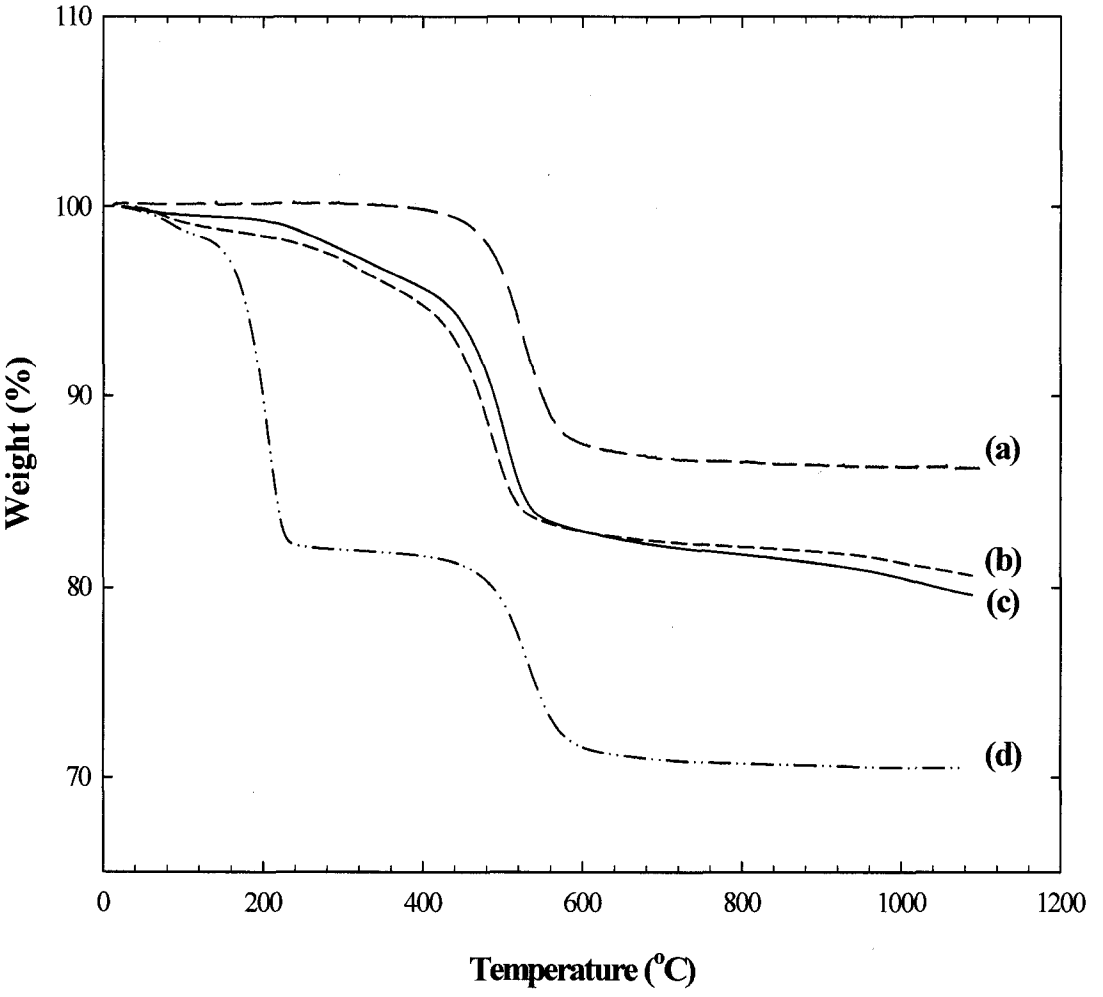


**Fig. 3.12.** TGA curves ($N_2$, 100 mL $min^{-1}$, 10 °C $min^{-1}$; RT–1100 °C) of (a) kaolinite, (b) Kao–D-sorbitol, (c) Kao–adonitol, and (d) Kao–DMSO.

# Part II: Direct interlamellar grafting of high melting-point polyols in kaolinite

## 3.10 Introduction

This part reports the modification of the interlamellar surface of kaolinite by the grafting of two different alditols, namely, D-mannitol and dulcitol (Chart 3.2), directly from the melt rather than thermal treatment of the intercalated alditols, as reported previously in Part I of this chapter. Several starting materials were used; however, Kao–DMSO intercalate was the most effective. The results of the XRD, FTIR, and TGA analyses confirmed the grafting of the polyol molecules on the aluminol surface of kaolinite. $^{13}C$ CP and DD/MAS spectra indicated the complete displacement of the guest molecules of the starting materials by the polyols and the rigidity of the latter in the interlamellar space. $^{29}Si$ and $^{27}Al$ NMR spectra of the starting materials and the products are also discussed. Analyses results show the possibility of the presence of an oligomeric form of the alditols grafted on the aluminol surface of kaolinite at more than one point in a bridging manner.

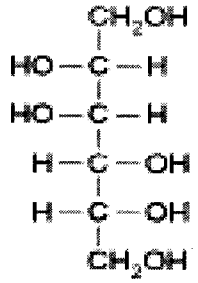

D-Mannitol

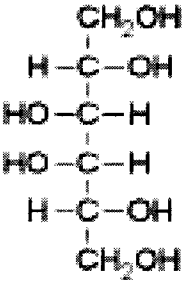

Dulcitol

**Chart 3.2.** Structures of D-mannitol and dulcitol.

## 3.11 Preparation and X-ray diffraction

The preparation of the nanohybrid materials was carried out following the method previously described in the cases of D-sorbitol and adonitol from the DMSO intercalate of kaolinite ((7); see Part I of this Chapter). Typically, 0.7 g of the starting material, e.g., Kao–DMSO intercalate was mixed with an excess (five- to seven-fold) of the polyols. Because of the higher melting points of D-mannitol and dulcitol, the reactions took place in an autoclave (Parr® bomb) at temperatures in the range of 190–250 °C under autogeneous pressures. Table 3.2 summarizes the product names and codes, the reaction conditions, and the $d_{001}$ values of the resulting materials. In the case of Kao–DMSO as a starting material, and when the reaction with D-mannitol is done in the presence of a solvent, deionized water or DMSO, even under a maximum autogeneous pressure of 120 psi, kaolinite was fully recovered, and only the characteristic $d_{001}$ reflection can be observed at 7.2 Å. In contrast, when the reaction is done in the melt, at temperatures ranging from155 °C to 215 °C, a reflection at 11.0 Å–11.5 Å is observed, indicative of the intercalation into the interlamellar spaces of kaolinite (68). The ratio of intercalation depends upon the reaction conditions, varying from 50% to 86%. The maximum ratio of intercalation was obtained for a reaction time of 48 h, at 205 °C, corresponding to a maximum autogenous pressure of 70 psi. The situation is similar with dulcitol, but no systematic studies were done to optimize the ratio of intercalation. Two other intercalates were used as starting materials, Kao – *N*-methylformamide (Kao–NMF) and Kao–potassium acetate (Kao–KOAc). The production of materials with $d_{001}$ in the range of 11.0 Å–11.6 Å was observed for both the NMF and potassium acetate (KOAc) intercalates, but

with relatively low ratios of intercalation, plausibly because of the decomposition of the starting materials at relatively low temperatures, compared with the temperature at which Kao–DMSO intercalate decomposes. When kaolinite itself was used as a starting material, it was recuperated unreacted.

Typical X-ray powder patterns of the starting materials (kaolinite and Kao–DMSO) and of the materials resulting from the reaction with the melts of D-mannitol and dulcitol are shown in Fig. 3.13, for the range of 2–16° $2\theta$. The remaining patterns are similar to those previously reported in the case of other alditols, and full patterns are shown in Fig. 3.14. It is worth noting that the $d_{060}$ reflection remains at 1.49 Å, characteristic of a dioctahedral clay mineral. The layered structure of kaolinite remains largely unaffected, the only major variation being the value of the *c*-spacing. The $d_{001}$ reflection is in the range of 11.0 Å to 11.5 Å, which corresponds to an expansion in the interlamellar distances by ~3.8 Å to ~4.3 Å (subtracting a kaolinite layer thickness of 7.2 Å from the observed $d_{001}$). Since the $^{13}C$ NMR results show the complete disappearance of the organic or salt intercalates (DMSO, NMF, or KOAc) after the reaction (see later sections), the expansion is attributed only to the intercalation of the alditol. Similar to Part I, the interlamellar distances are indicative of a flattened horizontal arrangement of the polyol, in a manner similar to what was obtained in the case of D-sorbitol (7). These values are also typical of other intercalations, such as ethylene glycol (16), polyethylene glycols (18), propanediols (21), or butanediols (23).

**Table 3.2.** Summary of product names, codes, reaction conditions, and results of the XRD analysis for the reaction of D-mannitol and dulcitol with different kaolinite intercalates.

| Code | SM[b] | RM[a] | Maximum Autogenous Pressure (psi) | Average $T_{rxn}$ (°C) | $t_{rxn}$ (h) | XRD results | | |
|---|---|---|---|---|---|---|---|---|
| | | | | | | $d_{001}$ (Å) | $d_{001}$(K) (Å) | RI[c] |
| **M1** | Kao–DMSO | D-Mannitol dissolved in DIW | – | 75 | 179 | – | 7.1 | – |
| *M2 | Kao–DMSO | D-Mannitol dissolved in DIW | 120 | 195 | 48 | – | 7.2 | – |
| **M3** | Kao–DMSO | D-Mannitol dispersed in DMSO | – | 60 | 156 | – | 7.1 | – |
| **M4** | Kao–DMSO | D-Mannitol in the melt under air | – | 195 | 146 | 11.5 | 7.1 | 70.0 |
| **M5** | Kao–DMSO | D-Mannitol in the melt under $N_2$ | – | 195 | 139 | 11.5 | 7.2 | 81.8 |
| *M6 | Kao–DMSO | D-Mannitol in the melt | 70 | 205 | 48 | 11.3 | 7.2 | 86.4 |
| *M7 | Kao–DMSO | D-Mannitol in the melt | 75 | 215 | 31 | 11.1 | 7.1 | 85.5 |
| *M8 | Kao–DMSO | D-Mannitol in the melt | 25 | 195 | 24 | 11.0 | 6.9 | 50.7 |
| *M9 | Kao–DMSO | D-Mannitol in the melt | 30 | 155 | 51 | 11.1 | 6.9 | 49.0 |
| *M10 | Kao–NMF | D-Mannitol in the melt | 90 | 230 | 54 | 11.3 | 7.2 | 4.7 |
| *M11 | Kao–NMF | D-Mannitol in the melt | 35 | 215 | 73 | 11.3 | 7.2 | 16.3 |
| *M12 | Kao–KOAc | D-Mannitol in the melt | 20 | 190 | 48 | 11.6 | 7.2 | 43.3 |
| *M13 | Kao–KOAc | D-Mannitol in the melt | 120 | 225 | 71 | 10.8 | 7.1 | 51.9 |
| *M14 | KGa-1b | D-Mannitol in the melt | 40 | 190 | 45 | – | 7.1 | – |
| *D1 | Kao–DMSO | Dulcitol in the melt | 45 | 235 | 22 | 11.4 | 7.1 | 71.5 |

[a]SM = starting mterial.
[b]RM = reaction medium.
[c]RI = ratio of intercalation (ratio of the intensities of the $d_{001}$ reflection of the product divided by the sum of intensities of the $d_{001}$ reflections of the product and residual kaolinite).
*Reactions performed in autoclave (Parr® Bomb).

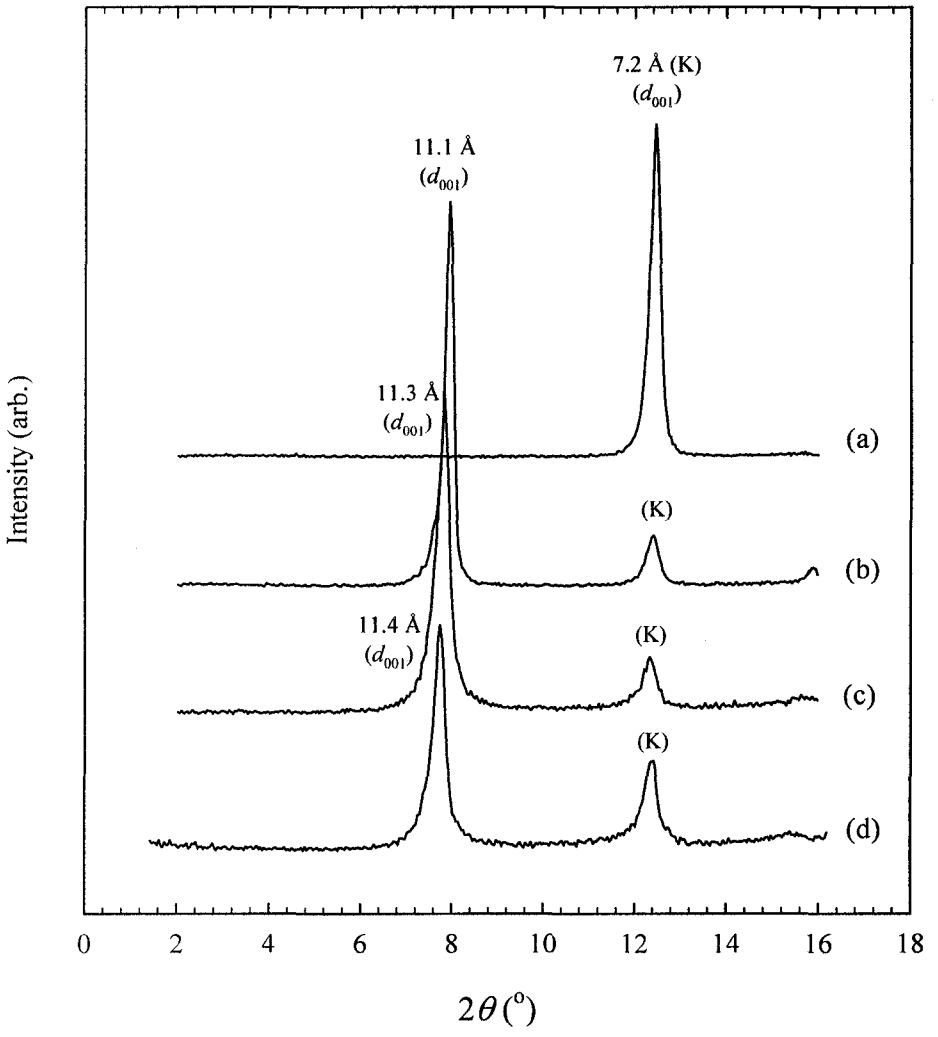


**Fig. 3.13.** XRD powder patterns (2–16°) of (a) kaolinite, (b) Kao–DMSO, (c) Kao–D-mannitol, and (d) Kao–dulcitol.

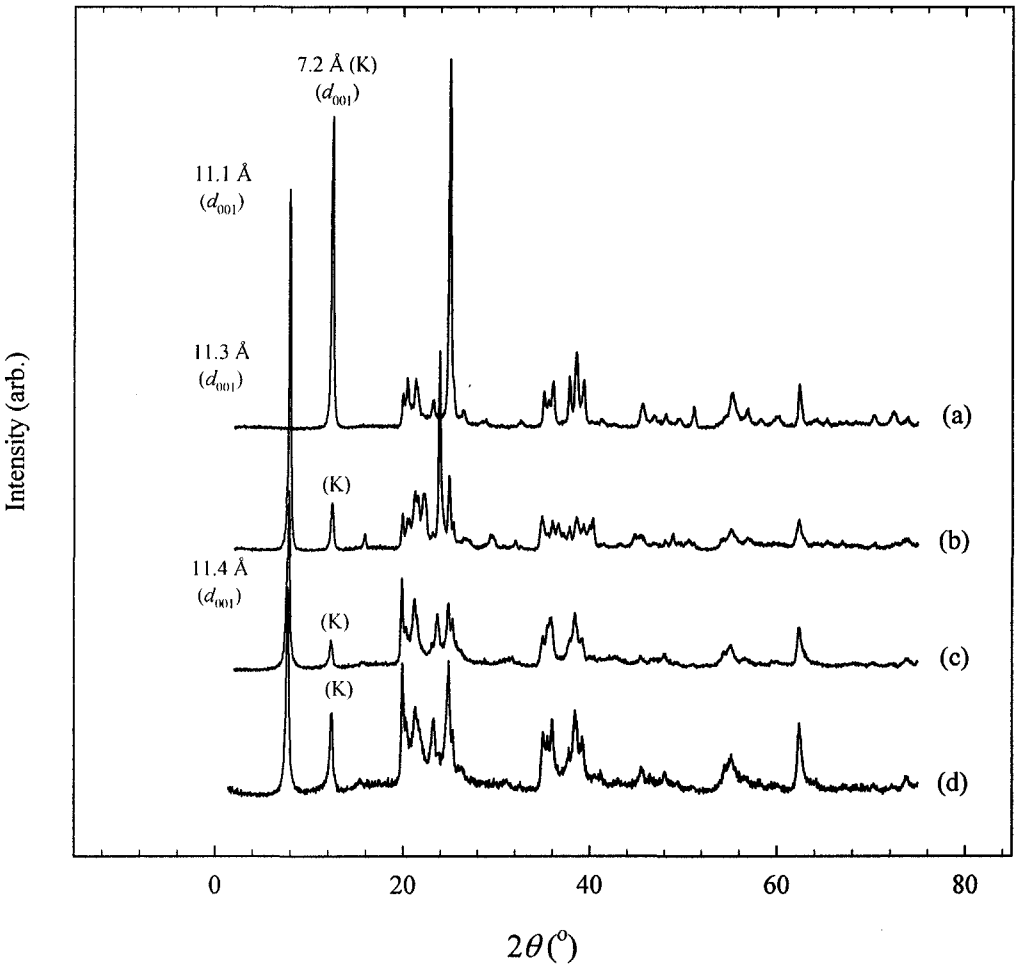


**Fig. 3.14.** XRD powder patterns (2–75°) of (a) kaolinite, (b) Kao–DMSO, (c) Kao–D-mannitol, and (d) Kao–dulcitol.

## 3.12 Resistance to hydrolysis

The produced Kao–D-mannitol nanohybrid exhibited remarkable resistance to de-intercalation attempts, including washing the product of experiment **M7** (see Table 3.2) with de-ionized water for 4 days. Washing at room temperature did not change neither the $d_{001}$ reflection (~11.1 Å) of the product nor the ratio of intercalation (~86.0%) (see Fig. 3.15), while refluxing in deionized water for 40 h resulted only in a slight decomposition of the nanohybrid ($d_{001}$ = ~10.8 Å, and the ratio of intercalation = ~80.0%), probably because of partial hydrolysis. Compared with the results of similar experiments on other kaolinite intercalates (see Chapter 2), this indicates a stable intercalate of kaolinite in which the alditol molecules are grafted on the aluminol interlamellar surface of kaolinite. Intercalated molecules can easily be de-intercalated upon washing with the appropriate solvent (16, 147).

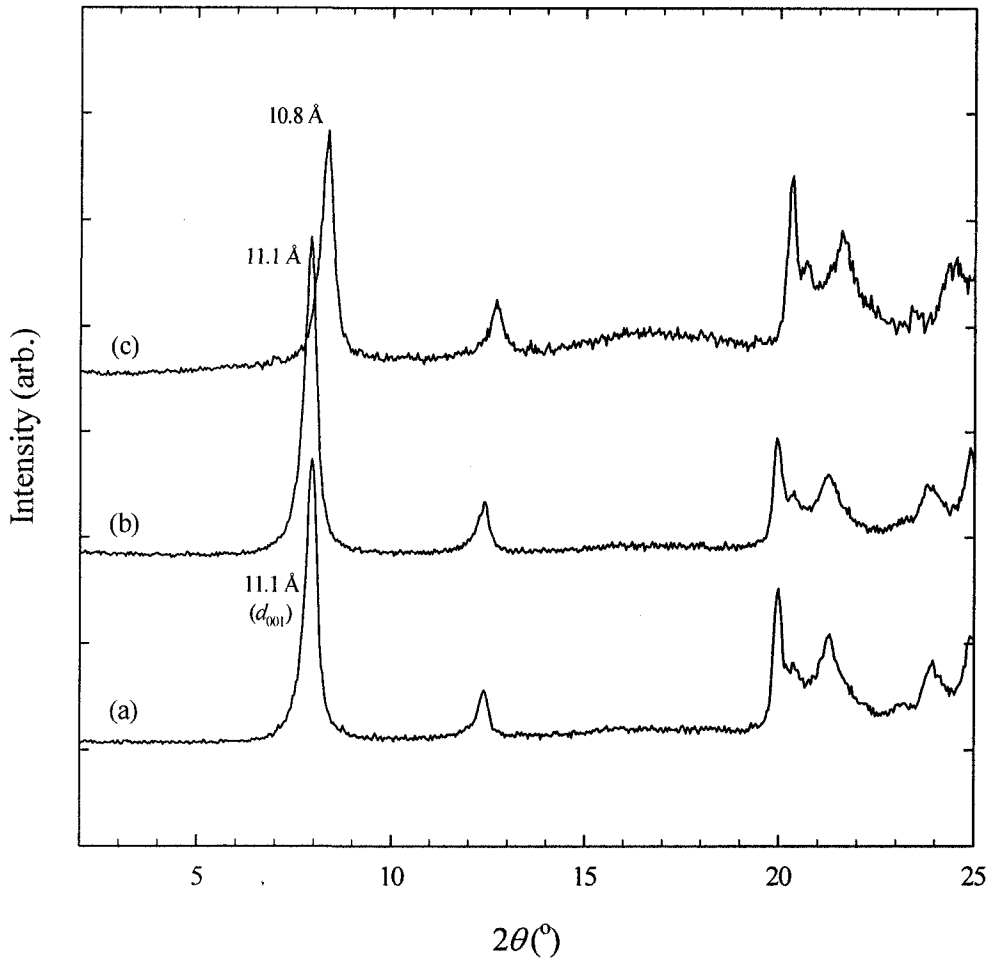


**Fig. 3.15.** XRD powder patterns (2–25°) of (a) Kao–D-mannitol, (b) Kao–D-mannitol, washed with DIW for 4 days, and (c) Kao–D-mannitol, refluxed in DIW for 40 h.

## 3.13 Solid-state $^{13}C$ NMR analysis

### 3.13.1 Identification of the intercalated species

The results of the $^{13}C$ cross polarization/magic-angle spinning (CP/MAS) NMR spectra of the Kao–KOAc intercalate, crude D-mannitol, and of the Kao–D-mannitol nanohybrid material are presented in Fig. 3.16. Summary of the detailed spectroscopic data can be found in Chapter 6 for the products listed in Table 3.2 (the Experimental Chapter).

Potassium acetate was completely removed from the interlayer space of kaolinite after reaction with D-mannitol under the conditions reported in Table 3.2. The $^{13}C$ spectrum of the polyol can be observed after reaction. The peaks are broadened compared with the pure D-mannitol, but are observed entirely in the same chemical shift region, from 65 to 75 ppm, characteristic of alditols. Similarly, no DMSO peak could be observed after reaction of Kao–DMSO with D-mannitol or dulcitol (see Experimental Chapter). Consequently, DMSO (or KOAc) molecules are fully replaced by the polyol in the interlamellar spaces of kaolinite after the reaction. This was also observed in the cases of D-sorbitol or adonitol (7), but in the case of the intercalation of polyethylene glycol, DMSO was found to be co-intercalated with the polymer (18).

### 3.13.2 Dipolar dephasing experiments

Figure 3.17 shows the $^{13}C$ dipolar dephasing spectra of Kao–D-mannitol, with dephasing times $\tau$ ranging from 0 to 40 μs. The complete disappearance of the mannitol signals for a

dephasing time of 40 μs indicates that the polyol chains are rigidly fixed in the interlamellar spaces of kaolinite (126–128). The results of a series of dipolar dephasing experiments revealed that the intensities of the $^{13}C$ signals show an exponential decay according to the equation previously reported (see Chapter 2) (127). The linear fitting of the plot of $\ln(I_{DD}/I_o)$, where $I_{DD}$ and $I_o$ are the peak intensities obtained with and without dipolar dephasing, respectively, vs. $\tau^2$ (dipolar dephasing delay time in μs) shows a statistical linear regression factor of 0.997, and $T_2$ which is the transverse relaxation time constant can be calculated to be ~16 μs (Fig. 3.18). This can be compared to the results obtained previously for the other organic nanohybrids of kaolinite, e.g., Kao–PEG nanocomposites (18).

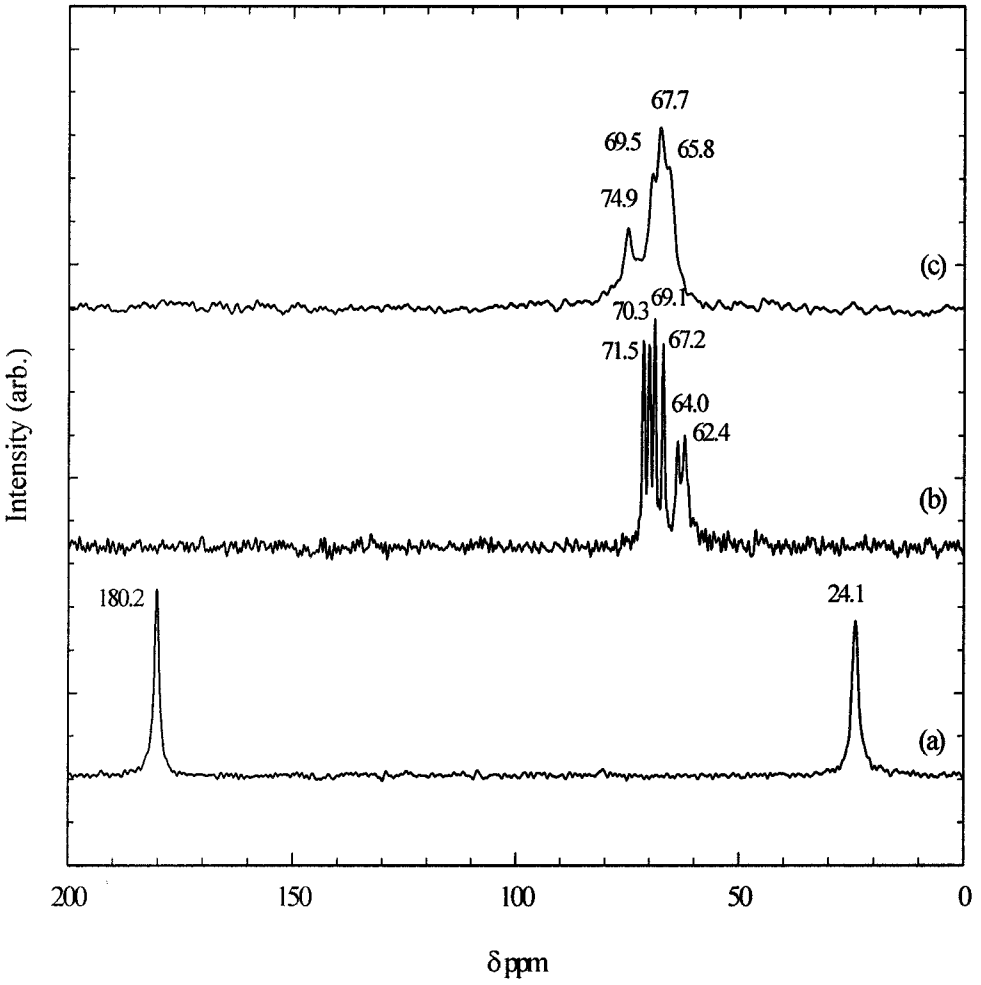


**Fig. 3.16.** Solid-state $^{13}C$ CP/MAS NMR spectra of (a) Kao–KOAc, (b) crude D-mannitol, and (c) Kao–D-mannitol.

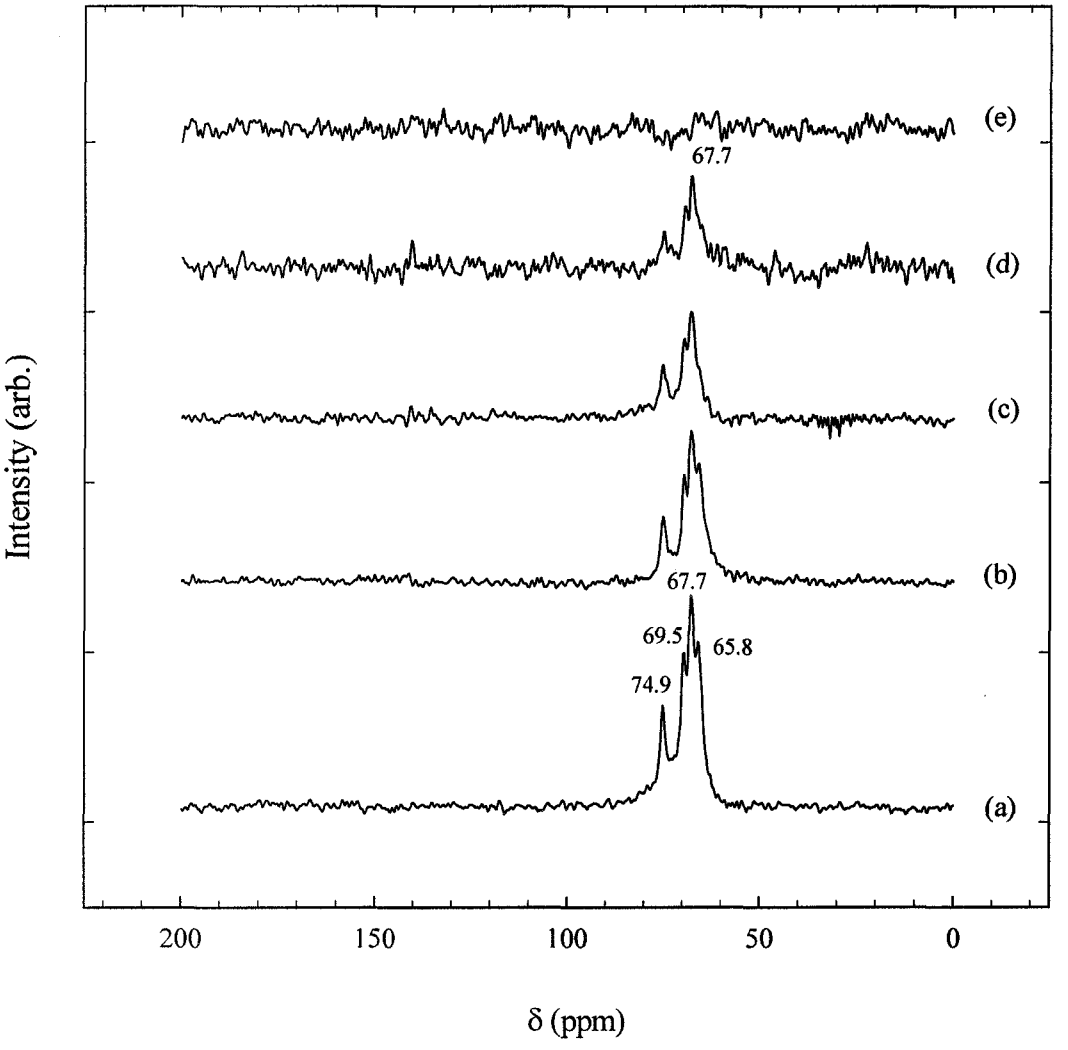


**Fig. 3.17.** Solid-state $^{13}C$ CP/MAS NMR spectra of Kao–D-mannitol: (a) no dipolar dephasing; (b–e) with dipolar dephasing, $\tau$ = (b), 10; (c), 20; (d), 30; and (e), 40 μs.

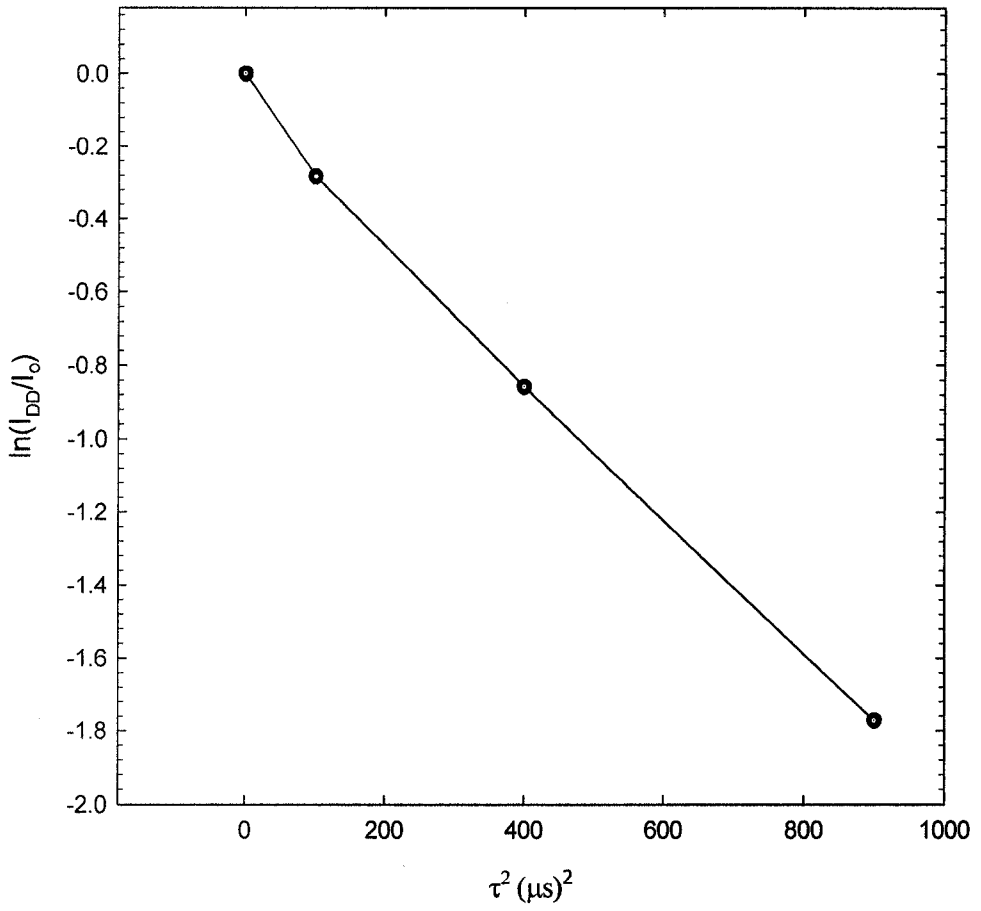


**Fig. 3.18.** Plots of $\ln(I_{DD}/I_o)$ vs. the square of the dipolar dephasing time ($\tau^2$) for the $^{13}C$ NMR DD/MAS spectra acquired for Kao–D-mannitol. Data for the 67.7 ppm signal (•).

## 3.14 $^{29}$Si CP/MAS NMR

The $^{29}$Si CP/MAS NMR spectrum (99.35 MHz) of kaolinite is given in Fig. 3.19. It displays two well-resolved signals at –91.5 and –90.9 ppm. The observation of two different $^{29}$Si NMR signals for kaolinite was reported previously (74, 129–132). The two signals were attributed to the existence of two different but equally populated silicon sites. Interlayer hydrogen bonding, causing two different silicon environments, is the main reason for signal splitting in kaolinite. $^{29}$Si CP/MAS spectrum of Kao–DMSO intercalate is given in Fig. 3.19b. In addition to the residual signals of unexpanded kaolinite, one signal is observed at –92.7 ppm. The degeneracy of the $^{29}$Si signals of kaolinite upon intercalation of organic molecules has been reported previously (129–132). This change corresponds to the loss of H-bonding dissymmetry observed in kaolinite and a well-ordered structure of the intercalated molecules, e.g., DMSO in the interlamellar space. Figure 3.19c and 3.19d give the $^{29}$Si CP/MAS NMR spectra of D-mannitol and dulcitol intercalates, respectively. Two broad signals are observed at –91.0 and –91.5 ppm with unequal intensities. This is similar to what was reported in the case of a bridged propanediol grafted to the interlayer aluminol surface (21) where broad dissymmetric signal with a maximum at –92.0 ppm was observed. Similar results were also observed in case of the thermally treated (grafted) alditols (see Part I of this chapter). The $^{29}$Si spectra reported here for the polyols suggest a multi-point grafting on the surface.

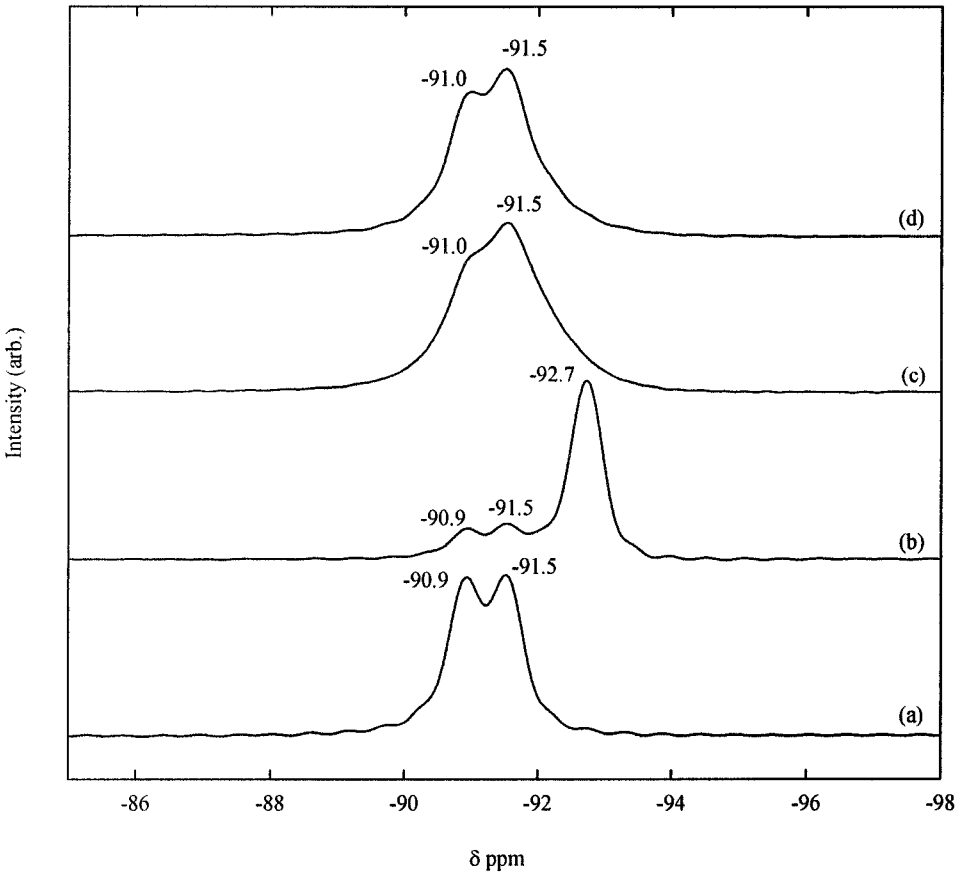


**Fig. 3.19.** $^{29}Si$ CP/MAS NMR spectra of (a) kaolinite, (b) Kao–DMSO, (c) Kao–D-mannitol, and (d) Kao–dulcitol.

## 3.15 $^{27}$Al NMR analysis

$^{27}$Al NMR spectra of kaolinite and intercalates show signals due to both octahedral and a small amount of tetrahedral aluminum sites (133). The $^{27}$Al MAS NMR spectra of kaolinite and of several polyol intercalates were obtained at 130.32 MHz at a spinning speed of 14.0 kHz. In all the cases, a broad signal is still observed, with a maximum in the range 4.0 to 4.5 ppm for the octahedral site in agreement with previous studies (Fig. 3.20) (72, 75, 134, 135).

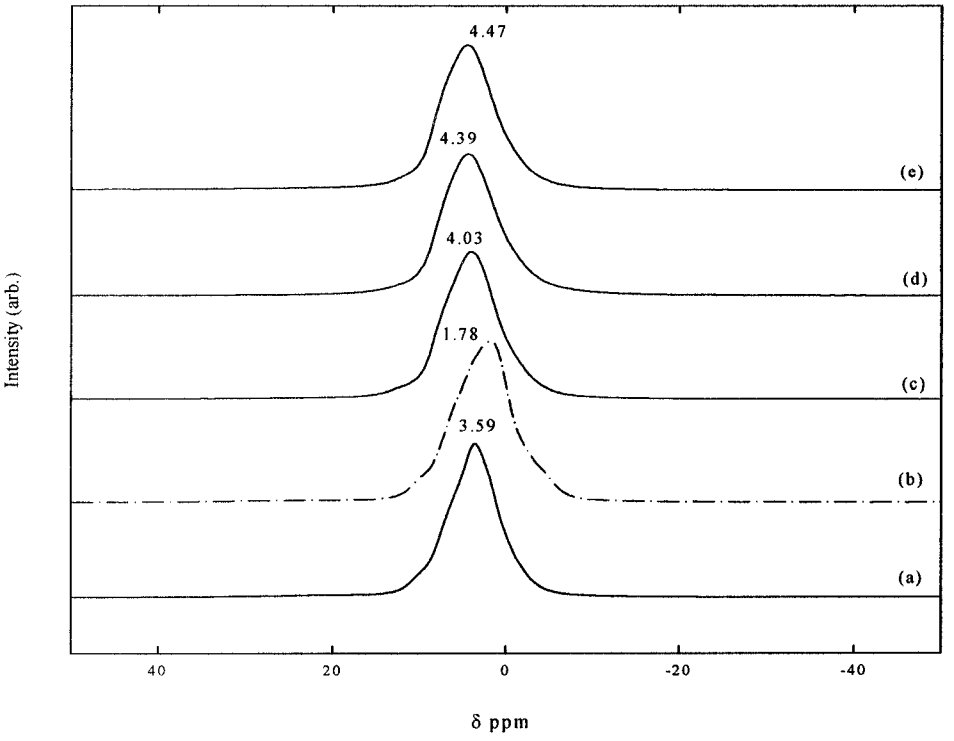


**Fig. 3.20.** $^{27}$Al MAS NMR spectra of (a) kaolinite, (b) Kao–DMSO, (c) intercalated Kao–D-sorbitol, (d) grafted Kao–D-sorbitol, and (e) grafted Kao–D-mannitol.

## 3.16 FTIR analysis

Figure 3.21 gives the infrared spectra in the O–H and C–H stretching regions of kaolinite, Kao–DMSO, Kao–D-mannitol, and Kao–dulcitol. The spectra of the starting materials were similar to the previously reported elsewhere (26, 70, 75). Upon the reaction of Kao–DMSO with the alditols, the C–H stretching bands of DMSO are replaced by three bands at 2854, 2926, and 2957 $cm^{-1}$, characteristic of the aliphatic backbone of mannitol. The band at 3620 $cm^{-1}$, corresponding to the OH stretching of the internal Al–OH group remains unaffected in all cases, while the bands, corresponding to the surface Al–OH groups, are affected by the reaction with mannitol and dulcitol. It is particularly striking to note that the O–H stretching patterns of the intercalated materials are very similar to those observed in the cases of adonitol and D-sorbitol after thermal treatment and grafting on the internal surfaces. Of particular interest is the strong reduction of the band at ~3602 $cm^{-1}$, a result also similar to what was observed in the case of the grafting of ethylene glycol (7, 16). The spectra of Kao–D-mannitol before and after heating for 1 h at 250 °C are essentially identical (Fig. 3.21), an indication that in the more drastic reaction conditions used for D-mannitol and dulcitol, the intercalation of these polyols in the interlamellar spaces of kaolinite is directly followed by the grafting on the internal surfaces, without the possibility of identifying an intercalation phase as intermediate.

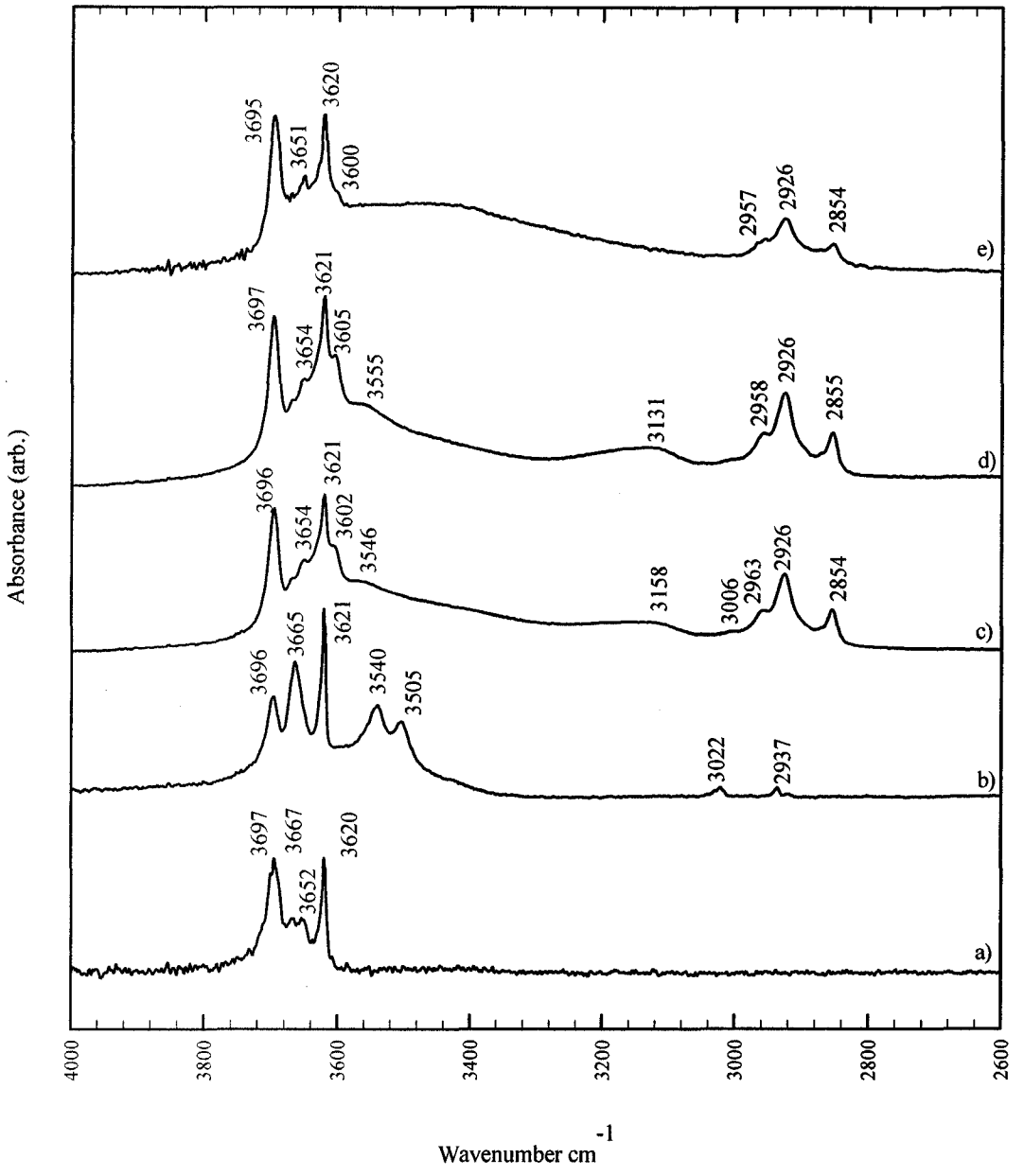


**Fig. 3.21.** FTIR spectra (4000–2600 $cm^{-1}$) of (a) kaolinite, (b) Kao–DMSO, (c) Kao–D-mannitol, (d) Kao–D-mannitol after heating for 1 h at 250 °C, and (e) Kao–dulcitol.

## 3.17 Thermogravimetric analysis

As mentioned before, the main feature of the DTA thermogram of kaolinite is the major endotherm near 550 °C, attributed to the loss of water because of the dehydroxylation of crystal lattice with formation of meta-kaolinite. This endotherm corresponds to ~13.8% weight loss in the TGA (Figs. 3.22a and 3.22b). Another feature of the DTA is a characteristic exotherm around 1000 °C, attributed to structural reorganization and formation of the spinel phase (136). As shown in Figs. 3.22a and 3.22b, the Kao–DMSO intercalate exhibits two weight losses in the TGA, accompanied with two endotherms centered at ~195 °C and 513 °C. The former is attributed to the loss of DMSO, and the latter is due to the dehydroxylation step of kaolinite.

In the case of the D-mannitol and dulcitol intercalates, one can observe the dehydroxylation steps at ~470 °C and 485 °C, respectively. This shift to lower temperatures, compared with the pristine kaolinite, is characteristic to the grafting of organic molecules to the hydroxyls of the aluminol surface of kaolinite. An additional weight loss is observed in both cases with $T_{exo}$ around 350 °C, corresponding to the loss of the organic moieties. These relatively high temperatures indicate the grafting of the polyols on the aluminol interlayer surface of kaolinite. Similar temperatures were previously reported in case of other polyols, grafted ethylene glycol, polyethylene glycol, ethanolamines, and diols (7, 16–19, 21, 23).

Again, The final weight loss ~1.9% for both Kao–D-mannitol and Kao–dulcitol is attributed to the carbonaceous residue of the decomposed alditols, trapped in the interlamellar spaces of kaolinite. The exothermic peak (DTA) accompanying the spinel-

phase crystallization is observed around 1003 °C in both cases.

The presence of the carbonaceous residue that hinders the interactions between the adjacent aluminosilicate layers suppressed the kaolinite dehydroxylation endotherms (Fig. 3.22b).

In general, endothermic peaks attributed to the fusion of the organic material do not appear in the DTA thermograms of the kaolinite intercalates reported in the literature, indicating different aggregation states for the organic molecules in the bulk and the intercalate or the absence of crystalline material in the intercalates (9, 18). Kao-D-mannitol and kao-dulcitol are no exception. The DTA thermograms of pure D-mannitol and dulcitol (148) revealed endothermic peaks at 169 °C and 190 °C, respectively, attributed to the melting of the alditols. In case of the intercalated alditols, no endothermic peaks were observed at the fusion temperatures of the pure alditols, thus ruling out the possibility of having any excess amount of the organic substances adsorbed on the sample or not intercalated in the interlamellar space of kaolinite.

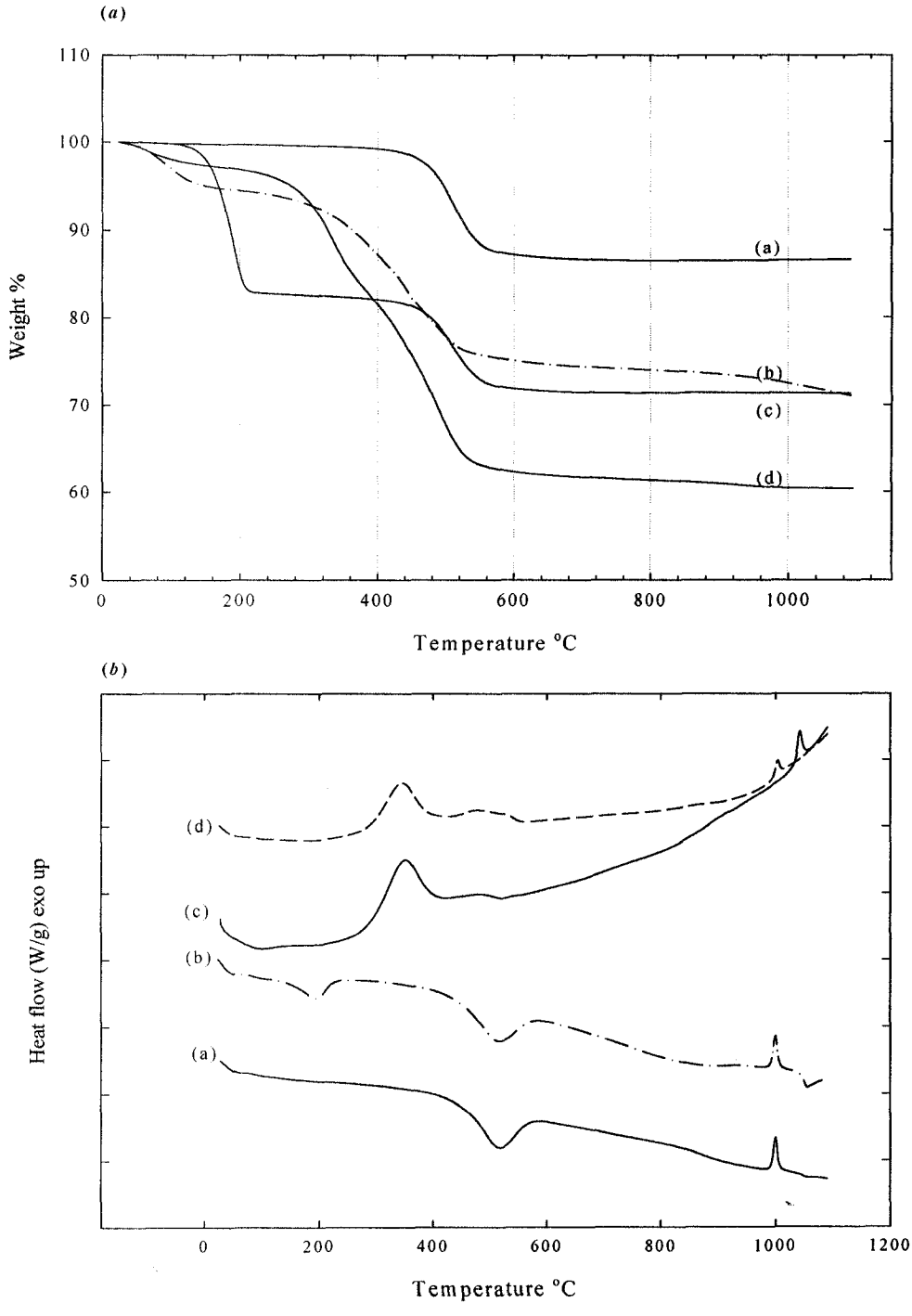


**Fig. 3.22.** ***(a)*** TGA curves (RT–1100 °C) for (a) kaolinite, (b) Kao–D-mannitol, (c) Kao–DMSO, and (d) Kao–dulcitol. ***(b)*** The corresponding DTA curves: (a) kaolinite, (b) Kao–DMSO,(c) Kao–D-mannitol, and (d) Kao–dulcitol.

## 3.18 Thermal transformation of the D-mannitol and Kao–D-mannitol compound

In a blank experiment, ~20 g of the pure D-mannitol were placed in a sealed autoclave (Parr bomb) under the same conditions of experiment M6 (see Table 3.2). The resulting material was dissolved in alcohol and the ES-MS was recorded. The spectrum showed an oligomeric structure with the molecular-ion peak value up to eight times the molecular mass of the D-mannitol and other fragments corresponding to the dimer, trimer, tetramer, and other multiplets of the molecule. The results of the HMQC $^{13}C$–$^{1}H$ NMR experiment performed on the product of the blank experiment dissolved in $D_2O$ confirmed the presence of methylene groups linked through an ether type linkage as a result of the polymerization of the alditol (see Appendix A1 and A2).

Clearly, from the TGA/DTA results, a carbonaceous material remained between the layers of kaolinite after the decomposition of the intercalate. Similar results were observed in case of other intercalates, especially polymers, e.g., polyacrylamide (149). Subsequently, the thermal behavior of the Kao–D-mannitol intercalate was investigated. Thus, Kao–D-mannitol was heated to temperatures of 150, 200, 250, and 300 °C at 4 °C $min^{-1}$ in a high-temperature chamber, and XRD patterns were measured at these temperatures. The XRD patterns before and after heat treatment at different temperatures are shown in Fig. 3.23. Clearly, peaks due to increased basal spacing were observed in all patterns. The shift of the basal spacing at high temperature (250 and 300 °C) is plausibly due to the conversion of the

polyol to the carbonaceous material. Similar broadening of the peaks at high temperatures was also observed for the Kao–poly(acrylamide) intercalate, and was attributed to the disordered stacking of the layers of the aluminosilicates (149). Again, analyses results confirmed the possibility of the grafting of an oligomeric form of the alditols on the aluminol surface of kaolinite in a bridging manner.

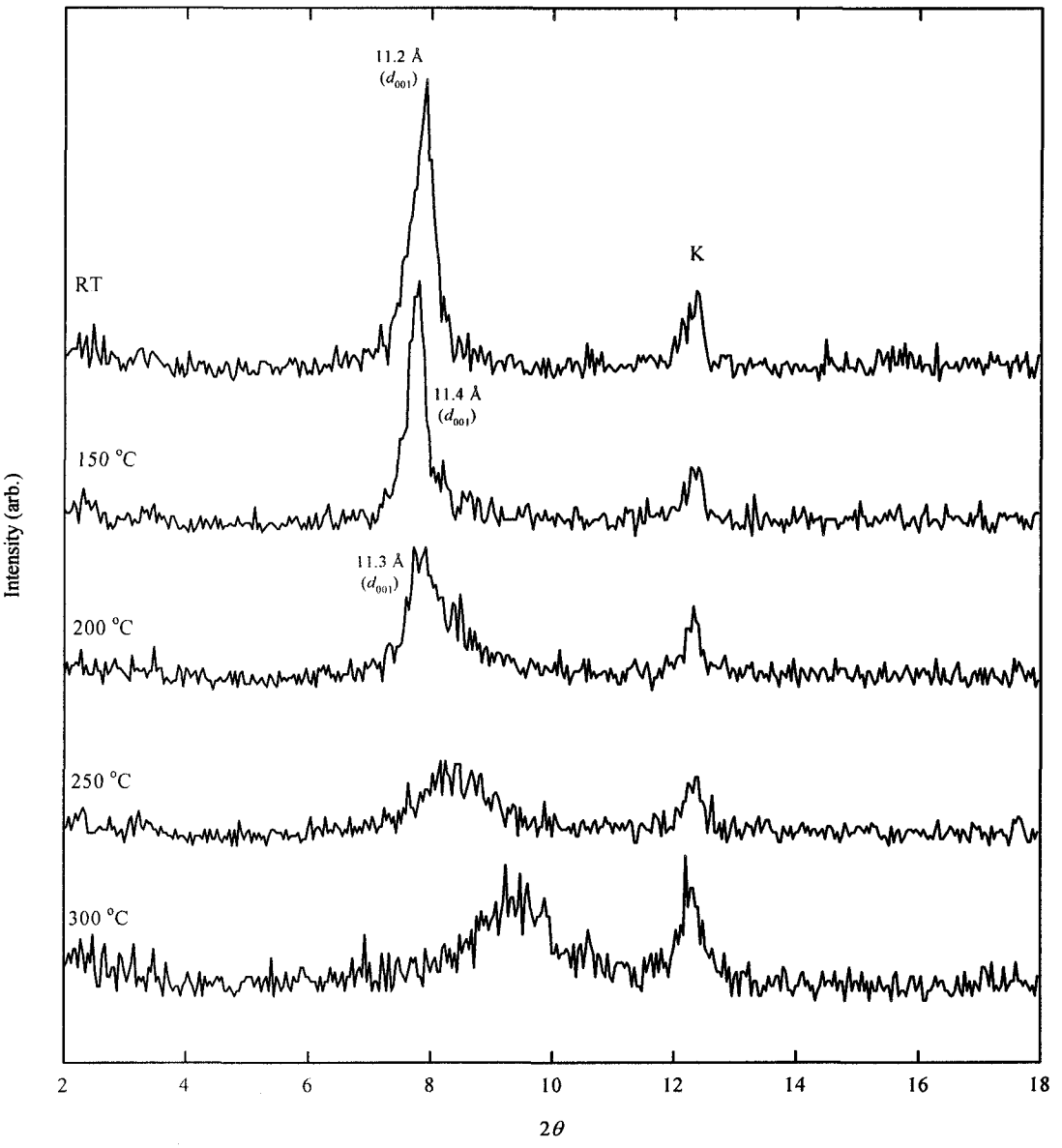


**Fig. 3.23.** High-temperature XRD patterns (2–18 °) of the Kao–D-mannitol for the temperature range RT–300 °C.

# Chapter 4

## Intercalated nanocomposites from kaolinite and biodegradable polyesters

### 4.1 Introduction

The rapidly growing use of polymers, followed by their disposal into the environment as undegradable waste, recently raised serious global environmental concerns. Consequently, the interest in developing "green" polymeric materials that can be biodegraded after disposal by the activity of microorganisms to CO and $H_2O$ is growing. Biodegradable polymers could be made from biosources, e.g., corn and cellulose, can be synthesized by bacteria, e.g., poly(hydroxy butyrate) (PHB), or can be derived from petroleum sources, e.g., aliphatic polyesters (150). Polymers of the latter category, such as poly(ethylene adipate) (PEA), poly(ethylene succinate) (PES), poly(butylene adipate) (PBA), have received a lot of attention as potential alternatives to commercial plastics. These are usually synthesized by the polycondensation of the diol moiety with the appropriate dicarboxylic acid (151). One of the major problems limiting the commercialization of these polyesters is their poor performance in terms of mechanical properties as well as controlling their rate of degradation. Aliphatic polyesters are the most promising polymers for the production of environment-friendly biodegradable plastics. Biodegradation of these polymers can occur by living microorganisms that produce enzymes that have the ability of degrading the polymer. In general, the commercialization of these biodegradable polymers is limited by

their poor physical properties as well as uncontrolled biodegradation (151).

In this chapter, the first intercalated kaolinite–polymer nanocomposite that involves the use of a commercial biodegradable polymer is reported. The nanoscale dispersion of the clay particles to form the Kao–polymer nanocomposite is believed to improve the properties of the polymer (31, 152). For the first time, the produced nanohybrids are free of co-intercalated intermediate guest molecules, thus allowing the produced material to be described as "green" nanocomposite.

## 4.2 Preparation and X-ray diffraction analysis

Several kaolinite–polymer nanocomposites were typically prepared, using a guest-displacement technique, by first preparing the dimethyl sulfoxide (DMSO) or potassium acetate (KOAc) intercalate of kaolinite, and then reacting this directly with the polymer, i.e., guest-displacement technique (see Chapter 1). Typically, 1–2 g of either Kao–DMSO or Kao–KOAc intercalate were mixed with an excess (approximately four-fold) of either dihydroxy terminated poly(ethylene adipate) (PEA) (Aldrich), poly(ethylene succinate) (PES) (Aldrich), or poly(butylene adipate) (PBA) (Aldrich) (see Chart 4.1). This was done directly in the melt of the appropriate polymer, without the use of a solvent. The mixture was maintained at a given temperature for a given period of time, followed by the reaction workup (mainly washing with excess solvents, vacuum filtration, and drying). The success of the intercalation by the melt method was previously attributed to the strong concentration effect of the polymer in the melt compared with the solutions, coupled with a possible

lower stabilization energy of each polymer unit in the melt and with a competition of the interlamellar hydrogen bonding sites of kaolinite by the solvent molecules. The reaction details for the individual reactions are given in the Experimental Section, and a summary of the main reactions is given in Table 4.1. The product codes and reaction conditions are given, along with the interlayer *d*-spacing, and the ratio of intercalation (RI). The interlayer or *d*-spacings were calculated from the first $d_{001}$ reflections of the principal phase.

The interlayer expansions for the products were comparable. Basal spacings of the nanocomposites ranged from 11.5 Å for Kao–PES to ~12.0 Å for Kao–PBA. After subtracting an average basal spacing of 7.15 Å for the pristine kaolinite (KGa-1b), this corresponds to an expansion of approximately 4.35–4.85 Å, which is the roughly expected interlayer expansion, corresponding to a flattened monolayer arrangement of the polymeric chains in the interlamellar space. Comparable values for the interlayer expansion because of the monolayer intercalation of the organic molecules into kaolinite were reported elsewhere, e.g., an expansion of ~3.7–4.8 Å for Kao–polyols (adonitol, D-sorbitol, dulcitol, and D-mannitol) ((7, 8); see Chapter 3), as well as 4.0 Å for Kao–PEG (18) and for other kaolinite–polymer intercalates (9, 24, 35, 97), and for other layered materials (113–117).

$$H\text{–}[OCH_2CH_2OOCCH_2CH_2CH_2CH_2CO\text{–}]_nOH$$

**I**

$$H\text{–}[OCH_2CH_2CH_2CH_2OOCCH_2CH_2CH_2CH_2CO\text{–}]_nOH$$

**II**

$$H\text{–}[OCH_2CH_2OOCCH_2CH_2CO\text{–}]_nOH$$

**III**

**Chart 4.1.** Molecular formulae for (**I**) PEA, (**II**) PBA, and (**III**) PES.

In a blank experiment, when kaolinite itself (KGa-1b) was used as a starting material, it was recuperated unreacted. Typical X-ray powder patterns of the starting materials (kaolinite and Kao–DMSO) and of the materials resulting from the reaction with the melts of PEA and PES are shown in Fig. 4.1 for the range of 2–15° ($2\theta$). The remaining patterns are similar to those previously reported in the case of other polymers (e.g, PEG) (18). In addition, full XRD patterns of the nanocomposites resulting from the reaction of Kao–DMSO with the molten polymers are shown in Fig. 4.2. It is worth noting that the $d_{060}$ reflection, characteristic of a dioctahedral clay mineral, remains at 1.49 Å in all cases. XRD patterns of the other Kao–polyesters reported in Table 4.1 are similar to this, and in all cases at least four (00l) reflections could be indexed. Thus, the layered structure of kaolinite remains largely unaffected, the only major variation being the value of the *d*-spacing.

It is noteworthy that the analyses of the products of the preliminary attempts indicated the presence of remaining (co-intercalated) starting materials in the interlamellar space of kaolinite, i.e., DMSO molecules were not completely displaced by the polymeric chains, as evident from the presence of DMSO peaks in $^{13}C$ NMR spectrum of Kao–PEA1. Subsequently, optimization of the reaction conditions (longer times and higher reaction temperatures, see Table 4.1) resulted in the complete displacement of the guest molecules, i.e., DMSO by the polymeric chains (see NMR Section); therefore , the reported interlayer expansion can only be attributed to the intercalated polymeric chains. Thus, these results are the first report of a complete displacement by an intercalated polymer from the melt, since the reported Kao–PEG results, for example, confirmed only the co-intercalation of

DMSO molecules and the polymer (18); same results were also obtained from Kao–PEG synthesis attempts performed in the course of this study (see Chapter 6). In case of Kao–KOAc starting material, both attempts (Table 4.1) only resulted in a co-intercalation of the salt molecules, possibly entangled in the polymeric chains and the products of the transesterification reaction between the acetate and the polyester, as evident by $^{13}C$ NMR data (see later sections).

The intercalation ratios achieved were always > 90% (see Table 4.1), as the reaction temperature was kept below the decomposition temperature of the Kao–DMSO intercalate (~190 °c) to avoid the collapse of the DMSO intercalate prior to the displacement by the polymeric chains. The lower intercalation ratio observed in case of Kao–PBA is plausibly due to the longer reaction time and higher temperature needed to melt the polymer, which might partially result in the de-intercalation of DMSO molecules from the starting material. Figure 4.3 shows a follow-up of the development of the interlayer expansion by the polymer molecules vs. reaction time for the Kao–PES nanocomposites. Clearly, the interlayer expansion increases with time.

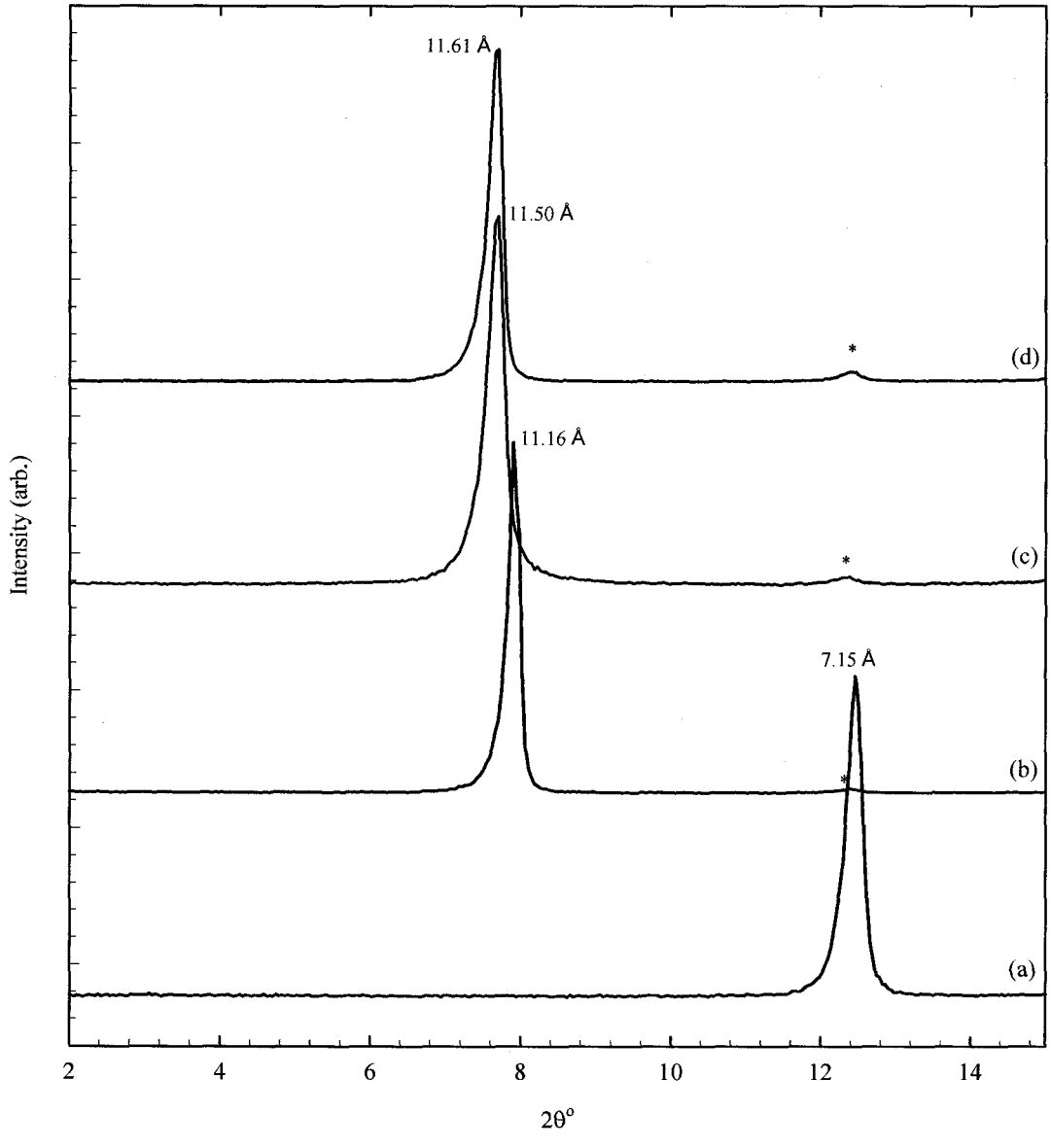


**Fig. 4.1.** XRD powder diffraction patterns ($2\theta$ = 2–15°) of (a) kaolinite, (b) Kao–DMSO, (c) Kao–PES, and (d) Kao–PEA. Residual kaolinite $d_{001}$ peaks are marked by asterisks.

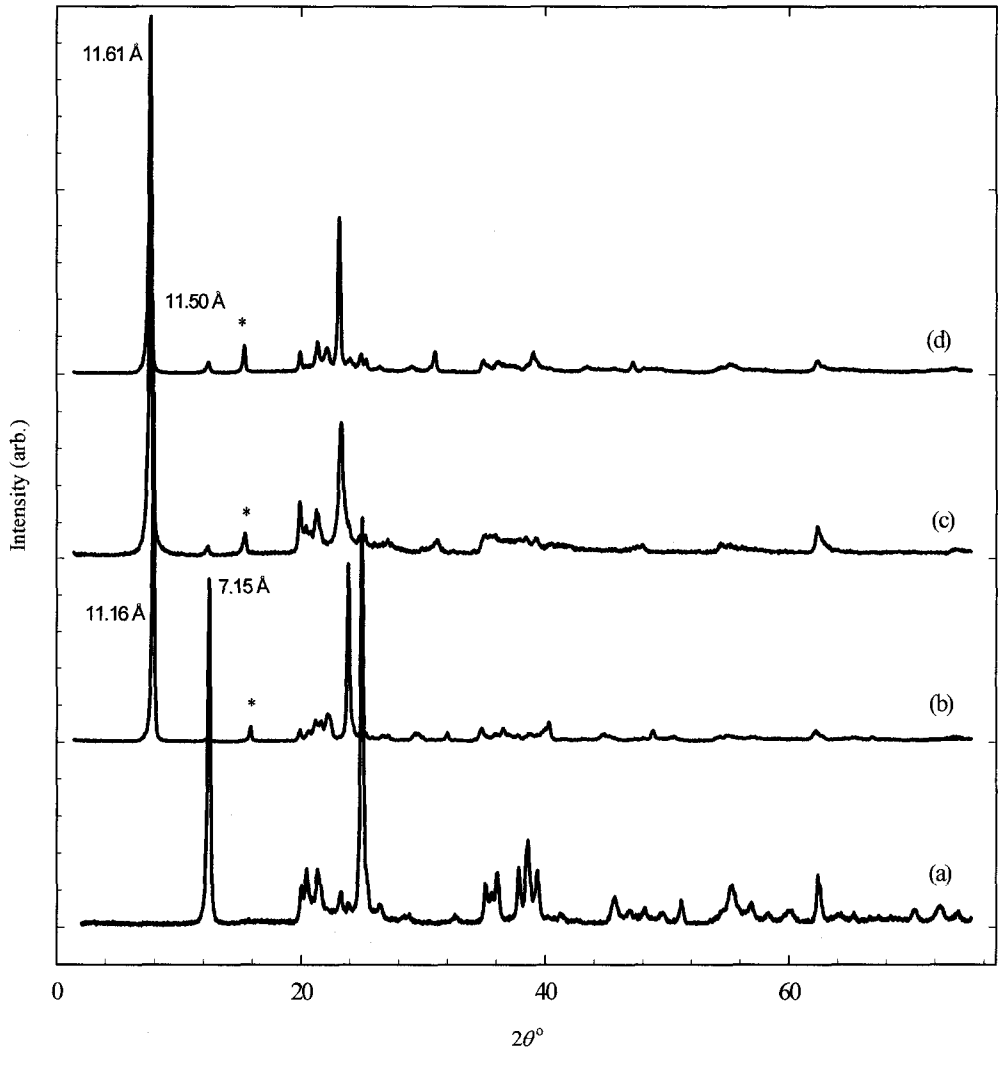


**Fig. 4.2.** XRD powder diffraction patterns ($2\theta$= 2–75°) of (a) kaolinite, (b) Kao–DMSO, (c) Kao–PES, and (d) Kao–PEA. Residual kaolinite $d_{001}$ peaks are marked by asterisks.

**Table 4.1.** Summary of the product codes, reaction conditions, and product X-ray characterization for the prepared nanocomposites.

| | Reaction conditions | | | | | Product X-ray characterization | | | Residual SM |
|---|---|---|---|---|---|---|---|---|---|
| Product code [a] | Starting material (SM) [a] | Reaction medium (RM) (polymer) | RM:SM (wt%) | $T_r$ [b] (°C) | $t_r$ [c] (h) | $d_{001}$ [d] (Å) | $d_{001}$(K) [e] (Å) | RI [f] (%) | detected in product [g] |
| Kao–PEA1 | Kao–DMSO | PEA | 4.3 | 146–152 | 120 | 11.52 | 7.13 | 97.4 | Yes |
| Kao–PEA2 | Kao–DMSO | PEA | 4.3 | 138–154 | 216 | 11.53 | 7.14 | 98.0 | NA[h] |
| Kao–PEA3 | Kao–DMSO | PEA | 4.1 | 155–186 | 90 | 11.63 | 7.15 | 97.9 | NA |
| Kao–PEA4 | Kao–DMSO | PEA | 3.4 | 160–178 | 165 | 11.61 | 7.13 | 98.7 | No |
| Kao–PEA5 | Kao–KOAc | PEA | 3.9 | 143–167 | 69 | 11.65 | 7.17 | 92.2 | NA |
| Kao–PEA6 | Kao–KOAc | PEA | 5.2 | 155–160 | 70 | 11.72 | 7.17 | 85.9 | Yes |
| Kao–PEA7 | Kaolinite (KGa-1b) | PEA | 4.3 | 169–180 | 282 | — | 7.17 | NR[i] | NR |
| Kao–PES1 | Kao–DMSO | PES | 4.1 | 154–158 | 404 | 11.48 | 7.14 | 97.6 | No |
| Kao–PES2 | Kao–DMSO | PES | 4.0 | 158–167 | 168 | 11.50 | 7.17 | 98.2 | No |
| Kao–PBA1 | Kao–DMSO | PBA | 4.0 | 155–164 | 266 | 11.78 | 7.17 | 70.0 | Yes |
| Kao–PBA2 | Kao–DMSO | PBA | 4.0 | 170–181 | 190 | 11.95 | 7.16 | 65.0 | Yes |
| Kao–PEG | Kao–DMSO | PEG | 5.0 | 155–160 | 216 | 11.53 | 7.29 | 91.6 | Yes |

**Note:** Reaction details are given in the experimental section.

[a] PEA, poly(ethylene adipate); PES, poly(ethylene succinate); PBA, poly(butylene adipate); PEG, poly(ethylene glycol); DMSO, dimethyl sulfoxide; KOAc, potassium acetate; and kao, kaolinite.

[b] Reaction tempaerature range recorded as oil-bath temperature.

[c] Approximate reaction time.

[d] The specified interlayer distance (*d*) is that of the principal product phase calculated using (00l) reflections (see Chapter 1).

[e] $d_{001}$ Reflections of the residual unexpanded kaolinite.

[f] Ratio of intercalation is the ratio of the intensities of the $d_{001}$ reflection of the modified phase over the sum total of all the $d_{001}$ reflections of the modified phase(s) and residual unexpanded kaolinite.

[g] Based on $^{13}C$ NMR results, obtained on a Bruker ASX-200 instrument, operating at 50.31 MHz.

[h] $^{13}C$ NMR spectra were not recorded.

[i] No reaction.

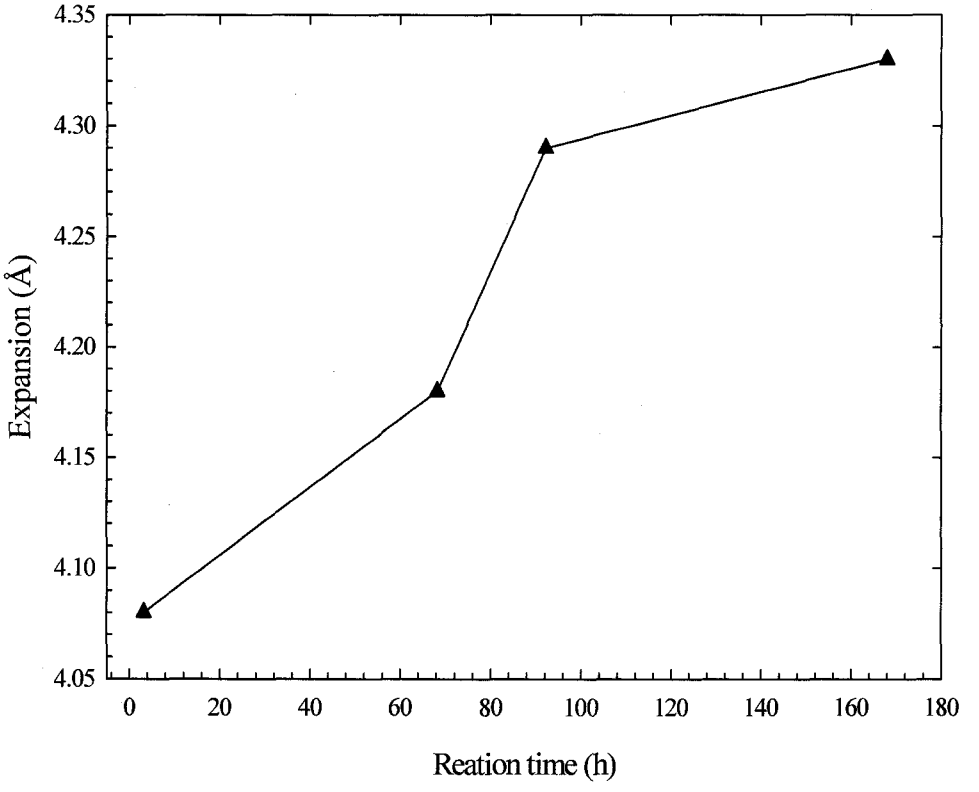


**Fig. 4.3.** Follow-up of the interlayer expansion vs. reaction time for the reaction of Kao–DMSO with poly(ethylene succinate).

## 4.3 Elemental analysis

The results of the elemental analyses of typical Kao–polymer samples are given in Table 2. Kao-PEA4 sample gives C: 9.12%, H: 2.46%, and N was not detected. This sample was proven to be free of residual co-intercalated DMSO (see NMR Section). The stoichiometry of the material is $Al_2Si_2O_5(OH)_4 \cdot (C_8H_{12}O_4)_{0.54}$, using the average of the C and H results. Kao-PES2 sample gives C: 10.24%, H: 2.22%, and N was not detected. Similar to Kao–PEA4, the calculated stoichiometry of Kao–PES2 is $Al_2Si_2O_5(OH)_4 \cdot (C_6H_8O_4)_{0.66}$. The higher occupancy value of 0.66 monomeric unit of PES per unit cell of kaolinite, compared with that of PEA (0.54), is expected because of the shorter chains (methylene spacers in the dicarboxylic ester moiety). Both samples had high intercalation ratios (see Table 1), and the observed c-spacings of 11.5–12.0 Å point to a flattened arrangement of the polymeric chain in all cases, in a manner described before for other Kao–polymer intercalates (9, 18, 20, 24, 30, 35, 97).

In case of Kao–PBA2, the calculated stoichiometry, based on elemental analysis data (Table 4.2), revealed an occupancy of 0.41 monomeric unit of PBA per unit cell of kaolinite, i.e., this corresponds to $Al_2Si_2O_5(OH)_4 \cdot (C_{10}H_{16}O_4)_{0.41}$. Again, the lower occupancy value is consistent with the larger monomeric unit (Chart 4.1) and the lower ratio of intercalation (Table 4.1).

**Table 4.2.** Summary of the elemental analysis results for some of the produced nanocomposites.

| Sample | C (%) | H (%) | N (%) |
|---|---|---|---|
| Kao–PEA4 | 9.12 | 2.46 | <0.5 |
| Kao–PES2 | 10.24 | 2.22 | <0.5 |
| Kao–PBA2 | 9.51 | 2.02 | <0.5 |

## 4.4 FTIR analysis

### 4.4.1 O–H stretching region (3800–3200 $cm^{-1}$)

The characteristic O–H stretching pattern of kaolinite that consists of four bands at approximately 3697, 3667, 3652, and 3620 $cm^{-1}$ can be observed in Fig. 4.4a. Previous extensive studies (59, 60) attributed the band at ~3620 $cm^{-1}$ to the stretching frequency of the internal (inner) hydroxyl group of kaolinite (see Fig. 1.4 for the structure of kaolinite). This inner-hydroxyl stretching band is not usually influenced by the interlamellar modification of kaolinite. The remaining bands (3697, 3667, and 3652 $cm^{-1}$) are associated with the inner-surface (outer) hydroxyl groups that are at an angle (60–73°) with the (001) plane (59, 60), and these groups are readily exposed to hydrogen bonding with the intercalated molecules. Therefore, these inner-surface hydroxyl stretching bands are very much influenced by interlamellar modifications, as it can be observed for Kao–DMSO ( Fig. 4.4b).

Observing the O–H stretching patterns for Kao–PEA and Kao–PES, one can notice significant differences from both kaolinite and Kao–DMSO (Fig. 4.4a and 4.4b). In case of the Kao–DMSO intermediate, the bands that appear at 3694 and 3665 $cm^{-1}$ were attributed to the non H-bonded, coupled inner-surface hydroxyls; the coupling of these inner-surface hydroxyls is lost in case of the new nanocomposites. The band at 3697 $cm^{-1}$ is reduced in intensity compared with the corresponding band in the kaolinite spectrum but not with Kao–DMSO band. The Kao–DMSO band at 3665 $cm^{-1}$ disappeared completely, and a new band appears, in both cases, at ~3647 $cm^{-1}$,

suggesting that one of these hydroxyls could be H-bonded to the intercalated polymer. Similarly, in case of the Kao–DMSO, the bands at 3540 and 3505 $cm^{-1}$ were attributed to the stretching frequency of the coupled inner-surface hydroxyls that are H-bonded to the intercalated DMSO molecules. These bands were replaced, in the spectra of the produced nanocomposites, by two weak bands at ~3589 and 3568 $cm^{-1}$, and a broad ill-defined band can be observed at ~3435 $cm^{-1}$ along with a weak shoulder at ~3600 $cm^{-1}$. The intensity of the band at 3620 $cm^{-1}$ is also considerably reduced; however, the band position remains unaffected. The significant modifications of the O–H stretching patterns, compared with those of the kaolinite and of the Kao–DMSO intercalate, indicate the replacement of the DMSO by the polymer chains in the interlamellar space of kaolinite (see Table 4.3).

Finally, for the Kao–PBA sample, major changes can be observed compared with the OH stretching pattern of the Kao–DMSO starting material; however, the bands are similar to those of the pristine kaolinite sample with reduced intensities (Fig. 4.5). Similar to the other polyester intercalates, two weak bands appeared at 3604 and 3438 $cm^{-1}$. This OH stretching pattern is plausibly due to the relatively low intercalation ratio for this sample, compared with Kao–PES and Kao–PEA samples. Nevertheless, the intercalation of the polymer (PBA) was confirmed by the XRD and NMR results.

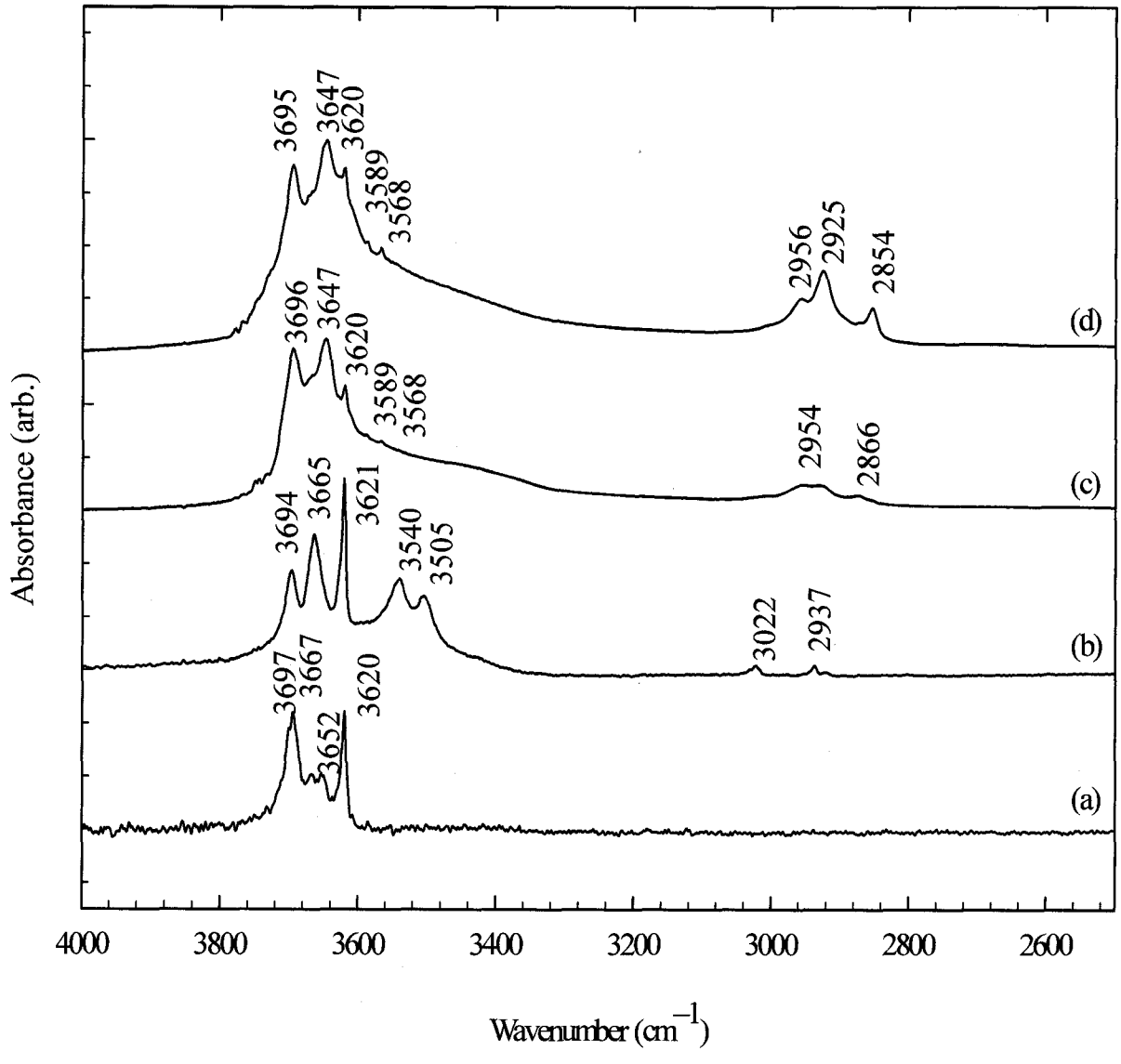


**Fig. 4.4.** FTIR spectra (4000–2500 cm$^{-1}$) of (a) kaolinite, (b) Kao–DMSO, (c) Kao–PEA, and (d) Kao–PES.

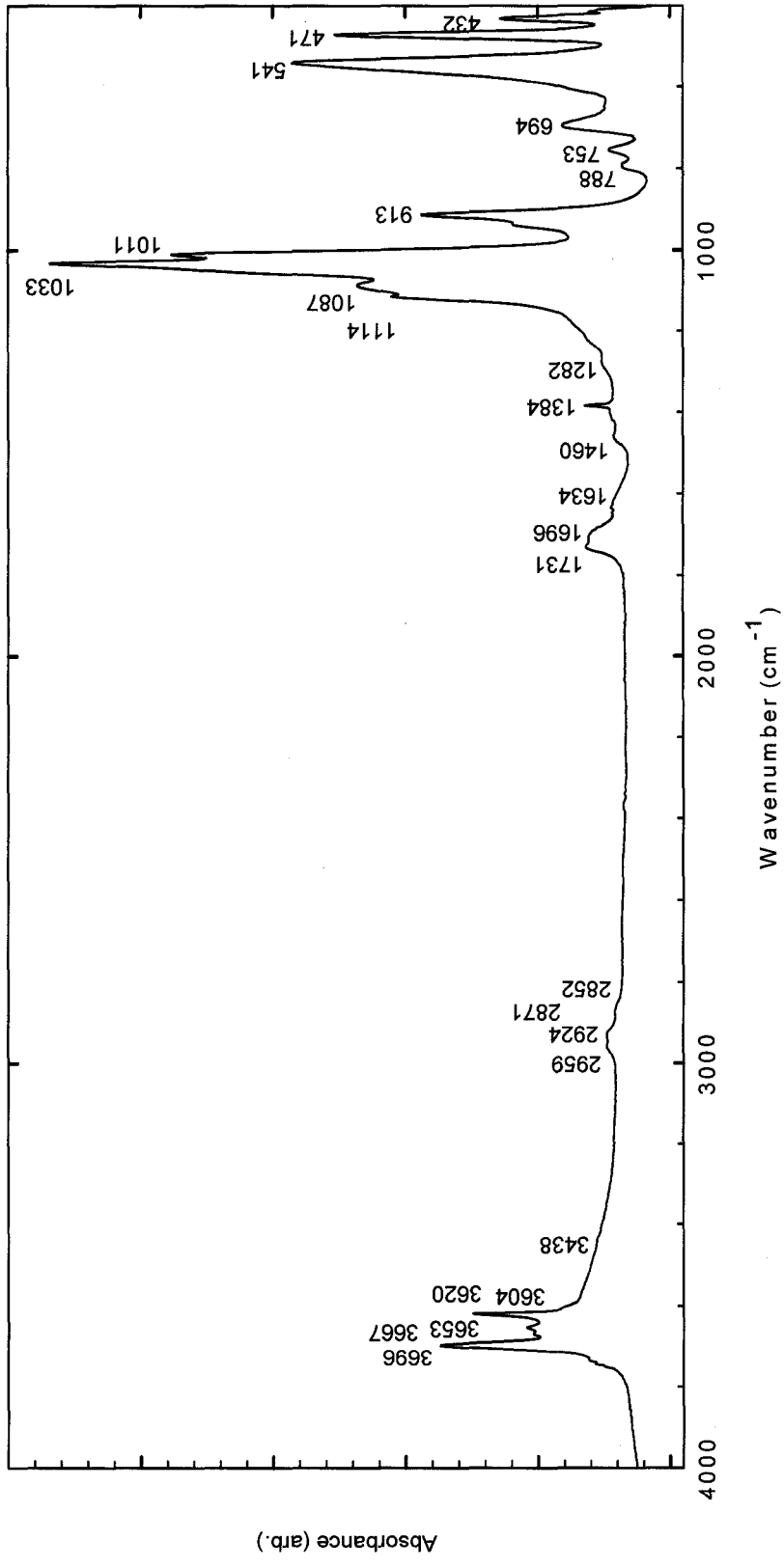


**Fig. 4.5.**FTIR spectrum (4000–400 $cm^{-1}$) of Kao–PBA nanocomposite.

**Table 4.3.** Observed FTIR absorbances, in the 4000–2000 $cm^{-1}$ range, and their assignments for the produced nanocomposites.

| Absorbance ($cm^{-1}$) | | | Assignments |
|---|---|---|---|
| Kao–PEA | Kao–PES | Kao–PBA | |
| 3696 (vs) | 3695 (vs) | 3696 (vs) | O–H stretching (outer) |
| 3648 (vs) | 3647 (vs) | 3668 (vw)<br>3653 (w) | O–H stretching (H-bonded) |
| 3620 (m) | 3620 (m) | 3620 (vs) | O–H stretching (inner) |
| 3600 (vw, sh)<br>3589 (w)<br>3562 (w)<br>3435 (vw, br) | 3600 (vw, sh)<br>3589 (w)<br>3568 (w)<br>3435 (vw, br) | 3604 (vw, sh)<br>3563 (w)<br>3438 (vw, br) | O–H stretching (H-bonded) |
| 2954 (w)<br>2925 (w) | 2956 (vw)<br>2925 (m) | 2959 (w)<br>2924 (w) | C–H stretching (asymmetric) |
| 2866 (vw)<br>2854 (vw) | 2854 (vw) | 2871 (vw)<br>2852 (vw) | C–H stretching (symmetric) |

**Note:** The absorptions are w, weak; m, medium; s, strong; vw, very weak; vs, very strong; sh, shoulder; and br, broad.

### 4.4.2 C–H stretching region (2800–3100 $cm^{-1}$)

These bands are diagnostic of the incorporation of oxyethylene-based organic moieties (18). Bands, associated with the methylene groups of both the oxyethylene moieties and the methylene spacers of the dicarboxylic ester moieties of these co-polymers, are observed upon intercalation into the interlayers of kaolinite. In case of Kao–PEA, the intercalated oxyethylene moiety shows distinct asymmetric and symmetric C–H stretching bands at about 2954, 2925, and 2854 $cm^{-1}$ (Fig. 4.4). These frequencies are characteristic for $CH_2$ bands attached to an oxygen (120, 153). Similarly, Kao–PES exhibited bands at about 2954, 2925, and 2854 $cm^{-1}$. As for the Kao–PBA sample (Fig. 4.5), the CH asymmetric and symmetric bands were observed at 2959, 2924, 2871, and 2852 $cm^{-1}$.

Clearly, for all the produced nanocomposites, close examination of this region reveals the absence of residual interlayer DMSO, as the bands at approximately 3022 and 2937 $cm^{-1}$, attributed to the symmetric and asymmetric stretching of the methylene groups of the DMSO molecules, respectively, completely disappeared in all cases (see Figs. 4.4 and 4.5).

Full assignment of the observed OH and CH stretching bands of three different novel nanocomposites is reported in Table 4.3.

### 4.4.3 C=O stretching region and the "rule-of-three" vibrations

Esters usually give rise to three characteristic bands at approximately 1700, 1200, and 1100 $cm^{-1}$. This diagnostic ester pattern is called the "rule of three" (120). The first of these three bands is attributed to the C=O stretching of the ester group. The second is due to the asymmetric stretching of both the C–C and C–O bands that are attached to the carbonyl group of the ester, and this is generally called the "C–C–O" stretching vibration. Finally, the third band of the "rule of three" is due to the vibration that involves the ester group and the next two carbons attached to it (from the oxyethylene moiety in our case), and this is usually called the "O–C–C" vibration.

Applying the "rule of three" to a saturated ester, which is generally similar to our case, The carbonyl stretching band is usually found from 1750 to 1735 $cm^{-1}$. This band can be observed at 1734, 1738, and 1731 $cm^{-1}$ in case of Kao–PEA, Kao–PES, and Kao–PBA, respectively (see Figs.4.5 and 4.6 and Table 4.4), along with the appearance of new, stronger bands at lower frequencies (~1723–1699 $cm^{-1}$) for all the produced nanocomposites (see Table 4.4 for details). These bands can be assigned to H-bonded carbonyl stretching, which indicates the presence of H-bonds between most of the ester carbonyl groups of the intercalated polymer and the hydroxyl groups of the interlamellar aluminol surface of kaolinite. Similar results were observed for inclusion complexes of aliphatic polyesters with cyclodextrins (154). Notably, this observation is indicative of the intercalation of the aliphatic polyesters in the interlamellar space of kaolinite.

The bands around 1220–1210 $cm^{-1}$ can be assigned to the C–C–O stretching, and the

bands around 1120 $cm^{-1}$ are attributed to the last vibration of the rule of three, which is the O–C–C vibration.

### 4.4.4 HOH bending region (1680–1600 $cm^{-1}$)

The observed ill-defined (HOH) band between ~1650 and 1630 $cm^{-1}$ for Kao–PEA and Kao-PES suggests that surface adsorbed and co-intercalated water molecules are present to some extent (Fig. 4.6). similar results were previously observed for other Kao–polymer intercalates (18).

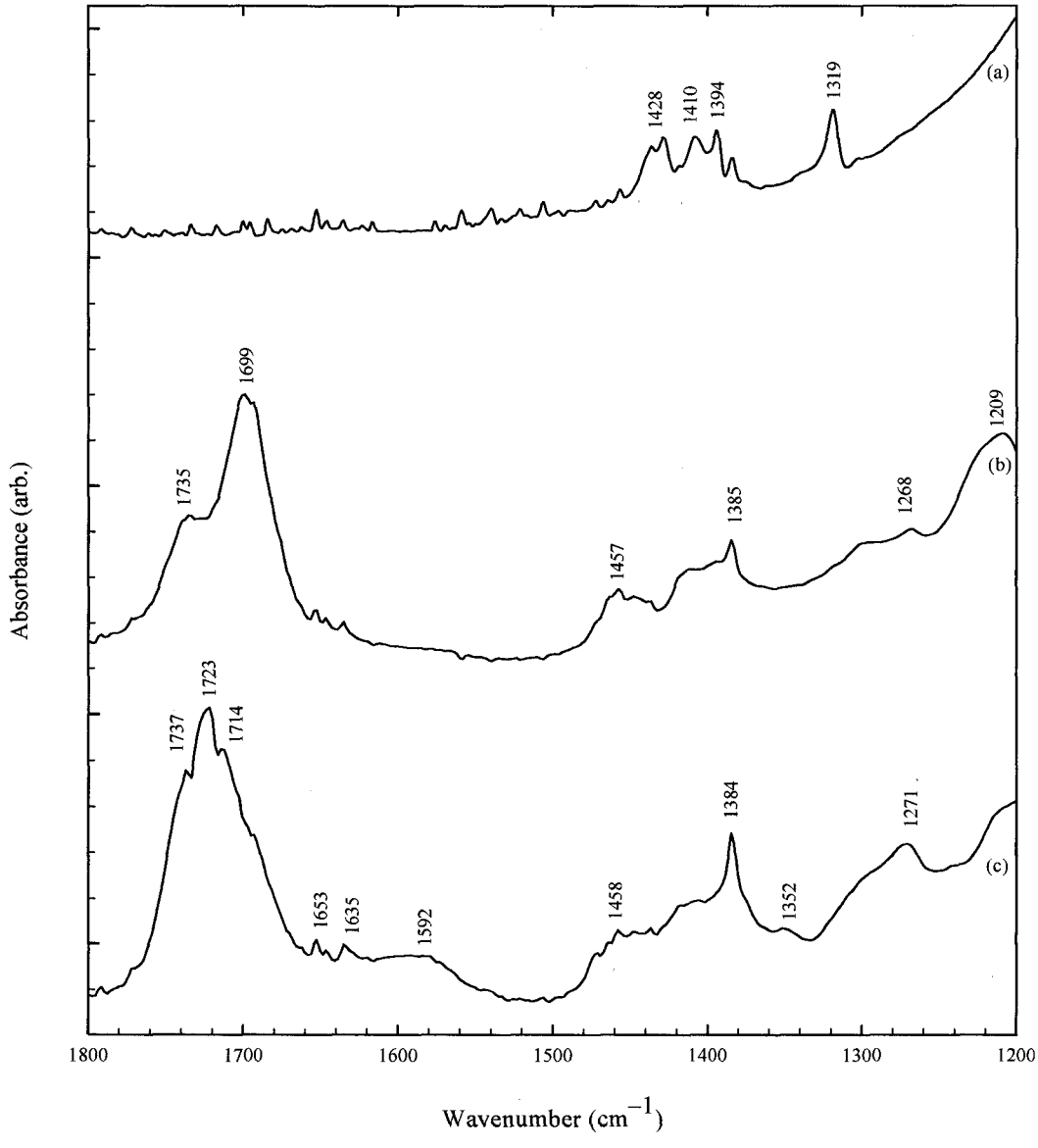


**Fig. 4.6.** FTIR spectra (1800–1200 cm$^{-1}$) of (a) Kao–DMSO, (b) Kao–PEA, and (c) Kao–PES.

**Table 4.4.** Observed FTIR absorbances, in the 1800–400 $cm^{-1}$ range, and their assignments for the produced nanocomposites.

| Absorbance ($cm^{-1}$) | | | Assignments |
|---|---|---|---|
| Kao–PEA | Kao–PES | Kao–PBA | |
| 1735 (s, sh)<br>1699 (vs) | 1737 (s, sh)<br>1723 (vs)<br>1714 (s, sh) | 1731 (s)<br>1696 (s) | C=O stretching |
| 1653 (vw)<br>1635 (vw) | 1653 (vw)<br>1635 (vw) | 1653 (vw)<br>1634 (vw) | δ(HOH) co-intercalated<br>d(HOH) adsorbed |
| 1457 (vw)<br>1411 (vw, sh)<br>1384 (m)<br>1350 (vw)<br>1302 (vw)<br>1272 (w)<br>1206 (m) | 1458 (vw)<br>1437 (w)<br>1384 (m)<br>1352 (vw)<br>1271 (w)<br>1211 (w) | 1460 (vw)<br>1384 (m)<br>1352 (vw)<br>1282 (w)<br>1220 (w, br) | C–H deformationbands & C–C–O stretching |
| 1125 (vs)<br>1079 (vs) | 1166 (m)<br>1122 (s) | 1114 (s)<br>1087 (s) | Si–O & O–C–C stretching |
| 1055 (vs)<br>1031 (vs) | 1054 (vs)<br>1033 (vs) | 1033 (vs)<br>1011 (vs) | Si–O–Si stretching |
| 913 (vs) | 913 (vs) | 913 (vs) | O–H bending (inner) |
| 801 (w)<br>745 (w)<br>679 (m)<br>431 (s) | 802 (w)<br>749 (w)<br>681 (m)<br>431 (s) | 788 (w)<br>753 (w)<br>694 (m)<br>432 (s) | Si–O |
| 538 (s) | 541 (s) | 541 (s) | Al–O–Si deformation |
| 472 (s) | 473 (vs) | 471 (s) | Si–O–Si deformation |

**Note:** The absorptions are w, weak; m, medium; s, strong; vw, very weak; vs, very strong; sh, shoulder; and br, broad.

### 4.4.5 C–H deformation bands (1500–1200 $cm^{-1}$)

A number of bands, indicative of various CH deformations originating from the oxyethylene species or in some instances from the methylene spacers of the ester moieties, can be observed in the FTIR spectra of these intercalated nanocomposites. Kao–DMSO shows deformation bands at 1428, 1410, 1394, and 1319 $cm^{-1}$ (see Fig. 4.7), which have been previously assigned (70). For Kao–PEA, Kao–PES, and Kao–PBA nanocomposites, the C–H deformation bands are in the range of 1460–1350 $cm^{-1}$. The broad ill-defined band(s) centered around 1460 $cm^{-1}$ can be attributed to $CH_2$ bending modes (scissoring) of the oxyethylene moiety. Other bands in this region cannot be attributed to residual DMSO, since these samples were shown to have no residual interlayer DMSO (see NMR section). Also, IR bands, indicating the presence of DMSO, at 3022 $cm^{-1}$ (Fig. 4.4) have completely disappeared.

Similar to previous observations (see Chapter 3), the presence of a band at 1384 $cm^{-1}$ for the produced nanocomposites is an indication that the oxyethylene moieties of the intercalated polymer chain adopt a gauche conformation, which is expected on the basis of the $d_{001}$ values of the intercalated nanocomposites. This is also supported by the lack of a band near 1325 $cm^{-1}$. In fact, the lack of the latter band for PEO–$M^{n+}$ montmorillonite has been used as evidence supporting the hypothesis that the O–$CH_2$–$CH_2$–O groups of the interlayer PEO chains are all in the gauche conformation (155), while the presence of a band at ~1318 for the Kao–PEG nanocomposites

suggested that at least a portion of the oxyethylene units are in the trans conformation (18). For Kao–EG 9.4 Å, the presence of a band at 1325 $cm^{-1}$ was also used to support the hypothesis that the ethylene glycol moiety was in the trans conformation, with one end of the EG grafted on the aluminol sheet, and the hydroxy group at the other end was keyed into the siloxane macro-rings of the silicate sheet (16). Again, that assumption was supported by the relatively smaller *d*-spacing in case of the Kao–EG.

Finally, the bands around 1280 and 1270 $cm^{-1}$ could be attributed to the $CH_2$ twisting vibrations of the oxyethylene units. Similar bands were found, for example, at 1268 and 1248 $cm^{-1}$ for Kao–PEG nanocomposites and at 1274 and 1248 $cm^{-1}$ for PEO–$Na^+$ montmorillonite (18, 155).

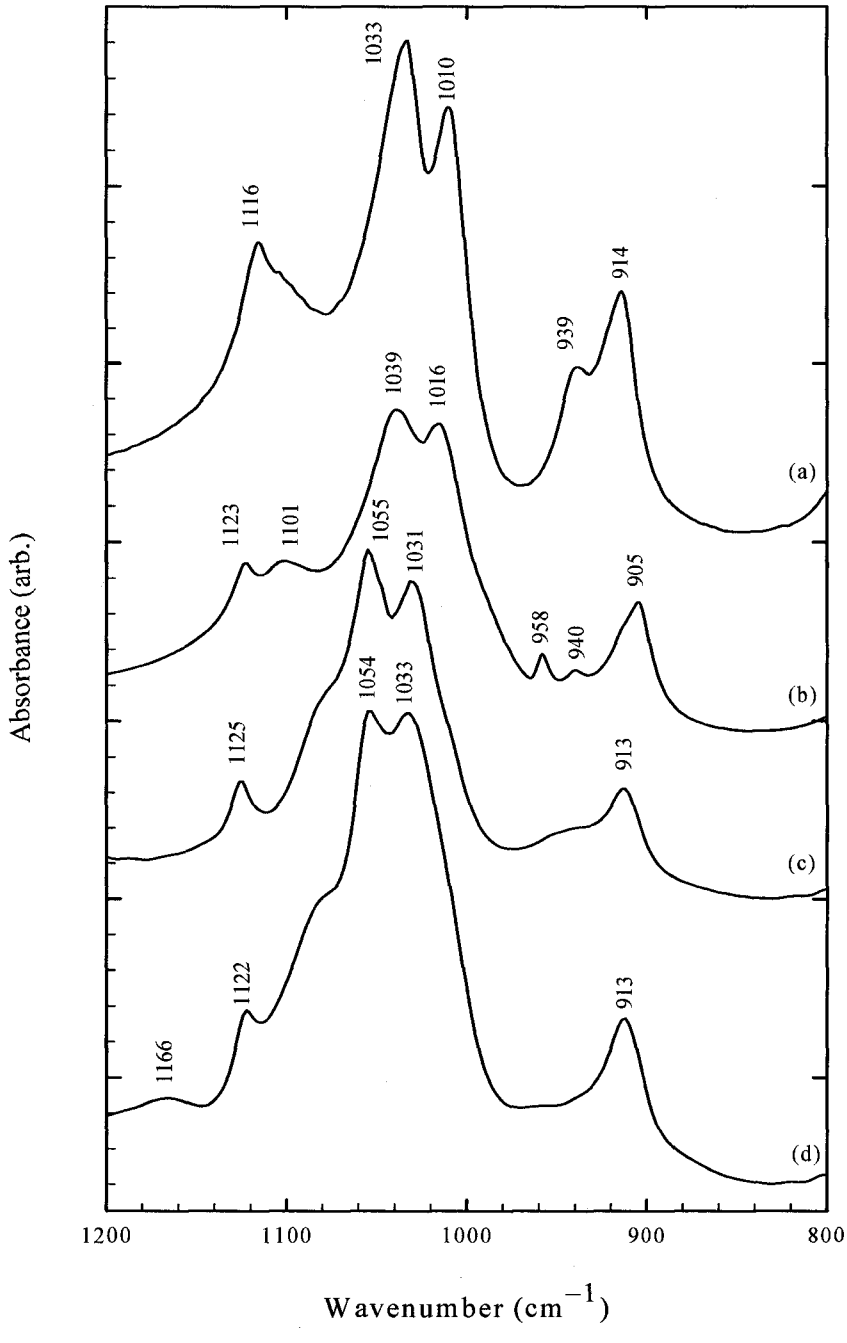


**Fig. 4.7.** FTIR spectra (1200–800 cm$^{-1}$) of (a) kaolinite, (b) Kao–DMSO, (c) Kao–PEA, and (d) Kao–PES.

### 4.4.6 The kaolinite-lattice vibrations and Al–O–H bending region (1200–800 $cm^{-1}$)

The bands at this region provide information regarding any perturbations to the kaolinite lattice vibrations (1150–1000 $cm^{-1}$) and any changes in the Al–O–H bending modes of kaolinite (900–980 $cm^{-1}$). Figure 4.7 shows the the FTIR patterns (1200–800 $cm^{-1}$) for kaolinite, Kao–DMSO, Kao–PEA, and Kao–PES, respectively. The patterns of Kao–PEA and Kao–PES show strong perturbation of the kaolinite lattice vibrations. The two most-intense vibrations of kaolinite at 1033 and 1010 $cm^{-1}$ are both shifted to higher frequencies (see Table 4.4). Slightly shifted upon intercalation, these bands have been previously assigned to the in-plane Si–O–Si stretching vibrations of kaolinite (59). For the Kao–DMSO, the bands are shifted to 1039 and 1016 $cm^{-1}$ (Fig. 4.7b). The fact that these bands are shifted to yet greater frequencies, compared with those previously reported for other Kao–polymer intercalates, such as Kao–PEG (18), or even compared with the Kao–DMSO starting material, indicates a greater perturbation of the silicate surface by the polymer chains. The perpendicular Si–O vibrations, found in kaolinite at 1102 and 1116 $cm^{-1}$ (59) (Fig. 4.7a), are also more perturbed for the Kao–PEA and for the Kao–PES compared with the pristine kaolinite and the starting material.

The kaolinite band at 939 $cm^{-1}$ has been assigned to the in-plane bending vibrations of the inner-surface (outer, accessible) hydroxyl groups, whereas the band at 914 $cm^{-1}$ has been assigned to the bending vibrations of the inner (internal, inaccessible) hydroxyls (59, 60). Upon intercalation of DMSO, the intensity of the band at 939 $cm^{-1}$ is greatly reduced, and another band of higher frequency appears at 958 $cm^{-1}$

(Fig. 4.7b). The band at 914 $cm^{-1}$ shows a characteristic slight shift to a lower frequency at 905 $cm^{-1}$, presumably because of the repulsive interaction between one methyl groups of the DMSO molecule, which is proposed to be keyed into the $(SiO)_6$ macro-ring of the silicate surface and the internal hydroxyls of kaolinite (72, 73, 75). For Kao–PEA and Kao–PES, the inner hydroxyl band of kaolinite is almost unaffected, and this is plausibly due to the inability of the polymeric chains to key in the $(SiO)_6$ macro-rings of the silicate surface. Similar results were observed in case of Kao–PEG and most other kaolinite intercalates (16, 18).

Upon intercalation of the polymers ( Fig. 4.7c and 4.7d), the kaolinite band at 939 $cm^{-1}$ almost disappeared, as well as the new Kao–DMSO starting material band at 958 $cm^{-1}$. This result, along with all the previously mentioned observations, is in agreement with the complete displacement of the DMSO molecules in the interlamellar space by the polymeric chains, and the formation of H-bonds between the polymers and the inner-surface hydroxyls. A complete list of all the observed vibrations is given in Tables 4.3 and 4.4.

## 4.5 Solid-state $^{13}C$ NMR analysis

### 4.5.1 $^{13}C$ NMR analysis

$^{13}C$ NMR analysis is a useful tool to identify and study the nature of the intercalated molecules. Information on the dynamics of the intercalated organic molecules could also be obtained using dipolar dephasing experiments. A series of $^{13}C$ cross polarization (CP)/MAS and dipolar dephasing (DD)/MAS experiments was performed on the produced Kao–polymer nanocomposites to obtain information regarding the interlayer structure and dynamics of the intercalated molecules.

Table 4.5 shows a list of the observed $^{13}C$ chemical-shift and linewidths (FWHM, $\nu_{1/2}$) values of the starting materials (crude polymers) and most of the produced nanocomposites. Assignments of the peaks are also shown in Table 4.5. The spectra of the crude polymers were in excellent agreement with the expected and the reported values (see Figs. 4.8, 4.10, and 4.11) (156–161).

The $^{13}C$ NMR spectra of the produced Kao–PEA1 and Kao–PEA4 are shown in Fig. 4.8b and 4.8c, respectively. The chemical shifts at ~24.5 and 34.0 ppm are unambiguously attributed to two different methylene carbons in the adipate moiety of the polymer, while the chemical shift at 62.8 ppm is attributed to the carbons of the methylene groups of the oxyethylene moiety of the polymeric chain. Finally, the chemical shift at ~180 ppm is attributed to the carbonyl carbon. Compared with the spectrum of the crude polymer (Fig. 4.8d), the results confirm that depolymerization of the PEA did not occur in the interlamellar space of kaolinite to yield the intercalated ethylene glycol or adipate fragments, i.e., The polymer remains intact in the interlayers. It is worth mentioning that the intercalated ethylene glycol would give

rise to a 9.4 Å *d*-spacing or 10.8 Å in case of the grafted ethylene glycol (16). In case of the intercalated polymers, the broadness of the measured linewidths at half-height of the peak $\nu_{1/2}$ (see Table 4.5), compared with the crude crystalline polymer, indicate that the polymeric chains are now present in a different conformation and a different environment. Thus, this increase in linewidths can plausibly be attributed to the fact that, upon intercalation, the molecular motion of the polymer is greatly reduced, it can also be due to the loss of polymer crystallinity upon intercalation.

In case of Kao–PEA1, the spectrum shows the presence of amounts of residual interlayer DMSO, as evidenced by a resonance at ~41.0 ppm. Only one $^{13}C$ methyl resonance could be found for DMSO, whereas for the pure Kao–DMSO intercalate, the spectrum measured on the same instrument shows two resonances at 43.1 and 44.1 ppm. This indicates that the co-intercalated DMSO molecules no longer adopt the preferred orientation, in which the two methylene groups are inequivalent, and the residual molecules are now entangled in the intercalated polymeric chains, i.e, the DMSO molecules are now in a different local environment.

The first "green" Kao–polymer nanocomposite (Kao–PEA4), obtained through melt intercalation, with complete displacement of the guest DMSO molecules of the starting material, was finally obtained by increasing the reaction temperature and extending the reaction time (Table 4.5 and Fig. 4.8c). No DMSO chemical shifts were observed in the spectrum of Kao–PEA4, thus indicating that only PEA polymeric chains were present in the interlamellar space.

**Table 4.5.** Observed $^{13}C$ NMR chemical shifts (δ), peakwidth at half height ($\nu_{1/2}$), and their assignments for the produced nanocomposites, using Kao–DMSO as a starting material.

| Crude PEA | | Kao–PEA1 | | Kao–PEA4 | | Crude PES | | Kao–PES1[a] | | Kao–PES1[b] | | Crude PBA | | Kao–PBA2 | | |
|---|---|---|---|---|---|---|---|---|---|---|---|---|---|---|---|---|
| δ (ppm) | $\nu_{1/2}$ (Hz) | δ (ppm) | $\nu_{1/2}$ (Hz) | δ (ppm) | $\nu_{1/2}$ (Hz) | δ (ppm) | $\nu_{1/2}$ (Hz) | δ (ppm) | $\nu_{1/2}$ (Hz)[d] | δ (ppm) | $\nu_{1/2}$ (Hz) | δ (ppm) | $\nu_{1/2}$ (Hz) | δ (ppm) | $\nu_{1/2}$ (Hz) | Assignment |
| 23.8 | 80 | 24.4 | 217 | 24.6 | 530 | 28.1 | 83 | 28.1[c]<br>30.4 | 144<br>182 | 30.3 | 478 | 24.8 | 91 | 24.8 | 580 | $CH_2CH_2$ (Succinate, adipate, or butylene) |
| 33.8 | 69 | 33.8 | 269 | 34.5 | 506 | —[e] | — | — | — | — | — | 34.5 | 95 | 34.1 | 473 | $CH_2$ (Terminal methylene of the adipate moiety) |
| — | — | 40.9 | 304 | — | — | — | — | — | — | — | — | — | — | 40.4 | 459 | $CH_3$ (Residual DMSO) |
| 60.5 | 41 | 62.8 | 183 | 62.8 | 667 | 64.9 | 74 | 62.7<br>64.8[c] | 190<br>— | 62.4 | 564 | 64.2 | 44 | 64.1 | 340 | $CH_2$ (Oxyethylene methylenes or terminal methylene of the oxybutylene moiety) |
| 174.2 | 37 | 180.3 | 181 | 180.1 | 367 | 174.2 | 61.4 | 174.1[c]<br>178.4 | 100<br>222 | 178.2 | 674 | 173.7 | 33 | 181.8 | 232 | C=O |

**Note:** The spectra were obtained on a Bruker AVANCE-500 instrument, operating at 125.77 MHz. Crude-polymers measurements were performed at a low spinning speed of 3–5 kHz to avoid generating heat that could melt the polymers

[a]Before washing with excess solvent.

[b]After washing with excess solvent.

[c]Peaks that are attributed to the excess non-intercalated polymer in the sample.

[d]Inaccurate measurements because of peak overlap.

[e]—: Non-applicable or not detected.

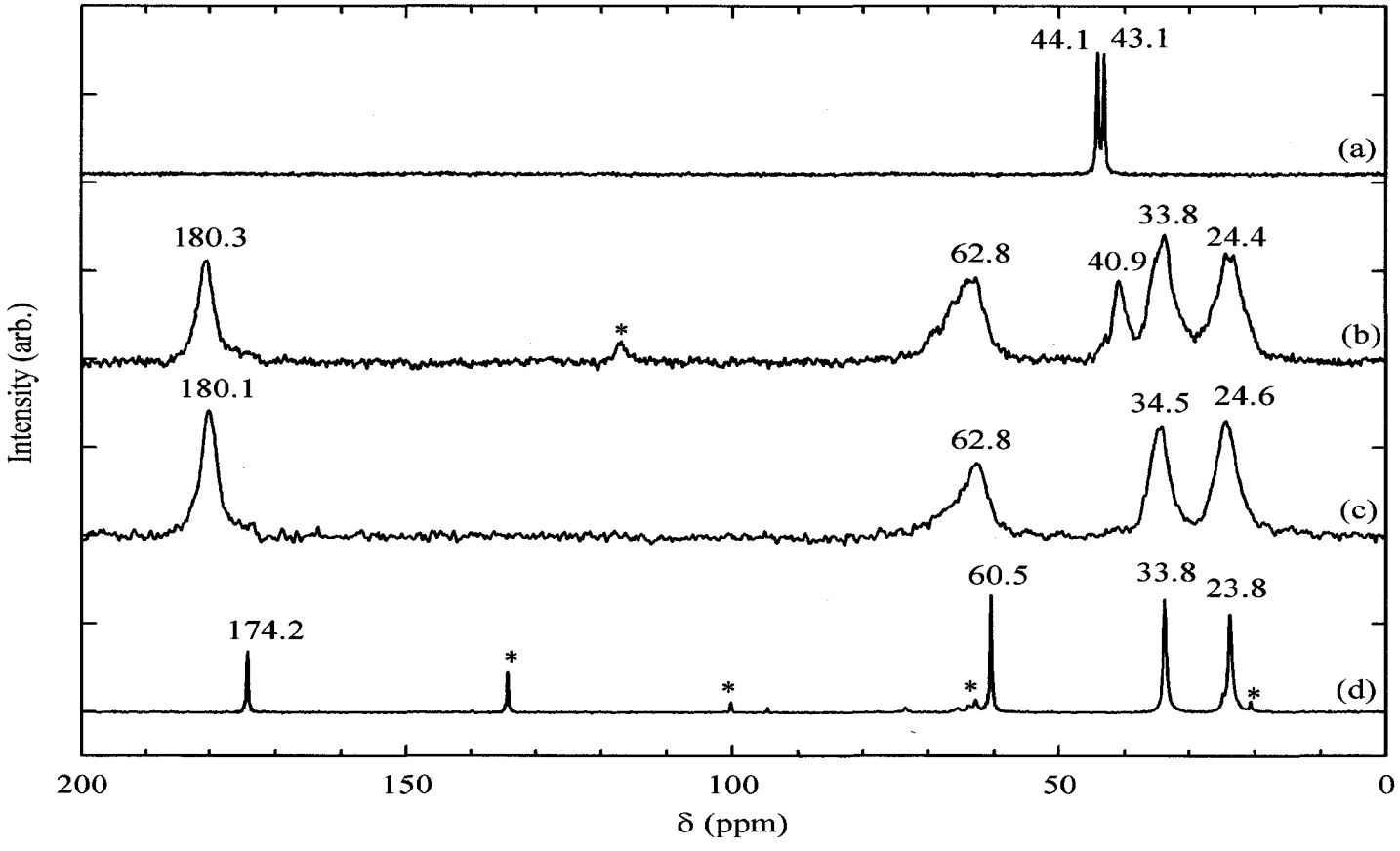


**Fig. 4.8.** Solid-state $^{13}C$ CP/MAS NMR spectra (125.77 MHz) of (a) Kao–DMSO, (b) Kao–PEA1, (c) Kao–PEA4, and (d) crude poly(ethylene adipate) (Aldrich). Spinning sidebands are marked with asterisks.

When Kao–KOAc was used as a starting material, only a co-intercalated nanocomposite was obtained, though it can also be considered "green", even with enhanced reaction conditions, as evident from the presence of the potassium acetate signals in the Kao–PEA6 spectrum (Fig. 4.9). Compared with both the bulk polymer and the Kao–KOAc starting material, new signals appeared in the spectrum of the other samples (see Fig. 4.9b and 4.9c), suggesting the fragmentation of the polymer and the transesterification reaction between the polyester fragments (oxyethylene moieties) and the acetate molecules. This assumption is supported by the reduction of the intensity of the signal around 65 ppm, which almost disappeared (Fig. 4.9). This signal is usually attributed to the methylenes of the oxyethylene moiety of the polymer. Moreover, the intensity of the polymer signal at ~34 ppm, attributed to the terminal methylene carbons of the adipate moiety, was greatly reduced, and a new signal appeared at ~28 ppm as well as an upfield strong signal appeared at ~40.0 ppm, which can be attributed to the methyl carbon of the transesterification product. Also, an additional carbonyl signal can be observed in the $^{13}C$ NMR spectrum obtained at 125.77 MHz.

In this study, other "green", intercalated nanocomposites, Kao–PES, gave resonances at about 30.5, 62.5, and 178 ppm (Fig. 4.10 and Table 4.5). These chemical shifts are attributed to the carbons of the succinate moiety, oxyethylene methylenes, and carbonyl groups, respectively. Similar to the case of Kao–PEA nanocomposites, the produced Kao–PES nanocomposites showed broader linewidths (FWHM), compared with the linewidths of the spectrum of the bulk polymer, but the signals were roughly at the same chemical shifts, confirming that the intercalated polymeric chains suffered no depolymerization or fragmentation. Figure 4.10c shows the spectrum of the Kao–PES

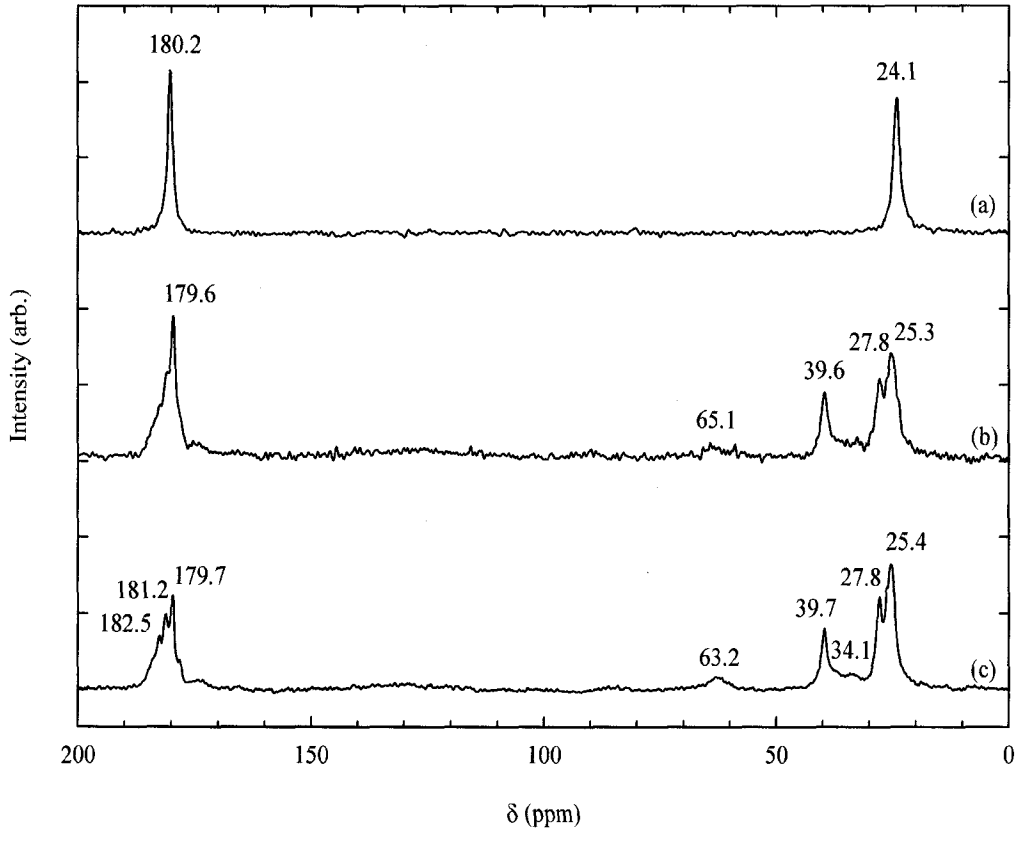


**Fig. 4.9.** Solid-state $^{13}C$ CP/MAS NMR spectra of (a) Kao–KOAc (50.31 MHz), (b) Kao–PEA6 (50.31 MHz) , and (c) Kao–PEA6 (125.77 MHz).

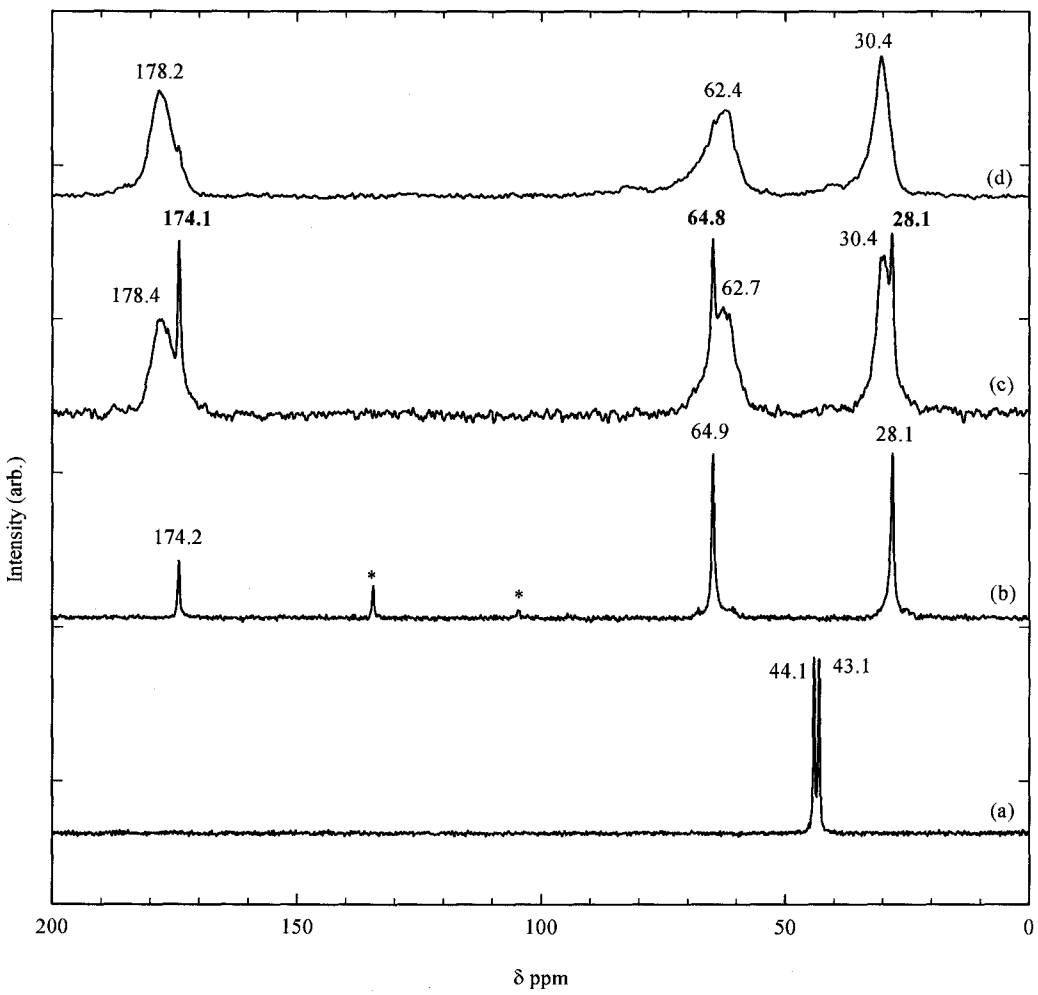


**Fig. 4.10.** Solid-state $^{13}C$ CP/MAS NMR spectra (125.77 MHz) of (a) Kao–DMSO, (b) crude poly(ethylene succinate) (Aldrich), (c) Kao–PES1, (d) Kao–PES1 after excessive washing with solvents to remove the excess polymer. Spinning sidebands are marked with asterisks.

nanocomposite that contained traces of excess non-intercalated polymer. In addition to the relatively broad intercalated-polymer lines, three other sharp signals are present in the spectrum at 28.1, 64.8, and 174.1 ppm. These chemical shifts are identical to those recorded for the crude polymer in Fig. 4.10b. Washing and centrifugation of the sample with excess solvents (toluene and chloroform), dissolved the excess polymer, and the $^{13}C$ NMR spectrum for the washed sample was recorded (Fig. 4.10d). Crude polymer peaks disappeared from the spectrum of the washed sample, *confirming that the broad signals can only be attributed to the intercalated polymer chains in the interlamellar space that are in different conformation compared with the bulk crystalline material.* The appearance of the excess-polymer peaks in the spectrum of the Kao–PEA (Fig. 4.10c) at exactly the same chemical shifts, compared with the spectrum of the pristine polymer (Fig. 4.10b), indicates that exposing the polymer to the elevated temperatures of the reaction for extended periods did not cause any deterioration or fragmentation of the polymeric chains. Notably, no residual DMSO signals were observed at all in the spectra of these so-called "green" Kao–PES nanocomposites.

The third attempt to intercalate a biodegradable polyester in kaolinite involved the reaction of PBA with Kao–DMSO. Figure 4.11 shows the $^{13}C$ NMR spectra of the crude polymer, Kao–DMSO (intermediate), and the products of two different attempts to displace DMSO molecules by the polymeric chains. In the first attempt (Fig. 4.11b), one can observe two DMSO signals at ~41 and 43 ppm, indicating the presence of co-intercalated DMSO; however, both signals are shifted, compared with those of the starting material. Optimizing the reaction conditions in the second attempt reduced the amount of the co-intercalated DMSO, as evident by the great reduction in the intensities

of the DMSO signals (see Fig. 4.11c). Other signals in the spectra of the intercalated Kao–PBA nanocomposites confirm the intercalation of PBA chains in kaolinite (see Table 4.5 for peak assignments).

In general, the increase in linewidth values of all polymer signals upon intercalation, compared with the signals of the bulk polymers, can be attributed to the loss of polymer crystallinity. The intercalated polymeric chains are now in different local environments, and XRD results indicated the intercalation of a single polymeric chain parallel to the interlamellar surfaces.

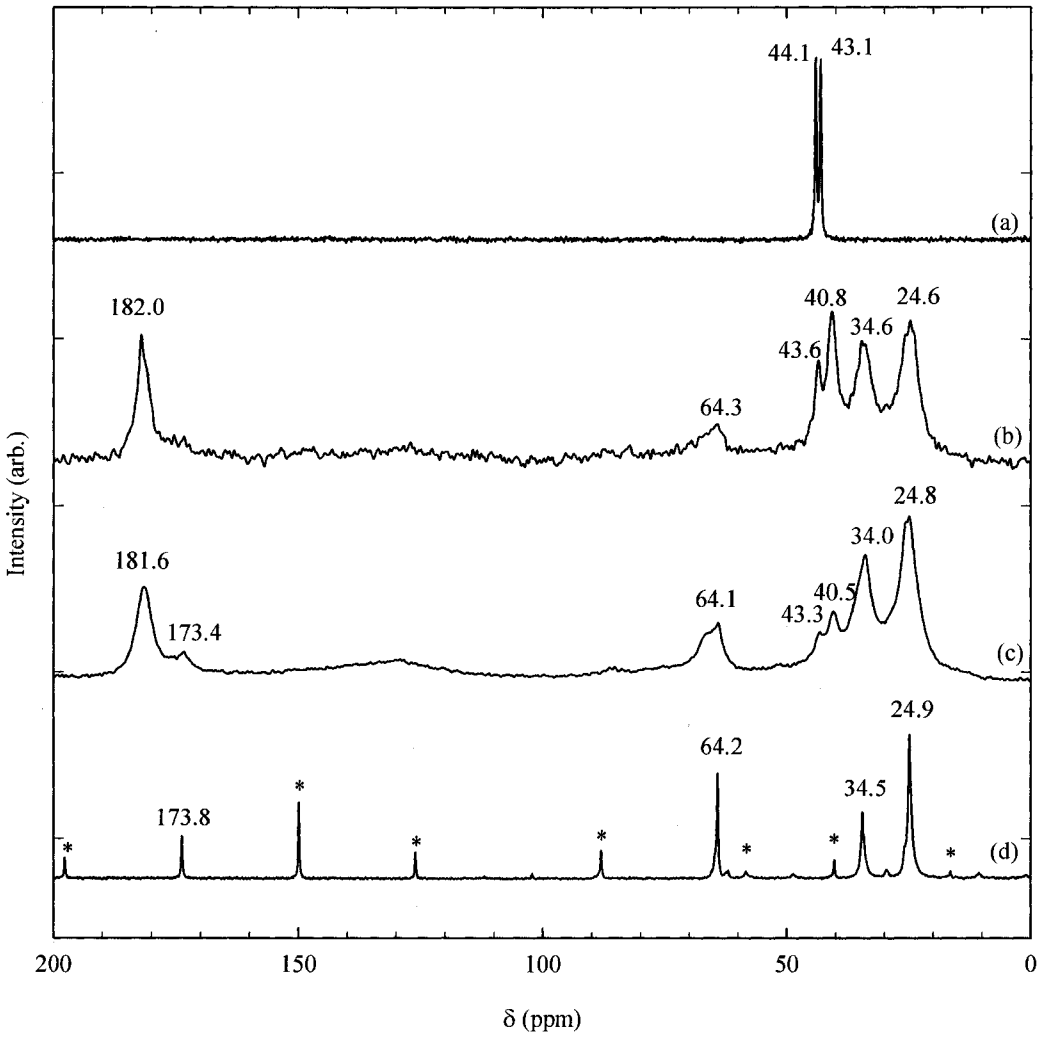


**Fig. 4.11.** Solid-state $^{13}C$ CP/MAS NMR spectra (125.77 MHz) of (a) Kao–DMSO, (b) Kao–PBA1, (c) Kao-PBA2 with enhanced reaction conditions, and (d) crude poly(butylene adipate) (Aldrich). Spinning sidebands are marked with asterisks.

### 4.5.2 Dipolar dephasing experiments

A series of dipolar dephasing (DD)/MAS experiments were performed on the Kao–polyester samples.

As previously mentioned, dipolar dephasing is a technique that can be used to differentiate between different types of carbons in the $^{13}C$ NMR spectrum. $I_{DD}/I_o$ is the ratio of the intensities of the $^{13}C$ resonances obtained with ($I_{DD}$) and without ($I_o$) dipolar dephasing, and this ratio is used to discriminate between carbons that are strongly bound to protons, e.g., methine and methyl carbons, for which the overall signal decay has been described by equation [2.1], and other types of carbons, i.e., weakly bound to protons, carbonyls, and methyl groups (126–128).

The DD/MAS results for Kao–PEA1, Kao–PEA4, and Kao–PES are illustrated in Figs. 4.12, 4.13, and 4.14, respectively. Additional data are also reported in Table 4.6. Thus, in a series of experiments, the dipolar dephasing time ($\tau$) was varied from 0 to 50 μs for these samples, and the variation in intensity was monitored (Figs. 4.12–4.14). This qualitatively showed that the polymer chains are constrained in the interlamellar spaces of kaolinite. After 40 μs dephasing time, almost no signal for the methylene carbons of the polymers could be detected ($I_{DD}/I_o$ = 0–0.10). The intensity of the carbonyl signal remained almost unaffected in all cases, even after 40–50 μs dephasing time (see Table 4.6). Clearly, the attribution of the signal at ~41 ppm in the spectrum of Kao–PEA1 sample to $CH_3$ of the residual DMSO molecules is confirmed by the fact that its intensity was not affected in the dipolar dephasing experiments (Fig. 4.12). Whereas, for Kao–PEA4 sample, all signals disappered, except for the carbonyl resonance, after a dipolar dephasing delay of 30 μs, thus confirming the absence of any residual co-

intercalated DMSO molecules (Fig. 4.13) in this "green" nanocomposite. Similar result were obtained for the Kao–PES sample (Fig. 4.14).

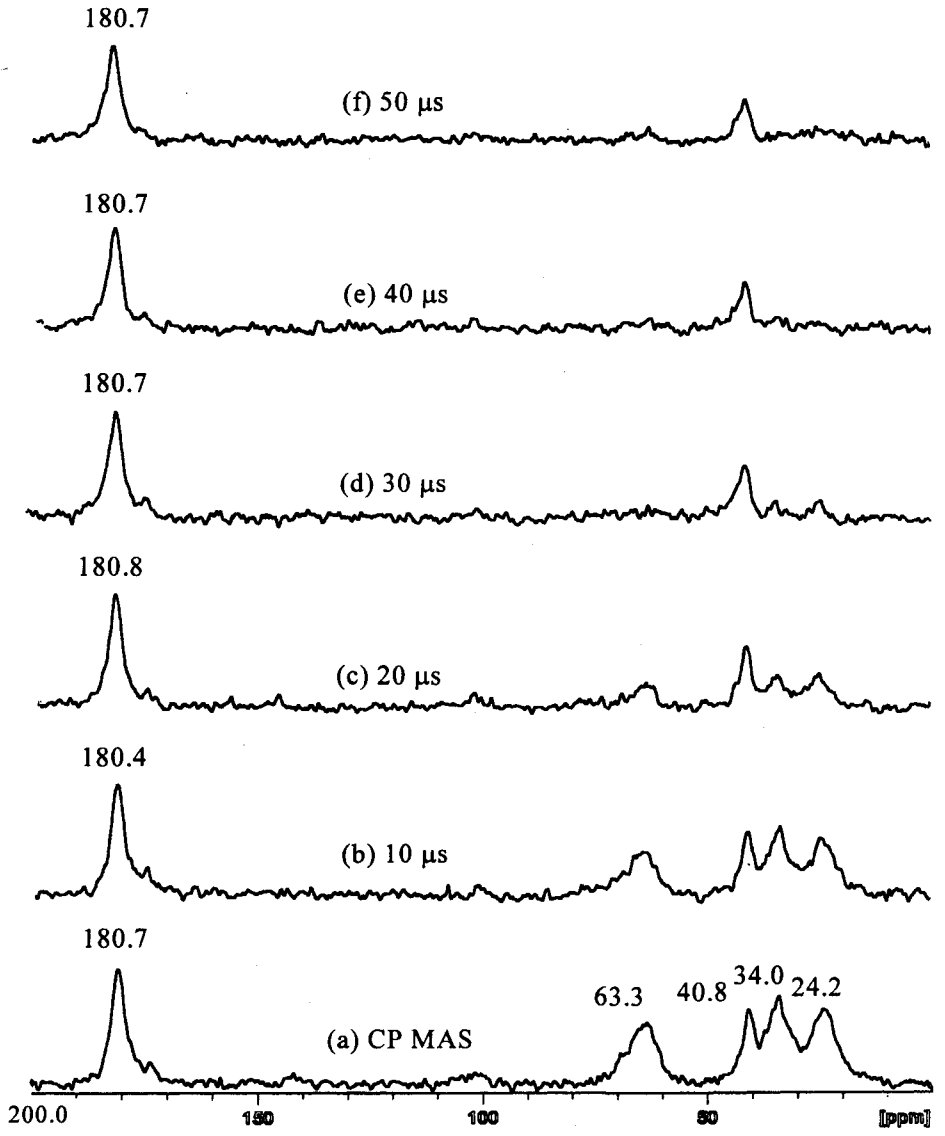


**Fig. 4.12.** Solid-state $^{13}C$ NMR spectra (50.31 MHz) of Kao–PEA1 (residual DMSO peak at 40.8 ppm): (a) CP/MAS; (b–f) dipolar dephasing, $\tau$= 10, 20, 30, 40, and 50 μs, respectively.

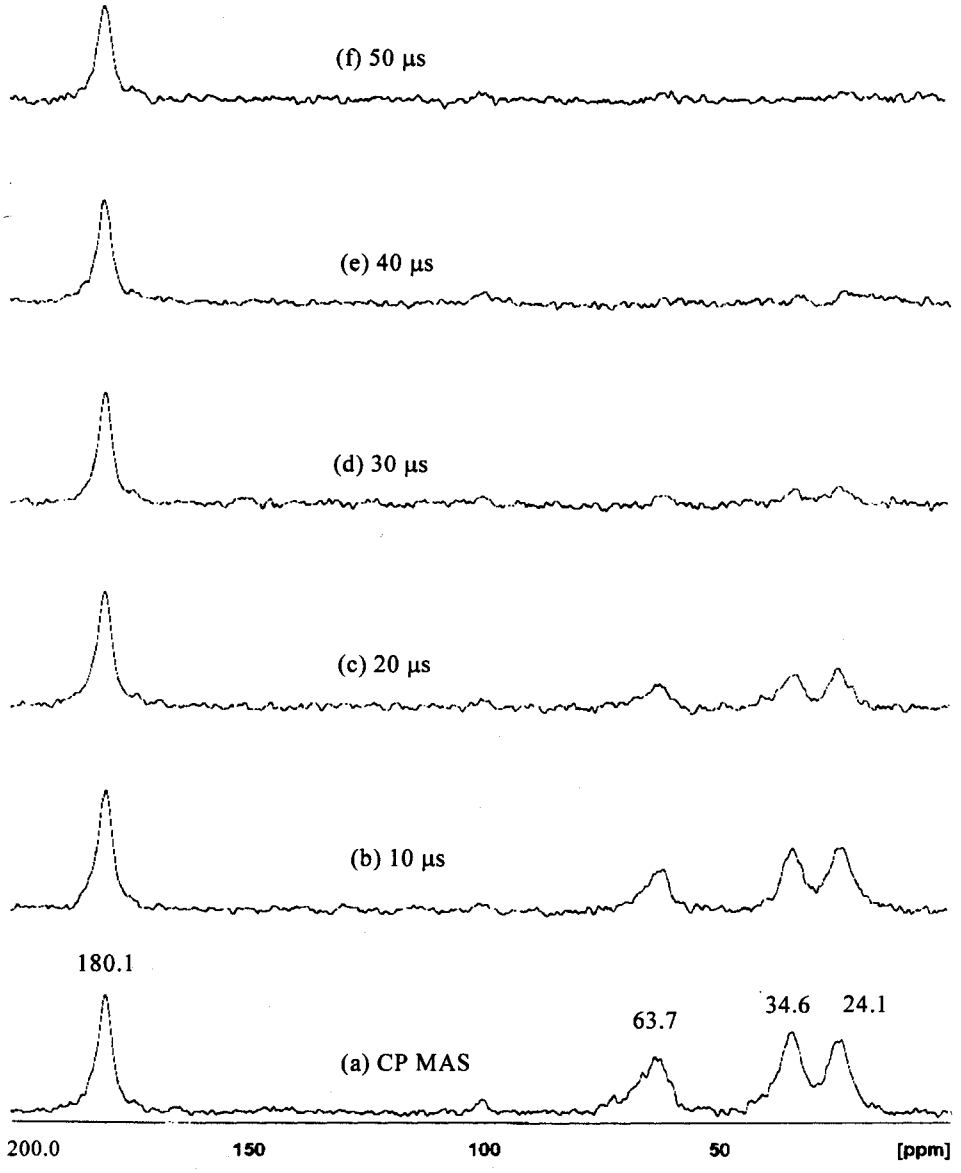


**Fig. 4.13.** Solid-state $^{13}C$ NMR spectra (50.32 MHz) of Kao–PEA4 (no residual DMSO): (a) CP/MAS; (b–f) dipolar dephasing, $\tau = 10$, 20, 30, 40, and 50 μs, respectively.

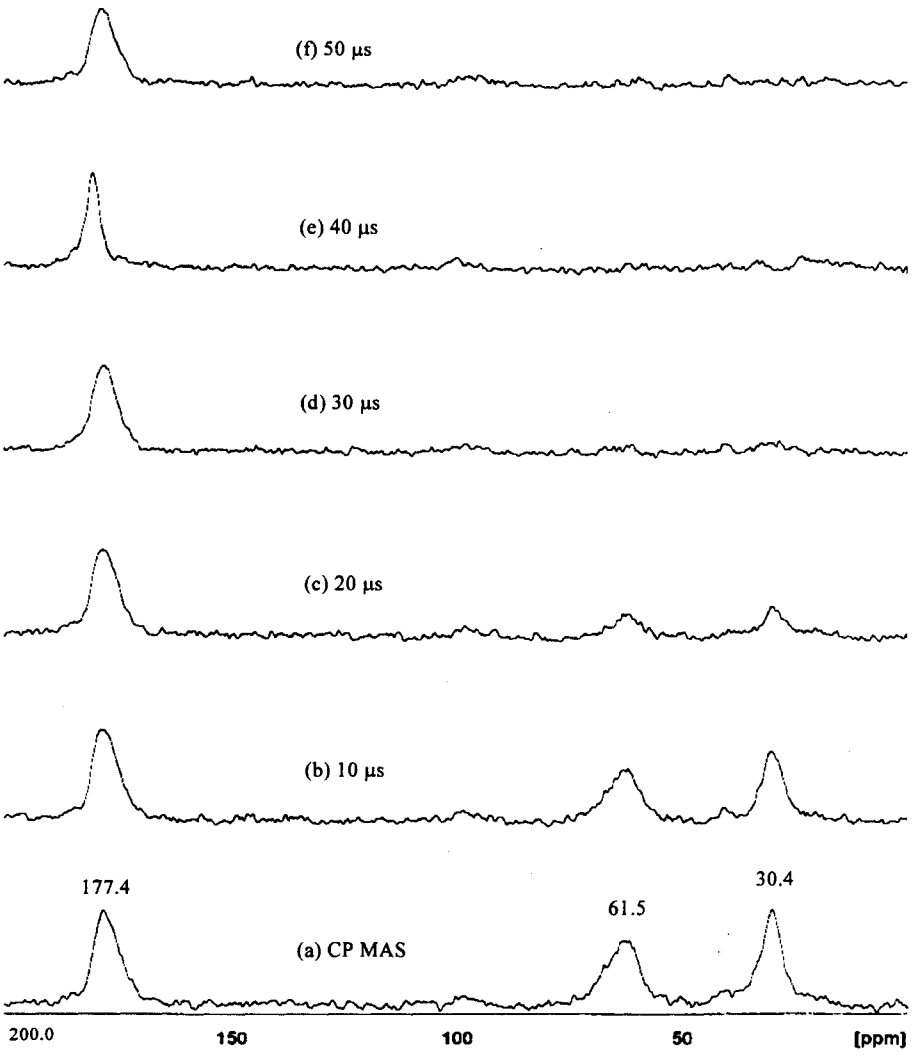


**Fig. 4.14.** Solid-state $^{13}C$ NMR spectra (50.32 MHz) of Kao–PES: (a) CP/MAS; (b–f) dipolar dephasing, $\tau$= 10, 20, 30, 40, and 50 μs, respectively.

**Table 4.6.** Summary of the $^{13}C$ CP/MAS and DD/MAS results for some of the produced nanocomposites.

| Nanocomposite | Chemical shift (δ ppm)[a] | $I_{DD}/I_o$[b] | $\nu_{1/2}$ (CP/MAS) (Hz) | $\nu_{1/2}$ (DD/MAS)[e] (Hz) |
|---|---|---|---|---|
| Kao–PEA1 | 24.2 | —[d] | 147 | — |
| | 34 | — | 234 | — |
| | 40.8[c] | 1.3 | 172 | 145 |
| | 63.3 | — | 171 | — |
| | 180.7 | 1.8 | 177 | 181 |
| Kao–PEA4 | 24.1 | — | 134 | — |
| | 34.6 | — | 267 | — |
| | 63.7 | — | 126 | — |
| | 180.1 | 0.88 | 176 | 172 |
| Kao–PES1[f] | 30.4 | — | 248 | — |
| | 61.5 | — | 150 | — |
| | 177.4 | 0.89 | 281 | 312 |

**Note:** The spectra were obtained on a Bruker ASX-200 instrument, operating at 50.31 MHz.
[a]For carbon types (assignments), see Table 5.
[b]$I_{DD}$ is the peak intensity obtained with $\tau = 40$ μs, and $I_o$ is the peak intensity obtained with the CP/MAS experiment, using the same number of scans.
[c]Residual DMSO.
[d]—: Residual or no signal for the peak in the DD/MAS spectrum.
[e]For $\tau = 40$ μs.
[f]Excess polymer was completely washed.

Similar to previous chapters, the results for Kao–PES sample are plotted in Fig. 4.15, as the ratio for each type of methylene carbons vs. the dipolar dephasing time. To test the validity of equation [2.1], the same data were plotted in Fig. 4.16 as $\ln(I_{DD}/I_o)$ vs. $\tau^2$. The result should be a straight line with a slope = $-1/(2T_2^2)$. For the methylene carbon signal at ~30 ppm, the graph was linear; the points were fitted to a first-order equation by a non-linear least-squares approach, using the "Solver" option of Microsoft® Excel (statistical linear regression factor $R^2$ of 0.996) with a $T_2$ value of ~14.0 μs for $\tau$ values up to 30 μs. For higher values of $\tau$ (40 and 50 μs), there were no residual dipolar dephased peaks detected. Similarly, for the signal at ~62 ppm, the graph was linear and the points were fitted to a first-order equation by a non-linear least-squares approach, resulting in a statistical linear regression factor $R^2$ of 0.95 with a $T_2$ value of ~17.0 μs for $\tau$ values up to 40 μs. Ignoring the intensity ratio at $\tau$ value of 40 μs, the statistical linear regression factor $R^2$ would be improved to be equal to 0.997 with a $T_2$ value of ~14.5 μs. This breakdown in the linearity at higher values of $\tau$ is again due to the difficulty in obtaining accurate intensity ratio measurement for the residual peaks.

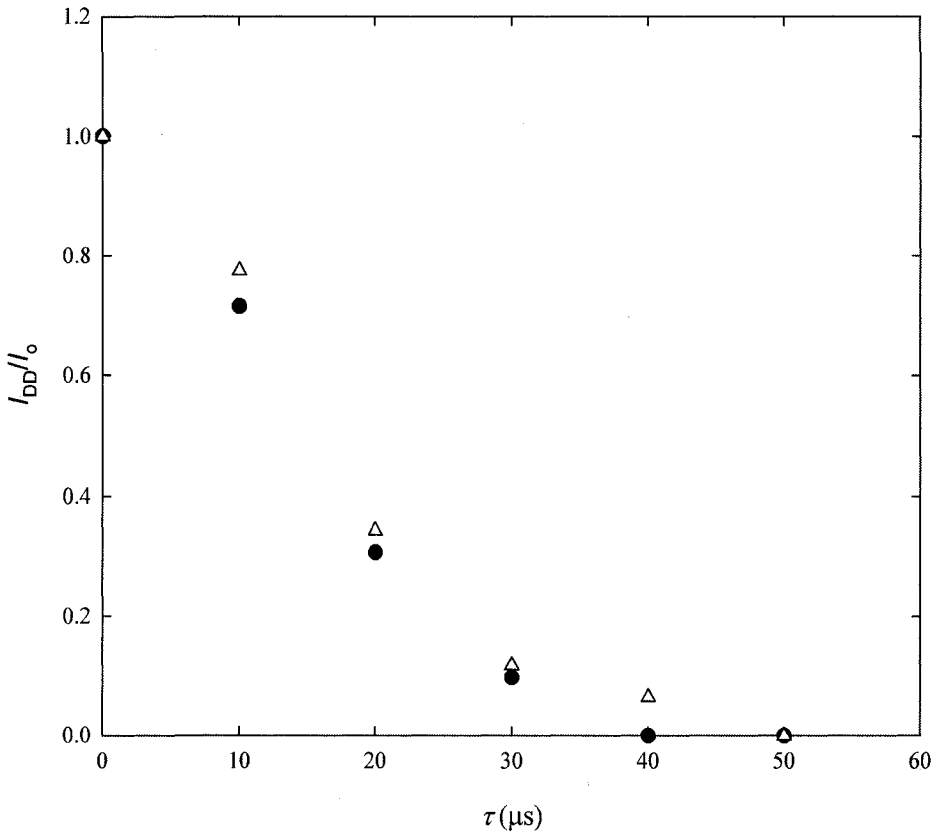


**Fig. 4.15.** Plots of $I_{DD}/I_o$ vs. dipolar dephasing time ($\tau$) for the $^{13}C$ NMR DD/MAS spectra acquired for Kao–PES; data for the 30 ppm signal: (•) and the 62 ppm signal: (Δ).

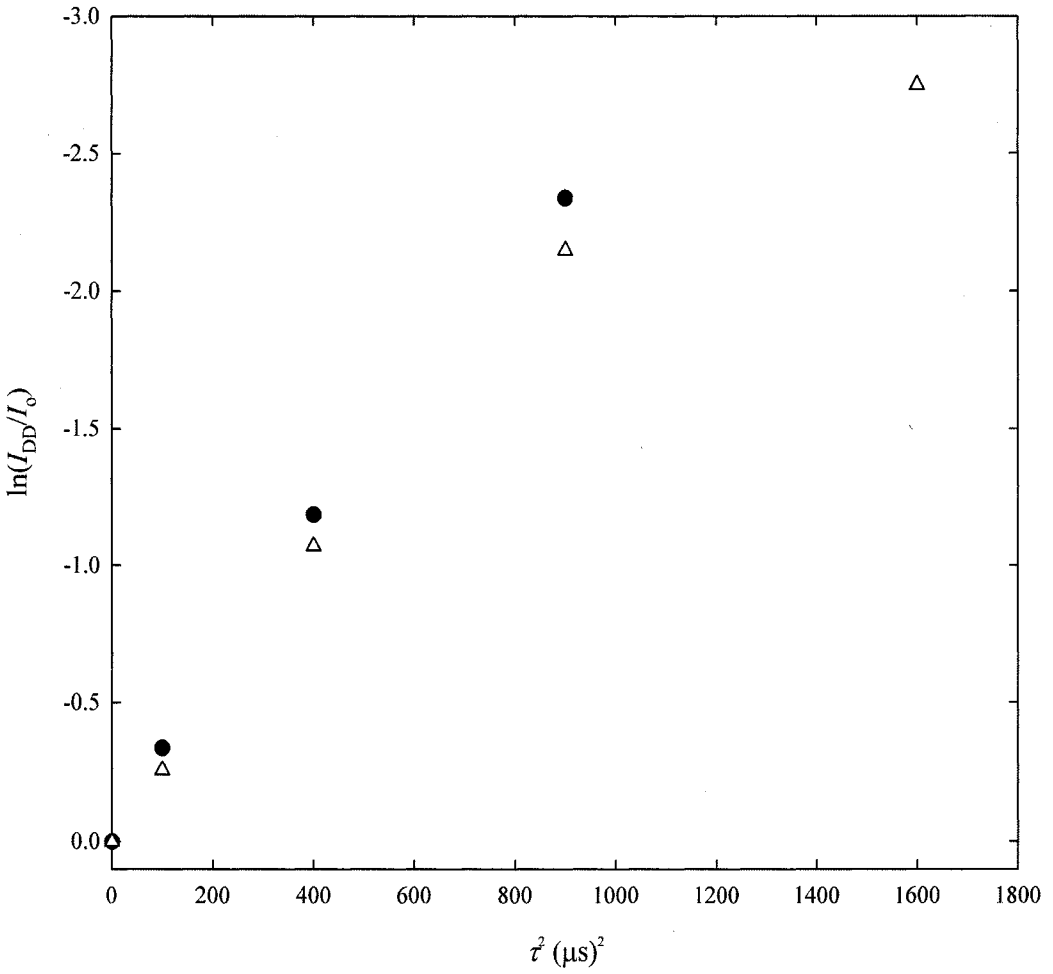


**Fig. 4.16.** Plots of $\ln(I_{DD}/I_o)$ vs. the square of the dipolar dephasing time ($\tau^2$) for the $^{13}C$ NMR DD/MAS spectra acquired for Kao–PES; data for the 30 ppm signal: (•) and the 62 ppm signal: (Δ).

## 4.6 $^{29}$Si NMR measurements

As mentioned before, the difference in chemical shift, causing the splitting of the kaolinite signal, is attributed to the existence of two different, but equally populated, silicon sites or environments. However, the small shift difference between the signals (<0.5 ppm) indicated only a slight difference between the two sites. It was concluded that interlayer hydrogen bonding, causing two different silicon environments, is the main reason for signal splitting in kaolinite (74, 129–132).

In this chapter, several $^{29}$Si MAS measurements were obtained for the starting materials and the produced nanocomposites on a Bruker AVANCE-500 instrument, operating at 99.35 MHz. The recorded chemical shifts, referenced to tetramethyl silane (TMS) at 0.0 ppm, are listed in Table 4.7, and the spectra are stacked in Fig. 4.17.

The recorded $^{29}$Si NMR results for the pristine kaolinite and for Kao–DMSO intercalate were in agreement with literature values. Concerning the produced nanocomposites, the spectra of the Kao–PEA samples generally showed a broad signal centered at about –92.9 ppm with two very weak (shoulders) at ~ –91.5 and – 90.9 ppm. These downfield shoulders can be attributed to the residual (non-intercalated) kaolinite.

For Kao–PES samples, one strong signal, with two maxima (splitting) at ~ –92.8 and – 92.6 ppm, was observed. This indicates a higher degree of H-bonding symmetry for this intercalate, thus supporting the assumption that interlayer hydrogen bonding that caused different silicon environments, was the main reason for signal splitting in kaolinite.

Finally, for Kao–PBA, the intensities of the observed signals for the residual kaolinite were greater than that of the intercalate resonance, plausibly because of the low intercalation ratio.

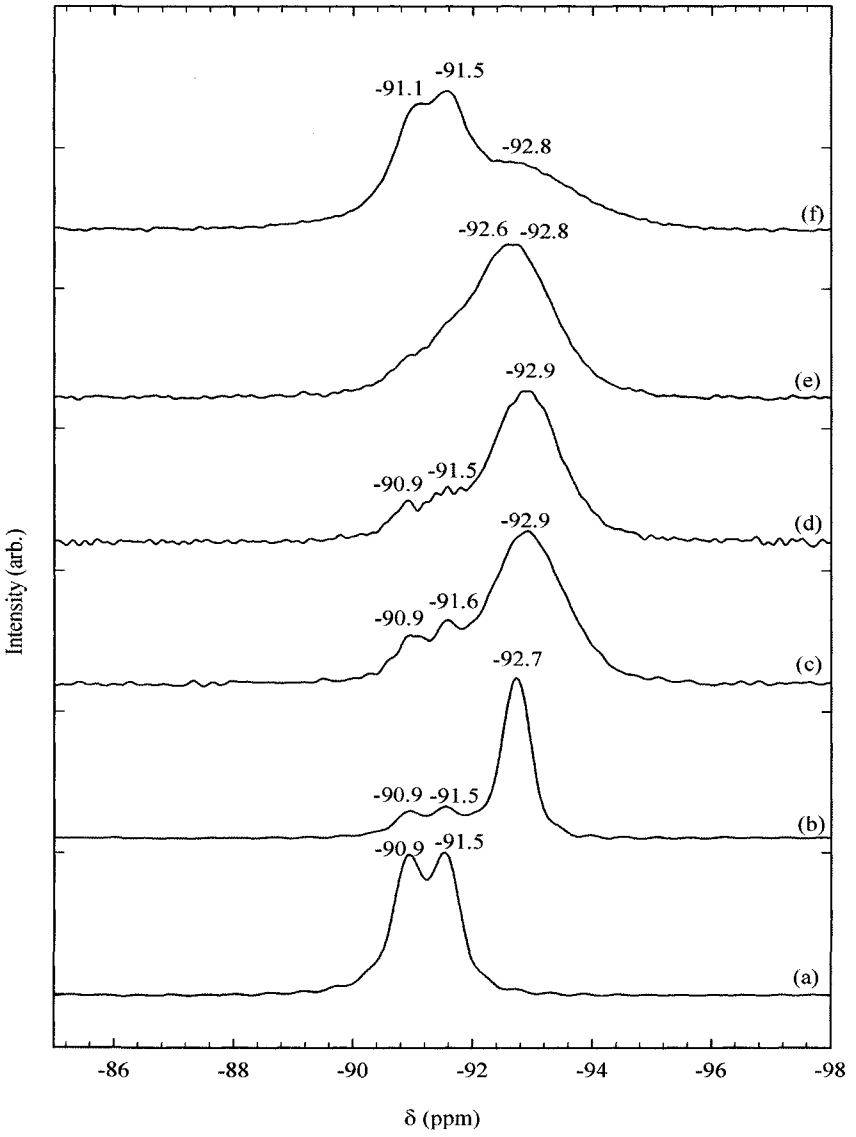


**Fig. 4.17.** $^{29}Si$ MAS NMR spectra (99.35 MHz) of (a) kaolinite, (b) Kao–DMSO, (c) Kao–PEA1, (d) Kao–PEA4, (e) Kao–PES, and (f) Kao–PBA.

**Table 4.7.** Summary of the $^{29}Si$ MAS signals for the starting materials and some of the produced nanocomposites.

| Sample | Chemical shift (δ ppm) |
|---|---|
| KGa-1b | One strong signal with two resolved maxima at –90.9 and –91.5. |
| Kao–DMSO | –90.9 (w)<br>–91.5 (w)<br>–92.7 (vs) |
| Kao–PEA1 | –90.9 (vw)<br>–91.5 (vw)<br>–92.9 (vs) |
| Kao–PEA4 | –90.9 (w)<br>–91.5 (w)<br>–92.9 (vs) |
| Kao–PES1 | One strong signal with two maxima at –92.6 and –92.8. |
| Kao–PBA | –91.1 (s)<br>–91.5 (s)<br>–92.8 (m) |

**Note:** The spectra were obtained on a Bruker AVANCE-500 instrument, operating at 99.35 MHz with a spinning speed of 6 kHz. Signal intensities: s, strong; m, medium; w, weak; vs, very strong; vw, very weak.

## 4.7 Thermogravimetric analysis

The thermal behavior and stability of the produced nanocomposites were invistigated with simultaneous thermogravimetric and differential thermal analysis (TGA/DTA). The results were compared with the thermal behavior of the starting materials and revealed that the produced nanocomposites possessed enhanced thermal stability compared with the individual components of the nanohybrid.

As mentioned in the previous chapters, one of the main features of the DTA thermogram of kaolinite is the major ~14% weight-loss endotherm near 550 °C that is attributed to the loss of water because of the dehydroxylation of the crystal lattice, i.e., formation of the meta-kaolinite. Another feature of the DTA of the pristine kaolinite is a characteristic exotherm around 1000 °C, attributed to structural reorganization and formation of the spinel phase. Another minor exotherm could be observed at 1150 °C and up and is attributed to mullite formation. The TGA of the well ordered kaolinite might also show another <0.2 % weight loss that is usually attributed to a very small amount of adsorbed water, accompanied by a very weak endotherm in the corresponding DTA thermogram (136–138).

In this chapter, these values for the $T_{max}$ in the DTA were observed using a heating rate of 10 °C/min. However, the peak positions are usually shifted to higher temperatures using faster heating rates.

**Table 4.8.** Summary of the TGA/DTA results for the starting materials and the produced nanocomposites.

| Sample (atmosphere) | Temperature range (°C) | TGA weight loss (%) | DTA event (°C) | | Total weight loss (%) |
|---|---|---|---|---|---|
| | | | Endo | Exo | |
| **KGa-1b (air)** | RT–300 | | 61 | | 13.5 |
| | 300–600 | | 516 | | |
| | 600–1100 | | | 1000 | |
| **Kao–DMSO (air)** | RT–245 | 17.3 | 98, 195 | | 28.7 |
| | 245–1000 | 11.4 | 513 | 1000 | |
| **Kao–PEA1 (air)** | RT–100 | 0.8 | 58 | | 40 |
| | 100–438 | 26.8 | | 238, 373, 412 (sh) | |
| | 438–600 | 6.5 | 492 | | |
| | 600–1100 | 5.4 | | 1004 | |
| **Kao–PEA4 (air)** | RT–100 | 0.7 | 57 | | 36.5 |
| | 100–436 | 24.8 | | 381 | |
| | 436–600 | 6.1 | 498 (br) | | |
| | 600–1100 | 4.9 | | 999 | |
| **Kao–PES (air)** | RT–100 | 1.2 | 49 | | 40.2 |
| | 100–443 | 16.0, 9.8 | | 344, 405 | |
| | 443–600 | 6.6 | 494 (br) | | |
| | 600–1100 | 6.8 | | 997 | |
| **Kao–PBA2 (air)** | RT–100 | 0.7 | 59 | | 32.3 |
| | 100–433 | 12.2, 4.9 | | 361, 425 (sh) | |
| | 433–600 | 10.9 | 490 (br) | | |
| | 600–1100 | 3.6 | | 1004 | |
| **Kao–KOAc ($N_2$)** | RT–100 | 9 | 86 | | 33 |
| | 100–585 | 22.6 | 305, 377 | | |
| | 585–1100 | 2.4 | | 1061 | |
| **Kao–PEA6 ($N_2$)** | RT–121 | 2.7 | 65 | | 31.3 |
| | 121–324 | 5.6 | 290 | | |
| | 324–633 | 18.4 | 388 | | |
| | 633–1100 | 5.6 | | 1036 | |

**Note:** All experiments were carried out at a flow rate of 100 mL $min^{-1}$ and at a heating rate of 10 °C $min^{-1}$; sh: shoulder, br: broad.

Herein, Kao–DMSO intercalate (starting materials) exhibited the two normal weight losses in the TGA, accompanied with two endotherms centered at ~190 °C (loss of the organic moiety) and 510 °C (dehydroxyalation of kaolinite). From the literature, thermogravimetric analyses of various kaolinite intercalates revealed similar results to that of Kao–DMSO. However, for the majority of kaolinite intercalates, the decomposition of kaolinite represented in the dehydroxylation temperature is usually altered from that of the unmodified kaolinite. Moreover, for the Kao–polymer nanocomposites, the dehydroxylation steps were generally shifted to be centered at lower temperatures, even relative to other intercalates. This can be observed in case of the previously reported Kao–PEG and Kao–PEO nanocomposites, as well as Kao–poly(hydroxy butyrate) (9, 18).

The thermal decomposition of the various produced Kao–polymer samples in air atmosphere can be observed in Figs. 4.18–4.20. The data obtained are also shown in Table 4.8. Generally, the decomposition followed a multistep process where some of the decomposition steps overlapped, with a total weight loss for the TGA run up to ~ 40%. In case of the nanocomposites prepared by displacing DMSO from the starting material, an initial 0.7%–1.2% weight loss from RT to 100 °C, attributed to the loss of surface-adsorbed water and other volatiles can be observed. For the Kao–PEA samples, the endotherm at ~58 °C cannot be attributed to the melting of the PEA, as PEA has a characteristic mp at ~39 °C (162). The characteristic endothermic DTA peak, associated with the melting of the polymer, was missing in the DTA of Kao–PEA samples (see Fig. 4.20). This was also found to be the case for Kao–PES, where the endothermic DTA melting peak of PES at ~69 °C was not observed for Kao–PES (Fig. 4.20). In

addition, DSC measurements under nitrogen atmosphere (not shown) revealed the mp of the crude PES used at ~100 °C; no endotherms were observed at this temperature in the DTA thermogram of the Kao–PES samples (Fig. 4.19). Finally, same type of observation was made for Kao–PBA samples (Fig. 4.18). This confirms that the polymer chains in the bulk and intercalated states are in different aggregation states. In general, endothermic peaks, attributed to the fusion of the polymers, do not appear in the DTA thermograms of the kaolinite intercalates reported, indicating different aggregation states for the polymer chains in the bulk and the intercalate as well as the absence of crystalline material in the intercalates.

From 100 to ~440 °C, one observes two weight losses, attributable to the combustion of organic material (Figs. 4.18 and 4.19). This was supported by the observance of two maxima in the corresponding DTA runs (Fig. 4.20), which indicated a very strong exothermic events at ~345–380 °C. For comparison, it was found that for the thermal decomposition of the pure polymers in air atmosphere (162), very strong exotherms were observed centered at 340–350 °C corresponding to the combustion weight loss. No thermal events for kaolinite and Kao–DMSO were detected in this region. For the decomposition of Kao–PEA1 sample, one observes an additional exothermic peak at ~240 °C that could be attributed to the combustion of residual DMSO entangled between the polymer chains in the interlamellar space, leading to the shift of this event to a higher temperature compared with the Kao–DMSO intercalate. This observation is supported by $^{13}C$ NMR results for the same sample. This exotherm disappeared in case of the Kao–PEA4 sample, thus also confirming that the sample is a pure Kao–PEA

nanocomposite, and that DMSO molecules were completely displaced by the polymer chains, as can be seen from $^{13}C$ NMR results.

Overlapping with the second weight loss of the organic decomposition reactions of Kao–polymer intercalates (an exothermic shoulder between 405 and 430 °C) is the dehydroxylation weight loss of kaolinite itself between 490 and 500 °C (Fig. 4.20). The dehydroxylation reaction of kaolinite was estimated to involve a ~6.5% weight loss, compared with a weight loss of 13.5% found for the kaolinite starting material (see Table 4.8). The dehydroxylation reaction for kaolinite exhibits an endothermic peak at 520 °C, whereas it appears at ~490°C for the Kao–polymer intercalates. The presence of the polymeric chains in the interlayers of kaolinite significantly reduced the peak dehydroxylation temperature.

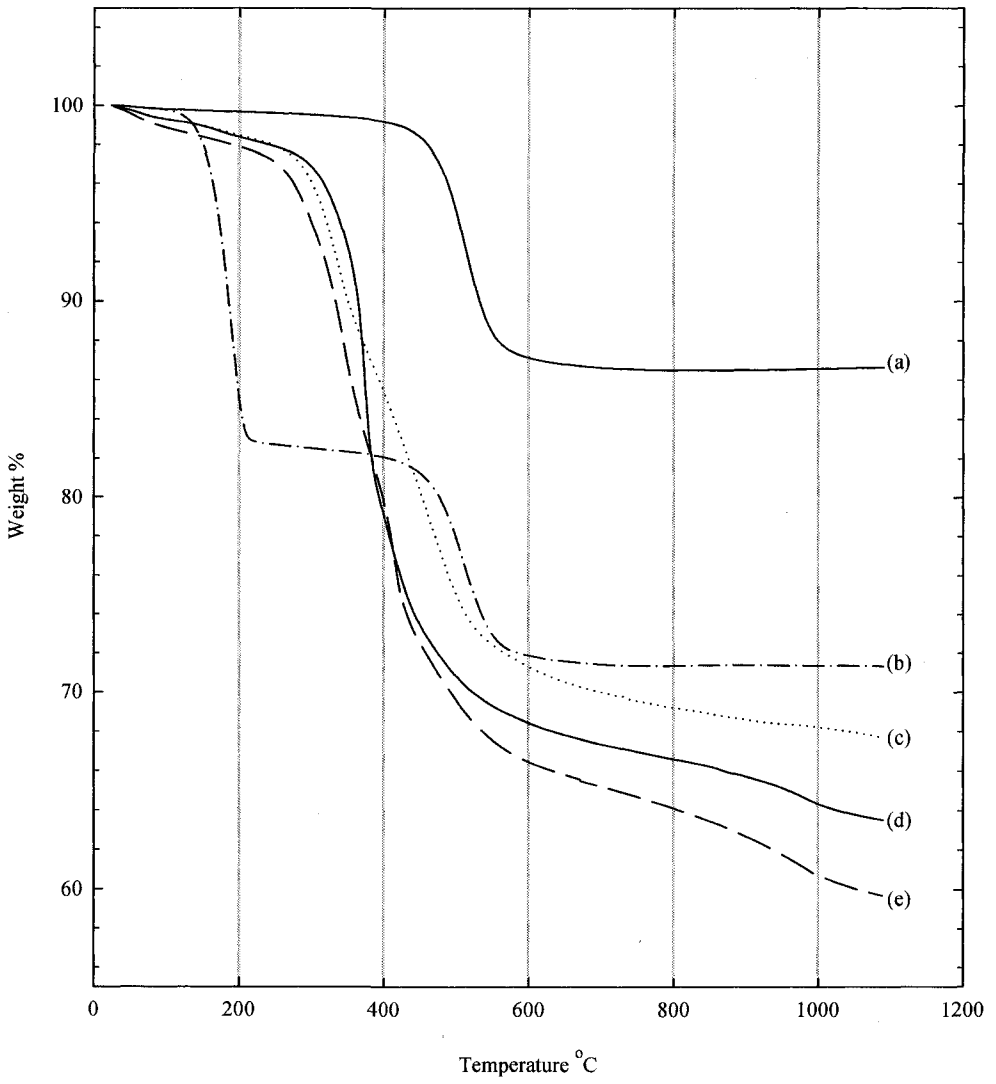


**Fig. 4.18.** TGA curves (RT–1100 °C) of (a) kaolinite, (b) Kao–DMSO, (c) Kao–PBA, (d) Kao–PEA4, and (e) Kao–PES. TGA runs were performed under air.

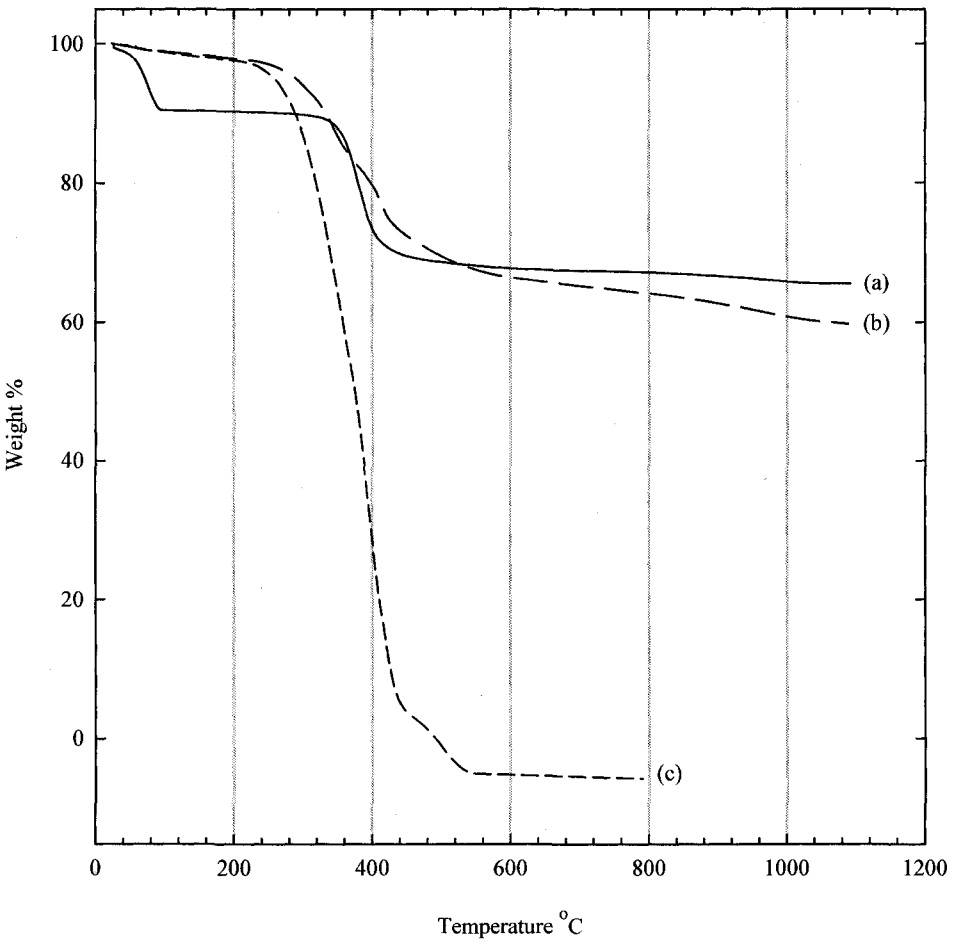


**Fig. 4.19.** TGA curves (RT–1100 °C) of (a) Kao–KOAc, (b) Kao–PEA6, and (c) crude poly(ethylene adipate) (Aldrich). TGA runs were performed under $N_2$.

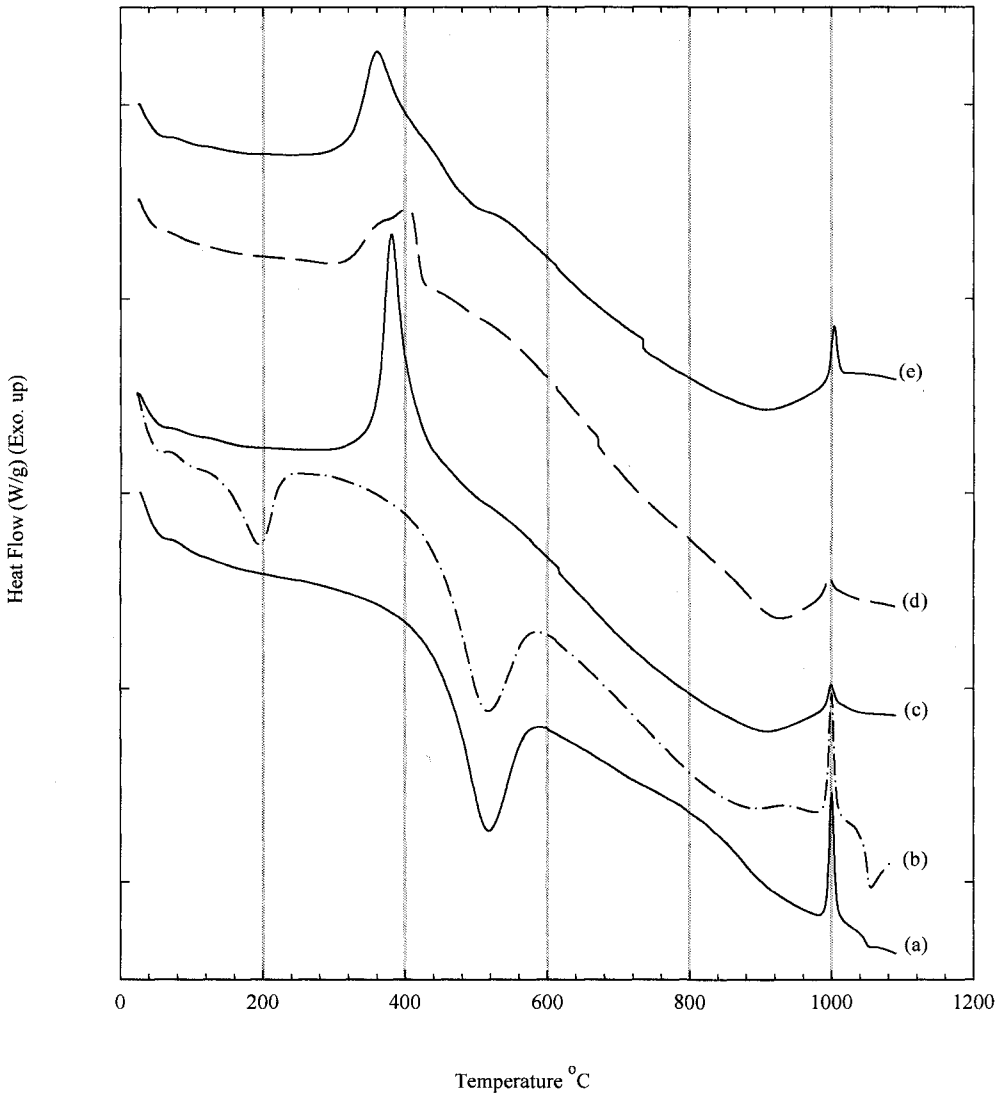


**Fig. 4.20.** DTA curves (RT–1100 °C) of (a) kaolinite, (b) Kao–DMSO, (c) Kao–PEA4, (d) Kao–PES, and (e) Kao–PBA. DTA runs were performed under air.

Finally, the characteristic exothermic event for the reorganization of the kaolinite structure is observed between 995 and 1005 °C (Fig. 4.20) for Kao–PEA, Kao–PES, and Kao–PBA samples under air. These events, which normally should have no associated weight loss, were associated with 5%–7% weight losses in case of Kao–PEA and Kao–PES. Similar to other Kao–polymer intercalates, it is believed that the complete combustion of the polymeric species cannot occur after the initial decomposition reactions before 400 °C. The overlapping of the structural collapse and the dehydroxylation of the kaolinite itself causes the residual interlayer carbonaceous material to be trapped within a metakaolinite matrix, forming a carbon–aluminosilicate nanocomposite material. Some of this carbonaceous material is then released upon the structural reorganization above 1000 °C, resulting in the observed weight losses. Notably, in case of Kao–PBA, the observed weight loss above 600 °C was only 3.6%. This is due to the lower ratio of intercalation for this nanocomposite (see Table 4.1).

Figure 4.19 shows the TGA under nitrogen of Kao–PEA6, produced from Kao–KOAc starting material, as well as the TGA of the starting material and the crude polymer. The data are also listed in Table 4.8. Clearly, the results obtained confirm the presence of two co-intercalated species, i.e., potassium acetate and the polymer and (or) transesterification products.

It is evident that the intercalation of the polymeric species into the interlamellar spaces of kaolinite has dramatically altered the decomposition sequence of kaolinite, in a manner that is totally different from the classical intercalates such as Kao–DMSO and Kao–KOAc starting materials. This is mainly seen in the reduced temperatures of kaolinite dehydroxylation.

# Chapter 5

# Alternative strategies for the synthesis of kaolinite–polymer nanocomposites

# Part I:Synthesis and characterization of a kaolinite–polystyrene intercalated nanocomposite

## 5.1 Introduction

As discussed before (see Chapter 1), two types of polymer–layered clay nanocomposites can be obtained, intercalates and exfoliates (31). Generally, melt intercalation is the most common method for the synthesis of PLS nanocomposites, as it is applicable to a wide range of polymers from non-polar polystyrene to the strongly polar nylon. In this chapter, other synthesis strategies will be explored, including in situ polymerization of a previously intercalated monomer and solution polymerization. Examples of the first approach were reported in the cases of polyacrylamide, nylon-6, poly(β-alanine), and polyacrylonitrile (12, 20, 22, 35). An example of the second strategy was in the case of poly(vinylpyrrolidone) (24). Since the mid-sixties, several polystyrene-montmorillonite nanocomposites were reported in the literature using different preparation techniques (30–32). The use of these nanocomposites as flame retardants has gained a lot of interest in the last few years (30, 33). Polystyrene is one of the most mass-productive commercialized polymers, and consequently, it must be flame-retarded. The polymerization of styrene catalyzed by dry kaolinite was reported by Solomon in the sixties (163–165). The polymerization takes place as a result of interactions of the styrene monomers with the edges of the aluminosilicate structure. The catalytic activity is

related to aluminum in octahedral coordination, situated at crystal edges and activated by heating in order to remove some of the coordinated water molecules, thereby generating Lewis-acid sites. This polymerization catalyzed by activated kaolinite should generate microcomposites, not intercalated or delaminated nanocomposites. A polystyrene nanocomposite of kaolinite was previously mentioned in the literature (166); however, the prepared nanocomposite was not fully characterized. In the first part of this chapter, the intercalation of polystyrene (PS) into the interlamellar spaces of kaolinite is reported with detailed characterization. The intercalation was achieved by a free-radical polymerization reaction of styrene in the presence of a kaolinite–DMSO intercalate, as a starting material. The results of the XRD, FTIR, and TGA analyses confirmed the intercalation of polystyrene in the interlamellar spaces of kaolinite. $^{13}C$ CP/MAS and DD/MAS spectra indicated the almost complete displacement of DMSO by polystyrene chains and the rigidity of the latter in the interlamellar spaces. $^{29}Si$ and $^{27}Al$ NMR spectra of the starting materials and the products are also discussed.

## 5.2 Preparation and X-ray diffraction

An intercalated polymer – layered aluminosilicate nanocomposite was prepared by a free radical initiated polymerization reaction of styrene in the presence of a Kao–DMSO intercalate. Figure 5.1 shows typical X-ray powder patterns of the starting materials (kaolinite and Kao–DMSO) and of the produced nanocomposite in the range of 2 to 18° $2\theta$. The structure of kaolinite remains largely unaffected as the $d_{060}$ reflection remains at 1.49 Å, characteristic of a dioctahedral clay mineral. The only major variation is the value of the *c*-spacing. The observed expansion to ~11.1 Å corresponds to a 4.0 Å expansion, compared with pure kaolinite (Fig. 5.1b). This value is indicative of the intercalation of a flattened monolayer arrangement of the polymer chains in the interlamellar space. This is similar to what was observed previously in the case of polyethylene glycol (18). Since the $^{13}C$ NMR results show the disappearance of the organic intercalates (DMSO) after the reaction (see NMR Section), the expansion is attributed only to the intercalation of polystyrene chains. The temperature was kept at 80 °C at the beginning of the reaction to avoid a fast deintercalation of DMSO from the Kao–DMSO intercalate, resulting in an unexpanded kaolinite. The temperature was then raised to 200 °C overnight to ensure the complete polymerization. This temperature is higher than the documented reported one for the decomposition of the Kao–DMSO intercalate (7, 8, 18), thus confirming that the observed expansion can only be attributed to the displacement of DMSO by polystyrene.

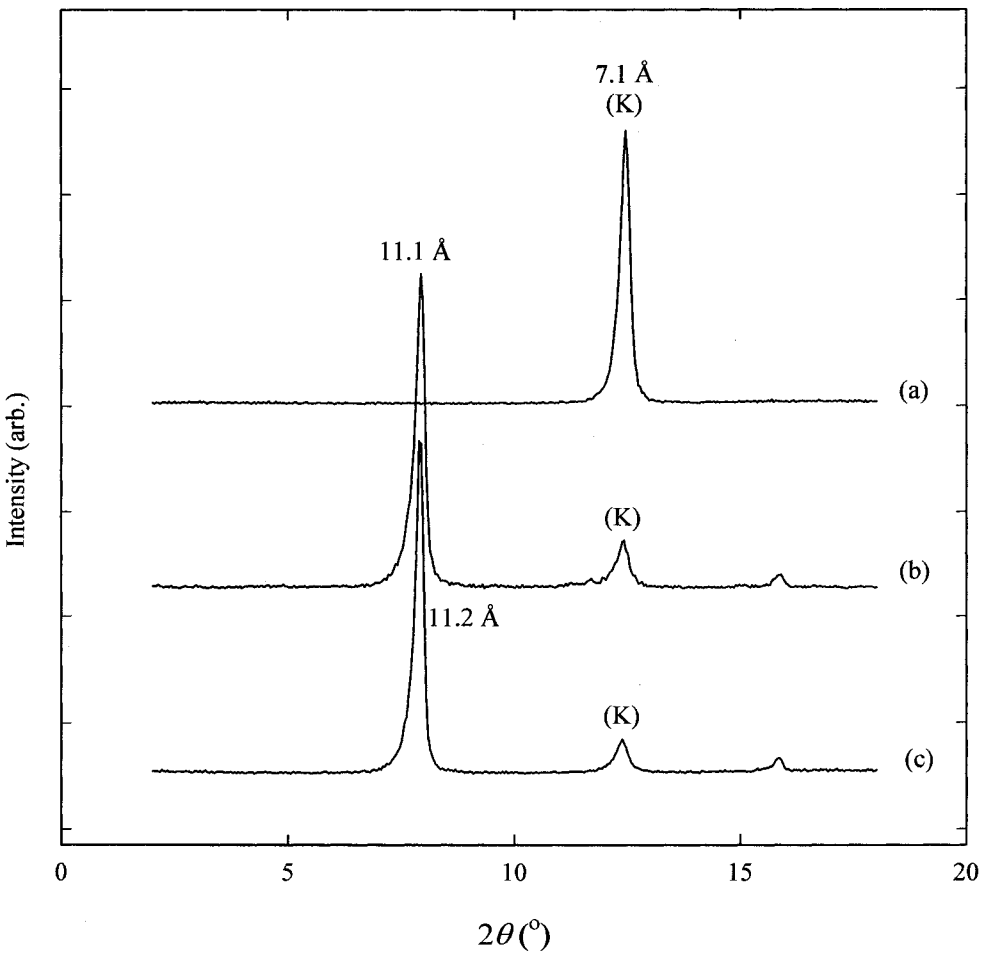


**Fig. 5.1.** XRD powder patterns ($2\theta$ = 2–18°) of (a) kaolinite, (b) Kao–polystyrene, and (c) Kao–DMSO.

## 5.3 FTIR analysis of the product

### 5.3.1 O–H and C–H stretching patterns

Figure 5.2 presents the O–H and C–H stretching patterns for kaolinite, Kao–DMSO, and Kao–polystyrene. The spectra of the starting materials were similar to those reported previously (see previous chapters). Kaolinite shows characteristic O–H stretching vibrations at 3697, 3667, and 3652 $cm^{-1}$, attributed to the inner-surface (i.e., outer) hydroxyl groups, and the intensity and location of these bands are usually sensitive to the intercalation of organic molecules. Another characteristic band at 3620 $cm^{-1}$ is attributed to the stretching of the inner hydroxyls and is usually not affected by intercalation. In case of the DMSO intercalate, new bands at 3540 and 3505 $cm^{-1}$ are normally attributed to the stretching frequency of the coupled inner-surface hydroxyl groups perpendicular to the (001) plane and hydrogen bonded to DMSO molecules, while bands at 3696 and 3665 $cm^{-1}$ were attributed to the equivalent, non H-bonded, coupled inner-surface hydroxyl groups (25, 59). In the case of the non-polar polystyrene intercalate (Fig. 5.2b), one cannot expect H-bonding interactions similar to those found in the case of an organic polar molecule. While the spectrum differs significantly from that of the starting material, Kao–DMSO, it is similar to that of pure kaolinite except that the intensities of the bands due to inner surface hydroxyls are dramatically reduced. The band at 3620 $cm^{-1}$ remains unperturbed. The C–H stretching patterns are also shown in Fig. 5.2. The spectrum of Kao–DMSO shows asymmetric and symmetric $CH_3$ stretching bands at 3022 and 2937 $cm^{-1}$, respectively. Upon intercalation of the polystyrene, these bands were replaced by several bands at 3062, 3026, 2923, and 2850 $cm^{-1}$, characteristic of the polystyrene structure.

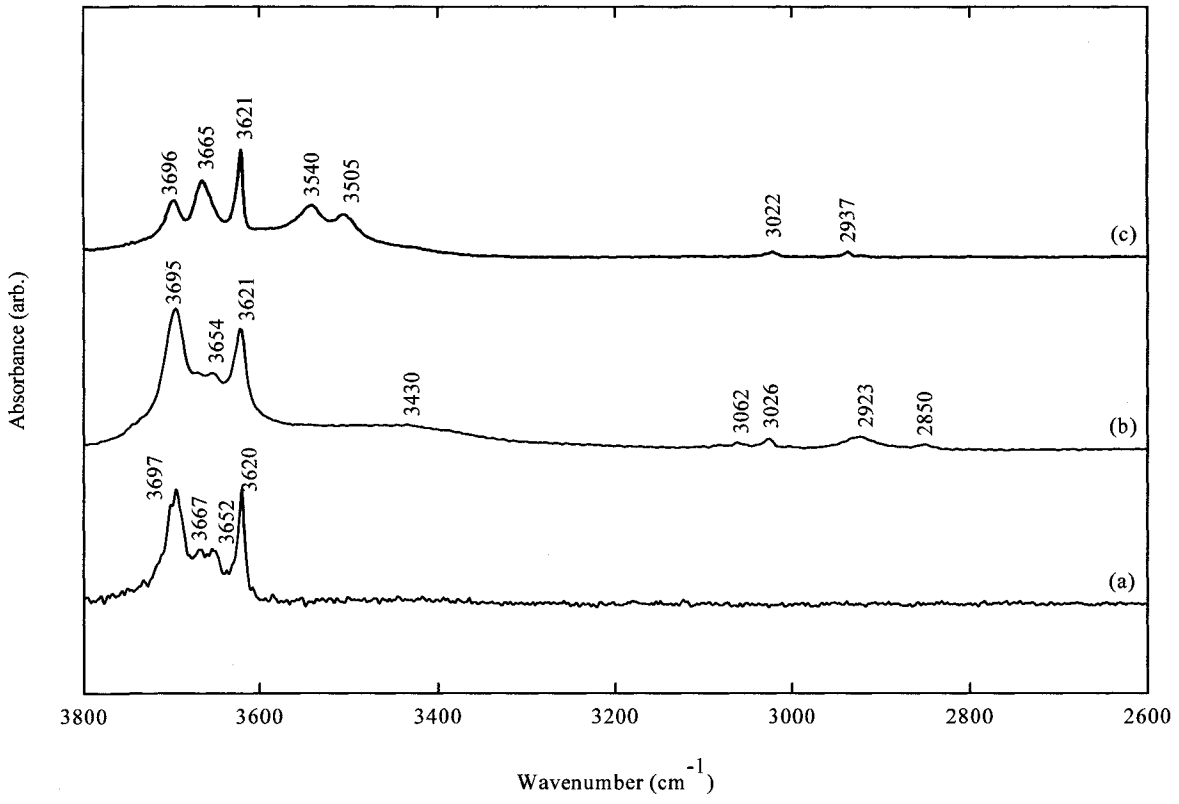


**Fig. 5.2.** FTIR spectra (3800–2600 $cm^{-1}$) of (a) kaolinite, (b) Kao–polystyrene, and (c) Kao–DMSO.

### 5.3.2 O–H and C–H deformation bands

Major changes are also observed in the O–H bending region of the spectra (Fig. 5.3), The kaolinite band at 938 $cm^{-1}$ has been assigned to the in-plane bending vibrations of the inner-surface (outer) hydroxyl groups (25, 26, 59). Upon intercalation of polystyrene, this band almost disappeared, and no new bands were observed. This is different from the case of DMSO where a new band appears at 958 $cm^{-1}$.

As shown in Fig. 5.4b, Kao–DMSO exhibits its normal C–H deformation bands at 1429, 1407, 1394, and 1318 $cm^{-1}$ (25, 27, 70). For Kao–polystyrene, the spectrum in Fig. 5.4a shows the aromatic ring bands overlapped with the methylene C–H bending vibrations at 1454, 1495, 1540, 1559, and 1604 $cm^{-1}$.

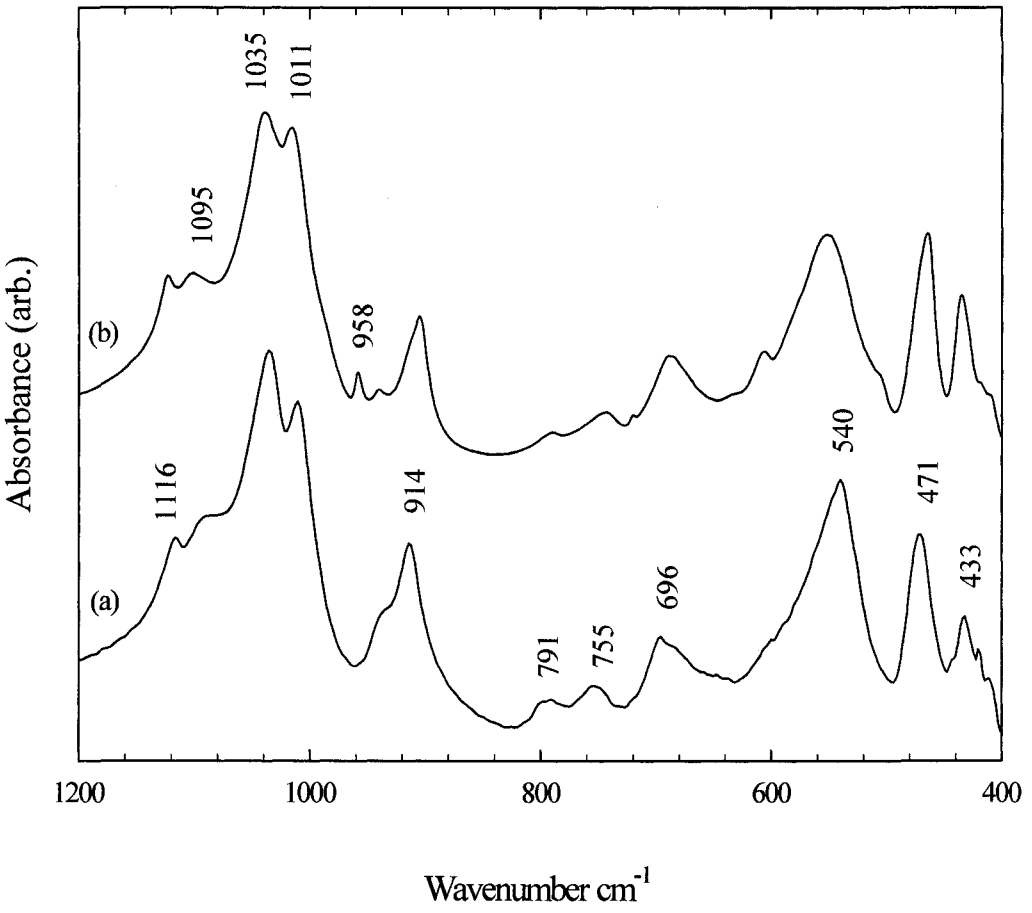


**Fig. 5.3.** FTIR spectra (1200–400 $cm^{-1}$) of (a) Kao–polystyrene and (b) Kao–DMSO.

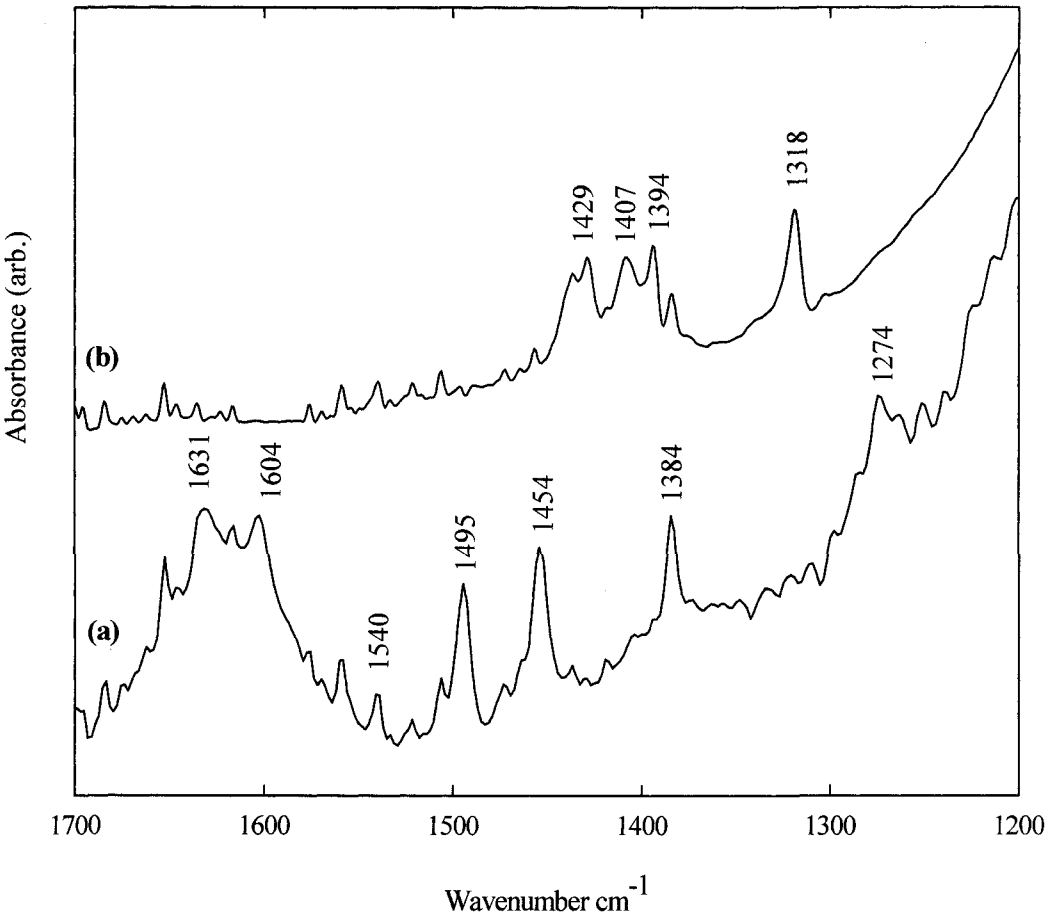


**Fig. 5.4.** FTIR spectra (1700–1200 $cm^{-1}$) of (a) Kao–polystyrene and (b) Kao–DMSO.

## 5.4 Identification of the intercalated species by solid-state $^{13}C$ CP/ and DD/NMR analysis

The $^{13}C$ CP/MAS (125.77 MHz) NMR spectra of the Kao–DMSO intercalate and of the Kao–polystyrene nanocomposite material are given in Fig. 5.5. The spectrum of Kao–DMSO intercalate (Fig. 5.5a) is similar to the reported in the literature (72, 75, 134). In the case of Kao–polystyrene (Fig. 5.5b), a broad signal is observed with two maxima at ~40.6 ppm and 42.6 ppm. The first is attributed to the methine carbon of the aliphatic backbone, and the latter can be attributed to the methylene carbon of the aliphatic backbone together with the methyl groups of a residual amount of DMSO (167). This is similar to the case of the intercalation of polyethylene glycol, where DMSO was found to be co-intercalated with the polymer (18). However, in the case of this study, the intensity of the residual DMSO signal compared to the intensities of the polystyrene signals indicates a rather small amount of DMSO molecules, compared with the amount of polymer in the interlamellar space. Other signals at ~128.3 and 146.4 ppm can be attributed to the protonated and non-protonated phenyl carbons, respectively. Figure 5.6 shows the $^{13}C$ CP/MAS (50.31 MHz) and dipolar dephasing spectra of Kao–polystyrene with a dephasing time $\tau = 40$ μs. The complete disappearance of the methine signal together with ~90 % reduction in the intensity of the signal for other protonated carbons after a dephasing time of 40 μs indicates that the polymer chains are rigidly fixed in the interlamellar spaces of kaolinite (126–128). The observation of one signal at 42.6 ppm in case of the dipolar dephasing (Fig. 5.6b) is in agreement with the presence of a small residual

amount of co-intercalated DMSO molecules entangled between the polymer chains. The $^{13}C$ NMR results indicate that DMSO molecules are almost fully replaced by the polymer in the interlamellar spaces of kaolinite after the reaction.

## 5.5 $^{29}Si$ CP/MAS NMR

The $^{29}Si$ CP/MAS NMR spectrum (99.35 MHz) of kaolinite is given in Fig. 5.7a. As expected, two well-resolved signals were observed at –91.5 and –90.9 ppm (74, 129–132). The two signals were attributed to the existence of two different but equally populated silicon sites. The $^{29}Si$ CP/MAS spectrum of the Kao–DMSO intercalate is given in Fig. 5.7b. In addition to the residual signals of unexpanded kaolinite, one signal is observed at –92.7 ppm. The observed degeneracy of the $^{29}Si$ signals of kaolinite upon intercalation of organic molecules corresponds to a higher degree of order in the intercalate with loss of the H-bonding dissymmetry observed in kaolinite and a well-ordered structuration of the organic molecules, DMSO in this case, in the interlamellar space. Figure 5.7c gives the $^{29}Si$ CP/MAS NMR spectra of the Kao–polystyrene intercalated nanocomposite. A broad signal is observed at –91.5 ppm with a shoulder at –91.0 ppm. This is similar to what was reported in the case of other Kao–polymer intercalates, e.g., Kao–polyacrylamide (12, 149). The intercalation of polymeric chains in the interlamellar space results in a dissymmetric environment in the silicate sheet.

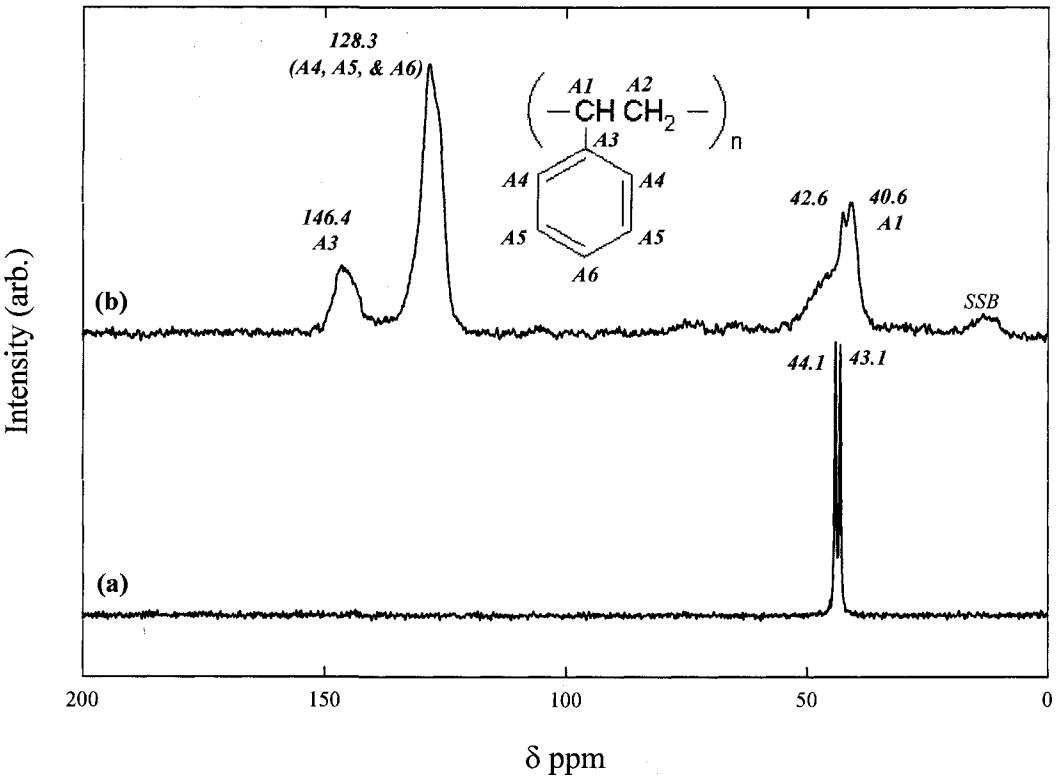


**Fig. 5.5.** Solid-state $^{13}C$ CP/MAS NMR spectra (125.77 MHz) of (a) Kao–DMSO and (b) Kao–polystyrene.

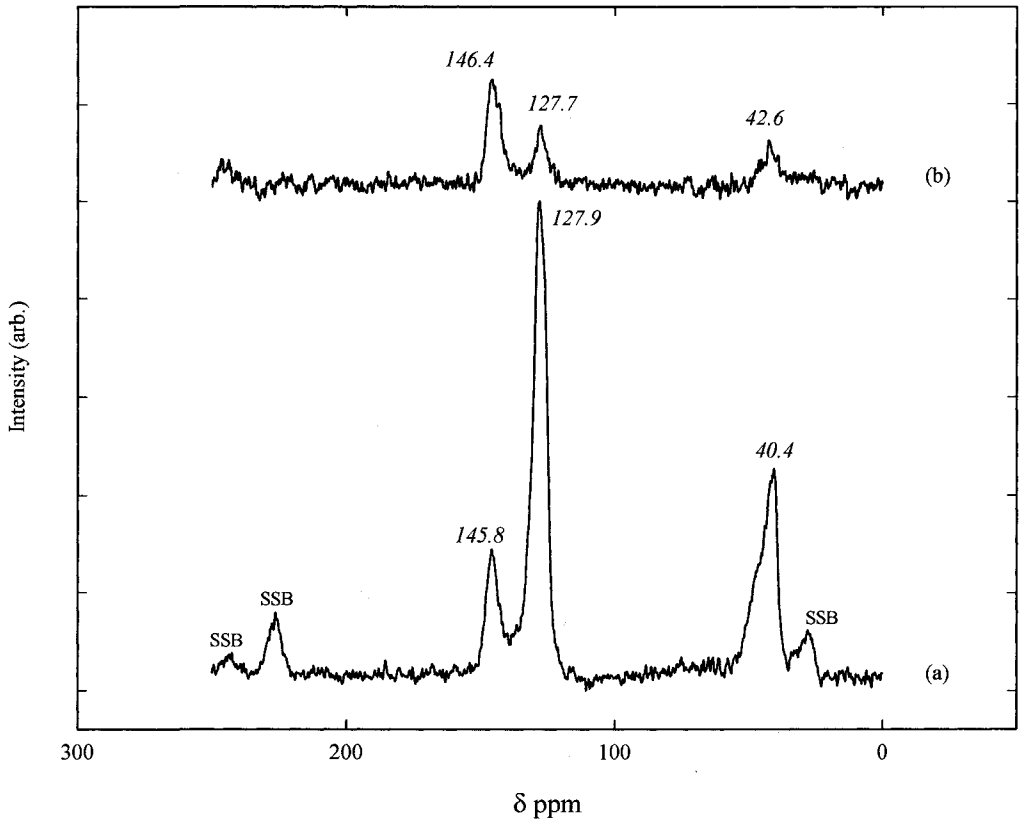


**Fig. 5.6.** Solid-state $^{13}C$ NMR spectra (50.31 MHz) of (a) Kao–polystyrene (CP/MAS) and b) Kao–polystyrene with dipolar dephasing, $\tau = 40\ \mu s$.

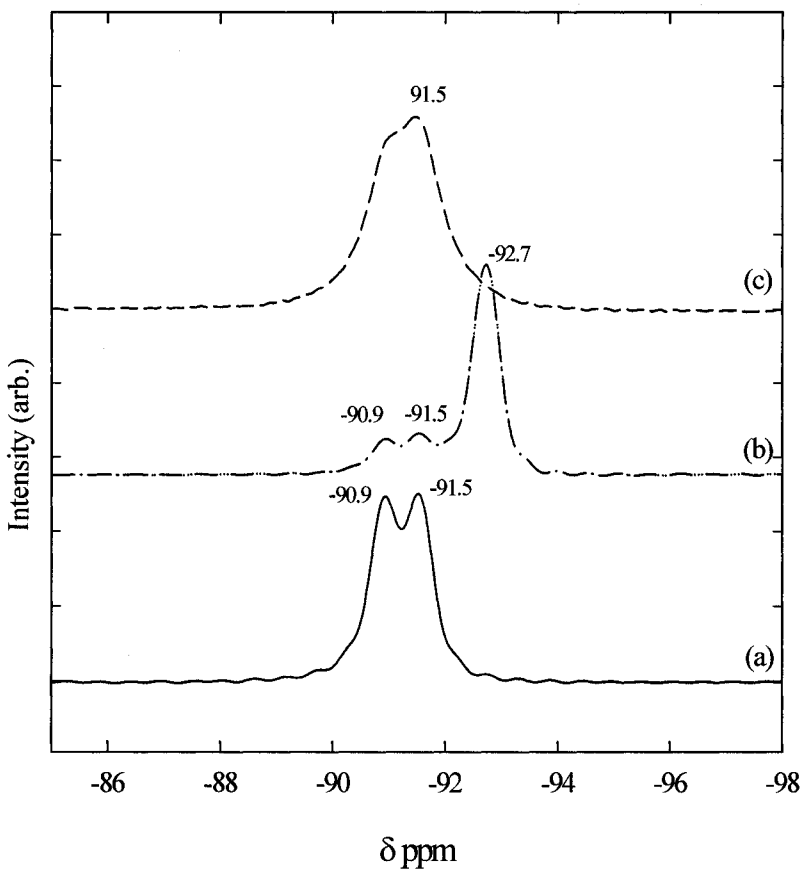


**Fig. 5.7.** $^{29}$Si CP/MAS NMR spectra of (a) kaolinite, (b) Kao–DMSO, and (c) Kao–polystyrene.

## 5.6 $^{27}$Al NMR analysis

$^{27}$Al NMR spectra of kaolinite and intercalates show signals due to both octahedral and a small amount of tetrahedral aluminum sites. The $^{27}$Al MAS NMR spectra of kaolinite, Kao–DMSO, and Kao–polystyrene were obtained at 130.32 MHz at a spinning rate of 14.0 kHz (Fig. 5.8). In all cases, a broad signal is observed, with a maximum at 4.1 ppm for the octahedral aluminum site of the nanocomposite. These results are in agreement with previous studies (75, 77, 133–135).

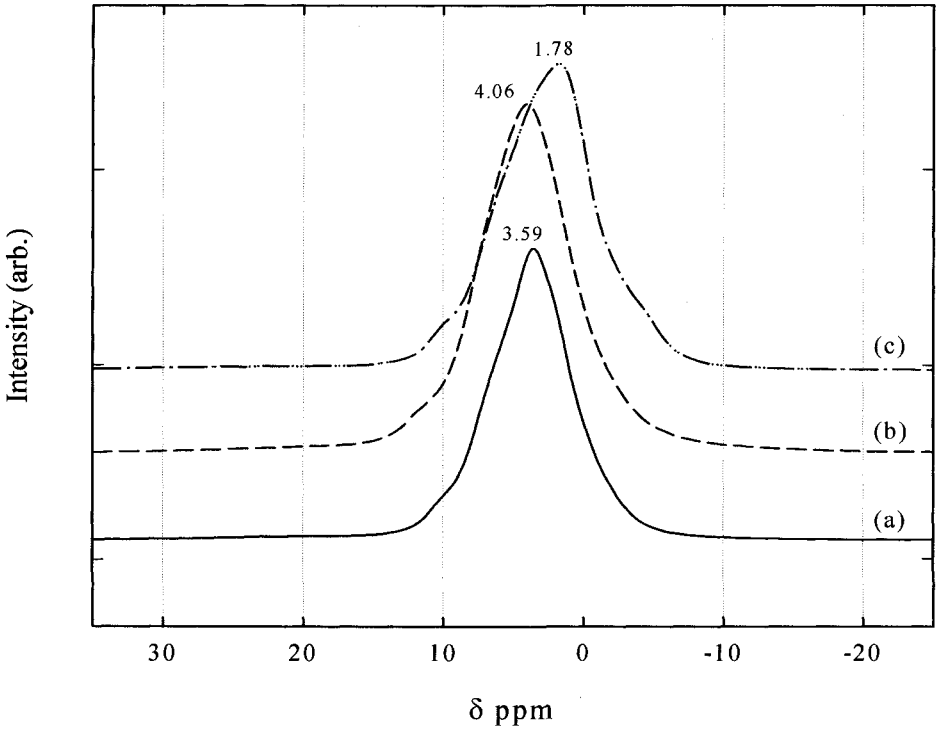


**Fig. 5.8.** $^{27}$Al MAS NMR spectra of (a) kaolinite, (b) Kao–polystyrene, and (c) Kao–DMSO.

## 5.7 Elemental analysis

The elemental analysis of a typical sample gives C: 11.82%, H: 2.33%, S: 0.58%, and N was not detected. This is in agreement with the presence of small amounts of residual DMSO. The stoichiometry of the material is $Al_2Si_2O_5(OH)_4 \cdot (C_8H_8)_{0.45}$, which is in good agreement with the calculated formula on the basis of the TGA results (see the thermogravimetric analysis). The observed *c*-spacing of 11.1 Å points to a flattened arrangement of the polymeric chain, in a manner described before for other kaolinite–polymer intercalates (18). An occupancy of 0.45 monomeric unit of PS per unit cell of kaolinite corresponds to a cross-sectional area of ~1.0 $nm^2$ for a monomeric unit, since the cross-sectional area of a kaolinite unit cell is 0.45 $nm^2$. Since the cross-sectional area of a styrene unit with its aromatic ring in the horizontal plane is approximately in the order of 0.5 $nm^2$, as estimated from CPK models, one can surmise that in the highly constrained interlamellar space of kaolinite, the polystyrene is in a flattened configuration with its aromatic groups regularly alternating on each side of the backbone aliphatic chain.

## 5.8 Thermogravimetric analysis

Basic features of the DTA thermogram of kaolinite can be observed in Fig. 5.9. The major endotherm near 550 °C is unambiguously attributed to the loss of water as a result of the crystal lattice dehydroxylation with formation of the meta-kaolinite (Fig. 5.9a). The characteristic exotherm near 1000 °C is also observed in Fig. 5.9a. Kao–DMSO intercalate exhibits two weight losses in the TGA accompanied by two endotherms, centered at ~195 °C and 513 °C (fig. 5.9c). The former is attributed to the loss of DMSO, and the latter is due to the dehydroxylation step of kaolinite (shifted to a lower temperature , as a result of the intercalation) (136–138).

In the case of the prepared Kao–polystyrene intercalated nanocomposite (Fig. 5.9b and 5.9d), one can observe the dehydroxylation step at ~505 °C. The shifted dehydroxylation temperature is normal for Kao–polymer intercalates (see Chapter 4). An additional weight loss is observed with $T_{exo}$ around 370 °C, corresponding to almost 16.3% weight loss (subtracting a calculated dehydroxylation weight loss of ~10%), and it is attributed to the loss of the organic moiety (de-intercalation of PS), i.e., decomposition of the intercalated nanocomposite. This relatively high temperature is similar to the temperatures previously reported in case of other polymers, such as polyethylene glycol, polyethylene oxide, and polyhydroxybutyrate (9, 18). On the basis of the TGA results (Total % of weight lost to form metakaolinite $Al_2O_3{\cdot}2SiO_2$), the following formula can be calculated: $Al_2Si_2O_5(OH)_4{\cdot}(C_8H_8)_{0.4}$. Finally, in the DTA of the Kao–polystyrene nanocomposite, no endothermic peaks were observed at the melting temperature of the pure polystyrene, ~240 °C, thus ruling out the possibility of the presence of any excess amount of

the crystalline organic substances in the sample, and indicating different aggregation states for the polymer chains in the bulk and in the intercalate.

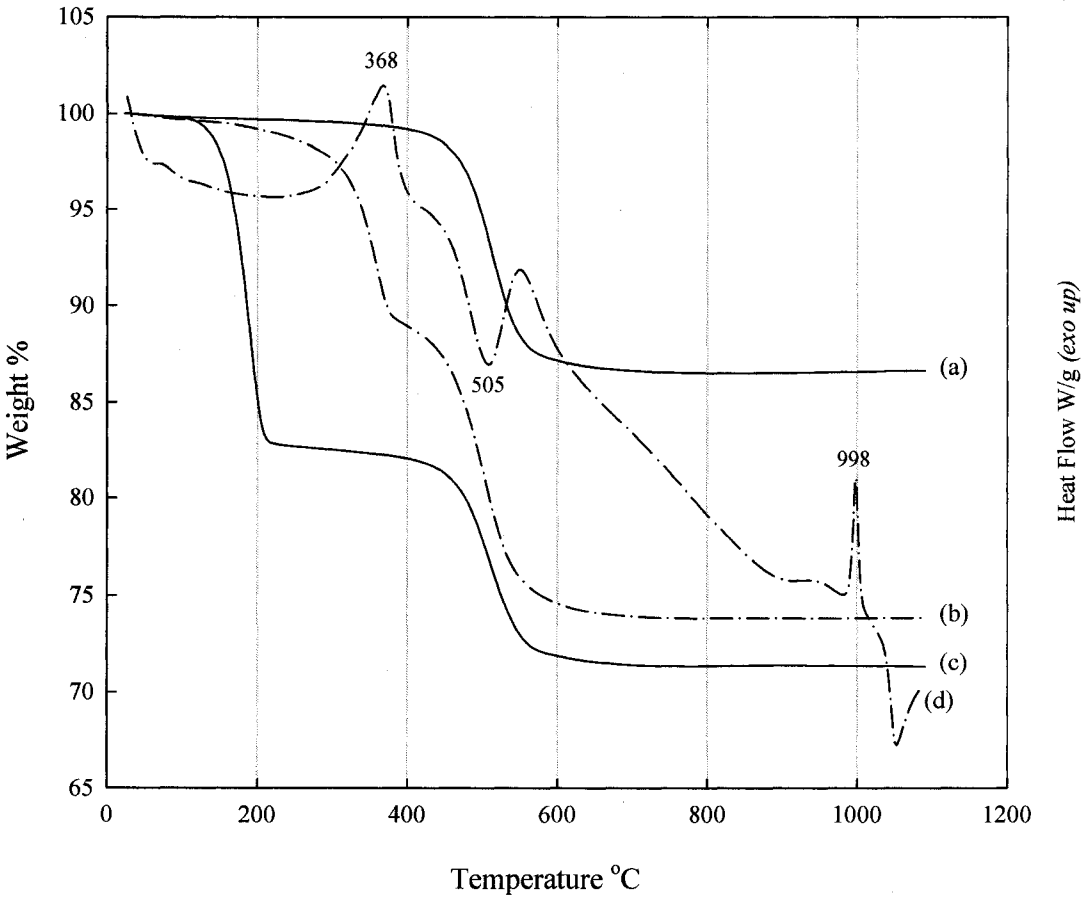


**Fig. 5.9.** TGA curves (RT–1100 °C) of (a) kaolinite, (b) Kao–polystyrene, and (c) Kao–DMSO; (d) DTA curve for Kao–polystyrene.

# Part II: Synthesis of a kaolinite–poly(methacrylamide) intercalated nanocomposite via in situ polymerization

## 5.9 Introduction

In this part, the synthesis of a new kaolinite–methacrylamide intercalation compound was achieved by direct treatment of an intermediate with an aqueous solution of methacrylamide. For the first time, a kaolinite–poly(methacrylamide) intercalated nanocomposite was synthesized by in situ polycondensation of the preintercalated methacrylamide monomer. Methacrylamide (see Chart 5.1) was first intercalated into kaolinite by a guest-displacement method, using kaolinite–DMSO as an effective intermediate. The intercalated monomer adopted a monolayer arrangement between the layers, confirmed by XRD analysis. Free-radical polymerization of methacrylamide was reported in the interlamellar spaces of Na-montmorillonite (168). Herein, the polymerization was achieved by thermal treatment of kaolinite–methacrylamide intercalation compound at ~150 °C for 2 h in air atmosphere. $^{13}C$ NMR analysis confirmed the polymerization with the presence of residual monomeric species in the interlamellar space. The polymerization product had a high thermal stability, compared with the kaolinite–methacrylamide intercalation compound, as evidenced by thermogravimetric analysis. In general, analyses results confirmed the feasibility of the synthesis of an intercalated Kao–polymer nanocomposite, using in situ polymerization strategy. For comparison, the Kao–acrylamide intercalation compound reported previously in the literature (12, 149) was prepared by the same method, and the analysis results revealed that the intercalation was less successful than the Kao–methacrylamide intercalate.

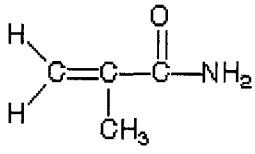

I

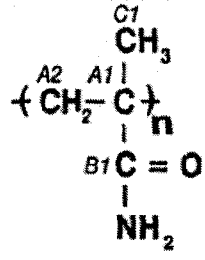

II

**Chart 5.1.** Methacrylamide (I) and poly(methacrylamide) (**II**).

## 5.10 Synthesis and XRD analysis

The preparation of the Kao–methacrylamide (MAC) nanohybrid materials was carried out at room temperature, most effectively from the DMSO intercalate of kaolinite by direct treatment with 10% aqueous solution of methacrylamide (Aldrich). First, a kaolinite–DMSO intercalation compound (abbreviated as Kao–DMSO) or a kaolinite – *N*-methyl formamide (Kao–NMF) was prepared as an intermediate according to the methods reported previously (5). Table 5.1 summarizes the product names and codes, the reaction conditions, and the $d_{001}$ values of the resulting materials. In the case of pure kaolinite (KGa-1b) as a starting material, kaolinite was fully recovered, and only the characteristic $d_{001}$ reflection can be observed at 7.2 Å. However, when the Kao–DMSO was used as an intermediate, a reflection at 12.5 Å is observed, indicative of the methacrylamide intercalation into the interlamellar spaces of kaolinite, since Kao–DMSO intercalate exhibits a $d_{001}$ reflection at ~11.1 Å (68) (see Fig. 5.10). In a typical reaction, 1–2 g of Kao–DMSO intercalate were mixed with ~50–100 mL of 10% solution (*w*/*v*) of methacrylamide (MAC) (Aldrich; see Chart 5.1). The mixture was stirred at room temperature for a given period of time, followed by the reaction workup (washing with excess 2-propanol, vacuum filtration, and drying in vacuum). The ratio of intercalation was up to ~92%. Another intercalate was used as a starting materials, Kao–NMF. The production of materials with $d_{001}$ = 12.6 Å was observed when the Kao–NMF intercalate was used ($d_{001}$ = 10.8 Å for Kao–NMF), but with relatively low ratio of intercalation, plausibly because of the decomposition of the starting material. It is worth noting that the reaction was unsuccessful from the melt, as methacrylamide sublimes at the melting temperature.

Typical X-ray powder patterns of the starting materials (kaolinite and Kao–DMSO) and of the materials resulting from a typical reaction are shown in Fig. 5.10, for the range of 2–18° 2$\theta$. The $d_{060}$ reflection remains at 1.49 Å, characteristic of a dioctahedral clay mineral. Again, the layered structure of kaolinite remains largely unaffected (Fig. 5.11). The $d_{001}$ reflection of the Kao–MAC intercalate corresponds to an expansion in the interlamellar distances by ~5.3 Å (subtracting a kaolinite layer thickness of 7.2 Å from the observed $d_{001}$). Since the $^{13}C$ NMR results show the complete disappearance of the intermediate organic intercalate (DMSO) after the reaction (see later sections), the expansion can be attributed only to the intercalation of the amide.

**Table 5.1.** Summary of product codes, reaction conditions, and product X-ray characterization for the preparation of kaolinite–methacrylamide nanohybrids.

| Produced nanohybrid code[a] | Reaction conditions[a] Starting material (SM)[b] | Reaction medium (RM) | $t_r$[c] (h) | Product X-ray characterization $d_{001}$[d] (Å) | $d_{001K}$[e] (Å) | RI[f] (%) |
|---|---|---|---|---|---|---|
| Kao–MAC1 | Kao–NMF | (10% methacrylamide solution, *w/v*) | 22 | 12.6 | 7.15 | 9.0 |
| Kao–MAC2 | Kao–DMSO | (10% methacrylamide solution, *w/v*) | 21 | 12.5 | 7.13 | 50.3 |
| Kao–MAC3 | Kao–DMSO | (10% methacrylamide solution, *w/v*) | 67 | 12.5 | 7.15 | 92.0 |
| Kao–MAC4 | Kao–DMSO | (10% methacrylamide solution, *w/v*) | 48 | 12.5 | 7.15 | 91.4 |
| Kao–MAC5 | Kaolinite (KGa-1b) | (10% methacrylamide solution, *w/v*) | 72 | — | 7.15 | — |

**Note:** Reaction details are given in the Experimental Section.

[a] All reactions took place at ambient tempaerature.

[b] Kao, kaolinite; MAC, methacrylamide; NMF, *N*-methyl formamide; and DMSO, dimethyl sulfoxide.

[c] Approximate reaction time.

[d] The specified interlayer distance (*d*) is that of the principal product phase calculated using (00l) reflections (see Chapter 1).

[e] *d*001 reflections of the residual unexpanded kaolinite.

[f] Ratio of intercalation is the ratio of the intensities of the $d_{001}$ reflection of the modified phase over the sum total of all the $d_{001}$ reflections of the modified phase(s) and residual unexpanded kaolinite.

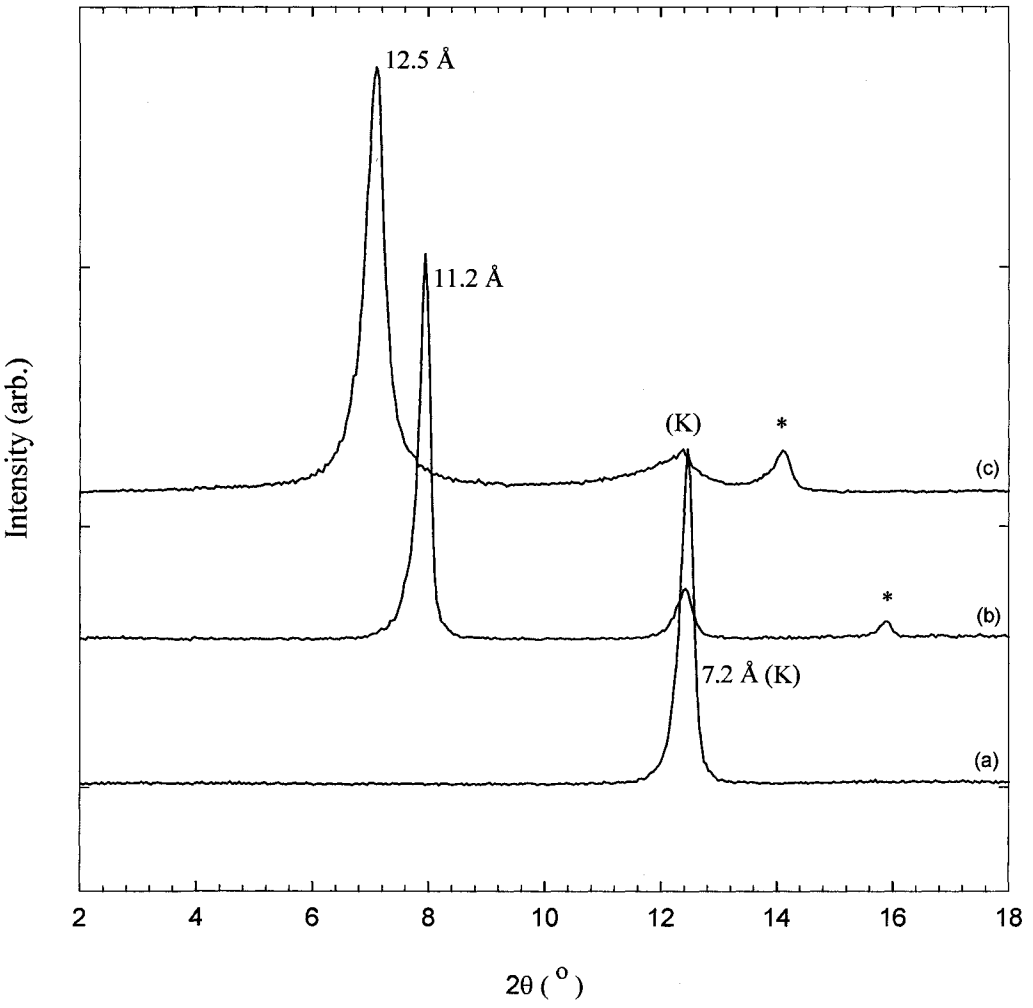


**Fig. 5.10.** XRD powder diffraction patterns ($2\theta = 2$–$18^{\circ}$) of (a) kaolinite, (b) Kao–DMSO, and (c) Kao–MAC. Residual kaolinite $d_{001}$ peaks. $d_{002}$ of the intercalate is marked by an asterisk.

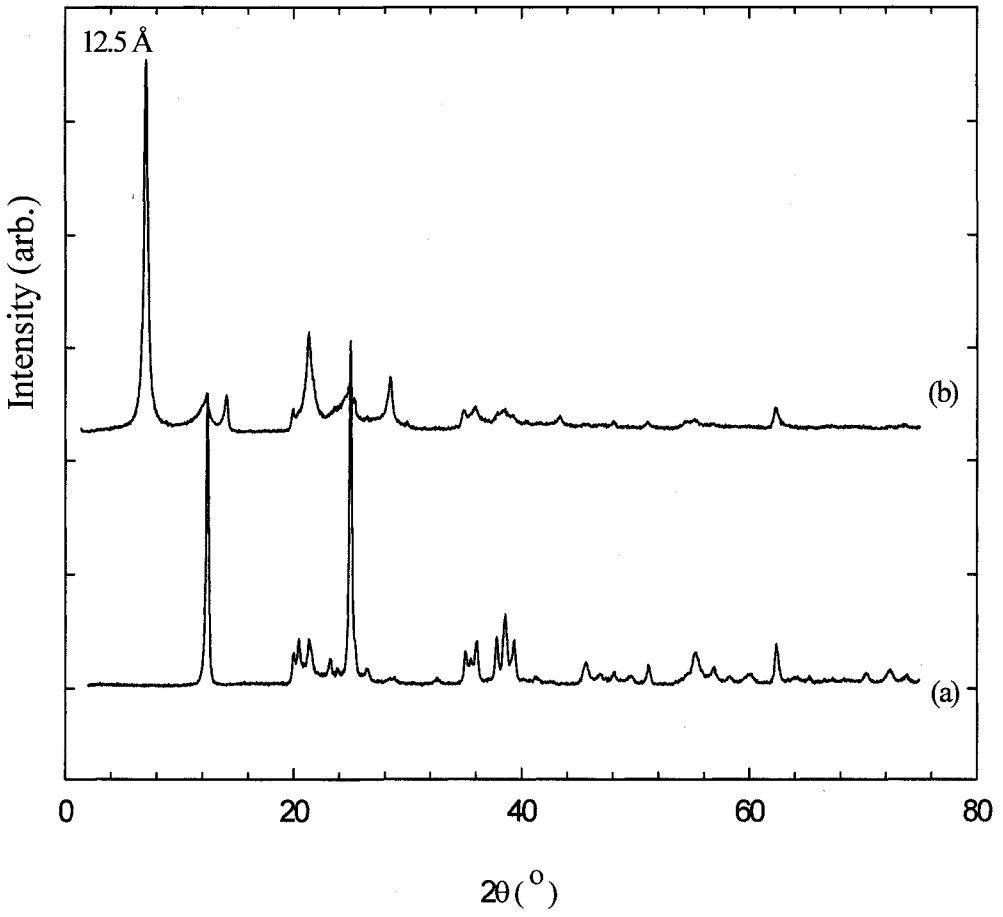


**Fig. 5.11.** XRD powder diffraction patterns ($2\theta$ = 2–75°) of (a) kaolinite and (b) Kao–MAC.

## 5.11 Thermal treatment: polymerization of methacrylamide in the interlamellar spaces of kaolinite

Methacrylamide is usually polymerized in aqueous solutions in the presence of a free radical initiator ,e.g., benzoyl peroxide (168). Thermal treatment is used in this study to polymerize the intercalated amide in the interlamellar spaces without using an initiator. Figure 5.12 shows powder XRD patterns of Kao–MAC sample before and after thermal treatment. The sample was heated at a rate of 4 °C $min^{-1}$ in a programmable furnace and then kept for 2 h at 150 °C or 30 h at 100 °C. The samples were allowed to cool to room temperature, and their XRD powder patterns were recorded. Heating the samples at higher temperatures would cause the intercalated kaolinite layers to collapse as a result of the deintercalation of the amide (see TGA Section).

Thermal treatment (Fig. 5.12) causes the condensation polymerization of the methacrylamide molecules into the interlayer spaces. This can be observed by an expansion the interlayer spacing from 12.5 Å to 12.9 Å for the polymerization product Kao–PMAC.

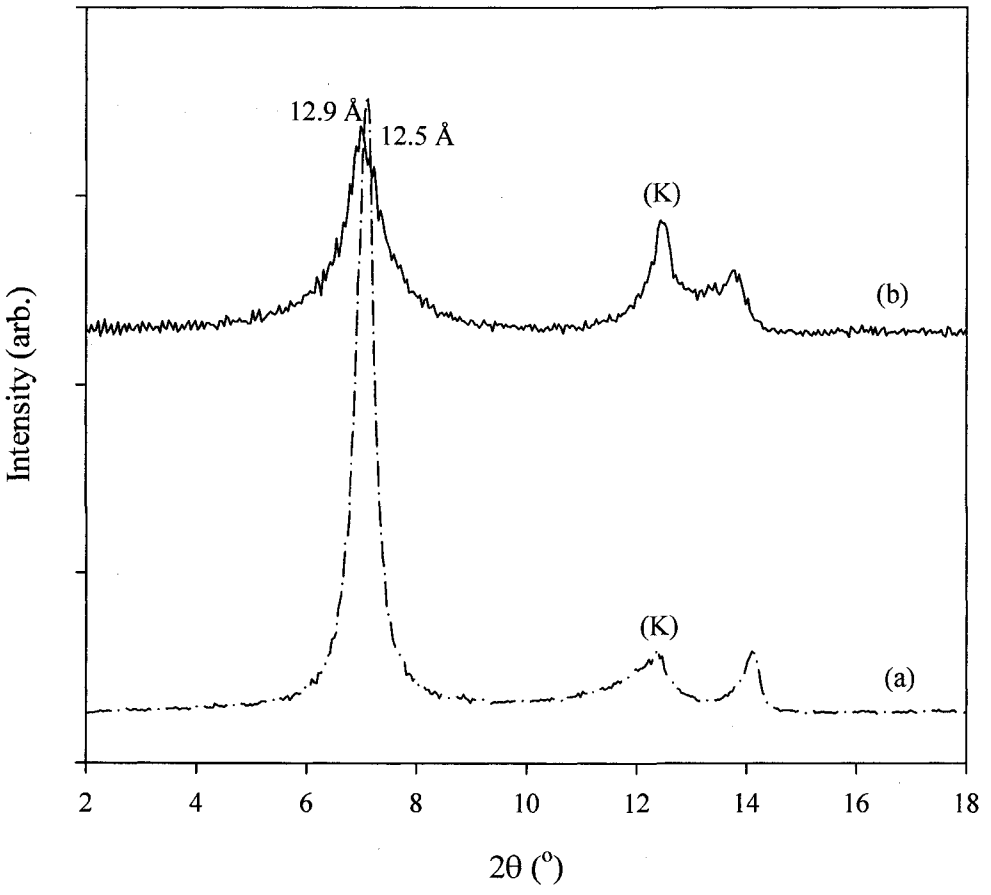


**Fig. 5.12.** XRD powder diffraction patterns ($2\theta$ = 2–18°) of Kao–MAC (a) before and (b) after thermal treatment.

## 5.12 FTIR analysis

Detailed assignments of the major observed bands in the FTIR spectra of the produced nanohybrids before and after polymerization are given in Table 5.2.

The O–H stretching patterns for Kao–MAC and Kao–PMAC (Fig. 5.13b and 5.13c, respectively) are significantly different from both kaolinite (see previous chapters) and Kao–DMSO (Fig. 5.13a). The Kao–DMSO band at 3665 $cm^{-1}$ disappeared completely, and new bands appear, for Kao–MAC, at ~3652, 3639, 3602, and 3547 $cm^{-1}$, suggesting the formation of a new pattern of strong H-bonding in the interlayer space between the intercalated methacrylamide molecules and the hydroxyls of the aluminol surface. After thermal treatment, the intensity of the band at 3652 $cm^{-1}$ is greatly reduced, and the bands at 3602 and 3547 $cm^{-1}$ disappeared. The NH stretching bands, characteristic of a primary amide, can be observed before and after the heat treatment (see Table 5.2). In both cases, the asymmetric and symmetric CH stretching bands are observed in the range of ~2980–2930 $cm^{-1}$; however, for the Kao–MAC, an additional weak band can be observed at ~3090 $cm^{-1}$, attributed to the CH stretching of the unsaturated moiety (120). This band disappeared upon condensation by thermal treatment.

### 5.12.1 Evidence for polymerization from IR spectra

The FTIR spectra for the intercalation products before and after thermal treatment are depicted in Fig. 5.14a and 5.14b, respectively. The C=O stretching band was observed at ~1663 $cm^{-1}$ in both cases. CH deformation bands and CN stretching band are also observed in the range of ~1380–1460 $cm^{-1}$ in both cases. Also, δ(NH) band is observed at ~1580 $cm^{-1}$ (120, 168). The major change in the IR spectrum after heating is that the band at ~1620 $cm^{-1}$, attributed to the C=C stretching of the intercalated monomer, almost completely disappeared after thermal treatment (Fig. 5.14), thus verifying that polymerization took place upon thermal treatment.

**Table 5.2.** Major observed FTIR absorbances in the 4000–1200 $cm^{-1}$ range, attributed to the intercalates, and their assignments for the Kao–MAC intercalate and the polymerization product (Kao–PMAC).

| Wavenumber ($cm^{-1}$) | | Assignments |
|---|---|---|
| Kao–MAC | Kao–PMAC | |
| 3696 (vs) | 3696 (vs) | ν(O–H) (outer) |
| 3652 (vs)<br>3639 (vs) | 3638 (vs) | ν(O–H) (H-bonded) |
| 3621 (vs) | 3622 (vs) | ν(O–H) (inner) |
| 3602 (w, sh)<br>3547 (m) | 3554 (m)<br>3540 (m, br) | ν(O–H) (H-bonded) |
| 3493 (s)<br>3360 (m, br)<br>3191 (w, br) | 3498 (m, br)<br>3387 (m, br)<br>3203 (w) | ν(N–H) (as. and sym.) |
| 3091 (w, br) | — | C–H as. stretch (unsaturated) |
| 2954 (vw)<br>2928 (vw) | 2954 (vw)<br>2932 (vw) | ν($CH_2$) asymmetric and symmetric stretching (saturated) |
| 1663 (vs) | 1663 (vs) | ν(C=O) |
| 1615 (vs) | 1622 (sh) | ν(C=C) |
| 1588 (s) | 1591 (m) | δ(N–H) (scissors) |
| 1407 (m) | 1410 (m) | ν(C–N) |
| 1456 (m)<br>1385 (m) | 1457 (m)<br>1386 (m) | δ($CH_2$) deformation bands |

**Note:** The absorptions are w, weak; m, medium; s, strong; vw, very weak; vs, very strong; sh, shoulder; and br, broad.

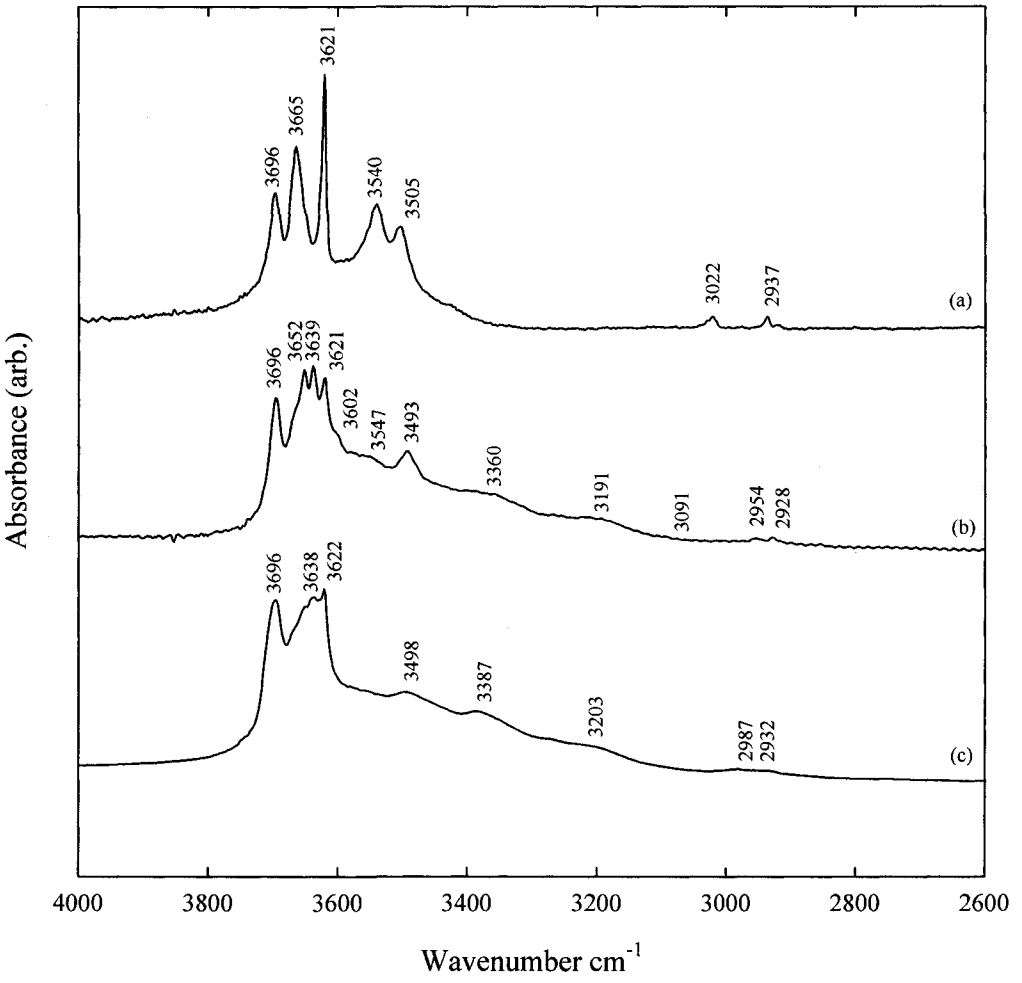


**Fig. 5.13.** FTIR spectra (4000–2600 $cm^{-1}$) of (a) Kao–DMSO, (b) Kao–MAC, and (c) Kao–PMAC.

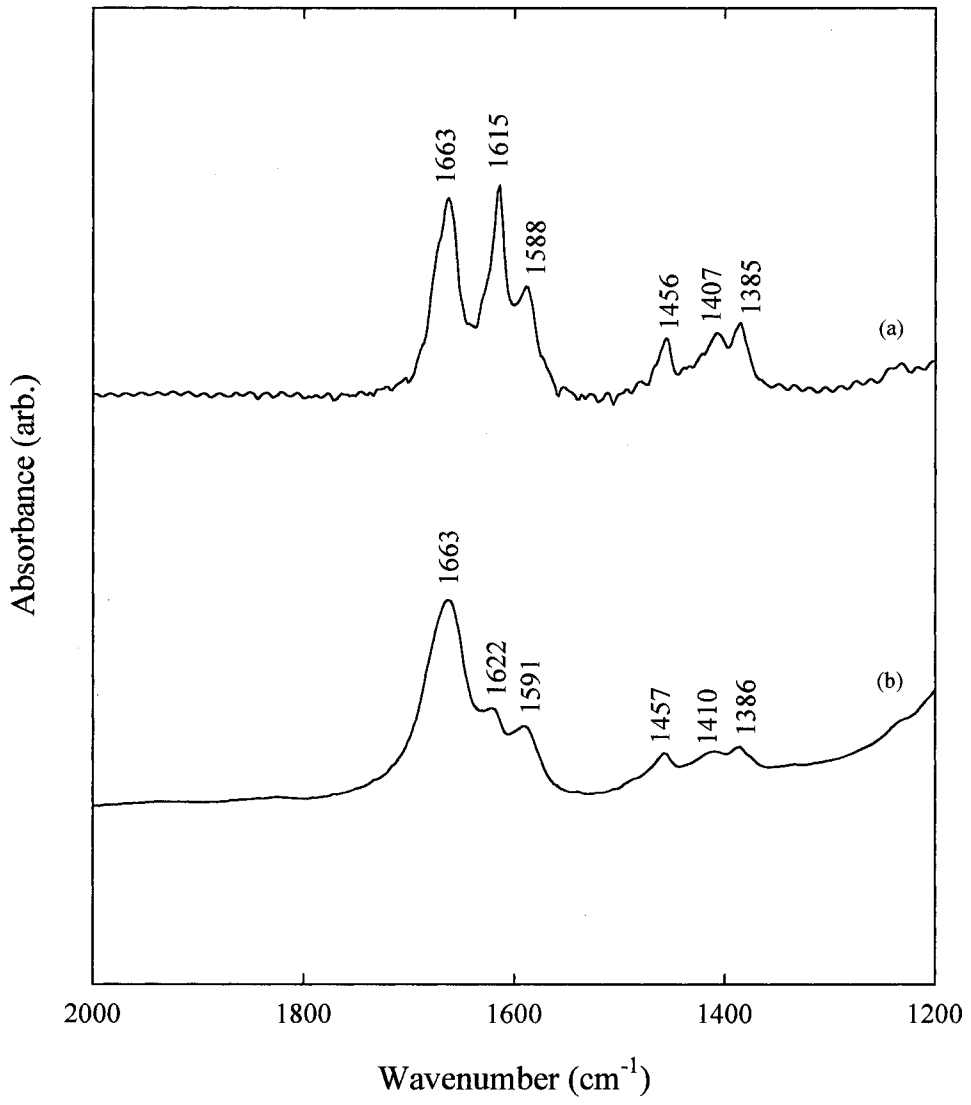


**Fig. 5.14.** FTIR spectra (2000–1200 $cm^{-1}$) of (a) Kao–MAC, and (b) Kao–PMAC.

## 5.13 Solid-state NMR analysis

### 5.13.1 $^{13}C$ NMR analysis

#### 5.13.1.1 Identification of the intercalated species and evidence for polymerization

To identify the nature of the intercalated molecules, the results of $^{13}C$ NMR CP/MAS experiments (50.31 MHz) on the produced Kao–MAC nanohybrid and the intercalated Kao–PMAC nanocomposite were studied. The spectra are stacked in Fig. 5.15.. The observed $^{13}C$ chemical shifts for the starting material (intermediate) (Kao–DMSO) are in agreement with the reported in the previous chapters (see Fig. 5.15a).

The $^{13}C$ NMR spectrum of the produced Kao–MAC nanohybrid confirmed the intercalation of methacrylamide in the interlayer spaces, and it is shown in Fig. 5.6b. Methacrylamide signals can be observed at ~19.0 ppm (methyl carbon), and two signals at ~126 and 139 ppm are unambiguously attributed to the unsaturated carbons of the methacrylamide molecule (see Chart 5.1). The signal at ~171 ppm is attributed to the amide carbonyl groups. No DMSO resonances were detected in the spectrum, indicating the complete displacement of the intermediate by the methacrylamide.

$^{13}C$ NMR spectroscopy also confirmed the polymerization of methacrylamide by both the 150 °C and the 100 °C treatments. The spectra in Fig. 5.6c and 5.6d belong to the heat treated Kao–MAC intercalate at 150 °C and 100 °C, respectively. The main features in the spectra of the polymerized samples are the shift of the carbonyl signal to ~183 ppm and the appearance of new signals at ~45 and 55 ppm, attributed to the saturated carbons ($sp^3$ hybridized) of the polymeric chain (see Chart

5.1). These signals are in excellent agreement with the values reported in the literature (156, 169) for the poly(methacrylamide). The spectra indicate that most C=C bonds disappeared, as the intensity of the bands in this region decreased, however, this also indicates the presence of residual amounts of the monomer.

#### 5.13.1.2 Dipolar dephasing experiments

Information on the dynamics of the intercalated organic molecules could also be obtained using dipolar dephasing experiments. Figure 5.16 shows the $^{13}C$ dipolar dephasing spectra of Kao–MAC, with dephasing times $\tau$ ranging from 0 to 50 μs. The signal at ~126 ppm, attributed to the protonated carbon of the methacrylamide molecule disappeared completely at a dephasing time of 30 μs, indicating that the molecules are rigidly constrained in the interlamellar spaces of kaolinite (126–128).

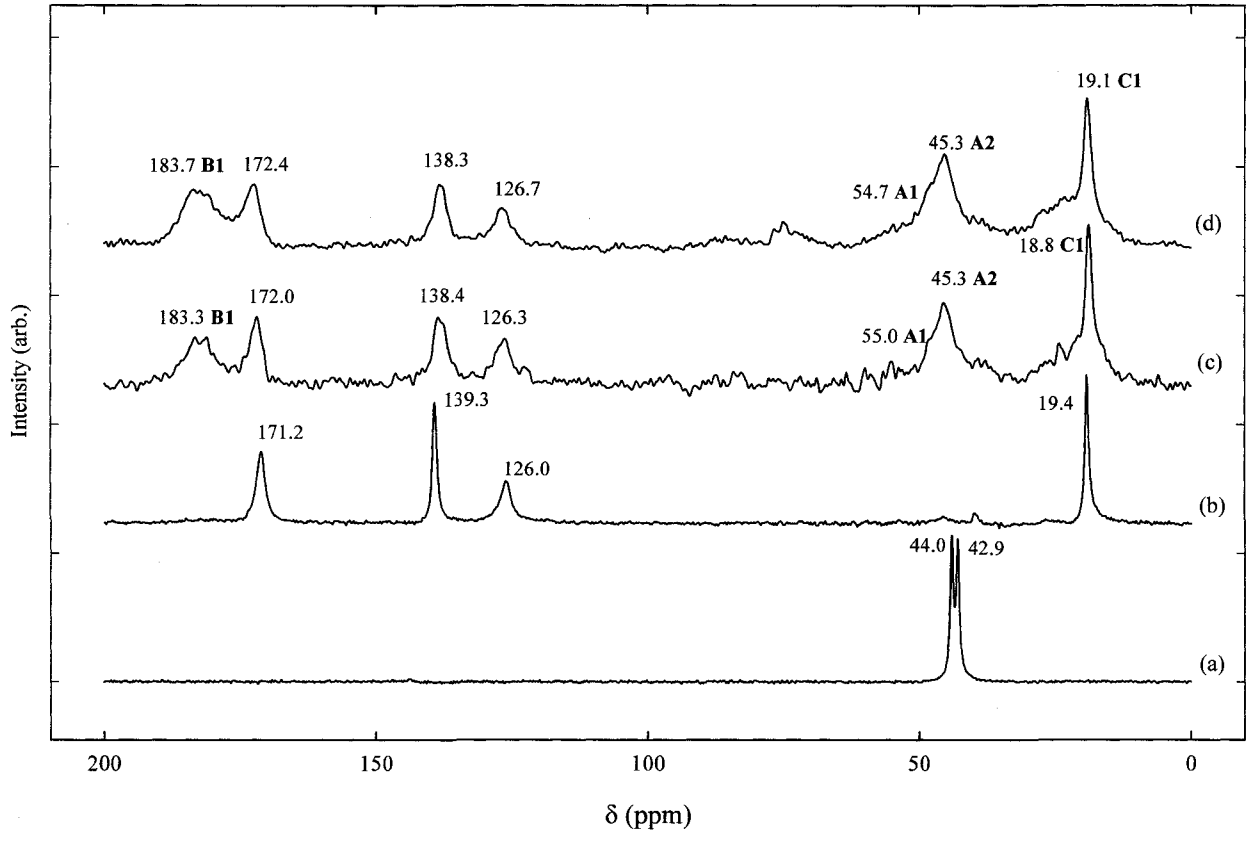


**Fig. 5.15.** Solid-state $^{13}C$ CP/MAS NMR spectra (50.31 MHz) of (a) Kao–DMSO, (b) Kao–MAC before thermal treatment, (c) Kao–MAC after heating at 150 °C for 2h, and (d) Kao–MAC after heating at 100 °C for 30 h.

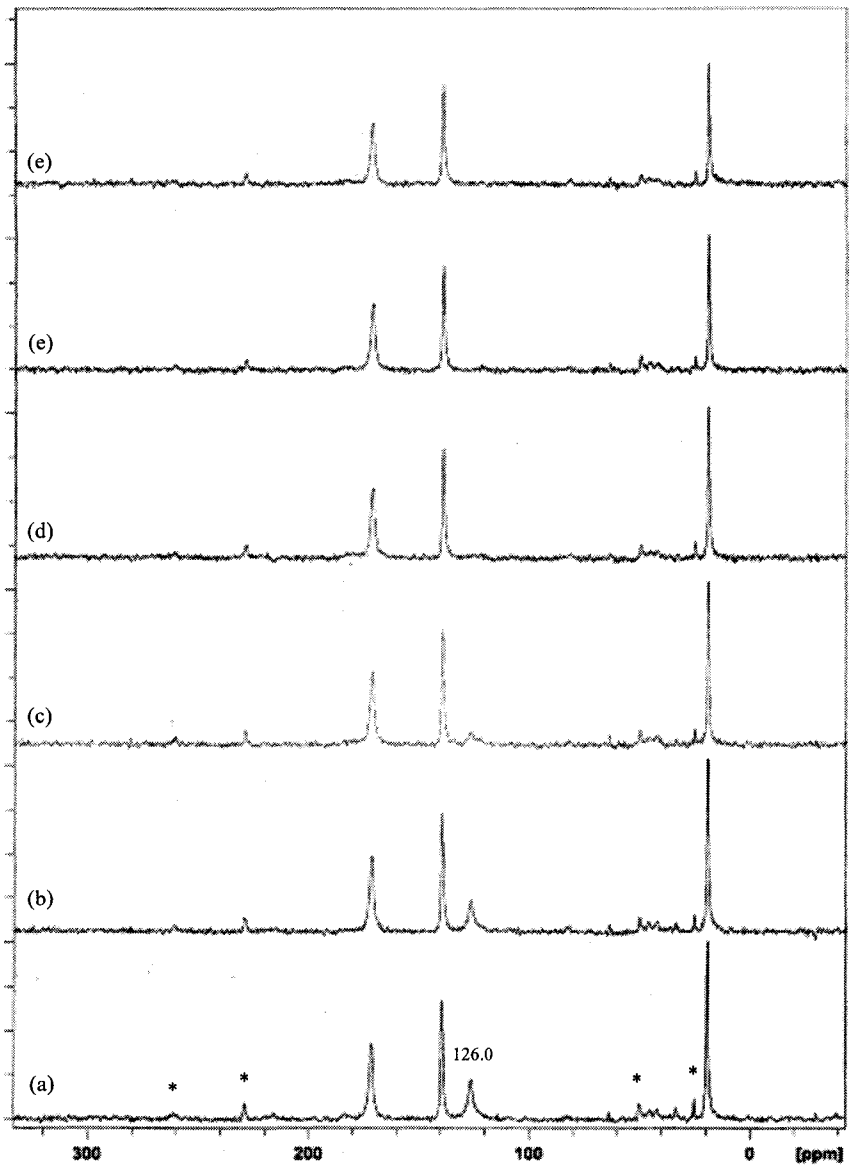


**Fig. 5.16.** Solid-state $^{13}C$ NMR spectra (50.31 MHz) of Kao–MAC: (a) CP/MAS; (b–f) dipolar dephasing, $\tau = 10$, 20, 30, 40, and 50 μs, respectively.

### 5.13.2 $^{29}$Si CP/MAS NMR

The normal $^{29}$Si CP/MAS NMR spectrum (99.35 MHz) of kaolinite is given in Fig. 5.17, displaying two well-resolved signals at –91.5 and –90.9 ppm. $^{29}$Si CP/MAS spectrum of Kao–DMSO intercalate is given in Fig. 5.17b. In addition to the residual signals of unexpanded kaolinite, one signal is observed at –92.7 ppm. Figure 5.17c gives the $^{29}$Si CP/MAS NMR spectra of the methacrylamide intercalate. The signal is slightly shifted to –92.9 ppm, and the signals due to the unexpanded kaolinite can also be observed, indicating a similar perturbation of the silicon environment by the intercalated methacrylamide molecules to that observed for the Kao–DMSO (74, 129–132).

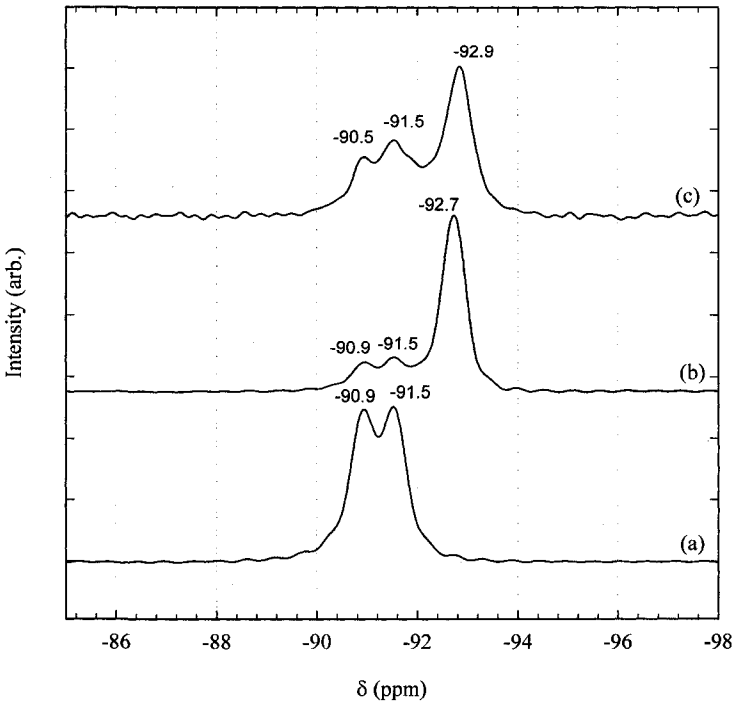


**Fig. 5.17.** $^{29}$Si MAS NMR spectra (99.35 MHz) of (a) kaolinite, (b) Kao–DMSO, and (c) Kao–MAC.

### 5.13.3 $^{27}$Al NMR analysis

Similar to the results obtained for other kaolinite intercalates (see previous chapters), $^{27}$Al NMR spectrum (130.32 MHz) of the intercalated Kao–MAC nanohybrid shows a maximum signal in the range of the octahedral aluminum (Fig. 5.18) (75, 77, 133–135).

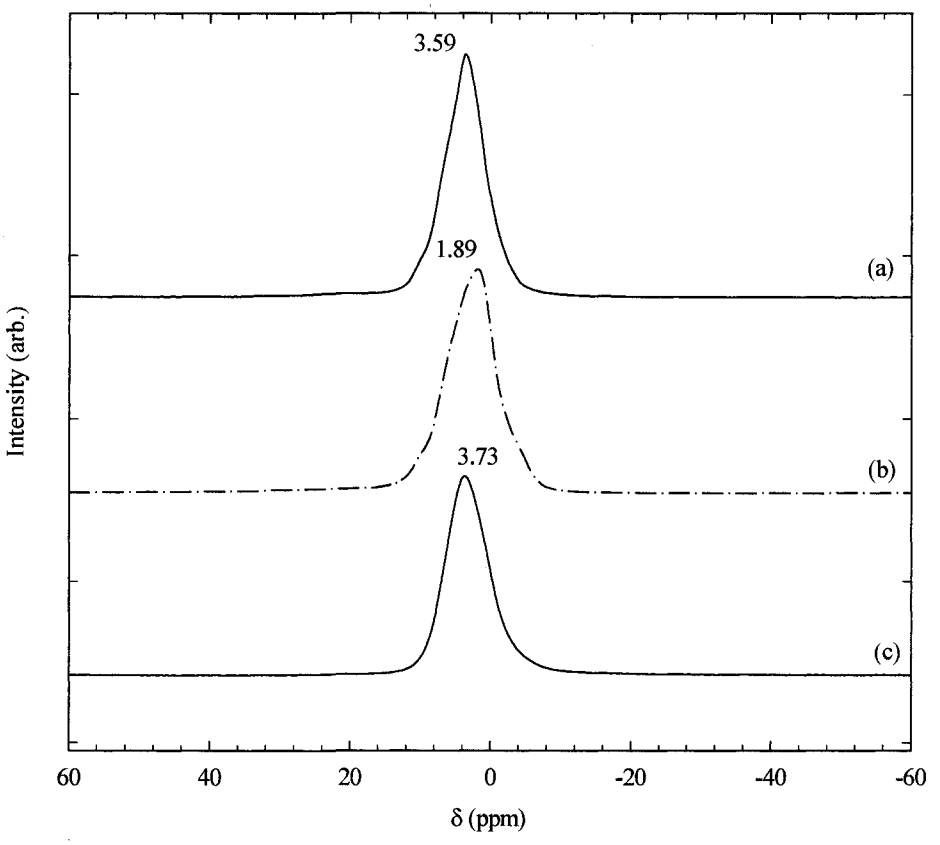


**Fig. 5.18.** $^{27}$Al MAS NMR spectra (99.35 MHz) of (a) kaolinite, (b) Kao–DMSO, and (c) Kao–MAC.

## 5.14 Thermogravimetric analysis

The TGA thermogram of the Kao–MAC intercalate in air atmosphere is exhibited in Fig. 5.19. The compound showed comparable thermal stability to that of the Kao–DMSO; however, the results also confirmed the complete displacement of DMSO molecules by methacrylamide in the interlayer spaces. In the case of Kao–MAC, the dehydroxylation step is observed at ~496 °C, accounting to ~ 13% dehydroxylation weight loss. An additional weight loss (~14%) is observed with $T_{endo}$ around 177 °C, corresponding to the loss of the organic moieties via deintercalation. Again, The final weight loss of ~1.0% is attributed to the trapped carbonaceous residue of the decomposed methacrylamide. The exothermic peak (DTA) accompanying the spinel-phase crystallization is observed around 1002 °C (136–138).

### 5.14.1 Enhanced thermal stability for the Kao–poly(methacrylamide) nanocomposite

The thermogram of the polymerized intercalated methacrylamide sample by prior thermal treatment shows enhanced thermal stability compared with the Kao–monomer sample (Fig. 5.19). The dehydroxylation stage of kaolinite, giving rise to 13% weight loss, was suppressed to a lower temperature ($T_{endo}$ = 485 °C), which is similar to other reported dehydroxylation temperatures for Kao–polymer intercalated nanocomposites (see chapter 4) (9, 18, 22). Moreover, the weight-loss stage due to the decomposition of the organic material was shifted to a much-higher temperature ($T_{exo}$ = 381 °C) with a total weight loss of ~13%. Also, the amount of the carbonaceous residue is increased to ~2.5%. The enhanced thermal stability of the polymerized sample Kao–PMAC, compared with the Kao–MAC sample, is an indication that the polymerization of methacrylamide was achieved in the interlamellar space by thermal treatment.

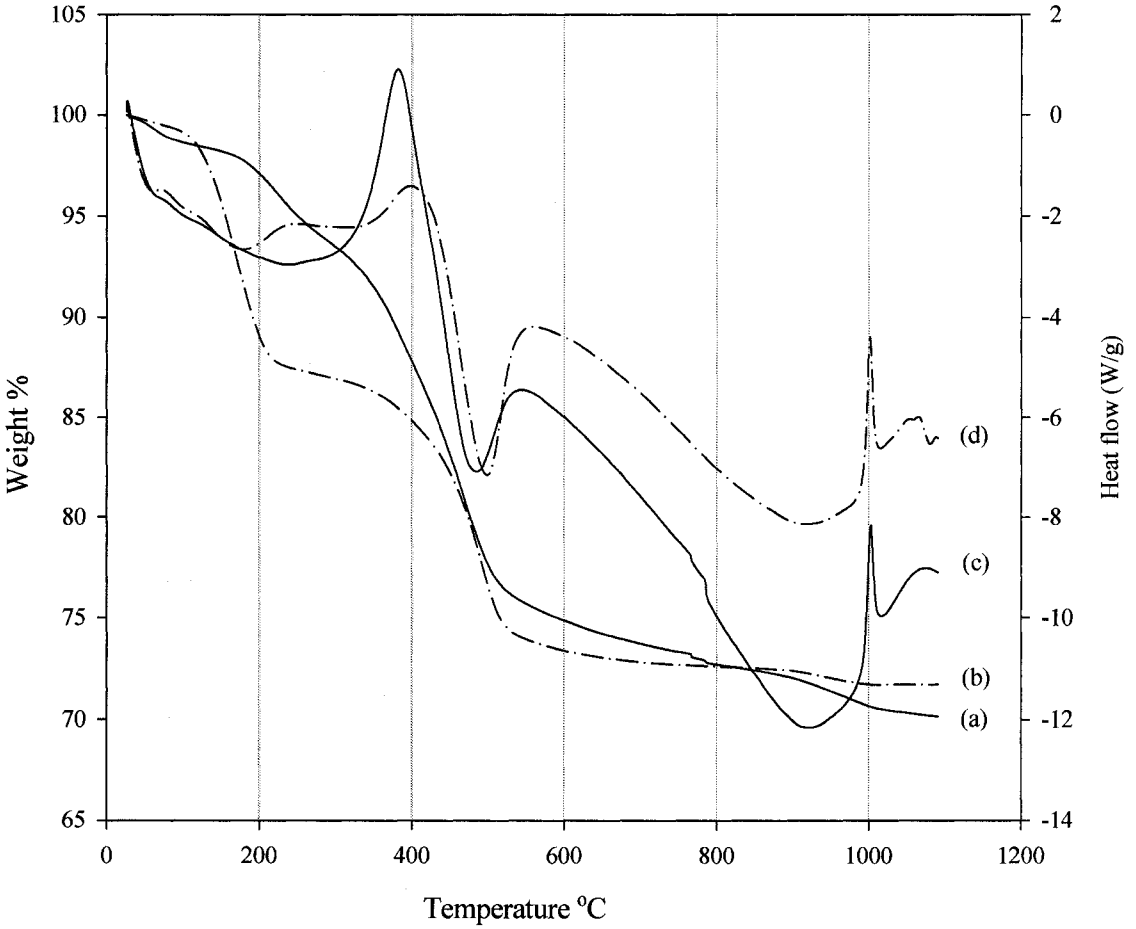


**Fig. 5.19.** TGA curves (RT–1100 °C) of (a) Kao–PMAC and (b) Kao–MAC; (c) and (d) are DTA curves of (a) and (b), respectively.

## 5.15 Elemental analysis

The results of the elemental analyses of typical Kao–MAC sample and of the polymerized sample (after thermal treatment) are given in Table 5.3. Kao–MAC sample gave C: 8.72%, H: 2.37%, and N: 2.60%. Thus, the calculated stoichiometry of this sample, based on the average of the results, is $Al_2Si_2O_5(OH)_4 \cdot (C_4H_7NO)_{0.66}$. Notably, this sample was free of the residual co-intercalated DMSO. After heat treatment, Kao–PMAC sample gave C: 6.24%, H: 2.16%, and N: 1.84%. Similarly, the stoichiometry of this sample is $Al_2Si_2O_5(OH)_4 \cdot (C_4H_7NO)_{0.52}$.

The higher average occupancy value of ~0.66 unit of MAC per unit cell of kaolinite, compared with that of the polymerized sample (0.52), is expected because of the partial deintercalation upon heat treatment, i.e., lower intercalation ratio (see Fig. 5.13).

**Table 5.3.** Summary of the CHN data of the Kao–MAC nanohybrid before and after thermal treatment.

| Sample | C (%) | H (%) | N (%) |
|---|---|---|---|
| Kao–MAC | 8.72 | 2.37 | 2.6 |
| Kao–PMAC | 6.24 | 2.16 | 1.84 |

## 5.16 An analogous attempt to prepare a kaolinite–acrylamide nanohybrid

A kaolinite–acrylamide (Kao–AC) intercalation compound was reported in the literature by Sugahara et al. (12). Acrylamide was intercalated by displacing NMF via a guest-displacement reaction. $^{13}C$ NMR confirmed the complete displacement of NMF by the acrylamide. Direct treatment with 10% acrylamide solution was unsuccessful, and the treatment had to be repeated twice to achieve the displacement. However, in this study, Kao–NMF was less successful than Kao–DMSO as an intermediate in the preparation of Kao–MAC intercalation compounds (see Table 5.1). An attempt to prepare a kaolinite–acrylamide compound using Kao–DMSO as an intermediate resulted in a product with an expansion of ~11.2 Å, similar to that observed from the literature (12, 149), after direct treatment with 10% acrylamide solution. However, $^{13}C$ NMR spectrum of the product confirmed the presence of co-intercalated residual DMSO molecules in the interlayer space (see Fig. 5.20). In conclusion, the choice of the appropriate intermediate is an important factor in achieving a successful guest-displacement intercalation.

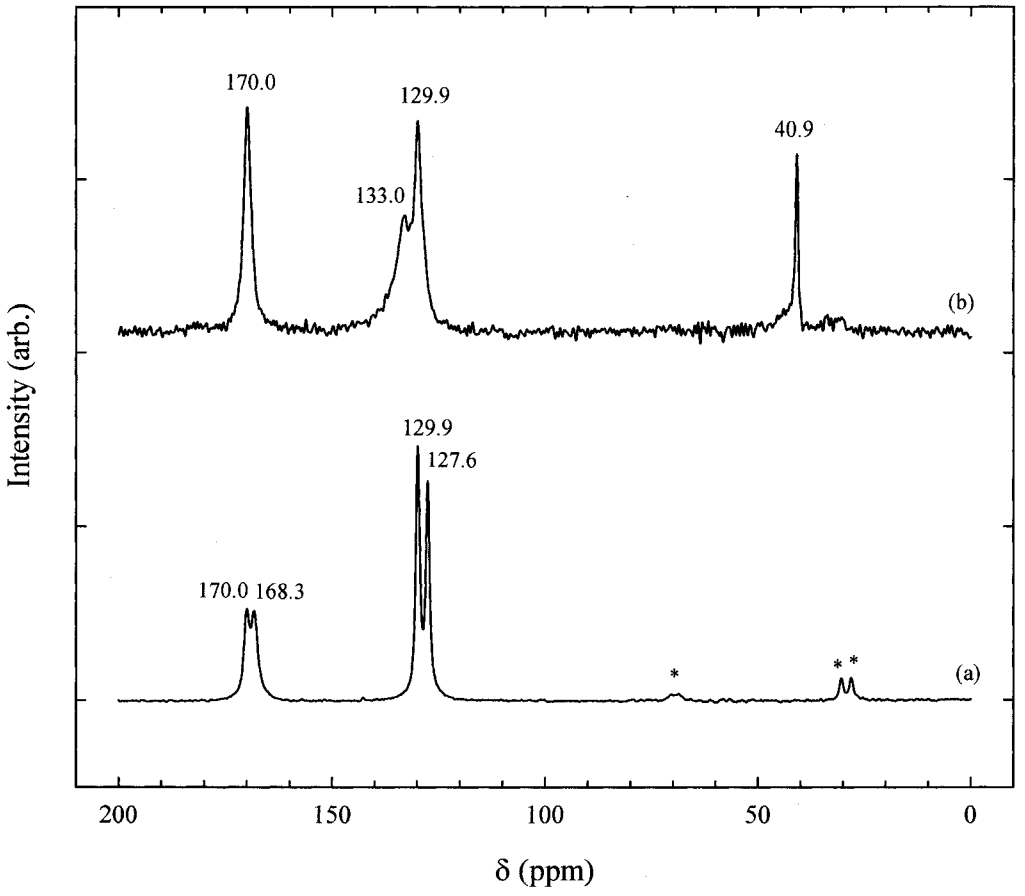


**Fig. 5.20.** Solid-state $^{13}C$ CP/MAS NMR spectra (50.31 MHz) of (a) crude acrylamide and (b) Kao–AC intercalate.

# Chapter 6

# Experimental work

## 6.1 Chemicals and reagents

All chemicals used were of reagent-grade quality and were not further purified unless otherwise specified. Well-crystallized kaolinite from Georgia (labeled KGa-1b) was obtained from the Source Clay Repository of the Clay Mineral Society (Department of Geology, University of Missouri). This was purified based on previously reported sedimentation techniques (170), and the <2 μm size fraction was used.

## 6.2 Instrumentation

### 6.2.1 X-ray diffraction (XRD)

XRD powder patterns were performed on a Philips PW 3710 diffractometer using a generator voltage of 45 kV and a generator current of 40 mA. Typically, a step size of 0.04° ($2\theta$) was used with a dwell time of 0.5 s/step in a continuous scan mode. The sample was spun during the acquisition, and a 12 mm automatic divergence slit was used together with a 0.2 mm fixed receiving slit, 1° secondary antiscatter slit, and a 10 mm fixed incident-beam mask. The ratio of intercalation (RI) was calculated from the relative intensities of the (001) reflections of the organo-kaolinite phase and of the residual kaolinite phase (see Chapter 1) (5). All the important XRD data are given in the appropriate tables in each Chapter.

### 6.2.2 Infrared spectroscopy (FTIR)

Infrared spectra were acquired on a Thermo–Nicolet Nexus 670 FT-IR spectrometer under dry air using 32–256 scans with a resolution of 2–4 $cm^{-1}$. The samples were prepared as KBr pellets from 50 mg of a mixture of 0.25–0.5 wt% sample in KBr. Peak positions were either picked manually or automatically, using the instrument installed software.

### 6.2.3 Nuclear magnetic resonance (NMR) spectroscopy

$^{13}C$ CP/MAS and DD/MAS NMR spectra were obtained on a Bruker ASX-200 instrument operating at 50.31 MHz at a spinning rate of 4.0–5.0 kHz and a contact time of 2 ms in most cases. $^{13}C$ DD/MAS spectra were obtained on the same instrument, using a dipolar dephasing time of $\tau$ = 10–50 μs with the same number of scans as used for the cross polarization experiment. The spectra were referenced to adamantane at $\delta$ = 38.4 ppm. Some spectra were obtained on a Bruker AVANCE-500 instrument operating at 125.77 MHz at a spinning rate of 12–14.5 kHz.

$^{29}Si$ CP/MAS NMR spectra were obtained on a Bruker AVANCE-500 instrument operating at 99.35 MHz at a spinning rate of 6.0 kHz and a contact time of 8–10 ms. The spectra were referenced to tetramethyl silane (TMS) at 0.0 ppm.

$^{27}Al$ MAS NMR spectra were obtained on a Bruker AVANCE-500 instrument operating at 130.32 MHz at a spinning rate of 12–14.0 kHz. All $^{27}Al$ spectra were referenced to a 0.1 mol/L solution of $Al(NO_3)_3 \cdot 9H_2O$.

Solution HMQC $^{13}C$–$^{1}H$ NMR experiment was performed on a Varian XL-300 instrument, and the sample was dissolved in $D_2O$.

### 6.2.4 Thermogravimetric analysis (TGA/DTA)

All thermal analyses (TGA and DTA) were carried out on an SDT 2960 Simultaneous DSC–TGA instrument (TA Instruments) under nitrogen or air flow (100 mL $min^{-1}$) at a heating rate of 10–20 °C $min^{-1}$. Approximately 10–20 mg samples were used for each run. In all cases, the given TGA weight-loss data was determined approximately using the instrument installed software (TA Analysis), which was also used for determining the DTA peak maxima $T_{exo}$ or $T_{endo}$.

### 6.2.5 Elemental analyses

Organic elemental analyses (CHNOS, combustion analysis) were performed on selected samples by Chemisar laboratories Inc., Guelph, ON, Canada. Essentially, the reference method is ASTM D5373/D5291, which is the standard method for the determination of elemental carbon, hydrogen, and nitrogen as well as oxygen and sulphur.

The method requires that an accurate weight (few milligrams) of the sample to be placed into an oxidation–reduction reactor tube and combusted at ~1000 °C. The combustion gases produced ($CO_2$, $N_2$, and $H_2O$) are then passed on to the gas chromatograph (GC) using ultra high purity helium as the carrier gas. The gas chromatograph is equipped with a TCD (Thermal Conductivity Detector), which analyzes the concentrations of $CO_2$, $N_2$,

$H_2O$, and $SO_2$ , then the percentages of carbon, hydrogen, nitrogen, and sulphur are calculated using the instrument software. The same procedure is used for oxygen determination. The instrument used was a Fisons/Carlo Erba EA 1108, and the balance was a Sartorius M2P MicroBalance. NIST traceable organic compounds were used as primary reference standards for instrument calibration. A NIST traceable standard was also used as an unknown or control sample.

### 6.2.6 Density measurements

The density of the kaolinite powder was measured using a Micromeritics pycnometer using helium as the filler gas. Calibration of the volume of the sample container was done using metal spheres whose volumes were accurately known. The powders were repeatedly purged with helium to remove as much nitrogen and oxygen as possible from the sample and the container.

### 6.2.7 Particle-size analysis

Particle-size analysis was performed using a Micromeritics Sedigraph 5100-series instrument. A 0.05% sodium metaphosphate solution was used as the background liquid and dispersant solution. The analysis was performed using the solvent parameters for pure water for the software data treatment, and a sample cell calibration was performed before each run together with a solvent background correction. The density values of the samples were measured using a helium pycnometer (see Section 7.2.6); however, in some cases,

typical values from the literature were used. The analysis was performed at room temperature, and the instrument bubble detection was set to low and pump speed to high.

## 6.3 Experimental procedures

### 6.3.1 Preparation and characterization of the starting materials

#### 6.3.1.1 Purification of kaolinite

Well crystallized Georgia KGa-1b kaolinite was purchased from the Source Clay Repository of the Clay Mineral Society (University of Missouri). KGa-1b was purified according to the previously reported sedimentation techniques (170–173). In a typical purification, the crude product (~60 g) was mixed with 4.0 L of deionized water. This gave a strongly flocculated suspension with a pH ranging from 4.5–6.0. Vigorous mechanical stirring was maintained, and the pH was adjusted to 9.0 through the careful dropwise addition of 0.1 N NaOH solution. At this pH, the particles were no longer flocculated, but were in the form of a suspension. Thus, the stirring was stopped, the 4 L beaker was covered with a watch glass, and the sedimentation was allowed to proceed. After 6 h, the top 15–20 cm of the mixture were carefully siphoned off. This process was repeated one more time with the remaining sediment. The supernatant colloidal solution from this was combined with that of the previous batch. The coarse sediment was then discarded.

The pH of the combined dispersed supernatant was then adjusted to pH = 6.0 through the careful dropwise addition of 0.1 N HCl, upon which the dispersion flocculated. Flocculation was allowed to occur until a well defined sediment was formed with a clear

supernatant solution above the sediment. The supernatant was then siphoned off and discarded. The sediment was suction filtered and washed with deionized water until the washings showed no trace of chloride from saturated $AgNO_3$ solution. The purified kaolinite was then air-dried followed by drying for at least 8 h in an oven at 100 °C. The product was then characterized by particle-size analysis, XRD, FTIR, NMR, and TGA/DTA, which all supported previously reported literature data on KGa-1b kaolinite.

XRD Å (intensity%): $d_{001}$ = 7.15 (73); $d_{020}$ = 4.47 (22); $d_{1\text{–}10}$, $d_{110}$ = 4.36 (33); $d_{11\text{–}1}$ = 4.18 (28); $d_{02\text{–}1}$ = 3.850 (15); $d_{021}$ = 3.740 (10); $d_{002}$ = 3.57 (100); Anatase ($TiO_2$) impurity: 3.51 (17.7); $d_{111}$ = 3.38 (11); $d_{1\text{–}1\text{–}2}$ = 3.11 (3.8); $d_{022}$ = 2.745 (3.8); $d_{060}$, $d_{33\text{–}1}$, $d_{3\text{–}3\text{–}1}$ = 1.490 (27).

FTIR (KBr, $cm^{-1}$): ν(O–H): 3695 (s), 3666 (m), 3654 (m), 3620 (s); Si–O: 1116 (s), 1033 (vs), 1010 (vs); δ(Al–OH): 939 (m, sh), 914 (s); other bands: 793 (w), 755 (w), 701 (m), 650 (w), 543 (s), 472 (s), 432 (m).

$^{29}Si$ CP/MAS (ppm): –90.9 and –91.5. $^{27}Al$ MAS (ppm): 3.54.

TGA/DTA (100 mL/min air, 10 °C/min, TGA wt. losses are approximate): $T_{endo}$ = 61 (w) and 516 °C (s), $T_{exo}$ = 1000 °C (s); total TGA weight loss = 13.5 %.

Several helium pycnometer measurements showed that the crude KGa-1b kaolinite had an average density of 2.55 g $cm^{-3}$, which is in agreement with the reported values (174). This density value was used for the particle-size analysis (Sedigraph 5100), which showed for all batches that at least 93% of the sample was less than 2 μm, i.e., the coarser fractions were removed by sedimentation.

XRD showed the presence of a small quantity of residual anatase ($TiO_2$) by a sharp reflection at $d$ = 3.51 Å. Otherwise, XRD confirmed the well-crystallized nature of

kaolinite (1). FTIR analysis of the O–H stretching region also confirmed the crystallinity of the purified material (59). Also, the recorded TGA/DTA and NMR results for representative purified samples were in agreement with what was reported in the literature studies on kaolinite (74, 75, 77, 129–138).

### 6.3.1.2 Preparation and characterization of Kao–DMSO intercalate

The Kao-DMSO intercalate was typically prepared by mixing 20 g of KGa-1b with 100 mL of DMSO in a sealed jar for a sufficient time (1–5 months) with occasional stirring to achieve maximum intercalation. The product was vacuum-filtered and washed with 1,4-dioxane to remove excess DMSO and then air-dried to yield an off-white powder. Characterization of a representative sample gave:

XRD: $d_{001}$ = 11.16 Å (100.0), $d_{001}$(Kao) = 7.15 Å (9.7), $d_{002}$ = 5.6 Å (4.2), $d_{003}$ = 3.72 Å (45.7), $d_{002}$(Kao) = 3.57 Å (14.6), $d_{004}$ = 2.8 Å (1.8), $d_{060}$ = 1.49 Å (7.6), RI = 0.91–0.98 (various samples). FTIR (KBr, $cm^{-1}$): ν(OH) 3696 (m), ν(OH) 3665 (s), ν(OH) 3621 (s), ν(OH) 3540 (m), ν(OH) 3505 (m), ν(C–H) 3022 (w), ν(C–H) 2937 (w), δ(C–H) 1429 (w), δ(C–H) 1407 (w), δ(C–H) 1394 (w), δ(C–H) 1318 (w); (Si–O) vibrations: 1123 (s), 1101 (s), 1039 (s), 1016 (s); δ(Al–OH): 958 (m), 940 (w), 905 (s); other bands: (Si–O–Si) 790 (w), (Si–O–Si) 744 (w), (Si–O–Si) 688 (m), 606 (w), (Al–O–Si) 552 (s), (Si–O) 465 (s), (Si–O) 435 (s). $^{13}C$ CP/MAS NMR (50.31 MHz, ppm) δ: 43.98 and 42.89 ($CH_3$). $^{29}Si$ CP/MAS (ppm): –90.9 , –91.5, and –92.7. $^{27}Al$ MAS (ppm): 1.78. TGA/DTA (air): RT–245 °C (17.5% wt. loss, $T_{endo}$ = 98 °C and 195 °C); 245–725 °C (11.4 % wt. loss, $T_{endo}$ = 513 °C); $T_{exo}$ = 1000 °C; total TGA weight loss = 28.7%.

### 6.3.1.3 Preparation of Kao–$CH_3COOK$ intercalate

Approximately 3.0 g of purified KGa-1b were ground together with ~3.0 g of potassium acetate $CH_3COOK$ using a mortar and pestle for 10–15 minutes. The mixture became pasty because of the hygroscopic nature of potassium acetate, then it was covered and left for two weeks with occasional grinding. Afterwards, it was washed was 2-propanol, centrifuged, and air-dried.

XRD: $d_{001}$ = 13.98 Å (100.0), $d_{001}$(Kao) = 7.02 Å (8.8), $d_{003}$ = 4.68 Å (2.4), $d_{002}$(Kao) = 3.52 Å (55.0), RI = 0.93. FTIR (KBr, $cm^{-1}$): ν(OH) 3695(m), ν(OH) 3670 (vw), ν(OH) 3649 (w), ν(OH) 3619 (s), ν(OH) 3605 (s), ν(OH) 3455 (s,br), ν(C–H) 2929 (w), ν(C–H) 2856 (w), δ(HOH) 1653 (m), ν($COO^-$) 1604 (s), 1419 (s), (Si–O) vibrations: 1114 (s), 1031 (vs), 1007 (vs), δ(Al–OH): 942 (w,sh), 911 (w,sh), 899 (s), other bands: Si–O–Si 794(w), Si–O–Si 753 (m), Si–O–Si 698 (m), 668 (m), 649 (m), Al–O–Si 559 (s), Si–O 472 (s), Si–O 436 (s). $^{13}C$ CP/MAS (ppm) δ: 24.07 ($CH_3$) and 180.21 (C=O). $^{29}Si$ CP/MAS (ppm): –90.7. $^{27}Al$ MAS (ppm): 4.02. TGA: RT–100 °C (9.0% wt. loss, $T_{endo}$ = 86.0 °C); 100–585 °C (22.6% wt. loss, $T_{endo}$ = 305 °C and 377 °C); 585–1053 °C (2.4% wt. loss); total TGA weight loss = 34.0%.

### 6.3.1.4 Preparation of Kao–NMF intercalate

Approximately 20 g of KGa-1b were mixed with 100 ml of *N*-methyl formamide in a sealed container for a sufficient time (~1 month) with occasional stirring to achieve

maximum intercalation. After that, the product was filtered and washed with 1,4-dioxane to remove excess NMF and then air-dried.

XRD: $d_{001}$ = 10.71 Å (100.0), $d_{001}$(Kao) = 7.15 Å (18.9), $d_{002}$ = 5.28 Å (0.6), $d_{003}$ = 3.58 Å (71.7), RI = 0.87. FTIR (KBr, $cm^{-1}$): ν(OH) 3695 (m), ν(OH) 3652 (vw), ν(OH) 3620 (s), ν(OH) 3600 (w), ν(OH) 3550 (m,br), ν(N-H) 3420 (s), ν(C–H) 2924 (w), ν(C–H) 2910 (w), ν(C=O) 1682 (s), (amide II) 1529 (m), δ(C–H) 1419 (w), δ(C–H) 1384 (m), δ(C–H) 1318 (w), δ(C–H) 1232 (vw); (Si–O) vibrations: 1104 (s), 1034 (s), 1009 (s); δ(Al–OH): 958 (m), 949 (vw), 911 (s); other bands: (Si–O–Si) 791 (w), (Si–O–Si) 746 (w), (Si–O–Si) 688 (m), 637 (w), (Al–O–Si) 545 (s), (Si–O) 470 (s), (Si–O) 434 (s). $^{13}C$ CP/MAS (ppm) δ: 26.81 (N–$CH_3$) and 163.98 (C=O). TGA: RT–300 °C (10.9% wt. loss, $T_{endo}$ = 55 °C and 190 °C); 300–704 °C (12.5% wt. loss, $T_{endo}$ = 519 °C); $T_{exo}$ = 1002 °C; total TGA weight loss = 23.8%.

## 6.3.2 Experiments of Chapter 2

### 6.3.2.1 Preparation of Kao–SIM by the reaction of succinimide with Kao–DMSO: Kao–SIM1, SIM2, and SIM4

In this series of experiments, Kao–SIM was prepared by the displacement of DMSO with succinimide. The mixture of Kao–DMSO (1 g) and an aqueous solution of succinimide (10% *w/v*, 100 mL) was stirred for 23–114 h at room temperature (see Table 2.1 for details), and the product was vacuum-filtered, washed with 2-propanol, and air-dried to yield an off-white powder. For detailed spectroscopic data, see the tables of Chapter 2.

#### 6.3.2.2 Preparation of Kao–SIM by the reaction of succinimide with Kao–NMF: Kao–SIM3

Kao–SIM was prepared by the displacement of NMF from the Kao–NMF intercalate with succinimide. The mixture of Kao–NMF (1 g) and an aqueous solution of succinimide (10% *w/v*, 100 mL) was stirred for 43 h at room temperature (see Table 2.1 for details), and the product was vacuum-filtered, washed with 2-propanol, and air-dried to yield an off-white powder.

#### 6.3.2.3 Preparation of Kao–GIM by the reaction of glutarimide with Kao–DMSO: Kao–GIM1 and GIM2

In this series of experiments, Kao–GIM was prepared by the displacement of DMSO with glutarimide. The mixture of Kao–DMSO (1 g) and an aqueous solution of glutarimide (10% *w/v*, 100 mL) was stirred for 69 and 24 h, respectively, at room temperature (see Table 2.1 for details), and the products were vacuum-filtered, washed with 2-propanol, and air-dried. For detailed spectroscopic data, see the tables of Chapter 2.

#### 6.3.2.4 The reaction of succinimide with KGa-1b

A mixture of KGa-1b (1 g) and an aqueous solution of succinimide (10% *w/v*, 100 mL) was stirred for 75 h at room temperature (see Table 2.1 for details), and the product was vacuum-filtered, washed with 2-propanol, and air-dried to yield an off-white powder. XRD showed that no reaction has taken place, as the $d_{001}$ obsereved was that of the pure kaolinite = 7.17 Å.

#### 6.3.2.5 Effect of water washing on the Kao–SIM intercalate

A portion of Kao–SIM1 sample was washed with approximately 20 mL of deionized water and then air-dried for a sufficient time. XRD analysis confirmed the partial de-intercalation of the sample after washing (see Chapter 2).

### 6.3.3 Experiments of Chapter 3

#### 6.3.3.1 Preparation of Kao–D-sorbitol (Ia)

D-Sorbitol (2.5 g, Aldrich) and Kao–DMSO (0.5 g, prepared from KGa-1b) were slowly heated to 125 °C in a 50 ml round-bottom flask placed in a heated oil bath to melt the D-sorbitol. The reaction was allowed to proceed with continuous stirring for a total of 9 days (216 h). The reaction mixture was light brown in color and was separated by centrifugation and repeated washing to remove excess D-sorbitol. The off-white product obtained was air-dried on a glass plate. XRD: $d_{001}$ = 11.88 Å (100.0), $d_{001}$(Kao) = 7.32 Å (21.3), $d_{002}$ = 5.82 Å (1.7), $d_{003}$ = 3.86 Å (10.6), $d_{002}$(Kao) = 3.62 Å (13.3), $d_{004}$ = 2.89 Å (0.5), $d_{003}$(Kao) = 2.4 Å (1.2), $d_{060}$ = 1.49 Å (0.4), RI = 0.82. FTIR (KBr, $cm^{-1}$): (OH) 3695 (m), 3619 (m), 3482 (br, m), (C–H) 2949 (vw), 1830 (vw), (HOH) 1635 (w), (C–H) 1466 (w), 1403 (w); Si–O vibrations: 1106 (s), 1025 (s); (Al–OH): 962 (w), 937 (w), 912 (s); other bands: 792 (w), 754 (w), 698 (m), 544 (s), 470 (s), 433 (s). $^{13}C$ CP/MAS: broad envelope of peaks with maxima at 64, 73, and 77 ppm. $^{13}C$ DD/MAS: no signal was observed for a dipolar dephasing time of 40 μs. TGA: 20–130 °C (2.6% wt. loss, $T_{endo}$ = 105 °C); 130–307 °C (3.0% wt. loss, $T_{endo}$ = 261 °C); 307–436 °C (6.0% wt. loss); 436–552

°C (9.8% wt. loss, $T_{endo}$ = 493 °C); 552–1100 °C (4.2% wt. loss, $T_{exo}$ = 1000 °C); total TGA weight loss: 25.6%.

### 6.3.3.2 Preparation of Kao–D-sorbitol (Ib and Ic)

D-Sorbitol (2.1 g, Aldrich) and Kao–DMSO (0.3 g, prepared from KGa-1b) were slowly heated to 125 °C in a 50 ml round-bottom flask placed in a heated oil bath to melt the D-sorbitol. The reaction was allowed to proceed with continuous stirring for a total of 11 days (264 h). After the reaction mixture was allowed to cool to room temperature, it was divided into two parts and half of it was worked up in water (**Ib**) and the other half of the reaction mixture was worked up in acetic acid (**Ic**) to remove the excess D-sorbitol. The product was separated by centrifugation and air-dried on a glass plate (color: off-white). XRD: **Ib**: $d_{001}$ = 11.88 Å (78.7) and 10.67 Å (100.0), $d_{001}$(Kao) = 7.31 Å (24.7), $d_{002}$ = 5.84 Å (3.7), $d_{003}$ = 3.84 Å (12.2), $d_{002}$(Kao) = 3.62 Å (9.6), $d_{003}$(Kao) = 2.4 Å (0.9), $d_{060}$ = 1.49 Å (0.3), RI = 0.80 (based on the peak intensity counts of the more intense $d_{001}$ peak); **Ic**: $d_{001}$ = 11.87 Å (59.9) and 10.43 Å (100.0), $d_{001}$(Kao) = 7.31 Å (55.0), $d_{002}$ = 5.87 Å (2.1), $d_{003}$ = 3.85 Å (13.2), $d_{002}$(Kao) = 3.62 Å (26), $d_{003}$(Kao) = 2.4 Å (1.9), $d_{060}$ = 1.49 Å (0.5), RI = 0.64 (based on the peak intensity counts of the more intense $d_{001}$ peak). FTIR (KBr, $cm^{-1}$): **Ib**: (OH) 3696 (s), 3620 (s), 3600 (s), 3555 (m), 3451 (br, w), (C–H) 2927 (vw), (HOH) 1628 (vw), (C–H) 1401 (w), 1384 (m), 1260 (vw); Si–O vibrations: 1108 (s), 1031 (s), 1009 (s); (Al–OH): 968 (w), 945 (w, sh), 911 (s); other bands: 791 (w), 756 (w), 698 (m), 672 (w, sh), 550 (s), 474 (s), 434 (s). FTIR (KBr, $cm^{-1}$) **Ic**: (OH) 3695(m), 3618 (m), 3598 (m), 3549 (m), (C–H) 2948 (vw), 1965 (w), 1818 (w), (HOH) 1630 (w), (C–H) 1404

(w); Si–O vibrations: 1108 (s), 1102 (s), 1095 (s), 1038 (s), 1030 (s), 1022 (s), 1011 (s), 1005 (s); (Al–OH): 969 (w), 940 (w), 909 (s); other bands: 789 (w), 756 (w), 700 (m), 672 (m), 545 (s), 472 (s), 428 (s). $^{13}$C CP/MAS: **Ib**: broad envelope of peaks with maxima at 66, 73, and 77 ppm; **Ic**: broad envelope of peaks with maxima at 66, 71, and 76 ppm. $^{13}$C DD/MAS (**Ib** and **Ic**): no signal was observed for a dipolar dephasing time of 40 μs. TGA: **Ib**: 20–117 °C (1.0% wt. loss, $T_{endo}$ = 69 °C); 117–356 °C (3.1% wt. loss, $T_{endo}$ = 199 °C and 323 °C); 356–759 °C (13.7% wt. loss, $T_{endo}$ = 493 °C); 759–1088 °C (1.6% wt. loss, $T_{exo}$ = 1007 °C); total TGA weight loss: 19.4%. **Ic**: 20–116 °C (2.4% wt. loss, $T_{endo}$ = 68 °C and shoulder at 94 °C); 116–342 °C (3.8% wt. loss, $T_{endo}$ = 177 °C, 215 °C, and 257 °C); 342–430 °C (2.4% wt. loss); 430–563 °C (10.8% wt. loss, $T_{endo}$ = 502 °C); 563–1101 °C (3.5% wt. loss, $T_{exo}$ = 998 °C); total TGA weight loss: 22.9%.

#### 6.3.3.3 Preparation of Kao–D-sorbitol (Id)

A mixture of D-sorbitol (1.5 g, Aldrich) and Kao–DMSO (~0.3 g, prepared from KGa-1b) was slowly heated to 110 °C in a round-bottom flask placed in an oil bath with continuous stirring for a period of 6 days (144 h). After the reaction mixture was allowed to cool to room temperature, it was washed repeatedly with deionized water (DIW), using centrifugation to dissolve the excess D-sorbitol. The off-white product was then air-dried. XRD: $d_{001}$ = 10.55 Å (86.6) with a shoulder at 8.52 Å (54.3), $d_{001}$(Kao) = 7.33 Å (100.0), $d_{002}$ = 5.8 Å (0.3), $d_{002}$(Kao) = 3.62 Å (50.0), $d_{060}$ = 1.50 Å (3.1), RI = 0.46. FTIR (KBr, cm$^{-1}$): (OH) 3694 (m), 3618 (m), 3599 (m), 3556 (m), (C–H) 2946 (w), 2894 (w), 1957 (w), 1819 (w), (HOH) 1630 (w), (C–H) 1400 (w), 1383 (w); Si–O vibrations: 1105 (s);

(Al–OH): 968 (m), 941 (m), 911 (m); other bands: 789 (w), 755 (w), 700 (m), 675 (m), 475 (s), 433 (m).

#### 6.3.3.4 Preparation of Kao–adonitol (IIa)

A mixture of adonitol (1.5 g, Aldrich) and Kao–DMSO (~0.3 g) was slowly heated in a round-bottom flask placed in an oil bath with continuous stirring so that the temperature of the oil bath was enough to keep that of the reaction mixture slightly above the melting point (102–104 °C). The reaction was allowed to proceed for a total of 6.5 days. After cooling the reaction mixture (beige in color) to room temperature, the product was separated by centrifugation and repeatedly washed with fresh DIW to dissolve the excess adonitol. The off-white product was air-dried on a glass plate. XRD: $d_{001}$ = 10.36 Å (100.0), $d_{001}$(Kao) = 7.32 Å (17.2), $d_{002}$ = 5.1 Å (0.5), $d_{002}$(Kao) = 3.62 Å (7.2), $d_{003}$ = 3.38 Å (2.6), $d_{004}$ = 2.58 Å (0.4), $d_{003}$(Kao) = 2.4 Å (0.7), $d_{060}$ = 1.49 Å (0.1), RI = 0.85. FTIR (KBr, $cm^{-1}$): (OH) 3693 (m), 3618 (m), 3598 (m), 3550 (m), 3434 (br, m), (C–H) 2941 (w), 1955 (w), 1817 (w), (HOH) 1630 (w), (C–H) 1383 (vw); Si–O vibrations: 1108 (s), 1102 (s), 1038 (s), 1029 (s), 1023 (s), 1011 (s), 1006 (s), 1000 (s); (Al–OH): 969 (w), 941 (w), 906 (s); other bands: 789 (w), 756 (w), 701 (m), 673 (m), 546 (s), 472 (s), 429 (s). $^{13}C$ CP MAS: broad envelope of peaks with maxima at 62 and 72 ppm. $^{13}C$ DD MAS: no signal was observed for a dipolar dephasing time of 40 μs. TGA: 20–115 °C (5.2% wt. loss, $T_{endo}$ = 75 °C and a shoulder at 106 °C); 115–409 °C (3.0% wt. loss); 409–569 °C (10.8% wt. loss, $T_{endo}$ = 516 °C); 569–1107 °C (2.4% wt. loss, $T_{exo}$ = 997 °C); total TGA weight loss: 21.4%.

### 6.3.3.5 Preparation of Kao–adonitol (IIb)

Adonitol (1.5 g, Aldrich) and Kao–DMSO (0.3 g, prepared from KGa-1b) were slowly heated to 110 °C in a round-bottom flask placed in an oil bath with continuous stirring for a period of 6 days (144 h). After the reaction mixture was allowed to cool to room temperature it was washed repeatedly with deionized distilled water using centrifugation in order to remove excess adonitol. The product was air-dried and was an off-white color. XRD: $d_{001}$ = 10.28 Å (100.0), $d_{001}$(Kao) = 7.35 Å (22.4), $d_{002}$ = 5.04 Å (0.3), $d_{002}$(Kao) = 3.62 Å (9.4), $d_{060}$ = 1.49 Å (0.4); I.R. = 0.82. FTIR (KBr, $cm^{-1}$): (OH) 3695 (s), 3620 (s), 3600 (s), 3551 (m), 3451 (br, w), (C–H) 2925 (w), 2850 (w), (HOH) 1636 (w), (C–H) 1384 (s), Si–O vibrations 1108 (s), 1028 (s), 1006 (m), (Al–OH) 969 (m), 941 (w), 907 (s), other bands 788 (w), 757 (m), 701 (m), 673 (m), 560 (s), 475 (s), 435 (s), 411 (w, sh). 13C CP MAS: broad envelope of peaks with maxima at 67, 74, 77, and 88 ppm. 13C DD MAS: no signal was observed for a dipolar dephasing time of 40 μs. TGA: 20–102 °C: 0.5% wt. loss, $T_{endo}$ = 49 °C; 102–373 °C: 3.3% wt. loss, $T_{endo}$ = 199 °C; 373–625 °C: 13.6% wt. loss, $T_{endo}$ = 508 °C; 625–1086 °C: 3.1% wt. loss, $T_{exo}$ = 1005 °C. Total TGA weight loss: 20.5%.

### 6.3.3.6 Intercalation with time

0.3 g Kao–DMSO and 1.5 g adonitol were heated in an oil bath at 125 °C with continuous stirring. At selected times, small aliquots of the reaction mixture were removed from the flask and worked up by repeated washings with deionized distilled water to remove excess adonitol. The resulting products were air-dried and their XRD patterns were obtained in order to monitor the progress of the intercalation process.

### 6.3.3.7 Thermal treatment of the intercalated samples

Powder XRD patterns of preferentially oriented thin films of adonitol–Kao on quartz slides were obtained after heating them first for 4 h at 100 °C, then for another 4 h at 150 °C, and subsequently at 50° intervals up to 250 °C (heating rate: 4 °C min–1). The samples were allowed to cool to room temperature and their XRD powder patterns were recorded after each heating interval.

### 6.3.3.8 Preparation of Kao–D-mannitol (M1 and M3)

D-Mannitol (3.0 and 4.0 g, respectively; Aldrich) was dissolved in deionized water (**M1**) or dispersed in DMSO (**M3**) and heated slowly to 75 and 60 °C, respectively, in a round-bottom flask placed in an oil bath. Kao–DMSO (1.0 and 0.6 g, respectively, prepared from KGa-1b) was added to the reaction media in both cases. The reaction mixture was refluxed with continuous stirring for a total of 7–8 days. The product was separated by centrifugation and repeatedly washed with DIW and 1,4-dioxane to remove excess D-mannitol and DMSO, respectively. The obtained product was air-dried on a glass plate and had an off-white color. XRD and FTIR confirmed that DMSO was deintercalated from the interlayer gallery of kaolinite.

**M1**: XRD: $d_{001}$ = 7.5 Å (sh) and $d_{001}$(Kao) = 7.1 Å (100.0). FTIR (KBr, $cm^{-1}$): The spectrum was similar to that of the KGa-1b with additional bands at ν(OH) 3547 (w), ν(OH) 3430(w, br), ν(C–H) 3128 (w, br), ν(C–H) 2926 (w), ν(C–H) 2850 (w), δ(HOH) 1653 (w), and δ(C–H) 1384 (s). $^{13}C$ CP/MAS: 44.3 ppm and 47.4 ppm.

**M3**: XRD: $d_{001}$ = 7.7 Å (sh) and $d_{001}$(Kao) = 7.1 Å (100.0). FTIR (KBr, $cm^{-1}$): The spectrum was similar to that of the KGa-1b with additional bands at ν(OH) 3546 (w), ν(OH) 3438(w, br), ν(C–H) 3131 (w, br), ν(C–H) 2963 (w), ν(C–H) 2926 (w), ν(C–H) 2850 (w), δ(HOH) 1654 (w), and δ(C–H) 1385 (s).

#### 6.3.3.9 Kao–D-mannitol (M2)

D-Mannitol (4.2 g, Aldrich) was dissolved in deionized water and heated with Kao–DMSO (0.7 g, prepared from KGa-1b) in a sealed stainless-steel glass-lined 300 mL Parr® bomb placed in a silicone-oil bath at an average temperature of 195 °C for a total of 48 h. The product was then separated by centrifugation and repeatedly washed with DIW to remove excess D-mannitol, and then it was air-dried. XRD: $d_{001}$(Kao) = 7.2 Å (100.0).

#### 6.3.3.10 Kao–D-mannitol (M4–M5)

D-Mannitol (5.0 and 6.0 g, respectively; Aldrich) and Kao–DMSO (1.0 g, prepared from KGa-1b) were slowly heated to 195 °C in a round-bottom flask placed in a silicone-oil bath for a total of 146 h (**M4**) and 139 h (**M5**). The reaction mixture was kept under nitrogen atmosphere for **M5**. The product was separated by centrifugation and repeatedly washed with DIW to remove excess D-mannitol, and then it was air-dried.

**M4**: XRD: $d_{001}$ = 11.5 Å, $d_{001}$(Kao) = 7.1 Å, RI = 0.70. FTIR (KBr, $cm^{-1}$): ν(OH) 3696 (m), ν(OH) 3670 (vw), ν(OH) 3651 (vw), ν(OH) 3620 (m), ν(OH) 3597 (w), ν(HOH) 3439 (vbr, m), ν(C–H) 2967 (vw), ν(C–H) 2929 (w), ν(C–H) 2882 (vw), ν(C=O) 1719 (m), δ(HOH) 1632 (w), δ(C–H) 1384 (s); (Si–O) vibrations: 1093 (s), 1035 (s), 1014 (s);

δ(Al–OH): 943 (w), 914 (s); other bands: (Si–O–Si) 793 (w), (Si–O–Si) 758 (w), (Si–O–Si) 693 (m), (Al–O–Si) 546 (s), (Si–O) 472 (s), (Si–O) 433 (s). $^{13}$C CP/MAS: broad envelope of peaks with maxima at 63.4, 73.5, 74.4, and 79.7 ppm; other peaks: 28.7 ppm, 127.6, 151.0, 172.0, and 208.4 ppm.

**M5**: XRD: $d_{001}$ = 11.5 Å, $d_{001}$(Kao) = 7.2 Å, RI = 0.82. FTIR (KBr, cm$^{-1}$): ν(OH) 3695 (m), ν(OH) 3620 (m), ν(OH) 3597 (w), ν(HOH) 3426 (w), ν(C–H) 2967 (vw), ν(C–H) 2928 (w), ν(C–H) 2868 (vw), ν(C=O) 1722 (w), δ(HOH) 1635 (w), δ(C–H) 1384 (s); (Si–O) vibrations: 1092 (s), 1034 (s), 1002 (s); δ(Al–OH): 938 (w), 911(s); other bands: (Si–O–Si) 796 (w), (Si–O–Si) 754 (w), (Si–O–Si) 690 (w), (Al–O–Si) 542 (s), (Si–O) 472 (s), (Si–O) 434 (s). $^{13}$C CP/MAS: broad envelope of peaks with maxima at 63.7, 73.8, and 79.8 ppm; other peaks: 32.6, 130.2, 151.9, 174.3, and 207.6 ppm.

#### 6.3.3.11 Kao–D-mannitol (M6)

A mixture of D-mannitol (4.2 g, Aldrich) and Kao–DMSO (0.7 g) was heated in a sealed stainless-steel glass-lined 45 mL Parr® bomb placed in a silicone-oil bath at an average temperature of 205 °C for a total of 48 h. The reaction vessel was then allowed to cool to room temperature, opened, and the reaction mixture was centrifuged and repeatedly washed with deionized water to remove excess D-mannitol, and then air-dried. XRD: $d_{001}$ = 11.3 Å $d_{001}$(Kao) = 7.2 Å, RI = 0.86. FTIR (KBr, cm$^{-1}$): ν(OH) 3696 (m), ν(OH) 3654 (vw), ν(OH) 3620 (m), ν(OH) 3602 (w), ν(OH) 3546 (w,br), ν(C–H) 3158 (w), ν(C–H) 3006 (vw), ν(C–H) 2963 (vw), ν(C–H) 2926 (m), ν(C–H) 2854 (w), ν(C=O) 1743 (w), δ(HOH) 1616 (w), δ(C–H) 1458 (w), δ(C–H) 1384 (s), δ(C–H) 1261 (w); (Si–O)

vibrations: 1099 (s), 1034 (vs), 1013 (vs); δ(Al–OH): 939 (w), 913 (s); other bands 797 (w), 754 (w), 697 (w), 544 (s), 474 (s), 432 (s). $^{13}$C CP/MAS: broad envelope of peaks with maxima at 61.9, 78.0, and 87.7 ppm. $^{13}$C DD/MAS: no signal was observed for a dipolar dephasing time of 40 μs. $^{29}$Si CP/MAS: –91.0 and –91.5 ppm. $^{27}$Al MAS: 4.47 ppm. TGA/DTA: RT–161 °C (5.2% wt. loss, $T_{endo}$ = 92.0 °C); 161–372 °C (9.1% wt. loss, $T_{exo}$ = 342 °C0; 372–560 °C (16.0% wt. loss, $T_{exo}$ = 468 °C); 560–1100 °C (3.0% wt. loss, $T_{exo}$ = 1004 °C); total TGA weight loss: 33.4%.

#### 6.3.3.12 Kao–D-mannitol (M7–M9)

A mixture of D-mannitol (5.0, 4.2, and 4.2 g, respectively; Aldrich) and Kao–DMSO (0.8, 0.7, and 0.7 g, respectively) was heated in a sealed stainless-steel glass-lined 300 mL Parr® bomb placed in a silicone-oil bath at an average temperature of 155–215 °C for a total of 24–51 h. The reaction vessel was then allowed to cool to room temperature, opened, and the reaction mixture was centrifuged, repeatedly washed with DIW to remove excess D-mannitol, and then air-dried.

**M7**: XRD: $d_{001}$ = 11.1 Å, $d_{001}$(Kao) = 7.1 Å, RI = 0.86. $^{13}$C CP/MAS: broad envelope of peaks with maxima at 62.2, 74.0, 72.9, 80.9, and 87.1 ppm. Other peaks: 18.7, 34.2, 128.6, and 151.8 ppm. $^{13}$C DD/MAS: no signal was observed for a dipolar dephasing time of 40 μs. $^{27}$Al MAS: 3.74 ppm.

**M8**: XRD: $d_{001}$ = 11.0 Å, $d_{001}$(Kao) = 6.9 Å, RI = 0.46.

**M9**: XRD: $d_{001}$ = 11.0 Å, $d_{001}$(Kao) = 7.0 Å, RI = 0.51. $^{13}$C CP/MAS: broad envelope of peaks with maxima at 66.1, 68.0, 70.0, 72.6, 75.6, 77.2, 79.8, and 87.4 ppm; other peaks: 32.7 ppm. $^{29}$Si CP/MAS: –91.0 and –91.5 ppm.

#### 6.3.3.13 Kao–D-mannitol (M10 and M11)

A mixture of D-mannitol (4.0 and 7.0 g, respectively; Aldrich) and Kao–NMF (1.0 g, prepared from KGa-1b) was heated in a sealed stainless-steel glass-lined 45 mL Parr® bomb placed in a silicone-oil bath at an average temperature of 230 and 215 °C, respectively, for a total of 54 and 73 h, respectively. The reaction vessel was then allowed to cool to room temperature, opened, and the reaction mixture was centrifuged and repeatedly washed with DIW to remove excess D-mannitol and then air-dried.

**M10**: XRD: $d_{001}$ = 11.3 Å, $d_{001}$(Kao) = 7.2 Å, RI = 0.05. FTIR (KBr, cm$^{-1}$): ν(OH) 3695 (m), ν(OH) 3669 (vw), ν(OH) 3651 (w), ν(OH) 3620 (s), ν(OH) 3547 (w, br), ν(N–H) 3435 (m, br), ν(C–H) 2956 (vw), ν(C–H) 2925 (w), ν(C–H) 2854 (w), ν(C=O) 1735 (vw), δ(HOH) 1653 (m), δ(C–H) 1400 (w), δ(C–H) 1385 (s), ν(C–O) 1094 (s); (Si–O) vibrations: 1094 (s), 1034 (s), 1011 (s); δ(Al–OH): 939 (w), 914 (s); other bands: (Si–O–Si) 795 (w), (Si–O–Si) 754 (w), (Si–O–Si) 696 (m), 639 (vw), (Al–O–Si) 542 (s), (Si–O) 473 (s), (Si–O) 433 (s).

**M11**: XRD: $d_{001}$ = 11.3 Å, $d_{001}$(Kao) = 7.2 Å, RI = 0.16. $^{13}$C CP/MAS: broad envelope of peaks with maxima at 70.0 and 75.5 ppm. Other peaks: 13.0 ppm, 32.5 ppm and 127.3 ppm.

### 6.3.3.14 Kao–D-mannitol (M12 and M13)

A mixture of D-mannitol (5.9 and 8.0 g, respectively; Aldrich) and Kao–$CH_3COOK$ (1.0 g, prepared from KGa-1b) was heated in a sealed stainless-steel glass-lined Parr® bomb placed in a silicone-oil bath at an average temperature of 190 and 225 °C for a total of 48 and 71 h, respectively. The reaction vessel was then allowed to cool to room temperature, opened, and the reaction mixture was centrifuged and repeatedly washed with DIW to remove excess D-mannitol and then air-dried.

**M12**: XRD: $d_{001}$ = 11.6 Å, $d_{001}$(Kao) = 7. Å, RI = 0.43. FTIR (KBr, $cm^{-1}$): ν(OH) 3696 (s), ν(OH) 3670 (vw), ν(OH) 3648 (vw), ν(OH) 3621 (s), ν(OH) 3591 (w, sh), ν(OH) 3456 (s, br), ν(C–H) 3218 (w, br), ν(C–H) 2984 (vw), ν(C–H) 2955 (vw), ν(C–H) 2930 (w), ν(C–H) 2854 (w), δ(HOH) 1631 (w), δ(C–H) 1465(w), δ(C–H) 1407(w), δ(C–H) 1385 (s), δ(C–H) 1241 (w), ν(C–O) 1096 (s); (Si–O) vibrations: 1114 (s), 1033 (vs), 1011 (vs); δ(Al–OH): 940 (vw, sh), 913 (s); other bands: Si–O–Si 793 (w), Si–O–Si 753 (m), Si–O–Si 694 (m), 647 (w, sh), Al–O–Si 538 (vs), Si–O 472 (s), Si–O 431 (s). $^{13}C$ CP/MAS: broad envelope of peaks with maxima at 65.8, 67.7, 69.5, and 74.9 ppm. $^{13}C$ DD/MAS: no signal was observed for a dipolar dephasing time of 40 μs. $^{29}Si$ CP/MAS: –91.0 and –91.5 ppm. $^{27}Al$ MAS: 4.48 ppm. TGA: RT–359 °C (7.1% wt. loss, $T_{endo}$ = 56.0 °C and $T_{exo}$ = 316 °C); 359–679 °C (13.1% wt. loss, $T_{endo}$ = 493 °C); $T_{exo}$ = 1002 °C; total TGA weight loss: 21.0%.

**M13**: XRD: $d_{001}$ = 10.8 Å, $d_{001}$(Kao) = 7.1 Å, RI = 0.52. FTIR (KBr, $cm^{-1}$): ν(OH) 3697 (s), ν(OH) 3651 (vw), ν(OH) 3621 (s), ν(OH) 3603 (w), ν(OH) 3588 (w, sh), ν(OH) 3446 (w,br), ν(C–H) 3222 (w, br), ν(C–H) 3017 (vw), ν(C–H) 2958 (vw), ν(C–H) 2928 (vw),

ν(C–H) 2862 (w), δ(HOH) 1631 (w), δ(C–H) 1460 (w), δ(C–H) 1384 (m), δ(C–H) 1272 (w); (Si–O) vibrations: 1102 (s), 1033 (vs), 1011 (vs); δ(Al–OH): 936 (w, sh), 913 (s); other bands: Si–O–Si 794 (w), Si–O–Si 751 (w), Si–O–Si 697 (m), 668 (m), Al–O–Si 541 (vs), Si–O 473 (s), Si–O 434 (s). $^{13}$C CP/MAS: broad envelope of peaks with maxima at 64.1 and 74.0 ppm; other peaks: 13.2, 30.6, 127.8, and 130.9 ppm. $^{13}$C DD MAS: no signal was observed for a dipolar dephasing time of 40 μs. $^{29}$Si CP/MAS: –91.0 and –91.5 ppm. $^{27}$Al MAS: 4.32 ppm. TGA: RT–148 °C (3.7% wt. loss, $T_{endo}$ = 95.5 °C); 148–426 °C (19.05% wt. loss, $T_{exo}$ = 320 °C and $T_{exo}$ = 386 °C); 426–1100 °C (9.2% wt. loss, $T_{endo}$ = 495 °C and $T_{exo}$ = 999 °C); total TGA weight loss: 32.0%.

#### 6.3.3.15 The reaction of D-mannitol with KGa-1b (M14)

A mixture of D-mannitol (5.9 g, Aldrich) and pure KGa-1b (1.0 g) was heated in a sealed stainless-steel glass-lined 300 mL Parr® bomb placed in a silicone-oil bath at an average temperature of 190 °C for 45 h. The reaction vessel was then allowed to cool to room temperature, opened, and the reaction mixture was centrifuged and repeatedly washed with DIW to remove excess D-mannitol and then air-dried. XRD: The data shows that no intercalation was detected in this case; $d_{001}$(Kao) = 7.1 Å.

#### 6.3.3.16 Kao–dulcitol (D1)

A mixture of dulcitol (4.2 g, Aldrich) and Kao–DMSO (0.7 g) was heated in a sealed stainless-steel glass-lined 45 mL Parr® bomb placed in a silicone-oil bath at an average oil-bath temperature of 235 °C for ~22 h. The reaction vessel was then allowed to cool to

room temperature, opened, and the reaction mixture was centrifuged, repeatedly washed with deionized water to remove excess dulcitol, and then air-dried. XRD: $d_{001}$ = 11.4 Å, $d_{001}$(Kao) = 7.1 Å, RI = 0.73. FTIR (KBr, $cm^{-1}$): ν(OH) 3695 (s), ν(OH) 3670 (vw), ν(OH) 3651 (vw), ν(OH) 3620 (s), ν(OH) 3603 (w, sh), ν(OH) 3497 (w, br), ν(C–H) 2957 (vw), ν(C–H) 2926 (m), ν(C–H) 2854 (w), δ(HOH) 1632 (w), δ(C–H) 1459 (w), δ(C–H) 1385 (m), δ(C–H) 1271 (w), δ(C–O) 1095 (w); (Si–O) vibrations: 1115 (w, sh), 1036 (vs), 1013 (vs); δ(Al–OH): 937 (vw, sh), 914 (s); other bands 791 (w), 756 (w), 698 (m), 542 (vs), 473 (vs), 432 (s). $^{13}C$ CP/MAS: broad envelope of peaks with maxima at 64.1, 73.3, and 79.2 ppm. $^{29}Si$ CP/MAS: –91.0 and –91.5 ppm. $^{27}Al$ MAS: 3.74 ppm. TGA/DTA: RT–107 °C (2.1% wt. loss, $T_{endo}$ = 59.0 °C and 101 °C); 107–374 °C (13.9% wt. loss, $T_{exo}$ = 344 °C); 374–574 °C (21.3% wt. loss, $T_{exo}$ = 483 °C); 573–1100 °C (2.3% wt. loss, $T_{exo}$ = 1003 °C); total TGA weight loss: 39.6%.

#### 6.3.3.17 Effect of water washing on Kao–D-mannitol

For details of this experiments, see Section 3.12.

## 6.3.4 Experiments of Chapter 4

### 6.3.4.1 The reaction of Kao–DMSO with PEA to produce Kao–PEA1 to Kao–PEA4

In a typical experiment, poly(ethylene adipate) (PEA, avg. 4–5 g, Aldrich) was placed in a dry 50 mL round-bottom flask fitted with a water-cooled condenser and placed in a silicone-oil bath heated to ~155 °C to melt the polymer. To this viscous melt, ~1.0 g of Kao–DMSO was added at once, the temperature of the oil bath was either kept at ~150 °C or ramped up to ~186 °C (see Table 4.1 for details), and the reaction was allowed to proceed for a total of 90–216 h (see Table 4.1 for details) with stirring. At selected times during the reaction, small aliquots were removed with a pipette, quenched by cooling, and worked up by repeatedly washing with 1,4-dioxane and (or) toluene to remove excess, unreacted poly(ethylene adipate). XRD patterns were taken for these aliquots to monitor the extent of reaction. The remaining final product was worked up by excessive washing with 1,4-dioxane and (or) toluene, vacuum filtration, followed by vacuum-drying at ambient temperature for extended time. Detailed spectroscopic data are given in the tables of Chapter 4.

### 6.3.4.2 The reaction of Kao–$CH_3COOK$ with PEA to produce Kao–PEA5 and Kao–PEA6

In a typical experiment, poly(ethylene adipate) (PEA, 4–5 g, Aldrich) was placed in a dry 50 mL round-bottom flask fitted with a water-cooled condenser and placed in a silicone-oil bath heated to ~150 °C to melt the polymer. To this viscous melt, ~1.0 g of

Kao–$CH_3COOK$ was added at once, the temperature of the oil bath was either kept at ~150 °C or ramped up to ~170 °C (see Table 4.1 for details), and the reaction was allowed to proceed for 70 h (see Table 4.1 for details) with stirring. At selected times during the reaction, small aliquots were removed with a pipette, quenched by cooling, and worked up by repeatedly washing with 1,4-dioxane and (or) toluene to remove excess, unreacted poly(ethylene adipate). XRD patterns were taken for these aliquots to monitor the extent of reaction. The remaining final product was worked up by excessive washing with 1,4-dioxane and (or) toluene, vacuum filtration, followed by vacuum-drying at ambient temperature for extended time. Detailed spectroscopic data are given in the tables of Chapter 4.

#### 6.3.4.3 The reaction of Kao–DMSO with PES to produce Kao–PES1 and Kao–PES2

Poly(ethylene succinate) (PES, Aldrich, 4 and 8 g, respectively) was placed in a dry 50 mL round-bottom flask fitted with a water-cooled condenser and placed in a silicone-oil bath heated to ~155 °C to melt the polymer. To this viscous melt, ~1 and 2 g, respectively, of Kao–DMSO was added at once, the temperature of the oil bath was ramped to ~160 (Kao–PES1) and ~170 °C (Kao–PES2) (see Table 4.1 for details), and the reaction was allowed to proceed for a total of 282 and 404 h, respectively (see Table 4.1 for details), with stirring. At selected times during the reaction, small aliquots were removed with a pipette, quenched by cooling, and worked up by repeatedly washing with 1,4-dioxane and (or) toluene to remove excess, unreacted poly(ethylene succinate). XRD patterns were taken for these aliquots to monitor the extent of reaction. The remaining final product was

worked up by excessive washing with 1,4-dioxane and (or) toluene, vacuum filtration, followed by vacuum-drying at ambient temperature for extended time. Detailed spectroscopic data are given in the tables of Chapter 4.

#### 6.3.4.4 The reaction of Kao–DMSO with PBA to produce Kao–PBA1 and Kao–PBA2

In a typical experiment, poly(butylene adipate) (PBA, avg. 4 g, Aldrich) was placed in a dry 50 mL round-bottom flask fitted with a water-cooled condenser and placed in a silicone-oil bath heated to ~155 °C to melt the polymer. To this viscous melt, ~1 g of Kao–DMSO was added at once, the temperature of the oil bath was ramped up to ~165–180 °C (see Table 4.1 for details), and the reaction was allowed to proceed for a total of 190–266 h (see Table 4.1 for details) with stirring. At selected times during the reaction, small aliquots were removed with a pipette, quenched by cooling, and worked up by repeatedly washing with 1,4-dioxane and (or) toluene to remove excess, unreacted poly(ethylene glycol). XRD patterns were taken for these aliquots to monitor the extent of reaction. The remaining final product was worked up by excessive washing with 1,4-dioxane and (or) toluene, vacuum filtration, followed by vacuum-drying at ambient temperature for extended time. Detailed spectroscopic data are given in the tables of Chapter 4.

#### 6.3.4.5 The reaction of KGa-1b with PEA (Kao–PEA7)

Poly(ethylene adipate) (PEA, ~4.5 g, Aldrich) was placed in a dry 50 mL round-bottom flask fitted with a water-cooled condenser and placed in a silicone-oil bath heated to the

melt. Immediately, ~1.0 g of KGa-1b was added, the temperature of the oil bath was ramped up to ~170–180 °C, and the reaction was allowed to proceed for ~282 h (see Table 4.1 for details) with stirring. The reaction mixture was allowed to cool relatively, then it was worked up by excessive washing with 1,4-dioxane and (or) toluene, vacuum filtration, followed by vacuum-drying at ambient temperature for extended time. Detailed spectroscopic data are given in the tables of Chapter 4.

#### 6.3.4.6 Preparation of a kaolinite–poly(ethylene glycol) (Kao–PEG) nanocomposite

Poly(ethylene glycol) 1000 (~10 g, Aldrich) was heated to ~155 °C in a 100 mL round-bottom flask fitted with a water-cooled condenser and placed in a silicone-oil bath. Approximately 2 g of Kao–DMSO was added to the viscous melt, and the reaction was allowed to continue for ~216 h (see Table 4.1 for details). The reaction mixture was then allowed to cool to room temperature, washed repeatedly with methanol, vacuum filtered, and finally air-dried and then dried at 100 °C in an oven for 3 days. The final product was an off-white powder.

XRD: $d_{001}$ = 11.53 Å, $d_{001}$(Kao) = 7.29 Å, RI = 0.92. $^{13}$C CP/MAS: 70.9 and 43.6 ppm (residual DMSO). $^{29}$Si CP/MAS: –90.9 and –91.6 ppm. TGA (10 °C/min, $N_2$): RT–140 °C (2.5% wt. loss, $T_{endo}$ = 79.5 °C); 140–425 °C (15.2% wt. loss, $T_{endo}$ = 395 °C and $T_{endo}$ = 450 °C, shoulder); 425–625 °C (9.6% wt. loss, $T_{endo}$ = 495 °C); 625–1100 °C (3.3% wt. loss, $T_{exo}$ = 1004 °C); total TGA weight loss: 30.7%.

## 6.3.5 Experiments of Chapter 5

### 6.3.5.1 Preparation of Kao–polystyrene nanocomposite

Kao–polystyrene was prepared by mixing 3.0 g of Kao–DMSO with ~25.0 mL of styrene (99%, Aldrich) in a round-bottom flask and stirring for 30 min at room temperature followed by the addition of 0.63 g of benzoyl peroxide (Aldrich), and the stirring was continued at room temperature overnight. After that, the reaction mixture was refluxed at 80 °C for 5 h and then at 200 °C overnight. The mixture was allowed to cool to room temperature, and the product was washed in 1,4-dioxane at elevated temperature for 4 h to dissolve the excess polystyrene and then filtered and air dried (166, 175). Details of the spectroscopic data are given in Chapter 5.

### 6.3.5.2 Preparation of Kao–MAC by the reaction of methacrylamide with Kao–NMF: Kao–MAC1

Kao–MAC1 was prepared by the displacement of NMF from the Kao–NMF intercalate with methacrylamide (Aldrich). The mixture of Kao–NMF (1 g) and an aqueous solution of methacrylamide (10% *w/v*, 100 mL) was stirred for 22 h at room temperature (see Table 5.1 for details), and the product was vacuum-filtered, washed with 2-propanol, and air-dried to yield an off-white powder.

#### 6.3.5.3 Preparation of Kao–MAC by the reaction of methacrylamide with Kao–DMSO: Kao–MAC2, –MAC3, and –MAC4

In a series of experiments, Kao–MAC was prepared by displacing DMSO with methacrylamide. A mixture of Kao–DMSO (1 g) and an aqueous solution of methacrylamide (10% *w/v*, 100 mL) was stirred for 21, 67, and 48 h, respectively, at room temperature (see Table 5.1 for details), and the products were vacuum-filtered, washed with 2-propanol, and air-dried. Prolonged reaction times had a positive effect on the ratio of intercalation with the optimum reaction time being ≈ 48 h. For detailed spectroscopic data, see the tables of Chapter 5.

#### 6.3.5.4 The reaction of methacrylamide with KGa-1b

A mixture of KGa-1b (1 g) and an aqueous solution of methacrylamide (10% *w/v*, 100 mL) was stirred for 72 h at room temperature (see Table 5.1 for details), and the product was vacuum-filtered, washed with 2-propanol, and air-dried to yield an off-white powder. XRD showed that no reaction has taken place, as the $d_{001}$ obsereved was that of the pure kaolinite = 7.15 Å.

#### 6.3.5.5 Thermal polymerization of methacrylamide in the interlamellar spaces

Details are given in Chapter 5, Section 5.11.

### 6.3.5.6 Preparation of Kao–AC by the reaction of acrylamide with Kao–DMSO

To an aqueous solution of acrylamide (10% *w/v*, 100 mL, EMD), ~ 1 g of Kao–DMSO was added, and the mixture was stirred for ~68 h at room temperature (see Section 5.16 for details). Then, the product was vacuum-filtered, washed with 2-propanol, and air-dried to yield an off-white powder.

# Chapter 7

# General conclusions

Recently, nanohybrid materials that result from the intimate mixing of organic and inorganic structural entities at the nanoscale level have received much attention, since such nanostructured materials open the way to the controlled design of advanced functional materials. Of particular interest to this work were the nanohybrid materials that are derived from the naturally occurring clay mineral, kaolinite.

With its aluminol surface and its non-centrosymmetric structure, kaolinite is an interesting mineral for the design of nanohybrid materials; thus, it is important to develop and extend its interlamellar chemistry.

Chemical modification of kaolinite was achieved in this work by various strategies, including the intercalation of organic molecules of biological significance, grafting of polyols, and the synthesis of new kaolinite–polymer intercalated nanocomposites. All the reported nanohybrids in this work are new materials and represent significant advancement in the intercalation chemistry of kaolinite.

The first part of this work presented the first intercalation of cyclic imides in the interlamellar spaces of kaolinite. This was achieved by the reaction of two different imides with preintercalated kaolinite at ambient conditions. The intercalation was confirmed by the observed interlayer expansion to 12–12.3 Å in the XRD results and by the results of $^{13}C$ NMR analysis.

The intercalation of polyols, such as alditols, into the interlamellar spaces of kaolinite was successfully achieved by mixing the kaolinite–DMSO intercalate with the neat alditols at a temperature just above their melting points.

The intercalation proceeds via a partially collapsed kaolinite–DMSO intercalate. Thermal treatment of the kaolinite–alditol intercalates leads to the formation of new grafted materials that are characterized by a shorter interlayer distance and a higher thermal stability. These organo-mineral nanohybrid materials result from the grafting of the intercalated polyols to the interlamellar aluminol sheets of kaolinite.

Moreover, D-mannitol and dulcitol were intercalated into the interlamellar spaces of kaolinite, with simultaneous covalent grafting on the interlamellar aluminol surfaces. The reaction can be successfully achieved by mixing the kaolinite–DMSO intercalate with the neat compounds at a temperature above their melting points. Similar results are obtained with other intercalates, such as Kao–NMF or Kao–KOAc, albeit with a reduced ratio of intercalation. The reaction does not proceed when the unexpanded kaolinite mineral is used. The nanohybrids are the result of multi-point covalent grafting of oligomeric forms of the alditols, bridging the methylenic backbone on the aluminol surface through Al–O–C bonds. These organo-mineral nanohybrids are resistant to de-intercalation and hydrolysis.

In Chapter 4, robust, green, intercalated nanocomposites were prepared from kaolinite and biodegradable polyesters. The results of the XRD, FTIR, and TGA analyses confirmed the intercalation of the polymers in the interlayer spaces of kaolinite. XRD showed that the intercalated polymers adopted flattened monolayer arrangements in the interlamellar spaces.

$^{13}C$ CP/MAS and DD/MAS spectra indicated the complete displacement of the guest species (DMSO) by the intercalated polymers and the rigidity of the latter in the interlayer spaces. The results of the TGA/DTA analyses showed enhanced thermal stabilities of the produced nanocomposites compared with the starting materials.

Exploratory work on the use of alternative strategies, other than the melt intercalation, for the synthesis of Kao–polymer nanocomposites showed promising results. An intercalated nanocomposite was prepared by a free-radical initiated polymerization reaction of styrene in the presence of a kaolinite–DMSO intercalate. The DMSO molecules are almost completely replaced in the interlamellar spaces of kaolinite by a monolayered polystyrene chain, arranged in a flattened configuration with the aromatic rings parallel to the kaolinite interlamellar surfaces. This nanohybrid is decomposed under air at temperatures above 300 °C, giving a maximum exotherm at 370 °C.

Finally, the intercalation of methacrylamide into the interlamellar spaces of kaolinite by displacing DMSO was followed by thermal in situ polymerization. A slight increase in the basal spacing was observed after polymerization. The results of the XRD, FTIR, and $^{13}C$ NMR analyses confirmed the polymerization of the methacrylamide molecules in the interlamellar spaces of kaolinite. The produced nanocomposite exhibited greatly enhanced thermal stability, compared with both the kaolinite–monomer intercalate and the starting material.

# References


1 Bailey, S. W., Ed. *Reviews in Mineralogy: Hydrous phyllosilicates*; Mineralogical Society of America: Washington, DC, 1988.

2 (*a*) Carrado, K. A. In *Advanced polymeric materials: structure–property relationships*; Advani, S. G.; Shonaike, G. O., Eds.; CRC Press LLC, Boca Raton, FL, 2003, pp. 349–396; (*b*) Ruiz-Hitzky, E. *Chem. Rec.* **2003,** *3*, 88.

3 MacEwan, D. M. C. *Nature (London, UK),* **1946,** *157*, 159.

4 Wada. K. *Amer. Miner.* **1961,** *46*, 78.

5 Theng, B. K. G. *The chemistry of clay–organo reactions*, Adam Hilger: London. 1974.

6 Letaief, S.; Elbokl, T. A.; Detellier, C. *J. Colloid Interface Sci.* **2006,** *302,* 254.

7 Brandt, K. B.; Elbokl, T. A.; Detellier, C. *J. Mater. Chem.* **2003,** *13*, 2566.

8 Elbokl, T. A.; Detellier, C. *Clay Sci.* **2005,** *12* (Suppl. 1), 38.

9 Gardolinski, J. E.; Carrera, L. C. M.; Cantao, M. P.; Wypych, F. *J. Mater. Sci.* **2000,** *35*, 3113.

10 Gardolinski, J. E.; Peralta-Zamora, P.; Wypych, F. *J. Colloid Interface Sci.* **1999,** *211*, 137.

11 Gardolinski, J. E.; Peralta-Zamora, P.; Wypych, F. *J. Colloid Interface Sci.* **1998,** *206*, 281.

12 Sugahara, Y.; Satokawa, S.; Kuroda, K.; Kato, C. *Clays Clay Miner.* **1990,** *38,* 137.

13 Sugahara, Y.; Sugiyama, T.; Nagayama, T.; Kuroda, K.; Kato, C. *J. Ceram. Soc. Jpn.* **1992**, *100*, 413.

14 Takenawa, R.; Komori, Y.; Hayashi, S.; Kawamata, J.; Kuroda, K. *Chem. Mater.* **2001,** *13*, 3741.

15 Tunney, J. J.; Detellier, C. *Chem. Mater.* **1993,** *5*, 747.

16 Tunney, J. J.; Detellier, C. *Clays Clay Miner.* **1994,** *42*, 552.

17 Tunney, J. J.; Detellier, C. *J. Mater. Chem.* **1996,** *10*, 1679.

18 Tunney, J. J.; Detellier, C. *Chem. Mater.* **1996,** *8*, 927.

19 Tunney, J. J.; Detellier, C. *Can. J. Chem.* **1997,** *75*, 1766.

20 Matsumura, A.; Komori, Y.; Itagaki, T.; Sugahara, Y.; Kuroda, K. *Bull. Chem. Soc. Jpn.* **2001,** *74*, 1153.

21 Itagaki, T.; Kuroda, K. *J. Mater. Chem.* **2003,** *13*, 1064.

22 Itagaki, T.; Komori, Y.; Sugahara, Y.; Kuroda, K. *J. Mater. Chem.* **2001,** *11*, 3291.

23 Murakami, J.; Itagaki, T.; Kuroda, K. *Solid State Ionics*, **2004,** *172*, 279.

24 Komori, Y.; Sugahara, Y.; Kuroda, K. *Chem. Mater.* **1999,** *11*, 3.

25 Johnston, C. T.; Sposito, G.; Bocian, D. F.; Birge, R. R. *J. Phys. Chem.* **1984,** *88*, 5959.

26 Ledoux, R. L.; White, J. L. *J. Colloid Interface Sci.* **1966,** *21*, 137.

27 Lipsicas, M.; Raythatha, R. R. F.; Giese, J.; Costanzo, P. M. *Clays Clay Miner.* **1986,** *34*, 635.

28 Brindley, G. W.; Brown, G., Eds. *Crystal structures of clay minerals and their*

*X-ray identification: interlayer and intercalation complexes of clay minerals;* Mineralogical Society: London, UK. 1984.

29 Franco, F.; Ruiz Cruz. M. D. *Clay Miner.* **2004,** *39*, 193.

30 Pinnavaia, T. J.; Beall, G. W., Eds. *Polymer-clay nanocomposites;* John Wiley and Sons: New York, 2000; and references cited therein.

31 Alexandre, M.; Dubois. P. *Mater. Sci. Eng. A.* **2000,** *28*, 1; and references cited therein..

32 LeBaron, P. C.; Wang, Z.; Pinnavaia, T. *J. Appl. Clay Sci.* **1999,** *15*, 11.

33 Giannelis, E. P. *Appl. Organometal. Chem.* **1998,** *12*, 675.

34 Zanetti, M.; Lomakin, S.; Camino, G. *Macromol. Mater. Eng.* **2000,** *279*, 1.

35 Sugahara, Y.; Satokawa, S.; Kuroda, K.; Kato, C. *Clays Clay Miner.* **1988,** *36*, 343.

36 Moore D. M.; Reynolds R. C., Jr. *X-ray diffraction and the identification and analysis of clay minerals*; Oxford University Press: Oxford, 1989.

37 Bailey, S. W. In *Crystal structures of clay minerals and their X-ray identification*; Brindley G. W.; Brown G., Eds.; Mineralogical Society: London, 1984; pp 1–124.

38 Martin, R. T.; Bailey, S. W.; Eberl, D. D.; Fanning, D. S.; Guggenheim, S.; Kodama, H.; Pevear, D. R.; Srodon, J.; Wicks, F. J. *Clays Clay Miner.* **1991,** *39*, 333.

39 Guggenheim, S.; Eggleton, R. A. In *Reviews in Mineralogy: Hydrous phyllosilicates*; Bailey S. W., Ed.; Mineralogical Society of America: Washington, DC, 1988; pp 675–725.

40 Jones, B. F.; Galan, E. In *Reviews in Mineralogy: Hydrous phyllosilicates*; Bailey S. W., Ed.; Mineralogical Society of America: Washington, DC, 1988; pp 631–674.

41 Wada, K. In *Minerals in the Soil Environment*; Dixon J. B.; Weeds S. B., Eds.; Soil Science Society of America: 1977; pp 603–638.

42 Murray, H. H. In *Reviews in Mineralogy: Hydrous phyllosilicates*; Bailey S. W., Ed.; Mineralogical Society of America: Washington, DC, 1993; pp 67–89.

43 Zheng, Z.; Lu, D.; Feng, M.; Feng, B.; Jin, T. In *International clay conference* 1981; *Developments in Sedimentology* 35; van Olphen, H.; Veniale, F., Eds.; Elsevier: Amsterdam, 1982; pp 719–731.

44 Giese, R. F. In *Reviews in Mineralogy: Hydrous phyllosilicates*; Bailey S. W., Ed.; Mineralogical Society of America: Washington, DC, 1988; pp 29–66.

45 Keller, W. A.; Cheng, H.; Johns, W. D.; Meng, C. S. *Clays Clay Miner.* **1980,** *28*, 97.

46 Talibudeen, O.; Goulding, K. W. T. *Clays Clay Miner.* **1983,** *31*, 137.

47 Brindley, G. W. In *Crystal structures of clay minerals and their X-ray identification*; Brindley G. W.; Brown G., Eds.; Mineralogical Society: London, 1984; pp 125-196.

48 Merino, E.; Harvey, C.; Murray, H. H. *Clays Clay Miner.* **1989,** *37*, 135.

49 Newnham, R. E. *Mineralog. Mag.* **1961,** *32*, 683.

50 Zvyagin, B. B. *Soviet Phys. Chrystallogr.* **1962,** *7,* 38.

51 Bailey, S. W. *Amer. Mineral.* **1963,** *48*, 1196.

52 Bailey, S. W. *Clays Clay Miner.* **1969,** *17*, 355.

53 Bookin, A. S.; Drits, V. A.; Plançon, A.; Tchoubar, C. *Clays Clay Miner.* **1989,** *37*, 297.

54 Pauling, L. *Proc. Natl. Acad. Sci. USA.* **1930,** *16*, 578.

55 Suitch, P. R.; Young, R. A. *Clays Clay Miner.* **1983,** *31*, 357.

56 Young, R. A.; Hewat, A. W. *Clays Clay Miner.* **1988,** *36*, 225.

57 Bish, D. L.; von Dreele, R. B. *Clays Clay Miner.* **1989,** *37*, 289.

58 Bish, D. L. *Clays Clay Miner.* **1993,** *41*, 738.

59 Farmer, V. C. In *The infra-red spectra of minerals*; Farmer V. C., Ed.; Mineralogical Society: London, 1974; pp 331–363.

60 Farmer, V. C.; Russell, J. D. *Spectrochim. Acta,* **1964,** *20*, 1149.

61 Deng, Y; White, G. N.; Dixon, J. B. *J. Colloid Interface Sci.* **2002,** *250*, 379.

62 Raussell-Colom, J. A.; Serratosa, J. M In *Chemistry of Clays and Clay Minerals*; Newman A. C. D., Ed.; Mineralogical Society: London, 1987; pp 371–422.

63 Weiss, A.; Becker, H. O.; Orth, H.; Mai, G.; Lechner, H.; Range, K. J. *Proceedings of the Int. Clay Conf. Tokyo* **1969,** *2,* 180.

64 Plançon, A.; Giese, R. F., Jr.; Snyder, R.; Drits, V. A.; Bookin, A. S. *Clays Clay Miner.* **1989,** *37*, 203.

65 Plançon, A.; Zacharie, C. *Clay Miner.* **1990,** *25*, 249.

66 MacEwan, D. M. C. *J. Chem. Soc., Faraday Trans.* **1948,** *44*, 349.

67 Carr, R. M.; Chih, H. W. A. *Clay Miner.* **1971,** *9,* 153.

68 MacEwan, D. M. C.; Wilson, M. J. In *Crystal structures of clay minerals and their X-ray identification;* Brindley G. W.; Brown G. Eds.; Mineralogical Society: London, 1984; pp 197–248.

69 Camazano, M. S.; Garcia, S. G. *Ann. Edafol Agrobiol.* **1966,** *25*, 9.

70 Olejnik, S.; Aylmore, L. A. G.; Posner, A. M.; Quirk, J. P. *J. Phys. Chem.* **1968,** *72*, 241.

71 Olejnik, S.; Posner, A. M.; Quirk, J. P. *Clay Miner.* **1970,** *8*, 421.

72 Duer, M. J.; Rocha, J.; Klinowski, J. *J. Am. Chem. Soc.* **1992,** *114,* 6867.

73 Thompson, J. G.; Cuff, C. *Clays Clay Miner.* **1985,** *33,* 490.

74 Thompson, J. G. *Clays Clay Miner.* **1985,** *33,* 173.

75 Raupach, M.; Barron, P. F. Thompson, J. G. *Clays Clay Miner.* **1987,** *35,* 208.

76 Olejnik, S.; Posner, A. M.; Quirk, J. P. *Clays Clay Miner.* **1971,** *19,* 83.

77 Uwins, P. J. R.; Mackinnon, I. D. R.; Thompson, J. G.; Yago, A. J. E. *Clays Clay Miner.* **1993,** *41,* 707.

78 Cruz, M.; Laycock, A.; White, J. L. *Proceedings of Int. Clay Conf.* **1969,** *1,* 775.

79 Ledoux, R. L.; White, J. L. *Proceedings of Int. Clay Conf.* **1966,** *1*, 361.

80 Barrios, J.; Plançon, A.; Cruz, M. I.; Tchoubar, C. *Clays Clay Miner.* **1977,** *25,* 422.

81 Johnston, C. T.; Stone, D. A. *Clays Clay Miner.* **1990,** *38,* 121.

82 Adams, J. M.; Reid, P. I.; Thomas, J. M.; Walters, M. J. *Clays Clay Miner.* **1976,** *24,* 267.

83 Weiss, A.; Thielepape, W.; Orth, H. *Proceedings of Int. Clay Conf.* **1966,** *1,* 277.

84 Weiss, A.; Thielepape, W.; Goring, G.; Ritter, W.; Schafer, H. *Proceedings of Int. Clay Conf.* **1963,** 287.

85 Thompson, J. G.; Uwins, P. J. R.; Whittaker, A. K.; Mackinnon, I. D. R. *Clays Clay Miner.* **1992,** *40,* 369.

86 Michaelian, K. H.; Yariv, S.; Nasser, A. *Can. J. Chem.* **1991,** *69,* 749.

87 Jackson, M. L.; Abdel-Kader, F. H. *Clays Clay Miner.* **1978,** *26,* 81.

88 Thompson, J. G.; Gabbitas, N.; Uwins, P. J. R. *Clays Clay Miner.* **1993,** *41,* 73.

89 Sugahara, Y.; Kitano, S.; Satokawa, S.; Kuroda, K.; Kato, C. *Bull. Chem. Soc. Jpn.* **1986,** *59,* 2607.

90 Range, K. J.; Range, A.; Weiss, A. Z. *Naturforsch.* **1968,** *B23,* 1144.

91 Range, K. J.; Range, A.; Weiss, A. *Proceedings of Int. Clay Conf.* **1969,** *1,* 3.

92 Costanzo, P. M.; Clemency, C. V.; Giese, R. F. *Clays Clay Miner.* **1980,** *28,* 155.

93 Costanzo, P. M.; Giese, R. F. *Clays Clay Miner.* **1985,** *33,* 415.

94 Costanzo, P. M.; Giese, R. F.; Clemency, C. V. *Clays Clay Miner.* **1984,** *32,* 29.

95 Costanzo, P. M.; Giese, R. F.; Lipsicas, M.; Straley, C. *Nature (London, UK),* **1982,** *296,* 549.

96 Costanzo, P. M.; Giese, R. F., Jr. *Clays Clay Miner.* **1990,** *38,* 160.

97 Sugahara, Y.; Satokawa, K.; Kuroda, K.; Kato, C. *Clays Clay Miner.* **1989,** *37,* 143.

98 Costanzo, P. M.; Giese, R. F.; Lipsicas, M. *Clays Clay Miner.* **1984,** *32,* 419.

99 Wada, N.; Raythatha, R.; Minomura, S. *Solid State Commun.* **1987,** *63,* 783.

100 Giese, R. F. *Clays Clay Miner.* **1978,** *26,* 51.

101 Cruz, M.; Jacobs, H.; Fripiat, J. J. *Proceedings of. Int. Clay Conf.* **1973,** 35.

102 Wiewiora, A.; Brindley, G. W. *Proceedings of the International Clay Conference,* **1969,** Tokyo, Japan.

103 Chekin, S. S. *Int. Geol. Rev.* **1982,** *11,* 1338.

104 Chekin, S. S. *Clays Clay Miner.* **1992,** *40,* 740.

105 Kawasumi, M. *J. Polym. Sci. A.* **2004,** *42,* 819; and references cited therein.

106 Stamboliyska, B. A.; Binev, Y. I.; Radomirska, V. B.; Tsenov, J. A.; Juchnovski, I. N. *J. Mol. Struct.* **2000,** *516,* 237; and references cited therein.

107 Matsuo, T. *Bull. Chem. Soc. Jpn.* **1964,** *37,* 1844.

108 Otani, T; Minami, T.; Matsumoto, H.; Marunaka, T.; Lou, Z.-X.; Yu, Q.-W. *J. Antibiot.* **1989,** *42,* 654.

109 Sugawara, K.; Nishiyama, Y.; Toda, S.; Komiyama, N.; Hatori, M.; Moriyama, T.; Sawada, Y.; Kamei, H.; Konishi, M.; Oki, T. *J. Antibiot.* **1992,** *45,* 1433.

110 Bieńko, D. C.; Michalska, D.; Roszak, S.; Wojciechowski, W.; Nowak, M. J.; Lapinski, L. J. *Phys. Chem. A.* **1997,** *101,* 7834.

111 Komori, Y.; Enoto, H.; Takenawa, R. J.; Hayashi, S.; Sugahara, Y. S.; Kuroda, K. *Langmuir,* **2000,** *16,* 5506.

112 Kelleher, B. P.; O'Dwyer, T. F. *Clays Clay Miner.* **2002,** *50,* 331.

113 Bradley, W. F.; Weiss, E. J.; Rowland, R. A. *Clays Clay Miner.* **1963,** *10,* 117.

114 Ruiz-Hitzky, E.; Casal, B. *Nature (London, UK),* **1978,** *276,* 596.

115 Casal, B.; Aranda, P.; Sanz, J.; Ruiz-Hitzky, E. *Clay Miner.* **1994,** *29,* 191.

116 Costantino, U.; Marmottini, F. *Mater. Chem. Phys.* **1993,** *35,* 193.

117 Liu, Y. J.; DeGroot, D. C.; Schindler, J. L.; Kannewurf, C. R.; Kanatzidis, M. G. *Chem. Mater.* **1991,** *3,* 992.

118 Leroux, N.; Zeegers-Huyskens, T. *Spectrosc. Lett.* **1999,** *32,* 47; and references cited therein.

119 Morzyk, B.; Michalska, D.; Baran, J. *J. Coord. Chem.* **1999,** *47,* 231; and references cited therein.

120 Smith, B. *Infrared spectral interpretation: a systematic approach;* CRC press: Washington, DC, 1999.

121 Vanclef, A.; Bouché, R. *Spectrosc. Lett.* **1979,** *12,* 371.

122 Uno, T.; Machida, K. *Bull. Chem. Soc. Jpn.* **1962,** *35,* 276.

123 McKittrick, P. T.; Katon, J. E. *Appl. Spectrosc.* **1990,** *44,* 812; and references cited therein.

124 Wada, K. *Clay Miner.* **1967,** *7,* 51.

125 Fronza, G.; Mondelli, R.; Randall, E. W.; Gardini, G.-P. *J. Chem. Soc., Perkin Trans. 2,* **1977,** 1746.

126 Opella, S. J.; Frey, M. H. *J. Am. Chem. Soc.* **1979,** *101,* 5854.

127 Alemany, L. B.; Grant, D. M.; Alger, T. D.; Pugmire, R. J. *J. Am. Chem. Soc.* **1983,** *105,* 6697.

128 Ripmeester, J. A.; Burlinson, N. E. *J. Am. Chem. Soc.* **1985,** *107,* 3713.

129 (*a*) Mägi, M.; Lippmaa, E.; Samoson, A.; Engelhardt, G.; Grimmer, A.-R. *J. Phys. Chem.* **1984,** *88,* 1518; (*b*) Hayashi, S.; Ueda, T; Hayamizu, K.; Akiba, E. *J. Phys. Chem.* **1992,** *96,* 10922.

130 P. F. Barron, R. L. Frost, J. O. Skjemstad, A. J. Koppi, *Nature (London, UK),* **1983,** *302,* 49.

131 Thompson, J. G. *Clays Clay Miner.* **1984,** *32,* 233.

132 Thompson, J. G.; Barron, P. F. *Clays Clay Miner.* **1987,** *35,* 38.

133 (*a*) Sanz, J.; Serratosa, J. M. *J. Am. Chem. Soc.* **1984,** *106,* 4790; (*b*) Kodama, H.; Kotlyar, L. S.; Ripmeester, J. A. *Clays Clay Miner.* **1989,** *37,* 364.

134 Hayashi, S. *Clays Clay Miner.* **1997,** *45,* 724.

135 Xie, X.; Hayashi, S. *J. Phys. Chem. B,* **1999,** *103,* 5949.

136 Earnest, C. M. *The application of differential thermal analysis and thermogravimetry to the study of kaolinite clay minerals;* PerkinElmer thermal analysis application study. Vol. 3. PerkinElmer: Connecticu, 1980.

137 Sanchez-Soto, P. J.; Justo, A.; Perez-Rodriguez, J. L. *J. Mater. Sci.* **1994,** *29,* 1276.

138 Perez-Maqueda, L. A.; Perez-Rodriguez, J. L.; Scheiffele, G. W.; Justo, A.; Sanchez-Soto, P. J. *J. Therm. Anal.* **1993,** *39,* 1055.

139 Sohn, J. R.; Ryun, S. G.; Song, J. H. *J. Mol. Catal.* **1990,** *62,* L1.

140 Schiffino, R. S.; Merrill, R. P. *J. Phys. Chem.* **1993,** *97,* 6425.

141 Inoue, M.; Kominami, H.; Inui, T. *J. Chem. Soc., Dalton Trans.,* **1991,** 3331.

142 Mercier, L.; Facey, G. A.; Detellier, C. *J. Chem. Soc., Chem. Commun.* **1994,** *18,*

2111.

143 Alberti, G; Lambardo, G. M.; Pappalardo, G. C.; Vivani, R. *Chem. Mater.* **2002,** *14,* 295; and references cited therein.

144 Kittaka, S.; Fukuhara, N.; Sumida, H. *J. Chem. Soc., Faraday Trans.* **1993,** *89,* 3827.

145 Komori, Y.; Sugahara, Y; Kuroda, K. *J. Mater. Res.* **1998,** *13,* 930.

146 Itagaki, T.; Matsumura, A.; Kato, M.; Usuki, A.; Kuroda, K. *J. Mater. Sci. Lett.* **2001,** *20,* 1483.

147 Letaief, S.; Detellier, C. *Chem. Commun.* **2007,** 2613.

148 Schwarz, E. M.; Grundstein, V. V.; Ievins, A. F. *J. Thermal Anal.* **1972,** *4,* 331.

149 Komori, Y.; Sugahara, Y.; Kuroda, K. *J. Mater. Chem.* **1999,** *9,* 3081.

150 Lindblad, M. S.; Liu, Y.; Albertsson, A.-C.; Ranucci, E.; Karlsson, S. *Adv. Polym. Sci.* **2002,** *157,* 139.

151 Sinha-Ray, S.; Bousmina, M. *Prog. Mater. Sci.* **2005,** *50,* 962; and references cited therein.

152 Carrado, K. A. *Appl. Clay Sci.* **2000,** *17,* 1.

153 Popescu, M.-C.; Vasile, C.; Filip, D.; Macocinschi, D.; Singurel, Gh. *J. Appl. Polym. Sci.* **2004,** *94,* 1156.

154 Harada, A.; Nishiyama, T.; Kawaguchi, Y.; Okada, M.; Kamachi, M. *Macromolecules,* **1997,** *30,* 7115.

155 Aranda, P.; Ruiz-Hitzky, E. *Chem. Mater.* **1992,** *4,* 1395.

156 Brandolini, A. J.; Hills, D. D. *NMR spectra of polymers and polymer additives,* CRC press: Washington, DC, 2000.

157 Baldissera, A. F.; Valério, C. E. S.; de S. Basso, N. R.; Guaragna, F.; Einloft, S.; Tessier, M.; Fradet, A. *Quim. Nova,* **2005,** *28,* 188.

158 Kuwabara, K.; Gan, Z.; Nakamura, T.; Abe, H.; Doi, Y. *Biomacromolecules,* **2002,** *3,* 1095.

159 Kuwabara, K.; Gan, Z.; Nakamura, T.; Abe, H.; Doi, Y. *Polym. Degrad. Stab.* **2004,** *84,* 105.

160 Gan, Z.; Abe, H.; Doi, Y. *Macromol. Chem Phys.* **2002,** *203,* 2369.

161 Iwata, T.; Doi, Y. *Macromol. Chem Phys.* **1999,** *200,* 2429.

162 McNeill, I. C.; Basan, S. *Polym. Degrad. Stab.* **1993,** *41,* 311.

163 Solomon, D. H.; Rosser, M. J. *J. Appl. Polym. Sci.* **1965,** *9,* 1261.

164 Solomon, D. H. *Clays Clay Miner.* **1968,** *16,* 31.

165 Solomon, D. H.; Swift, J. D.; Murphy, A. J. *J. Macromol. Sci., Chem.* **1971,** *A5,* 587.

166 Wang, X.; Zhou, P.; Li, B.; Yu, H. *Guisuanyan Xuebao,* **2003,** *31,* 955.

167 Ebdon, J. R.; Huckerby, T. N. *Polymer,* **1976,** *17,* 170.

168 Önal, M.; Çelik, M. *Mater. Lett.* **2006,** *60,* 48.

169 Stein, M. *J. Appl. Polym. Sci.* **1992,** *46,* 2217.

170 Jackson, M. L.; Whittig, L. D.; Pennington, R. P. *Soil Sci. Soc. Am. Proc.* **1949,** *14,*77.

171 Tanner, C. B.; Jackson, M. L. *Soil Sci. Soc. Am. Proc.* **1947,** *12,* 60.

172 van Olphen, H. In *An introduction to clay colloid chemistry;* John Wiley and Sons: New York, 1977; 2nd ed. pp 249–253.

173 Schofield, R. K.; Samson, H. R. *Disc. Faraday Soc.* **1954,** *18,* 135.

174 van Olphen H.; Fripiat J. J. *Data handbook for clay minerals and other non-metallic minerals;* Pergamon Press: Oxford, 1979.

175 Elbokl, T. A.; Detellier, C. *J. Phys. Chem. Solids,* **2006,** *67,* 950.

# Appendix

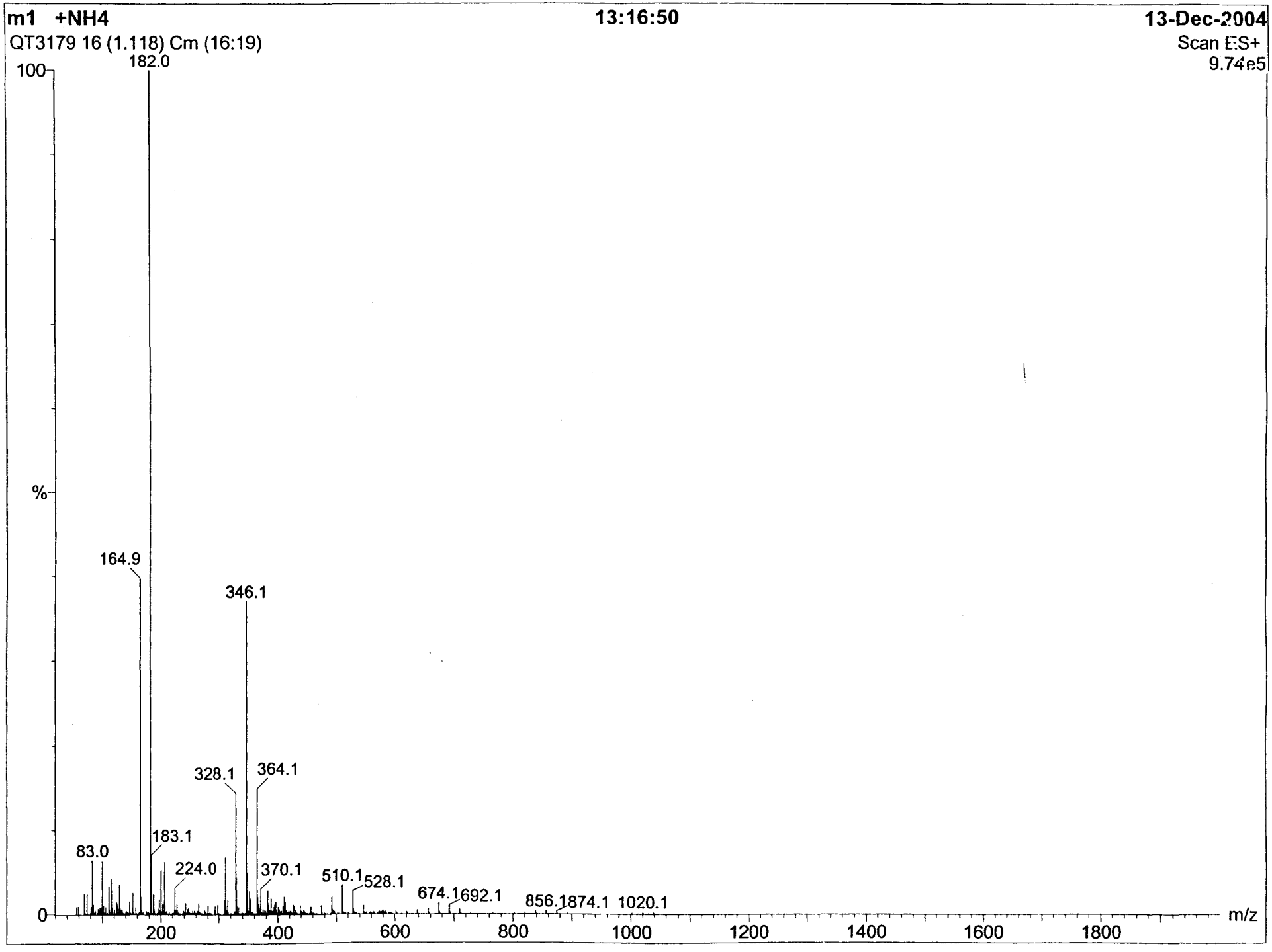
m1 +NH4
13:16:50
13-Dec-2004
QT3179 16 (1.118) Cm (16:19)
Scan ES+
9.74e5
100
%
0
182.0
164.9
346.1
328.1
364.1
183.1
83.0
224.0
370.1
510.1
528.1
674.1
692.1
856.1
874.1
1020.1
200
400
600
800
1000
1200
1400
1600
1800
m/z
A1

Tamer

Archive directory: /export/home/vnmr1/vnmrsys/data
Sample directory:
File: PROTON

Pulse Sequence: gHMQC

Solvent: D2O
Temp. 20.0 C / 293.1 K
User: 1-14-87
INOVA-500 "inova500"

Relax. delay 1.000 sec
Acq. time 0.221 sec
Width 1156.7 Hz
2D Width 4958.5 Hz
8 repetitions
2 x 128 increments
OBSERVE H1, 500.1752334 MHz
DECOUPLE C13, 125.7781122 MHz
Power 44 dB
on during acquisition
off during delay
W40_tr7302 modulated
DATA PROCESSING
Gauss apodization 0.102 sec
F1 DATA PROCESSING
Gauss apodization 0.012 sec
FT size 512 x 2048
Total time 44 min, 33 sec

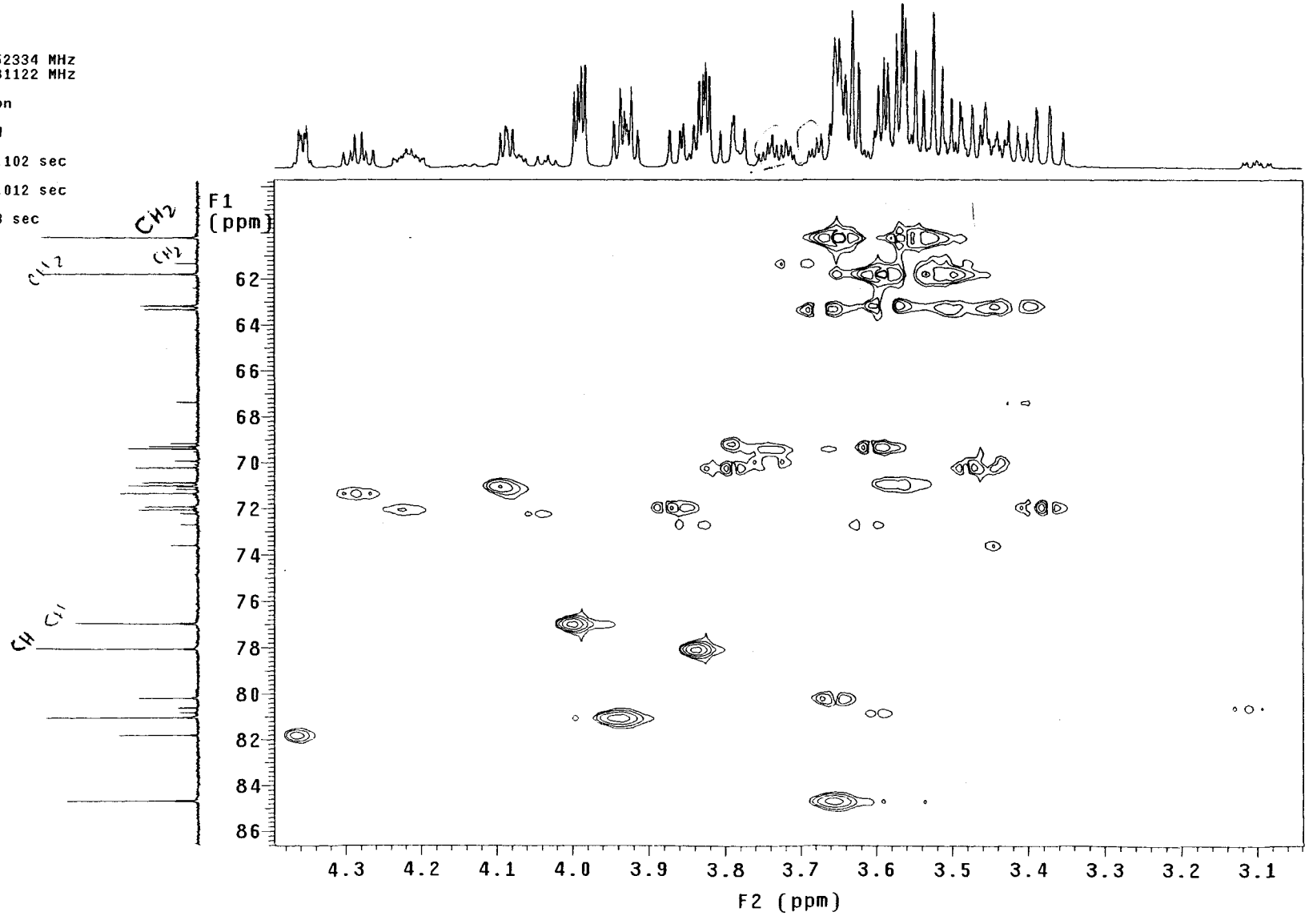


A2

MINERALOGICAL SOCIETY OF AMERICA
3635 Concorde Pkwy Ste 500 • Chantilly VA 20151-1125 • USA
Tel: 1 (703) 652-9950 • Fax: 1 (703) 652-9951 • Internet: www.minsocam.org

August 12, 2007

Tamer A. El Bokl
1114 Halton Terrace
Kanata ON K2W 1G8
CANADA

Dear M. El Bokl:

I received your 2007-08-14 requests for permission to reproduce the following table and figures from the following two articles in your dissertation:

[1] Figure 1 from Jones, B. F., Galan, E., Sepiolite and palygorskite, *Reviews in Mineralogy and Geochemistry* 1988 19: 631-674
[2] Figures number 1 and 2, and Table 1 from Bailey, Sturges Williams, Introduction, *Reviews in Mineralogy and Geochemistry* 1988 19: 1-8

It is with pleasure that we grant you permission to reproduce these figures and tables without cost on the condition that the authors are properly cited and that reference is given to the original publication of the Mineralogical Society of America.

Sincerely,

J. Alexander Speer
Executive Director, MSA

YAHOO! MAIL

Print - Close Window

**From:** "Kevin Murphy" <

**To:** "'TAMER EL BOKL'" <

**Subject:** RE: permission to use figures

**Date:** Fri, 17 Aug 2007 16:02:25 +0100

Hi Tamer

The Society is happy to grant you permission to reproduce Table 1.1, Figs. 1.1, 1.2, 1.34, and 1.35 from the book by Brindley and Brown. Our only stipulation is that full acknowledgement of the source must be provided in the form "Reproduced with the from *'Crystal Structures of Clay Minerals and their X-ray Identification'* published by the Mineralogical Society of Great Britain & Ireland.

Yours sincerely

**Kevin Murphy**
**Editorial Manager, Mineralogical Society**
**Inchafune**
**Dunmanway, Co. Cork**
**Ireland**

**Visit the Society website at: *www.minersoc.org***
***MinAbs Online: www.minabs.com***

---

**From:** TAMER EL BOKL [mailto:
**Sent:** 15 August 2007 15:01
**To:**
**Subject:** RE: permission to use figures

Dear Kevin,
Thank you for your reply. I would like to reproduce: Table 1.1, Figs. 1.1, 1.2, 1.34, and 1.35. Thanks and best regards.
Tamer El Bokl

***Kevin Murphy*** wrote:

> Dear colleague
>
> Please specify the images which you would like to reproduce.
>
> Thanks
>
> **Kevin Murphy**
> **Editorial Manager, Mineralogical Society**
> **Inchafune**
> **Dunmanway, Co. Cork**
> **Ireland**
> **Tel.** <

From: "Downing, Hannah \(ELS-OXF\)" <
Subject: RE: Obtain Permission
Date: Tue, 1 May, 2007 11:13 am
To:

---

Dear Mr. Tamer A. El Bokl

We hereby grant you permission to reprint the material detailed below at no charge in your thesis subject to the following conditions:

1. If any part of the material to be used (for example, figures) has appeared in our publication with credit or acknowledgement to another source, permission must also be sought from that source. If such permission is not obtained then that material may not be included in your publication/copies.

2. Suitable acknowledgment to the source must be made, either as a footnote or in a reference list at the end of your publication, as follows:

"This article was published in Publication title, Vol number, Author(s), Title of article, Page Nos, Copyright Elsevier (or appropriate Society name) (Year)."

3. Your thesis may be submitted to your institution in either print or electronic form.

4. Reproduction of this material is confined to the purpose for which permission is hereby given.

5. This permission is granted for non-exclusive world English rights only. For other languages please reapply separately for each one required. Permission excludes use in an electronic form other than submission. Should you have a specific electronic project in mind please reapply for permission.

6. This includes permission for the Library and Archives of Canada to supply single copies, on demand, of the complete thesis. Should your thesis be published commercially, please reapply for permission.

Yours sincerely

Clare Truter

Rights Manager, S&T

-----Original Message-----
From: [redacted]
Sent: 27 April 2007 14:36
To: Rights and Permissions (ELS)
Subject: Obtain Permission

This Email was sent from the Elsevier Corporate Web Site and is related to Obtain Permission form:

---

Product: Customer Support
Component: Obtain Permission
Web server: http://www.elsevier.com
IP address: 10.10.24.149
Client: Mozilla/4.0 (compatible; MSIE 6.0; Windows NT 5.0)
Invoked from:
http://www.elsevier.com/wps/find/obtainpermissionform.cws_home?isSubmitted=yes&navigateXmlFileName=/store/prod_webcache_act/framework_support/obtainpermission.xml

Request From:
Mr. Tamer A. El Bokl
U of Ottawa
1114 Halton Terrace
K2W 1G8
Kanata, ON
Canada

Contact Details:
Telephone:
Fax:
Email Address:

To use the following material:
ISSN/ISBN:
Title: Journal of Colloid and Interface Science
Author(s): Youjun Deng, G. Norman White, and Joe B. Dixon
Volume: 250
Issue: 2
Year: 2002
Pages: 379 - 393
Article title: Effect of Str. Stress on the Intercal Rate of Kao.

How much of the requested material is to be used:

Are you the author: No
Author at institute: No

How/where will the requested material be used: [how_used]

Details:

Figure 1 to be reprinted in the Ph.D. thesis of Tamer A. El Bokl at the

U of Ottawa, Department of Chemistry and related presentations (seminars) + the oral presentation at the 90th CSC meeting, May 2007, Winnipeg, MB.

Additional Info:

- end -

For further info regarding this automatic email, please contact:
WEB APPLICATIONS TEAM ( esweb.admin@elsevier.co.uk )

---

**Attachments:**

| untitled-1.2 | |
|---|---|
| Size: | 8.5 kb |
| Type: | text/html |

| att78735.gif | |
|---|---|
| Size: | 2.2 kb |
| Type: | image/gif |
| Info: | att78735.gif |

| att78736.jpg | |
|---|---|
| Size: | 1.9 kb |
| Type: | image/jpeg |
| Info: | att78736.jpg |

---

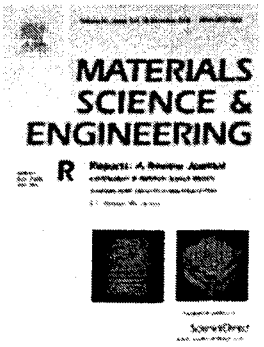


**Title:** Polymer-layered silicate nanocomposites: preparation, properties and uses of a new class of materials

**Author:** Michael Alexandre and Philippe Dubois

**Publication:** Materials Science and Engineering: R: Reports

**Publisher:** Elsevier Limited

**Date:** 15 June 2000





## Order Completed

Thank you very much for your order.

This is a License Agreement between TAMER A EL BOKL ("You") and Elsevier Limited ("Elsevier Limited"). The license consists of your order details, the terms and conditions provided by Elsevier Limited, and the payment terms and conditions.

Get the printable license.

Order Details | Billing & Contact Info

| | |
|---|---|
| License Number | 1764460771862 |
| License date | Aug 08, 2007 |
| Licensed content publisher | Elsevier Limited |
| Licensed content publication | Materials Science and Engineering: R: Reports |
| Licensed content title | Polymer-layered silicate nanocomposites: preparation, properties and uses of a new class of materials |
| Licensed content author | Michael Alexandre and Philippe Dubois |
| Licensed content date | 15 June 2000 |
| Volume number | 28 |
| Issue number | 1-2 |
| Pages | 63 |
| Type of Use | Thesis / Dissertation |
| Portion | Figures/table/illustration/abstracts |
| Quantity | 4 |
| Format | Print |
| You are the author of this Elsevier article | No |
| Are you translating? | No |
| Purchase order number | |
| Expected publication date | Sep 2007 |
| Elsevier VAT number | GB 494 6272 12 |
| Permissions price | 0.00 USD |
| Value added tax 0.0% | 0.00 USD |